

Department of Chemistry

The Surface Oxidation States of Copper Nanoparticles Generated  
by Ligand-Mediated Laser Ablation

Ashley Jade Mulder

This thesis is presented for the Degree of  
Doctor of Philosophy  
of  
Curtin University

June 2017



## *DECLARATION*

To the best of my knowledge and belief this thesis contains no material previously published by any other person except where due acknowledgment has been made.

This thesis contains no material which has been accepted for the award of any other degree or diploma in any university.

Signature:

Date: December 6, 2017



## ***ABSTRACT***

This thesis investigates the modification of the surface oxide of copper nanoparticles (CuNPs) generated by laser ablation. The copper nanoparticles are generated by exploiting the laser ablation synthesis in solution (LASiS) technique, whereby a piece of pure copper is ablated by an Nd:YAG pulsed laser. Studies were conducted on the role that nitrogen-based ligands had on the CuNPs formed, and it was shown that nitrogen containing tetrazole-based ligands had a profound effect on the UV-visible spectra of the formed CuNPs.

Further investigation reveals that the deprotonating ability of select tetrazole-based ligands is the cause for the differences in the UV-visible spectra. It is shown that the differences in the spectra are due to oxide formation on the CuNPs. The UV-visible results indicate that deprotonated tetrazoles provide oxidative control of the CuNPs, while the other ligands do not. Successive investigations into the size of the CuNPs formed showed, via various methods, that the CuNPs formed by LASiS have a similar size distribution. Exploratory investigations were done on the bandgap values of the formed CuNPs, as a difference in bandgap value is an indication of changes in the composition of the copper oxide present on the CuNPs. Qualitative chemical composition studies were also undertaken, namely XPS, revealing that the deprotonated tetrazole ligands have no Cu(II) present. This suggests that the oxide formed on the surface of the CuNPs is either Cu(I) oxide or Cu(II) oxide, depending on what ligand solution is present.

Further discussion about the oxide formation process is presented, demonstrating that it seems likely that all the CuNPs undergo oxidation to Cu(I) oxide initially. It is explained that the presence of Cu(II) oxide seen in the XPS is due to uncontrolled oxidation of the CuNPs, wherein the Cu(I)

oxide further oxidises to form Cu(II) oxide. It is concluded then that the deprotonated tetrazole ligands prevent this further oxidation from taking place.

Studies were conducted as a function of laser irradiation time in representative ligand solutions to give a mechanistic insight into the formation processes of CuNP. It was found that the formation of CuNPs followed a very similar trend across all three solutions, which indicates that the oxidation of the CuNPs occurs during the ablation process and not once the ablation is finished. It was shown in a previous chapter that the addition of a deprotonated tetrazole to a CuNP solution created in pure water once LASiS was finished did not replicate the result if the CuNPs were created in the deprotonated solution. This demonstrates that the oxidative control occurs during the LASiS process.

In conclusion, this thesis illustrates a method of controlling the oxidation of CuNPs formed by LASiS in aqueous solutions through the use of deprotonated tetrazole ligands.

## MANUSCRIPTS PUBLISHED AND IN PREPARATION

Mulder, A. J.; Tilbury, R. D.; Wright, P. J.; Becker, T.; Massi, M.; Buntine, M. A.; Laser-Based Formation of Copper Nanoparticles in Aqueous Solution: Optical Properties, Particle Size Distributions and Formation Kinetics.; *Australian Journal of Chemistry*, August **2017**.

Mulder, A. J.; Tilbury, R. D.; Werrett, M. V.; Wright, P. J.; Becker, T.; Jones, F.; Stagni, S.; Massi, M.; Buntine, M. A.; The Surface Oxidation States of Copper Nanoparticles Following Ligand-Mediated Laser Ablation.; *Manuscript in Preparation* **2017**.

## *ACKNOWLEDGEMENTS*

I first must thank my supervisor Professor Mark Buntine. For the length of this project he has always been full of knowledge and enthusiasm for the research undertaken. He always gave me an avenue to pursue my research in a manner that suited me, and knew when to chip in with some thoughtful guidance on a route to take. It has been an immense privilege to be able to do my research under your tutelage, and for the experience and skills gained I am incredibly grateful.

To Assoc. Professor Max Massi I extend immense thanks as well. The ability to work under your guidance and to further my knowledge is greatly appreciated. Being able to partake in research group meetings allowed me to broaden my chemistry knowledge and my critical scientific thinking. Grazie mille!

Dr. Thomas Becker and Dr. Franca Jones both deserve huge thanks for the assistance given while undertaking this research. Thank you to both for teaching me and guiding me in using the variety of microscopy apparatus that allowed me to undertake key research.

Thanks also goes to Peter Chapman for his immense technical knowledge. Some would suggest that without it, the department wouldn't run as well as it does.

To all the friends and colleagues in the department; thank you. It has been an incredible ride over the last few years. Thanks especially goes to Dr Phillip Wright and Dr Melissa Werrett for their knowledge and skill in synthetic chemistry that allowed me to use the tetrazole compounds presented in this research. To everybody else, thanks for the enjoyable times and the ability to work beside you all.

A huge thanks goes to my family and friends. Many years ago you gave up trying to understand what exactly it was that I was researching. Despite that, there was always ongoing encouragement and support. I am immensely grateful for what you allowed me to do and supported me whenever I needed it. To my Oma, thank you very much for taking the time to read and edit this thesis, highlighting my poor grammar and generally educating me in the finer points of the English language.

Last, but by no means least, I would like to thank my GOD and Father in Heaven who has given me this opportunity to do what I love.

# ***TABLE OF CONTENTS***

DECLARATION .....	iii
ABSTRACT .....	v
ACKNOWLEDGEMENTS.....	vii
TABLE OF CONTENTS .....	ix
LIST OF FIGURES.....	xiii
LIST OF TABLES AND SCHEMES.....	xxiv
COMMONLY USED ABBREVIATIONS AND SYMBOLS.....	xxvi
<b>Chapter 1: Introduction.....</b>	<b>1</b>
1.1 What is a Nanoparticle?.....	1
1.2 Noble Metal Nanoparticles .....	2
1.3 Metal Nanoparticle Synthesis .....	6
1.3.1 Bottom-Up Synthesis .....	6
1.3.2 Top-Down Synthesis .....	7
1.3.3 Laser Ablation Synthesis in Solution .....	8
1.4 Nanoparticle Characterisation .....	10
1.4.1 Methods of characterisation .....	10
1.4.2 Surface Plasmon Resonance .....	11
1.5 Copper Nanoparticles and Oxidation .....	15
1.6 Encapsulation of Nanoparticles .....	17
1.7 Research Objectives.....	18
<b>Chapter 2: Experimental Details .....</b>	<b>23</b>

2.1	N-donor ligands .....	23
2.2	Ablation Details .....	23
2.3	Atomic Force Microscopy (AFM) and Transmission Electron Microscopy (TEM) .....	26
2.4	pH Measurements .....	27
2.5	Bandgap Analysis .....	27
2.6	X-Ray Photoelectron Spectroscopy (XPS) .....	28
<b>Chapter 3: Copper Nanoparticles Generated by LASiS.....</b>		<b>31</b>
3.1	Copper Nanoparticle Surface Plasmon Resonance.....	31
3.2	LASiS in Aqueous Solutions .....	40
3.2.1	Pure Water .....	40
3.2.2	Neutral N-Donor Ligands.....	41
3.2.3	Deprotonated Tetrazolato Ligands.....	44
3.2.4	Alkylated Tetrazolato Ligands .....	47
3.2.5	The Curiosity of T-2Py .....	48
3.3	Conclusion .....	50
<b>Chapter 4: CuNPs and Oxidative Control .....</b>		<b>53</b>
4.1	Oxide Formation on CuNPs.....	53
4.2	Preventing Oxide Formation .....	61
4.3	The effect of charged species .....	64
4.3.1	Surfactants .....	64
4.3.2	Carboxylic Acid Analogues .....	66
4.3.3	Hydrazine .....	67

4.4	Conclusions.....	69
<b>Chapter 5: Particle Size Analysis .....</b>		<b>71</b>
5.1	Imaging Techniques.....	71
5.2	Principles of Microscopy.....	74
5.2.1	Electron Microscopy.....	74
5.2.2	Scanning Probe Microscopy .....	75
5.3	Imaging of Nanoparticles.....	76
5.3.1	Imaging Considerations.....	76
5.3.2	Analysis Considerations .....	78
5.3.3	AFM Analysis Results.....	78
5.3.4	TEM Analysis Results.....	91
5.3.5	Interpreting the Results .....	94
5.4	Conclusions.....	96
<b>Chapter 6: Further Exploration of CuNP-Ligand Interaction.....</b>		<b>97</b>
6.1	Changes in the pH of the solution.....	97
6.2	Bandgap Analysis.....	101
6.2.1	Calculating the bandgap of CuNPs.....	101
6.2.2	Experimental considerations .....	104
6.2.3	Results.....	104
6.3	XPS Studies.....	116
6.4	Conclusions.....	120
<b>Chapter 7: Further Theoretical Modelling of the Copper Oxide coated CuNPs .....</b>		<b>123</b>

<b>Chapter 8: Exploration of the Formation Process of CuNPs.....</b>	<b>131</b>
8.1 Time Dependent Formation Studies.....	131
8.1.1 Kinetic Analysis .....	131
8.1.2 Kinetic Analysis Results.....	134
8.1.3 Inferences .....	149
<b>Chapter 9: Conclusions and Future Work.....</b>	<b>151</b>
9.1 Future Work.....	151
9.1.1 Modification of CuNPs after LASiS .....	151
9.1.2 Annealing .....	152
9.2 Conclusions.....	157
<b>Chapter 10: References .....</b>	<b>163</b>
<b>Chapter 11: Appendices.....</b>	<b>177</b>
Appendix 2A .....	177
Appendix 4A .....	178
Appendix 5A .....	179
Appendix 5B .....	184
Appendix 6A .....	186

## LIST OF FIGURES

- Figure 1.1** Periodic table highlighting (in yellow) the elements that have been used to generate NPs via LASiS. Oxygen, chlorine and bromine have been highlighted since metal oxide and metal chloride/bromide NPs have been generated via LASiS. For more information see reference <sup>[39]</sup> from where the figure is adapted. ....3
- Figure 1.2** Illustrative representation of the surface plasmon resonance in a metal nanoparticle. This illustrates how the entire cloud of electrons that cover the surface of the nanoparticle oscillates in phase with the electric field of the incident light. Adapted with permission from reference <sup>[29]</sup>. Copyright 2013 John Wiley and Sons. ....13
- Figure 1.3** Structure of the ligands used in this study and their representative abbreviations used within this work: 1,10-phenanthroline (**phen**), 4,4'-bipyridine (**bipy**), pyridine (**Py**), 4-phenylpyridine (**4Ph-Py**), 1H-5-methyltetrazole (**T-Me**), 1H-5-phenyltetrazole (**T-Ph**), 3-(1H-tetrazol-5-yl)-pyridine (**T-3Py**), 4-(1H-tetrazol-5-yl)-pyridine (**T-4Py**), 2-*t*-butyl-5-methyltetrazole (**BuT-Me**), 2-*t*-butyl-5-phenyltetrazole (**BuT-Ph**), 3-(2-*t*-butyl-tetrazol-5-yl)-pyridine (**BuT-3Py**), 4-(2-*t*-butyl-tetrazol-5-yl)-pyridine (**BuT-4Py**), 2-(1H-tetrazol-5-yl)-pyridine (**T-2Py**) and 2-(2-*t*-butyl-tetrazol-5-yl)-pyridine (**BuT-2Py**).....21
- Figure 2.1** Schematics of the LASiS and annealing setup. TOP PANEL: Schematic of the LASiS setup, with the laser entering from the top of the vial and focused onto the copper plate. The vial is rotated on a stage to prevent the laser ablating a hole in the Cu plate. BOTTOM PANEL: Schematic of the annealing setup, with the laser entering from the side of the vial and focused in the middle of the vial. The focused laser energy then anneals the CuNPs in solution, rather than ablating away the glass vial. A small magnetic stirrer was placed in the bottom to ensure constant movement of the solution to prevent any localisation of the annealing process. ....25

<b>Figure 2.2</b>	Schematic representation of the contribution of Cu(I) and Cu(II) species to the $2p_{3/2}$ transition of copper. The shake-up transition, denoted by B, is due to the presence of Cu(II) species, with A1 being the direct contribution of all Cu(II) species, while the contribution of A2 is due to the presence of Cu(0) and Cu(I) .....	30
<b>Figure 3.1</b>	Simulated absorption spectrum of CuNPs of 10 nanometres in diameter demonstrating the SPB absorption feature present at 540 nm. The spectrum was generated from solving Equation 3.1 using tabulated values for $\epsilon_1$ and $\epsilon_2$ as described in the text. ....	33
<b>Figure 3.2</b>	Simulated absorption spectra of CuNPs of varying diameters, from 5 nm down to 1 nm in 1 nm steps generated by solving Equation 3.1. The dashed line is to draw the eye of the reader to illustrate the lack of damping and similarity in the shape of the spectra as the diameter decreases.....	34
<b>Figure 3.3</b>	Simulated absorption spectrum of CuNPs of 10 nanometres in diameter demonstrating the SPB absorption feature present at 550 nm. The spectrum was generated from solving Equation 3.5 using tabulated values for $\epsilon_1$ and size dependent values for $\epsilon_2$ modified via Equation 3.3 as described in the text. ....	35
<b>Figure 3.4</b>	Simulated absorption spectra of CuNPs of varying diameters, from 5 nm down to 1 nm in 1 nm steps generated by solving Equation 3.5 using size dependent values for $\epsilon_2$ modified via Equation 3.3. The dashed line is to draw the eye of the reader to illustrate how as the diameter of the CuNPs decrease, the SPB absorption feature peak wavelength position red-shifts and the feature broadens. ....	36
<b>Figure 3.5</b>	TOP PANEL: UV-visible spectrum of CuNPs prepared in pure water by laser ablation for 60 minutes. BOTTOM PANEL: SPB-normalised absorption spectrum of the data presented in the top panel to highlight the SPB feature and its position. The trace is presented in grey as it will be used for comparison for all the UV-visible spectra that will follow.....	42

<b>Figure 3.6</b>	SPB-normalised UV-visible absorption spectra of CuNPs generated by 60 minutes of LASiS in solutions of <b>bipy</b> (blue), <b>phen</b> (green), <b>Py</b> (purple) and <b>4Ph-Py</b> (red). The grey trace is that of CuNPs generated by 60 minutes of LASiS in pure water for the sake of comparison. INSET demonstrates the slight blue-shift w.r.t. CuNPs generated in pure water. ....	43
<b>Figure 3.7</b>	SPB-normalised UV-visible absorption spectra of CuNPs generated by 60 minutes of LASiS in solutions of <b>T-Ph</b> (blue), <b>T-4Py</b> (green), <b>T-3Py</b> (purple) and <b>T-Me</b> (red). The grey trace is that of CuNPs generated by 60 minutes of LASiS in pure water for the sake of comparison.....	45
<b>Figure 3.8</b>	SPB normalised UV-visible absorption spectra of CuNPs generated by 60 minutes of LASiS in solutions of <b>BuT-Ph</b> (blue), <b>BuT-4Py</b> (green), <b>BuT-3Py</b> (purple) and <b>BuT-Me</b> (red). The grey trace is that of CuNPs generated by 60 minutes of LASiS in blank water for the sake of comparison. INSET demonstrates the slight blue and red-shift w.r.t. CuNPs generated in pure water. ....	48
<b>Figure 3.9</b>	SPB normalised UV-visible absorption spectra of CuNPs generated by 60 minutes of LASiS in solutions of <b>T-2Py</b> (blue) and <b>BuT-2Py</b> (red). The grey trace is that of CuNPs generated by 60 minutes of LASiS in blank water for the sake of comparison.....	49
<b>Figure 3.10</b>	Representation of the tautomerisation of <b>T-2Py</b> . The pyridine substituent rotates about the C-C bond between the tetrazole and pyridine, therefore allowing the nitrogen to be in close proximity to the hydrogen from the tetrazole ring. While it is illustrated that the hydrogen is covalently bonded to both nitrogens, in reality the hydrogen would not be bonded. ....	50
<b>Figure 4.1</b>	Simulated absorbance spectra of Cu <sub>2</sub> O NPs (solid line) and CuO NPs (dashed line) both of 10 nanometres in diameter. The spectra were generated from solving Equation 3.1 using tabulated values for $\epsilon_1$ and $\epsilon_2$ as described in the text. ....	54

- Figure 4.2** Schematic representation of the studied Cu@Cu<sub>x</sub>O structures, where the x in Cu<sub>x</sub>O is either 1 or 2, for CuO or Cu<sub>2</sub>O, respectively.  $R_{Cu}$  is the radius of the copper core, while  $R_t$  is the radius of the entire NP. The thickness of the copper core,  $t_{Cu}$ , is the radius of the copper core,  $R_{Cu}$ . The thickness of the copper oxide,  $t_{Cu_xO}$ , is the radius of the copper core,  $R_{Cu}$ , subtracted from the total radius,  $R_t$ . When there is no Cu<sub>x</sub>O shell,  $R_t$  is equal to  $R_{Cu}$ , and  $t_{Cu_xO}$  is equal to 0. ....56
- Figure 4.3** TOP: Contour plot of simulated spectra of CuNPs of 10 nm in diameter and increasing  $t_{Cu_2O}/R_t$  ratio. The line is to draw the readers eye to illustrate the peak position of the SPB and how it red-shifts with increasing Cu<sub>2</sub>O shell thickness. BOTTOM: Individual simulated spectra of CuNPs of 10 nm in diameter at different  $t_{Cu_2O}/R_t$  ratios; 0 (red), 0.2 (orange), 0.4 (green), 0.6 (blue), 0.8 (purple). INSET illustrates how the SPB absorption intensity initially increases before damping.....58
- Figure 4.4** TOP: Contour plot of simulated spectra of CuNPs of 10 nm in diameter and increasing  $t_{CuO}/R_t$  ratio. The line is to draw the readers eye to illustrate the peak position of the SPB and how it red-shifts with increasing CuO shell thickness. BOTTOM: Individual simulated spectra of CuNPs of 10 nm in diameter at different  $t_{CuO}/R_t$  ratios; 0 (red), 0.2 (orange), 0.4 (green), 0.6 (blue), 0.8 (purple). INSET illustrates how the SPB absorption intensity initially increases before damping.....59
- Figure 4.5** SPB normalised UV-visible absorption spectra of CuNPs generated by 60 minutes of LASiS in acetone (blue). The grey trace is that of CuNPs generated by 60 minutes of LASiS in pure water for the sake of comparison. ....63
- Figure 4.6** SPB normalised UV-visible absorption spectra of CuNPs generated by 60 minutes of LASiS in 10<sup>-4</sup> molar solutions of CTAB (blue) and SDS (red). The grey trace is that of CuNPs generated by 60 minutes of LASiS in pure water for the sake of comparison. ....65

<b>Figure 4.7</b>	Structure of the two carboxylic acids used in this study. Benzoic acid ( <b>ben-acid</b> ) is an analogue of <b>T-Ph</b> and nicotinic acid ( <b>nic-acid</b> ) is an analogue of <b>T-3Py</b> . .....	66
<b>Figure 4.8</b>	SPB normalised UV-visible absorption spectra of CuNPs generated by 60 minutes of LASiS in $10^{-4}$ molar solutions of <b>ben-acid</b> (blue) and <b>nic-acid</b> (red). The grey trace is that of CuNPs generated by 60 minutes of LASiS in blank water for the sake of comparison. ....	67
<b>Figure 4.9</b>	SPB normalised UV-visible absorption spectra of CuNPs generated by 60 minutes of LASiS in $10^{-4}$ molar solution of hydrazine (blue). The grey trace is that of CuNPs generated by 60 minutes of LASiS in blank water for the sake of comparison.....	69
<b>Figure 5.1</b>	Combined particle size distribution and cumulative function distribution plot of the diameter of CuNPs generated by 60 minutes of LASiS in pure water. ....	79
<b>Figure 5.2</b>	Combined CuNP particle size distribution histogram (top panel) and cumulative function distribution (bottom panel) for NPs generated by 60 minutes of LASiS in $10^{-4}$ molar solutions of (from left to right, top to bottom): <b>bipy</b> , <b>phen</b> , <b>Py</b> and <b>4Ph-Py</b> . ....	81
<b>Figure 5.3</b>	Combined CuNP particle size distribution histogram (top) and cumulative function distribution (bottom) for NPs generated by 60 minutes of LASiS in $10^{-4}$ molar solutions of (from left to right, top to bottom): <b>T-Me</b> , <b>T-Ph</b> , <b>T-3Py</b> and <b>T-4Py</b> . ....	83
<b>Figure 5.4</b>	Combined CuNP particle size distribution histogram (top) and cumulative function distribution (bottom) for NPs generated by 60 minutes of LASiS in $10^{-4}$ molar solutions of (from left to right, top to bottom): <b>BuT-Me</b> , <b>BuT-Ph</b> , <b>BuT-3Py</b> and <b>BuT-4Py</b> .....	84
<b>Figure 5.5</b>	Combined CuNP particle size distribution histogram (top) and cumulative function distribution (bottom) for NPs generated by 60 minutes of LASiS in $10^{-4}$ molar solutions of (from left to right): <b>T-2Py</b> and <b>BuT-2Py</b> .....	85

<b>Figure 5.6</b>	Combined CuNP particle size distribution histogram (top) and cumulative function distribution (bottom) for NPs generated by 60 minutes of LASiS in acetone (left) and $10^{-4}$ molar solutions of CTAB (middle) and SDS (right). .....	87
<b>Figure 5.7</b>	Combined CuNP particle size distribution histogram (top) and cumulative function distribution (bottom) for NPs generated by 60 minutes of LASiS in $10^{-4}$ molar solutions of <b>nic-acid</b> (left), <b>ben-acid</b> (middle) and hydrazine (right).....	88
<b>Figure 5.8</b>	Combined CuNP particle size distribution histogram (top) and cumulative function distribution (bottom) for NPs generated by 60 minutes of LASiS in pure water (left) and $10^{-4}$ molar solutions of <b>bipy</b> (middle) and <b>phen</b> (right) .....	90
<b>Figure 5.9</b>	Combined CuNP particle size distribution histogram (top) and cumulative function distribution (bottom) for NPs generated by 60 minutes of LASiS in $10^{-4}$ molar solutions of (left to right, top to bottom) <b>T-3Py</b> , <b>T-4Py</b> , <b>BuT-3Py</b> and <b>T-2Py</b> . .....	93
<b>Figure 6.1</b>	Plot demonstrating the pH change in the solutions before N <sub>2</sub> bubbling, after N <sub>2</sub> bubbling and then after 60 minutes of LASiS. Not all data is presented here (see Table 6.1 for all the data) but a selection to illustrate the general trend. The solutions presented here are: <b>T-Me</b> (closed circle), <b>BuT-Me</b> (open circle), pure water (closed square), <b>Py</b> (open square), <b>T-2Py</b> (closed down triangle) and <b>BuT-2Py</b> (open up triangle). All solutions are $10^{-4}$ molar.....	98
<b>Figure 6.2</b>	SPB normalised UV-visible absorption spectra of CuNPs generated by 60 minutes of LASiS in pure water. One sample (blue trace) was degassed with N <sub>2</sub> gas for 60 minutes prior to LASiS, with continual degassing during LASiS, while the other sample (black trace) received no degassing treatment. ....	100

<b>Figure 6.3</b>	Tauc plot of CuNPs generated following 60 minutes of LASiS in pure water. The thin black line represents the extrapolation of the first linear portion of the spectra down to the abscissa. ....	105
<b>Figure 6.4</b>	Tauc plots of CuNPs generated following 60 minutes of LASiS in four $10^{-4}$ molar ligand solutions: a (red) <b>phen</b> ; b (purple) <b>Py</b> ; c, (green) <b>bipy</b> ; d, (blue) <b>4Ph-Py</b> . The thin black line represents the extrapolation of the first linear portion of the spectra down to the abscissa.....	106
<b>Figure 6.5</b>	Tauc plot of CuNPs generated following 60 minutes of LASiS in four $10^{-4}$ molar ligand solutions: a (red) <b>T-Ph</b> ; b (purple) <b>T-3Py</b> ; c, (green) <b>T-4Py</b> ; d, (blue) <b>T-Me</b> . The thin black lines represent the extrapolation of the first linear portion of the spectra down to the abscissa.....	108
<b>Figure 6.6</b>	Tauc plot generated from a theoretical absorption spectrum of CuNPs which are 10 nm in diameter, as derived by Equation 3.5. The thin black line represents the extrapolation of the first linear portion of the spectra down to the abscissa. ....	109
<b>Figure 6.7</b>	Tauc plot of CuNPs generated following 60 minutes of LASiS in acetone (neat, TOP PANEL) and four $10^{-4}$ molar ligand solutions (BOTTOM PANEL): a (red) <b>BuT-4Py</b> ; b (purple) <b>BuT-Me</b> ; c, (green) <b>BuT-3Py</b> ; d, (blue) <b>BuT-Ph</b> . The thin black line represents the extrapolation of the first linear portion of the spectra down to the abscissa. There is no linear extrapolation down to the abscissa in the case of acetone (see text). ....	111
<b>Figure 6.8</b>	Tauc plot of CuNPs generated following 60 minutes of LASiS in two $10^{-4}$ molar ligand solutions: a (red) <b>BuT-2Py</b> ; b (blue) <b>T-2Py</b> . The thin black line represents the extrapolation of the first linear portion of the spectra down to the abscissa. ....	112
<b>Figure 6.9</b>	Tauc plots of CuNPs generated by 60 minutes of LASiS in four $10^{-4}$ molar ligand solutions. TOP PANEL: a (red) SDS; b (blue) CTAB. BOTTOM PANEL: a (red) <b>ben-acid</b> ; b (blue) <b>nic-acid</b> . The thin black lines represent the extrapolation of the first linear portion of the spectra down to the abscissa. ....	114

**Figure 6.10** UV-visible spectra of CuNPs generated following 60 minutes of LASiS in pure water, with the addition of two ligands post-LASiS. TOP PLOT: UV-visible spectra of pure water (black trace), immediately after the addition of an equivalent amount of **T-Me** to bring the concentration to  $10^{-4}$  molar (red trace), and 72 hours after the addition of **T-Me** (green trace). BOTTOM PLOT: UV-visible spectra of pure water (black trace), immediately after the addition of an equivalent amount of hydrazine to bring the concentration to  $10^{-4}$  molar (red trace), 48 hours after the addition of hydrazine (green trace), and 120 hours after the addition of hydrazine (blue trace). ..... 118

**Figure 6.11** Correlation plot between SPB wavelength position and % Cu(II) content of CuNPs generated in the various solutions. The blue dots represent CuNPs generated in the deprotonated tetrazole solutions, the red dots represent CuNPs generated in the remaining ligand solutions, while the grey triangle represents CuNPs generated in pure water. .... 120

**Figure 7.1** Plots of the UV-visible absorbance data (grey trace) with the fitted theoretical data of a Cu@Cu<sub>2</sub>O NP as determined by MieLab (red trace). CuNPs are formed following 60 minutes of LASiS in pure water (TOP PLOT) and  $10^{-4}$  molar **T-Ph** (BOTTOM PLOT)..... 127

**Figure 7.2** Plot of the UV-visible absorbance data (grey trace) with the fitted theoretical data of a Cu@CuO NP as determined by MieLab (red trace). CuNPs are formed following 60 minutes of LASiS in pure water ..... 129

**Figure 8.1** Kinetic plots of the formation of CuNPs generated by LASiS in pure water. TOP PANEL: demonstration of the increase in the SPB absorption feature maxima over time. BOTTOM PANEL: demonstration of the variation in the location of the SPB absorption feature over time. In both panels the Y error bars represent one standard deviation from the mean. .... 135

**Figure 8.2** Kinetic plots of the formation of CuNPs generated by LASiS in a  $10^{-4}$  molar aqueous solution of **bipy**. TOP PANEL: demonstration of the increase in the SPB absorption feature maxima over time. BOTTOM

PANEL: demonstration of the variation in the location of the SPB absorption feature over time. In both panels the Y error bars represent one standard deviation from the mean..... 138

**Figure 8.3** Kinetic plots of the formation of CuNPs generated by LASiS in a  $10^{-4}$  molar aqueous solution of **T-4Py**. TOP PANEL: demonstration of the increase in the SPB absorption feature maxima over time. BOTTOM PANEL: demonstration of the variation in the location of the SPB absorption feature over time. In both panels the Y error bars represent one standard deviation from the mean..... 140

**Figure 8.4** Plots of the numerical integration and least squares fit of the UV-visible spectra of CuNPs generated by LASiS. The dots represent the experimental absorbance data shown in Figures 8.1 – 8.3, while the solid line represents the line of best fit to the data after applying the two-size regime illustrated in Scheme 8.1. TOP PANEL: CuNPs generated in pure water. MIDDLE PLOT: CuNPs generated in  $10^{-4}$  molar solution of **bipy**. BOTTOM PLOT: CuNPs generated in a  $10^{-4}$  molar solution of **T-4Py**..... 144

**Figure 8.5** Plots of the numerical integration and least squares fit of the UV-visible spectra of CuNPs generated by LASiS. The dots represent the experimental data obtained from Figures 8.1 – 8.3, while the solid line represents the line of best fit to the data after applying the three-size regime illustrated in Scheme 8.2. TOP PANEL: CuNPs generated in pure water. MIDDLE PLOT: CuNPs generated in  $10^{-4}$  molar solution of **bipy**. BOTTOM PLOT: CuNPs generated in a  $10^{-4}$  molar solution of **T-4Py**..... 146

**Figure 9.1** UV-visible plots of CuNP solutions taken during the annealing process. All CuNP solutions were generated by 60 minutes of LASiS. TOP PLOT: CuNPs generated in pure water after (red) 0 minutes of annealing, (green) 10 minutes of annealing, (blue) 20 minutes of annealing, (purple) 30 minutes of annealing. BOTTOM PLOT: CuNPs generated in a  $10^{-4}$  molar solution of **T-Me** after (red) 0 minutes of

	annealing, (green) 10 minutes of annealing, (blue) 20 minutes of annealing, (purple) 30 minutes of annealing, (pink) 40 minutes of annealing. ....	153
<b>Figure 9.2</b>	UV-visible plot of a CuNP solution taken during the annealing process. The CuNP solution was generated by 60 minutes of LASiS. The UV-visible plots of CuNPs generated in a $10^{-4}$ molar solution of <b>T-2Py</b> after (red) 0 minutes of annealing, (green) 10 minutes of annealing, (blue) 20 minutes of annealing, (purple) 30 minutes of annealing. ....	154
<b>Figure 9.3</b>	Size distribution histograms of CuNPs generated following 60 minutes of LASiS in a $10^{-4}$ molar solution of <b>T-2Py</b> followed by an annealing process. TOP PANEL: Size distribution of CuNPs after 0 minutes of annealing. MIDDLE PANEL: Size distribution of CuNPs after 10 minutes of annealing. BOTTOM PANEL: Size distribution of CuNPs after 20 minutes of annealing. ....	155
<b>Figure 11.1</b>	SPB-Normalised UV-vis absorption spectra of CuNPs generated by 60 minutes of LASiS in pure water (TOP PANEL) and $10^{-4}$ molar <b>T-4Py</b> solution (BOTTOM PANEL). In the top panel are six spectra from six different experiments conducted under identical conditions, and in the bottom panel are five spectra from five different experiments. The SPB location in the top panel varies from 638 – 655 nm, while in the bottom panel it varies from 594 – 602 nm. ....	177
<b>Figure 11.2</b>	SPB-Normalised UV-vis absorption spectra of CuNPs generated by 60 minutes of LASiS in $10^{-4}$ molar <b>Py</b> solution. In this plot are five spectra from five different experiments conducted under identical conditions. The SPB location varies from 632 – 642 nm. ....	178
<b>Figure 11.3</b>	UV-vis absorption spectra of CuNPs generated by 60 minutes of LASiS in $10^{-4}$ molar <b>T-4Py</b> solution (blue trace) and in neat acetone (black trace). ....	178
<b>Figure 11.4</b>	Representative AFM images of CuNPs generated in: (Left to right, top to bottom) Pure Water, <b>phen</b> , <b>bipy</b> , <b>Py</b> , and <b>4Ph-Py</b> . ....	179

<b>Figure 11.5</b> Representative AFM images of CuNPs generated in: (Left to right, top to bottom) <b>T-Me, T-Ph, T-3Py,</b> and <b>T-4Py</b> . .....	180
<b>Figure 11.6</b> Representative AFM images of CuNPs generated in: (Left to right, top to bottom) <b>BuT-Me, BuT-Ph, BuT-3Py,</b> and <b>BuT-4Py</b> . .....	181
<b>Figure 11.7</b> Representative AFM images of CuNPs generated in: (Left to right, top to bottom) <b>T-2Py, BuT-2Py,</b> acetone, CTAB, and SDS.....	182
<b>Figure 11.8</b> Representative AFM images of CuNPs generated in: (Left to right) <b>nic-acid, ben-acid,</b> and hydrazine.....	183
<b>Figure 11.9</b> Representative TEM images of CuNPs generated in: (Left to right) blank water, <b>Phen,</b> and <b>Bipy</b> .....	184
<b>Figure 11.10</b> Representative TEM images of CuNPs generated in: (Left to right, top to bottom) <b>T-3Py, T-4Py, BuT-3Py</b> and <b>T-2Py</b> .....	185
<b>Figure 11.11</b> UV-visible absorption data prior to Tauc analysis of CuNPs generated by 60 minutes of LASiS in: (left to right, top to bottom) pure water, <b>bipy, phen, Pyr</b> and <b>4Ph-Py</b> . .....	186
<b>Figure 11.12</b> UV-visible absorption data prior to Tauc analysis of CuNPs generated by 60 minutes of LASiS in: (left to right, top to bottom) <b>T-3Py, T-4Py, T-Me</b> and <b>T-Ph</b> . .....	187
<b>Figure 11.13</b> UV-visible absorption data prior to Tauc analysis of theoretical 10 nm diameter CuNPs (top left) and CuNPs generated by 60 minutes of LASiS in: (left to right, top to bottom) neat acetone, <b>BuT-3Py, BuT-4Py, BuT-Me</b> and <b>BuT-Ph</b> .....	188
<b>Figure 11.14</b> UV-visible absorption data prior to Tauc analysis of CuNPs generated by 60 minutes of LASiS in: (left to right, top to bottom) <b>T-2Py, BuT-2Py, nic-acid, ben-acid,</b> CTAB and SDS.....	189

## ***LIST OF TABLES AND SCHEMES***

<b>Table 1.1:</b>	Web of Science SCI-Expanded Database query .....	5
<b>Table 5.1</b>	Descriptive statistics of the particle size distributions determined by AFM of CuNPs generated by 60 minutes of LASiS in the listed solutions. ....	80
<b>Table 5.2</b>	Descriptive statistics of the particle size distributions as determined by TEM of CuNPs generated by 60 minutes of LASiS in the listed solutions. ....	91
<b>Table 6.1</b>	pH data for various ligand solutions before nitrogen gas bubbling, after nitrogen gas bubbling and after 60 minutes of LASiS.....	101
<b>Table 6.2</b>	CuNPs formed by LASiS in various solutions, their corresponding SPB absorption feature wavelength location, and the %Cu(II) present as calculated by Equation 2.1.....	117
<b>Table 7.1</b>	Table of statistics from the MieLab fitting. The values reported represent the thickness of each layer (in nm). Included is the $t_{\text{Cu}_2\text{O}}/R_t$ ratio which is calculated from the determined diameters/thicknesses.....	128
<b>Table 8.1</b>	The rate constants for the various transformations that result in the presented Chi-squared values from the numerical integration and least-squares fit of the absorbance data presented in Figures 8.1, 8.2 and 8.3. ...	143
<b>Table 8.2</b>	The rate constants for the various transformations that result in the presented Chi-squared values from the numerical integration and least-squares fit of the absorbance data presented in Figures 8.1, 8.2 and 8.3. ...	147
<b>Table 9.1</b>	Statistical data of the size distributions of CuNPs as presented in the histograms in Figure 9.3.....	156

<b>Scheme 8.1</b>	Illustration of the two-size regime for the formation of CuNPs. The model demonstrates the six different transformations that can take place in the formation of CuNPs. See text for an explanation of all terms highlighted in this model.....	142
<b>Scheme 8.2</b>	Illustration of the three-size regime for the formation of CuNPs. The model demonstrates the twelve different transformations that can take place in the formation of CuNPs. See text for an explanation of all terms highlighted in this model.....	145
<b>Scheme 8.3</b>	Illustration of the three-size regime for the formation of CuNPs. The model demonstrates the four different transformations that can take place in the formation of CuNPs as determined by the fitting of the experimental data. The TOP PANEL is representative of Scenario 1, while the BOTTOM PANEL is representative of Scenario 2, both described in Table 8.2. In both Scenarios, the red crosses demonstrate that the transformations between those species are not taking place.....	148

# *COMMONLY USED ABBREVIATIONS AND SYMBOLS*

$L_{\infty}$	Mean free path of electrons
$Q_{ext}$	Extinction cross section
$R_{Cu}$	Radius of Cu layer
$R_t$	Radius of NP
$t_{Cu}$	Thickness of Cu layer
$t_{Cu_xO}$	Thickness of $Cu_xO$ layer
$v_F$	Fermi velocity
$\epsilon_1$	Real part of the dielectric function
$\epsilon_2$	Imaginary part of the dielectric function
$\epsilon_m$	Permittivity of the medium
$\omega_p$	Bulk plasma frequency
$A(\lambda)$	Absorbance at wavelength $\lambda$
AFM	Atomic force microscopy
AgNP(s)	Silver nanoparticle(s)
AuNP(s)	Gold nanoparticle(s)
CCD	Charge-coupled device
CFD	Cumulative function distribution
CMC	Critical micelle concentration
core@shell	Coated nanoparticle with a core coated in a shell

CTAB	Cetyltrimethylammonium bromide
CTAC	Cetyltrimethylammonium chloride
Cu@Cu <sub>2</sub> O	Coated nanoparticle with a Cu core and a Cu <sub>2</sub> O coating
Cu@CuO	Coated nanoparticle with a Cu core and CuO coating
Cu <sub>2</sub> O	Copper (I) oxide
CuNP(s)	Copper nanoparticle(s)
CuO	Copper (II) oxide
Cu <sub>x</sub> O	Copper oxide where x = 1,2
DLS	Dynamic light scattering
EM	Electron microscopy
eV	Electron volt
FWHM	Full width half max
HOMO	Highest occupied molecular orbital
HRTEM	High-resolution TEM
<i>hν</i>	Photon energy
LASiS	Laser ablation synthesis in solution
LUMO	Lowest unoccupied molecular orbital
MNPs	Metal nanoparticles
Nd:YAG	Neodymium-doped yttrium aluminium garnet
NP(s)	Nanoparticle(s)
PLA	Pulsed laser ablation
PWD	Pulsed wire discharge

SDS	Sodium dodecyl sulphate
SEM	Scanning electron microscope
SPB	Surface plasmon band
SPR	Surface plasmon resonance
TEM	Transmission electron microscope
UV-visible	Ultra-violet visible
$V$	Volume of the NP
XPS	X-ray photoelectron spectroscopy
XRD	X-ray diffraction
$\gamma$	Damping constant
$\varepsilon$	Bulk dielectric function
$\varepsilon(\omega)$	Bulk dielectric function at $\omega$
$\lambda$	Wavelength
$\sigma$	Absorption cross section
$\sigma(\lambda)$	Absorption cross section at wavelength $\lambda$
$\omega$	Angular frequency

## Chapter 1: Introduction

### *1.1 What is a Nanoparticle?*

According to the Oxford English dictionary, a particle is “a minute fragment or a quantity of matter; the smallest perceptible or discernible part of an aggregation or mass.”<sup>[1]</sup> From a physical science point of view, however, this definition is not sufficient to accurately describe the wide-ranging sizes of particles that exist. From subatomic particles like the electron, to macroscopic particles such as powders, the size variation is many orders of magnitude. There are various classification criteria that exist to further refine the definition of ‘particle’, such as the United States Environmental Protection Agency’s classification which classifies a particle into one of the four following groups: supercoarse, coarse, fine and ultrafine.<sup>[2]</sup>

One well accepted refinement is the definition of a nanoparticle (NP), which according to the International Organization for Standardization is classified as a “nano-object with all external dimensions being in the nanoscale where the lengths of the longest and the shortest axes of the nano-object do not differ significantly.” A nanoparticle is then an object with three dimensions being in the nanoscale range, which is “approximately from 1 nm to 100 nm.”<sup>[3]</sup>

As the size and dimensionality of a material is reduced, its properties start to deviate from that of the bulk, with the emergence of new properties occurring. Many of these unique properties manifest when the dimensions of the material are reduced to approximately 100 nm. There is a certain amount of variation with this, however, with some unique properties emerging before the material is down to 100 nm in size, with others not appearing until well below 100 nm.<sup>[3]</sup> Nonetheless, because the majority of these novel properties

appear at around 100 nm in size, the upper limit is thusly set.<sup>[3,4]</sup> A lower size limit meanwhile has been set at 1 nm primarily to create a distinction between nanoparticles (NPs) and particles that are smaller, such as atomic clusters.<sup>[4,5]</sup> These smaller particles often have different properties to that of nanoparticles.

It is because of the emergence of these changed and new properties that nanoparticles are of significant scientific & industrial interest. A large body of research has been conducted on metal-based nanoparticles, with research being undertaken in many different fields. These include fundamental research,<sup>[6-10]</sup> imaging and sensing,<sup>[11-16]</sup> drug delivery and cancer therapy,<sup>[17-19]</sup> catalysis,<sup>[20-22]</sup> solar harvesting and semiconductors,<sup>[23-27]</sup> as well as niche areas such as magnetic nanoparticles.<sup>[28]</sup> More recent research has focused on using the changed and new properties of the metal NPs themselves to guide the synthesis and modification of a diverse range of nanostructures<sup>[29-31]</sup> and metamaterials.<sup>[32]</sup>

Of recent interest in the last few years is the manufacture of non-spherical NPs, and their various applications and uses.<sup>[10,29,33,34]</sup> As the shape of the NPs change, their properties start to differ from that of spherical NPs, leading to some interesting uses.<sup>[34,35]</sup> Of great interest is the role of non-spherical NPs in targeted drug delivery, with certain shapes of NPs resulting in different and/or improved biological interaction compared to spherical NPs of the same chemical makeup.<sup>[36,37]</sup>

## ***1.2 Noble Metal Nanoparticles***

Of some of the greatest interest to researchers has been the noble metal nanoparticles, with noble metals being metals that are resistant to corrosion and oxidation in moist air. This group of noble metals comprises

ruthenium, rhodium, palladium, silver, osmium, iridium, platinum and gold.<sup>[38]</sup> Mercury, rhenium and copper may also be included in this list, though these three are not resistant to oxidation and acidic attack. The two metals of most interest to nanoparticulate researchers are gold and silver as the physical properties of the other six noble metals (high melting point and high resistivity to acids) make them less attractive to work with. This is not to say that NP research does not occur in these other metals and metals that are not considered noble, it is just that gold and silver hold so much allure to researchers.

To illustrate the level of NP research that has been conducted on the elements in the periodic table, Figure 1.1 highlights the elements in the periodic table that have been studied in nanoparticulate form, while the 1987 review paper by Sugimoto highlights over 50 separate NP systems that had been studied until then.<sup>[33]</sup>

H																	He
Li	Be											B	C	N	O	F	Ne
Na	Mg											Al	Si	P	Se	Cl	Ar
K	Ca	Sc	Ti	V	Cr	Mn	Fe	Co	Ni	Cu	Zn	Ga	Ge	As	Se	Br	Kr
Rb	Sr	Y	Zr	Nb	Mo	Tc	Ru	Th	Pd	Ag	Cd	In	Sn	Sb	Te	I	Xe
Cs	Ba	*	Hf	Ta	W	Re	Os	Ir	Pt	Au	Hg	Tl	Pb	Bi	Po	At	Rn
Fr	Ra	^	Rf	Db	Sg	Bh	Hs	Mt	Ds	Rg	Cn	Nh	Fl	Mc	Lv	Ts	Og
		*	La	Ce	Pr	Nd	Pm	Sm	Eu	Gd	Tb	Dy	Ho	Er	Tm	Yb	Lu
		^	Ac	Th	Pa	U	Np	Pu	Am	Cm	Bk	Cf	Es	Fm	Md	No	Lr

**Figure 1.1** Periodic table highlighting (in yellow) the elements that have been used to generate NPs via LASiS. Oxygen, chlorine and bromine have been highlighted since metal oxide and metal chloride/bromide NPs have been generated via LASiS. For more information see reference <sup>[39]</sup> from where the figure is adapted.

As mentioned, of particular interest over the years has been nanoparticulate gold. Most famously a key component in the Lycurgus Cup, a 4<sup>th</sup> century Roman glass cage cup,<sup>[4,40]</sup> nanoparticulate gold has been used for centuries to stain glass. In 1857 Michael Faraday first recognised that it was very finely divided gold that was causing the red colour in stained glass, and it is attributed that he undertook the first modern chemical synthesis of gold nanoparticles.<sup>[41]</sup> In 1951 Turkevich pioneered a synthetic method of chemical reduction of gold nanoparticles (AuNPs),<sup>[42]</sup> which was refined by Frens in the 1970's.<sup>[43,44]</sup> Brust developed a new synthetic method in the early 1990's, specifically targeted at nanoparticle synthesis in organic liquids.<sup>[45]</sup> Silver nanoparticles (AgNPs) have also been the focus of a large amount of research over the years, though to not as great an extent as that of gold. AgNP synthesis was reported in the 1980's,<sup>[46]</sup> with interest increasing in the early 1990's.<sup>[47-49]</sup>

As a whole, research into nanoparticles has been steadily increasing since the 1990's. Barcikowski *et al.* reported that from 1998 up till early 2009 there were just over 185,000 results from a series of nanoparticle search terms (see Search #1 in Table 1) in Web of Sciences' Science Citation Index (SCI).<sup>[50]</sup> As of May 2017, using their same search terms and starting in 1998, this number has jumped up to over 870,000 results, as seen in Table 1. This increase represents a more than a fourfold increase in 9 years, though since then the SCI has been changed to the SCI-Expanded database and it is possible that this has increased the article count.

To determine in what areas this research is being conducted, a second search modifier was added to the original terms derived by Barcikowski *et al.*, the term being an AND Boolean operator of the six individual noble metals as well as copper. The results from the individual searches are shown

in Table 1, with the results showing that of the nearly 875,000 results, only 185,000, or 21%, of publications have dealt with noble metal NPs. An interesting find is that the total number of search results from Searches #4 through #12 total around 230,000, which is some 44,000 higher than Search #3. This would suggest that there is a certain amount of research being published where the focus is on more than one single noble metal, but rather two or more at one time.

**Table 1.1:** Web of Science SCI-Expanded Database query

Search set	Search string	SCI results
	“nanoparticles”	as of 8/5/17
#1	nanoparticle* OR nanocrystal* OR nanowire* OR nanotub* OR nanofibre* OR nanofiber* OR nanosphere* OR nanorod* OR nanodot* OR quantum dot* OR quantum wire*	873,921
#2	“noble nanoparticles” gold OR silver OR copper OR platinum OR palladium OR ruthenium OR rhodium OR iridium OR osmium	as of 8/5/17
#3	#1 AND #2	185,040
#4	#1 AND gold	95,771
#5	#1 AND silver	57,384
#6	#1 AND copper	30,032
#7	#1 AND platinum	21,329
#8	#1 AND palladium	14,616
#9	#1 AND ruthenium	6,648
#10	#1 AND rhodium	1,489
#11	#1 AND iridium	1,304
#12	#1 AND osmium	264

The reason for including copper into this search, despite its debated nature of noble metal status, becomes clear when one notices that it has the third highest number of hits. Copper nanoparticle (CuNP) synthesis was reported in the mid 1990's by Lisiecki and co-workers<sup>[51,52]</sup> and saw a surge in research in the mid 2000's.<sup>[53]</sup> Copper nanoparticles (CuNPs) have many potential uses, due to their excellent electrical conductivity, catalytic properties, nanolubrication applications as well their low cost in comparison to all the other noble metals. Copper also is bio-available and has excellent Raman scattering properties. However, the level of research conducted into CuNPs still isn't as extensive as that of gold or silver NPs. This might be due to the fact that copper oxidises very rapidly; the main reason of contention as to whether it should be classified as a noble metal. A lot of nanoparticle synthesis has thus been focused on oxide-free CuNPs, most successfully prepared and studied in an inert atmosphere.<sup>[52,54,55]</sup>

### ***1.3 Metal Nanoparticle Synthesis***

#### **1.3.1 Bottom-Up Synthesis**

There are two very different approaches to metal NP synthesis, these being 'bottom-up' or 'top-down' methods. The traditional reductive synthesis methods of reducing metal salts to metal nanoparticles can be considered a bottom-up method. The emergence of new techniques such as photochemical reduction,<sup>[53,56-60]</sup> electrochemical reduction<sup>[53,59-61]</sup> and microemulsion<sup>[53,57,59,61,62]</sup> methods can also be considered as bottom-up techniques. These methods start with the desired metal in a defined oxidation state (most often as a metal salt), and during the synthesis become reduced to the metal (0) form. Over time nanometre sized metal nanoparticles are formed from individual atoms. There is, however, an inherent problem with

the classical bottom-up chemical reduction synthesis. Unless the nanoparticles are separated from their original solutions, they are at risk of further side-reactions; side-reactions can occur between the nanoparticles themselves, or between the nanoparticles and any residual reactants. A drive in the last three decades to develop new, cleaner, and greener methods of nanoparticle synthesis led to the development of physical top-down methods.<sup>[53,60]</sup>

### 1.3.2 Top-Down Synthesis

In contrast to bottom-up methods, top-down methods start with a bulk source of metal that is most often already in the required metal (0) form. The bulk metal is physically reduced in size to the desired nanometre form. Top-down methods are also referred to as physical methods, as most of them employ a physical manipulation of the bulk to reduce it down in size. The two most common top-down methods are pulsed wire discharge (PWD)<sup>[53,59,60]</sup> (which includes a slightly modified form called the exploding wire method) and pulsed laser ablation (PLA).<sup>[29,39,53,59,60,63-69]</sup>

A less well-used technique employs the use of a ball mill, but there are many factors that can influence the quality of the final product.<sup>[53,59,60,70-72]</sup> PLA is not a new technique, being first mentioned in the early 1990's<sup>[73]</sup> with further development in the early 2000's. There are a few variations by research groups over the years in the exact nature of the PLA setup employed; however, the same basic elements exist: a high-powered pulsed laser system focused onto, and ablating away, a metal target within a liquid. It has been shown to be an easy manufacturing method and it is also relatively clean. Simply by ablating a sample of gold, silver or platinum in pure water has resulted in metal nanoparticles (MNPs) in solution.<sup>[74-76]</sup> The research presented in this thesis focuses on the use of PLA, specifically, a

method of PLA that has been termed ‘Laser Ablation Synthesis in Solution’ (LASiS) a method first reported by Amendola *et al.* in 2007.<sup>[77]</sup>

### 1.3.3 Laser Ablation Synthesis in Solution

Laser ablation synthesis in solution (LASiS) is a physical method of manufacturing NPs that is fast, easy and negates the use of potentially harmful chemical reducing agents. The NP solution that is created is clean, free of excess (or unwanted) reactants, and can be performed in aqueous or organic solvents. Ablation solutions can contain capping or encapsulating molecules to increase NP chemical functionality, stop oxidation, and/or contain and prevent coagulation.

The LASiS method employs the use of a high-powered laser to ablate a metal target. In most cases the laser is pulsed, most commonly pulsing in the 10’s of Hertz range and on the nanosecond full-width, half-maximum (FWHM) time scale. However, picosecond and femtosecond lasers have also been used for the ablation process.<sup>[53,59,60]</sup> Typically, due to availability and convenience, Nd:YAG lasers are the laser of choice, with the 1064 nm fundamental output most commonly being used. The first and second harmonic outputs (532 nm and 355 nm, respectively) of Nd:YAG lasers have also been used in various cases.<sup>[39,59,67,75,76,78-81]</sup>

The principle of the LASiS technique is the focusing of a pulsed laser source onto the surface of a target metal which is immersed in a liquid. The power of the laser is chosen such that the focused output is sufficient to ablate the surface of the metal, and the result of having the metal target immersed in a liquid is that the material that is ablated away is immediately dispersed into solution. With sufficient laser energy, the ablation of the target metal surface results in the formation of NPs.<sup>[39]</sup>

The LASiS process is quite complex in its nature, and the understanding of the formation processes of NPs in solution is something that has intrigued many research groups. The nature of the LASiS system leads to complexities that are not seen with bottom-up synthetic methods, as it is a complex dynamic mechanism. The nature of the pulsed laser system means that the dynamics of the system from shot-to-shot can be quite variable. Amendola and Meneghetti, in their review paper, summarise the substantial amount of work done by research groups and break down the LASiS process into various ultra-short time domains to explain the formation of NPs in solution.<sup>[39]</sup>

The actual ablation process on the surface of the metal target is relatively violent, and this is due to the presence of a localised plasma plume on the surface of the metal target. This plasma gives rise to a very localised, very sudden and large temperature change in the solution, such that, in aqueous solutions, bubbles are seen rising from the surface of the metal. It is likely that this is indicative of localised boiling water, but equally as likely that it is oxygen and hydrogen gas from dissociated water. Further, in volatile organic solvents, the power of the laser increases the rate of evaporation, and, given enough headspace gas, will catch alight from the laser passing through the gas.

It is important to characterise the NPs that are formed and these complexities in the LASiS process mean that analysing the solutions and the formation processes of NPs *in-situ* while LASiS is occurring is somewhat prohibitive. Therefore, the easiest way to analyse the solutions and examine the formation of NPs and to characterise the NPs is to study the solutions once the ablation process is concluded.

## ***1.4 Nanoparticle Characterisation***

### **1.4.1 Methods of characterisation**

No matter the route involved to produce NPs, the methods employed to identify and characterise the nanoparticles are common. Visualising the NPs is often the first step in characterising the NP solutions, and this can be achieved through various means, including scanning electron microscopy (SEM) or atomic force microscopy (AFM), but the more commonly used imaging technique is transmission electron microscopy (TEM). These various techniques allow for the imaging and inspection of the morphology and structure of the synthesised nanoparticles as well as the average size of the nanoparticles.<sup>[9,10,60,66]</sup> Dynamic light scattering (DLS) can also be used to determine the average size of nanoparticles, though the nature of the technique means that the determined size of the NPs is in most cases larger than when determined by SEM or TEM.<sup>[82,83]</sup> This is due to the DLS measuring the Brownian motion of particles in solution, which yields the diffusion coefficient of the NPs, from which the hydrodynamic radius of the NPs is determined.<sup>[84]</sup> The hydrodynamic radius incorporates solvent molecules that are static on the surface of the NP during motion, and thus the DLS incorporates these solvent molecules into the determined size. This results in the size of the NPs as found by DLS to be larger than that of the size found by SEM or TEM. The use of high resolution TEM (HRTEM) can also give information about the lattice structure of the nanoparticles.<sup>[85]</sup>

Aside from these imaging techniques, there are other techniques that can probe the elemental composition and structure of the nanoparticles. These include X-ray photoelectron spectroscopy (XPS) and X-ray diffraction (XRD) respectively.<sup>[86,87]</sup> Another very commonly used analysis technique is ultraviolet-visible (UV-visible) spectroscopy. The reason UV-visible

spectroscopy is used extensively is that there is an interesting absorption phenomenon that arises in NPs. Particles that have a small enough size absorb certain wavelengths of light and, in the case of metal nanoparticles, when dispersed in a liquid solution can change the colour of the solution. This phenomenon is due to surface plasmon resonance (SPR) and gives rise to a feature in the UV-visible absorption spectra referred to as the surface plasmon band (SPB).

#### 1.4.2 Surface Plasmon Resonance

This interesting absorption phenomenon that arises in small metallic particles may seem surprising at first: small-particle absorption spectra can have absorption features where the bulk has none, or multiple features where the bulk has only one absorption feature. This is due to the physical size of the particles. As the size of the particle decreases, the influence of the electromagnetic modes on the surface has a greater influence on the overall electromagnetic modes. This means that as the particle shape changes, and the dielectric function varies, the number, position and width of the absorption features changes.<sup>[88]</sup> This phenomenon of small metallic particles having absorption spectral features arise as the size of the material reduces, can be explained by first considering what occurs in the bulk material.

When one considers a bulk material, there is a vast number of electrons moving throughout the material lattice, with many different modes. Within the metal lattice there exists collective electron oscillations in the bulk material, first investigated by Tonks and Langmuir in 1929,<sup>[89]</sup> called plasma oscillations. These plasma oscillations are known as plasmons, and should be considered not as the movement of a single electron, but rather as a group of electrons moving under the urging of a Coulombic force.<sup>[88]</sup> These plasmons are referred to as bulk plasmons, as one considers them to be not

able to interact with the surface of the metal and are bound in the core of the bulk metal. As one can imagine, if you then take a bulk material and reduce its size, the plasmons no longer remain bounded but start to interact with the surface of the material. This was first realised by Ritchie in 1957,<sup>[90]</sup> when it was proposed that plasmons could exist on the surface of the material, in this case thin films, and became known as surface plasmons. Surface plasmons are therefore collective electron oscillations, which instead of occurring in the bulk, occur and exist at the interface of two materials.

When the size of the material is reduced such that we are now talking about a nanoparticle, the behaviour of surface plasmons changes. The surface-to-bulk ratio of the nanoparticle is highly tipped towards the surface, and as a consequence, the surface plasmons result in the exhibition of absorption features that are dominated by shape, and bear little resemblance to those of the bulk material (which has a greater density of bulk plasmons).<sup>[88]</sup> With the nanoparticles being so small, there exist wavelengths of light that can interact strongly with the surface plasmons, resulting in a polariton, and also giving rise to the unique absorption features.

If we consider a plasmon in a classical picture as an oscillation of free electrons in an object, the electrons will move to the left side of the object if placed in an electric field facing to the right. The electrons will try to cancel the field that is present, and, upon removing the electric field, the electrons will move to the right, being repelled by one another, and thence also being attracted to the bare positive ions on the right, as shown in Figure 1.2. This oscillation of electrons happens until the energy is lost due to resistance or dampening. In the case of a nanoparticle, the electric field of the incoming light interacts with the surface plasmons, oscillating the electric field back and forth. However, now the surface plasmons can oscillate resonantly if they

are excited by the correct wavelength of light, overcoming the resistance and dampening. This gives rise to surface plasmon resonance (SPR), the reason for the unique absorption features that are found in metal nanoparticles.<sup>[6,8,13,91,92]</sup>

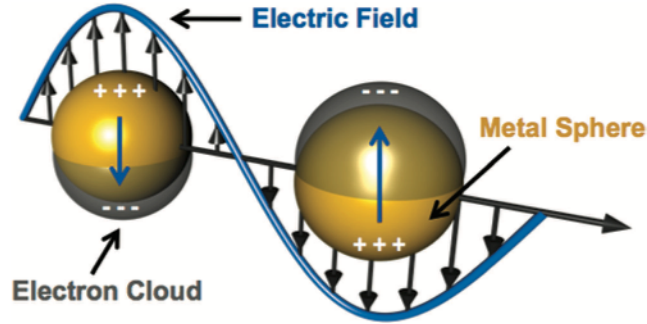


**Figure 1.2** Illustrative representation of the surface plasmon resonance in a metal nanoparticle. This illustrates how the entire cloud of electrons that cover the surface of the nanoparticle oscillates in phase with the electric field of the incident light. Adapted with permission from reference <sup>[29]</sup>. Copyright 2013 John Wiley and Sons.

The frequency of light that is required to resonate the surface plasmons is often called the Fröhlich frequency, named after Fröhlich who obtained an expression for the frequency of polarisation oscillation due to lattice vibrations in small dielectric crystals.<sup>[93]</sup> Although his work was with small dielectric crystals, it has been applied to small metallic nanoparticles. The reason for this is that this polarisation oscillation is in fact the lowest-order surface mode, the dipole oscillation, the mode that gives rise to SPR. The frequency that Fröhlich derived occurs when the real part of the permittivity equation ( $\epsilon_1$ ) is equal to twice the inverse of the surrounding medium ( $\epsilon_m$ ), and where the imaginary part ( $\epsilon_2$ ) is equal to zero:

$$\epsilon_1 = -2\epsilon_m; \epsilon_2 = 0. \quad (1.1)$$

The frequency where these conditions in Equation 1.1 are met is the frequency at which the SPR occurs in small metal nanoparticles, and gives rise to the unique absorption features seen in the spectra which we call the surface plasmon band (SPB).<sup>[6,8,91,94,95]</sup> This absorption feature arises due to the NPs absorbing a small amount of the incident electro-magnetic radiation at the Fröhlich frequency to maintain the resonance condition that is the SPR.

However, Equation 1.1 is only valid under the condition that the nanoparticles are small (<25 nm in diameter) and that, importantly,  $\varepsilon_2$  is weakly dependent on wavelength.<sup>[88,91]</sup> An extension to Equation 1.1 is therefore necessary to consider finite-sized particles, when  $\varepsilon_2$  is somewhat dependent on wavelength:<sup>[88]</sup>

$$\varepsilon = -\left(2 + \frac{12}{5}x^2\right)\varepsilon_m \quad (1.2)$$

where  $x$  is a size parameter related to the diameter of the spherical NP as described by Bohren and Huffman,<sup>[88]</sup> and  $\varepsilon = \varepsilon_1 + i\varepsilon_2$ , being the classical description of the material's permittivity. As  $x$  increases,  $\varepsilon$  therefore increases and the Fröhlich frequency will shift to longer wavelengths. When  $x$  is small, the shift in the frequency is minimal, but as the size increases the frequency shifts more markedly, and the SPB absorption feature will red-shift to longer wavelengths.

An interesting case arises for the case of a coated sphere. The reason for this is that the Fröhlich frequency of the metal nanoparticle changes as coatings are applied. If we were to consider the dielectric functions of the core and shell separately, and we also assume that the core volume is small

compared to the shell (which is a very reasonable assumption), then the Fröhlich mode for a coated particle becomes:

$$\varepsilon'_1 \simeq -2\varepsilon'_2 \quad (1.3)$$

where  $\varepsilon'_1$  is the dielectric function for a homogeneous sphere in a medium with dielectric function  $\varepsilon'_2$ . This is similar to Equation 1.1; however, it is now clear that  $\varepsilon_m$  has been replaced with  $\varepsilon'_2$ , with the dielectric of the medium now being less important than that of the coating. The effect of coating a sphere will result in the value of  $\varepsilon'_1$  changing, becoming more  $\varepsilon'_2$  in nature. The magnitude of the shift is dependent on the behaviour of the core ( $\varepsilon'_1$ ), as well as the thickness of the coating ( $\varepsilon'_2$ ).<sup>[88]</sup>

The thicker the coating becomes, the less influence the core has on the Fröhlich frequency, and this leads to the coated NP having a Fröhlich frequency that is more like the coating and less like the core, resulting in the SPB absorption feature changing. This change can either be a change in the intensity of the absorption feature, the wavelength position of the absorption feature, or a combination of the two.

### ***1.5 Copper Nanoparticles and Oxidation***

As previously mentioned, copper has received a lot of attention in the world of NP manufacture, not in the least due to its interesting properties and applications. However, the biggest challenge with copper, be it bulk or in nanoparticle form, is that it will start to oxidise in a matter of hours under ambient conditions.<sup>[96]</sup> It has been shown that if there is oxygen present during traditional chemical reduction synthesis of CuNPs, copper oxide nanoparticles are formed. Most often the NPs that are formed are either

complete copper oxide, or have a copper core with a copper oxide shell, with CuO and Cu<sub>2</sub>O being the oxides that form.<sup>[55,60,62,96-101]</sup>

To combat this, synthesis has to be undertaken in a completely inert atmosphere, and, for best success, completely de-oxygenated solvents, to prevent the oxidation of the NPs during their formation.<sup>[55]</sup> Gawande *et al.* in their review paper demonstrate how various methods are employed to combat oxidation formation, the chief method being the use of additives that cap the nascent CuNP surface to protect from oxidation, which even then is often only partially successful.<sup>[60]</sup>

Theoretical modelling of Mie's solution to Maxwell's equations has shown that the SPB feature of CuNPs should be centred around 550 nm,<sup>[51,52,102]</sup> and previous research has shown that chemical synthesis in anaerobic conditions gives a SPB centred between 570 – 590 nm.<sup>[51,52,102,103]</sup> Ablating CuNPs in pure acetone has yielded a SPB centred around 580 nm, and given that this is similar to CuNPs synthesised in anaerobic conditions, it can be assumed that the NPs formed are oxide free.<sup>[55,104,105]</sup>

When this ablation is undertaken in pure water, however, the SPB is weak, broad and centred around 670 nm, indicative of copper oxide on the surface of the NP.<sup>[106]</sup> As the SPB has been red-shifted, it is indicative of a change in the surface chemistry, that is, oxidation has taken place and the surface of the nanoparticle is no longer pure copper.<sup>[55]</sup> If we consider again the expression in Equation 1.3, we can regard the copper oxide coating to be the shell, and the pure copper centre to be the core. Coating with a copper oxide shell has changed the dielectric of the nanoparticle, and has shifted the SPB from 580 nm to 670 nm. This shift in the location of the SPB has been theorised to be tuneable by controlling the level of oxidation present, with

the larger the amount of oxide, the greater the red-shift,<sup>[107]</sup> and this has also been experimentally demonstrated.<sup>[99]</sup>

To combat oxide formation during LASiS experiments, additives can be incorporated into the solution to assist in preventing oxide formation. Typically, the additives are in aqueous solution, and either are surfactants or ligands, depending on their intended use. A common use is to prevent agglomeration of the NP solution. Here, typically surfactants such as sodium dodecyl sulphate (SDS) and cetyltrimethylammonium bromide (CTAB) or cetyltrimethylammonium chloride (CTAC) are used.<sup>[4,66,108-111]</sup> These are long chain organic molecules with a hydrophobic end and a hydrophilic end, which means they can form micelles and prevent the nanoparticles coming in close proximity to each other and agglomerating out of solution.

It's important to note that the literature demonstrates that the presence of these surfactants does little to prevent oxidation from occurring, as most report the formation of copper oxide coated CuNPs or pure copper oxide NPs.<sup>[59]</sup> Another way to try and prevent agglomeration, and also then to try and prevent oxide formation, is to use aqueous ligand solutions. The ligand choice is dictated by intended function: whether to increase NP surface chemical functionality, to prevent oxidation, to prevent coagulation, or a combination of the three. This concept lies at the heart of the project described herein.

## ***1.6 Encapsulation of Nanoparticles***

Encapsulation of metal nanoparticles by chelating ligands is an effective way to modify or create new properties in the nanoparticles themselves, and has seen the development of new catalytic pathways for chemical and biological transformations.<sup>[109,112,113]</sup> For example, chelating

metal nanoparticles with fluorophores has been shown to result in fluorescence enhancement,<sup>[114-117]</sup> quenching<sup>[118]</sup> and switching.<sup>[119]</sup> The behaviour of the chelating ligands in these examples opens up a possibility to protect the surface of, in this case, the CuNPs from oxidation.

Because common surfactants, such as SDS and CTAB, only offer micellar protection of the NPs, they potentially cannot stop oxidation of the NPs. Ligands however have a potentially stronger ligand binding affinity for the NPs, and by their nature of electronic interaction they have the potential to bind to the surface of the NPs.<sup>[79,80,111,120,121]</sup> This means that the ligands are potentially better suited to prohibit oxidation of the NPs. It is known that nitrogen has a strong affinity for copper<sup>[122,123]</sup> (much like sulphur does for gold<sup>[4,124,125]</sup>), and this is potentially due to the lone pair of electrons on the nitrogen. This affinity that nitrogen has for copper suggests that nitrogen based ligands would bind well to the CuNP surface.<sup>[80,121,126-128]</sup> It has been shown that changing the polarity of the solvent changes the level of oxidation of CuNPs, which indicates an electronic interaction between, in this case, the solvent and the NP, leading to a prohibition of oxide formation.<sup>[55]</sup>

Two well-known nitrogen based ligands, 1,10-phenanthroline and 4,4'-bipyridine, have successfully been used as ligands for CuNP, and the results indicate that there is binding to the copper surface.<sup>[80]</sup> When aqueous solutions of these two ligands were used, the SPB was centred around 610-615 nm, a good indication of reduced oxide formation.<sup>[80]</sup>

## ***1.7 Research Objectives***

A remaining challenge then is to easily generate CuNPs via LASiS in aqueous solutions that are oxide free. There is also a real advantage to being able to reliably create NPs that have a quasi-tuneable surface plasmon band

(SPB) location. Having the ability to control at what wavelength the SPB feature occurs, opens the door for novel CuNP applications, while also understanding somewhat better the formation processes allows for fine-tuning of the properties of the CuNPs generated.

It has been illustrated with previous literature that CuNPs can have their SPB absorption feature location shifted from 570 nm all the way to 680 nm due to the presence of an oxide coating, which has potential to allow for tunability in the absorption feature location in CuNPs. To this end an objective of this research is to see if it is possible to generate oxide-free CuNPs via LASiS in aqueous solutions with the use of nitrogen based ligands. This will be investigated through, in part, the use of UV-visible spectroscopy that will allow the SPB absorption feature to be studied. The employment of classical imaging techniques will allow for the visualisation of the created NPs as well as an analysis of the distribution of the particle size diameters. It is important to study the particle size distributions of the generated CuNPs, as it is possible that fluctuations in the particle size distributions can affect the position of the SPB absorption feature, as Equation 1.3 demonstrates.

The ligands chosen to be examined in this research are tetrazole-based compounds. Tetrazoles are a bioisostere of the carboxylate group, consisting of a five-membered ring containing four nitrogen atoms and one carbon atom. They have garnered attention recently due to their use in organometallic complexes,<sup>[129,130]</sup> and with the large number of nitrogen atoms present should have some chemical interaction with the CuNP surface, hopefully preventing oxidation. A variety of tetrazole-based ligands were chosen to be examined, with a focus in particular on pyridine-substituted tetrazole ligands.

The ligands that have been studied in this research are illustrated in Figure 1.3. Along with the tetrazole-based ligands, four pyridine-based ligands were studied for the sake of comparison. This was done due to **phen** and **bipy** having previously researched in relation to CuNPs,<sup>[80]</sup> and both **Py** and **4Ph-Py** were studied to see if there was any difference in the results due to bulkiness of ligand and slight variations in structure. **T-2Py**, **T-3Py** and **T-4Py** were studied to see if there was any difference in the interaction between the ligand and the CuNPs when the relative position of the pyridine nitrogen changed with respect to the tetrazole motif. As shown in Figure 1.3, for these compounds, the pyridine-based nitrogen is in the 2, 3 or 4 position, respectively. **T-Me** and **T-Ph** were examined to see what effect the presence or the absence of a pyridine ring has, with **T-Me** having no ring substituent, while **T-Ph** only has a phenyl ring substituent. These last two ligands then primarily focus on the effect of the tetrazole, and whether the size of the substituent on the tetrazole ring influences the interaction the ligands have with the CuNPs. All five tetrazole-based ligands have been alkylated with 2-Methylpropan-2-ol to form a *t*-Butyl substituent on the tetrazole ring. The alkylation has the effect of removing the ability of these ligand to deprotonate in aqueous solutions.

The results of the research undertaken as part of this project are presented in the following chapters. Chapter Two outlines the experimental conditions under which the LASiS of CuNPs was conducted, along with the details of the various analysis techniques employed to examine the CuNPs that were generated. Chapter Three starts by introducing the concept of the surface plasmon band (SPB), and at what wavelength, theoretically, the SPB of CuNPs should be centred at. It then shows and explains the results seen from the UV-visible absorption of CuNPs generated by LASiS in a range of ligand solutions. Primarily, it examines the differences in the UV-visible

spectra of CuNP solutions generated in pure water and the ligands shown in Figure 1.3, and how they compare to the theoretical spectra.

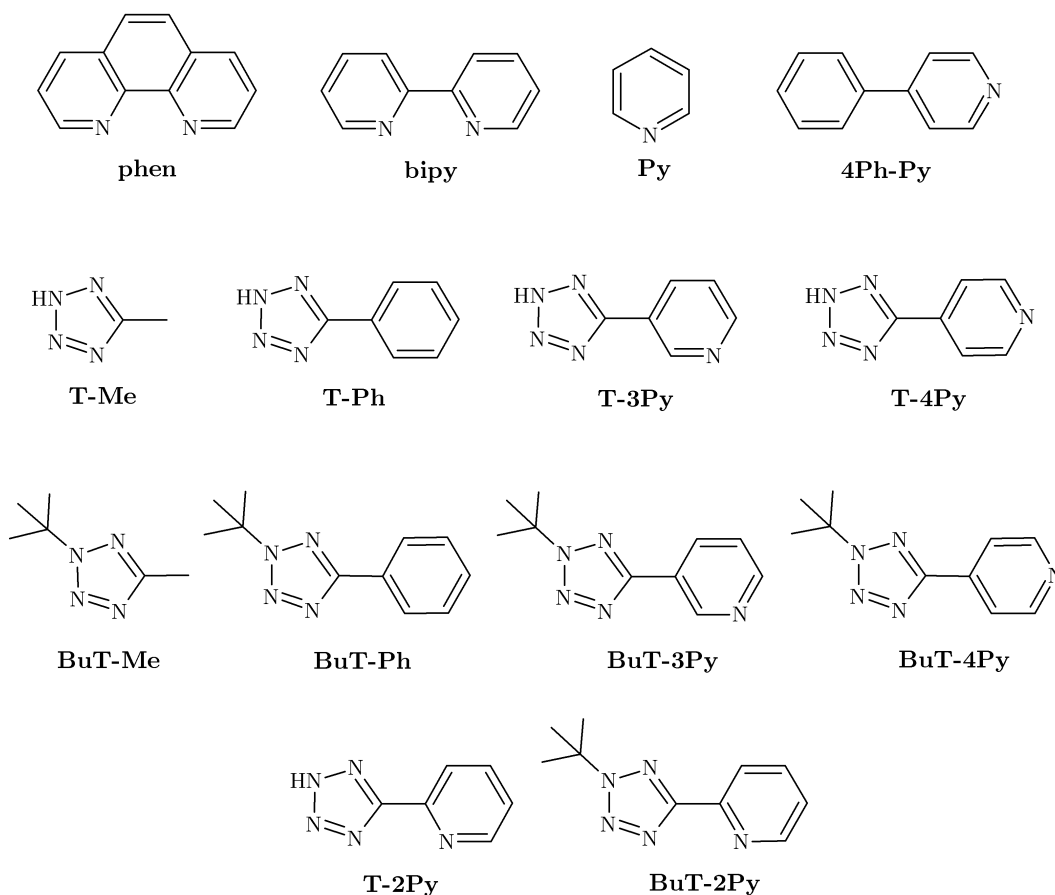


**Figure 1.3** Structure of the ligands used in this study and their representative abbreviations used within this work: 1,10-phenanthroline (**phen**), 4,4'-bipyridine (**bipy**), pyridine (**Py**), 4-phenylpyridine (**4Ph-Py**), 1H-5-methyltetrazole (**T-Me**), 1H-5-phenyltetrazole (**T-Ph**), 3-(1H-tetrazol-5-yl)-pyridine (**T-3Py**), 4-(1H-tetrazol-5-yl)-pyridine (**T-4Py**), 2-*t*-butyl-5-methyltetrazole (**BuT-Me**), 2-*t*-butyl-5-phenyltetrazole (**BuT-Ph**), 3-(2-*t*-butyl-tetrazol-5-yl)-pyridine (**BuT-3Py**), 4-(2-*t*-butyl-tetrazol-5-yl)-pyridine (**BuT-4Py**), 2-(1H-tetrazol-5-yl)-pyridine (**T-2Py**) and 2-(2-*t*-butyl-tetrazol-5-yl)-pyridine (**BuT-2Py**).

Chapter Four goes into the principle of using electron microscopy to visualise the CuNPs that are formed, and demonstrates that the particle size distributions of the CuNPs, as determined by AFM and TEM, are fairly

consistent between all ligand solutions. Chapter Five starts by explaining how CuNPs can oxidise and cause a shift in the SPB position, and demonstrates this with a theoretical model. It then examines the formation of CuNPs in several different solutions to investigate and try to explain the results that are seen in Chapter Three. These solutions were chosen to illustrate how the oxidation of CuNPs may be prevented by the presence of a tetrazole-based ligand.

Chapter Six describes the pH analysis which was undertaken on select ligand solutions, with the results showing that the pH variation does not account for the results observed. Bandgap analysis was employed to try and get a better understanding of the oxidation of the CuNPs, with XPS analysis providing further chemical information on the makeup of the CuNPs. Chapter Seven goes into further discussion about the theoretical calculations presented in Chapter Four, namely how the results presented in Chapters Three and Four seem to be at odds with what is presented in Chapter Six. An explanation for the variation in the results is proposed, such that the CuNPs are being oxidised similarly to copper (I) oxide across all ligand solutions, but that select tetrazole-based ligand solutions are prohibiting further oxidation of the CuNPs to copper (II) oxide.

Chapter Eight describes some time dependent formation studies, illustrating that the formation of the CuNPs seems to be independent of the ligand solution, and that the CuNPs appear to be undergoing a similar oxidation process. Finally, Chapter Nine demonstrates some proof-of-concept experiments showing that modification of the size distribution of the CuNPs by an annealing process once LASiS is completed, is possible. The chapter then concludes by summarising all the results that are presented in this thesis and offering final remarks.

## Chapter 2: Experimental Details

### 2.1 *N-donor ligands*

1,10-phenanthroline (**phen**), 4,4'-bipyridine (**bipy**), pyridine (**Py**), 4-phenylpyridine (**4Ph-Py**) and 1H-5-methyltetrazole (**T-Me**) were obtained from Sigma Aldrich and used as received without any further purification. Benzoic acid (**ben-acid**), pyridine-3-carboxylic acid (**nic-acid**), sodium lauryl sulphate (**SDS**) and hexadecyl-trimethyl-ammonium bromide (**CTAB**) were obtained from Chem-Supply and used without any further purification. 2-(1H-tetrazol-5-yl)-pyridine (**T-2py**),<sup>[129]</sup> 2-(2-*t*-butyl-tetrazol-5-yl)-pyridine (**BuT-2py**),<sup>[131]</sup> 3-(1H-tetrazol-5-yl)-pyridine (**T-3py**)<sup>[132]</sup>, 3-(2-*t*-butyl-tetrazol-5-yl)-pyridine (**BuT-3py**),<sup>[133]</sup> 4-(1H-tetrazol-5-yl)-pyridine (**T-4py**),<sup>[134]</sup> 4-(2-*t*-butyl-tetrazol-5-yl)-pyridine (**BuT-4py**),<sup>[134]</sup> 1H-5-phenyltetrazole (**T-Ph**),<sup>[132]</sup> 2-*t*-butyl-5-phenyltetrazole (**BuT-Ph**)<sup>[135]</sup> and 2-*t*-butyl-5-methyltetrazole (**BuT-Me**)<sup>[135]</sup> were provided for use in this project, having been prepared according to previously published procedures.

### 2.2 *Ablation Details*

The LASiS experimental method employed in our laboratory has been previously reported.<sup>[108,136,137]</sup> CuNPs were prepared in a similar method to that reported by Tilaki and co-workers,<sup>[138]</sup> and by Haram and Ahmad,<sup>[139]</sup> which had its beginnings in a method that was used by Nedersen and co-workers in 1993,<sup>[73]</sup> and which was further developed by the group of Kondow in the early 2000's.<sup>[74-76]</sup> CuNPs presented here in this research were prepared in either ultrapure water (purified with a Lab PURE Plus UV system) or in the presence of a variety of N-donor ligands at a concentration of  $1 \times 10^{-4}$  M.

Laser ablation was performed for 60 minutes at 1064 nm using a Continuum Surelite II Nd:YAG laser operating at 10 Hz and 7.5 mJ/pulse with a pulse width of 7 ns (FWHM) and a beam diameter (before focussing) of 8 mm. The laser was focused with a plano-convex lens having a focal length of 250 mm (see the schematic in Figure 2.1). This equates to a fluence of approximately  $2 \times 10^5$  Joules per  $\text{m}^2$ , as calculated by the following equation as presented in Siegman:<sup>[140]</sup>

$$d_0 \approx \frac{2f\lambda}{D} \quad (2.1)$$

where  $d_0$  is the effective diameter of a focused Gaussian beam,  $f$  is the focal length of the lens,  $\lambda$  is the wavelength of the laser radiation and  $D$  is the diameter of the laser beam before focusing.

The copper substrate is high purity, electronic grade oxygen-free copper alloy C101 (99.90%). To prevent the laser ablation process burning a hole through the metal target, a rotation stage rotating at  $1 \text{ rev min}^{-1}$  was employed.

The UV-visible absorption spectra of samples prepared by the above method were recorded using a Cary 4000 UV-visible spectrometer for the spectra reported in Chapters 3, 4, 5 and 6. The bandgap plots in Chapter 5.5 were also generated from absorption data obtained from this instrument.

The annealing of CuNPs performed in Chapter 9.1 was performed at 600 nm using a Spectra-Physics Quanta-Ray Pro-230-10 Nd:YAG laser operating at 532 nm and 10 Hz pumping a Spectra-Physics Cobra-Stretch dye laser. The dye that was pumped was Rhodamine B at 0.35 g/L in pure ethanol, generating irradiation at 600 nm at 5 mJ/pulse and 6 mm in diameter before focusing. The laser was focused with a plano-convex lens having a focal length of 250 mm (see the Schematic in Figure 2.1).

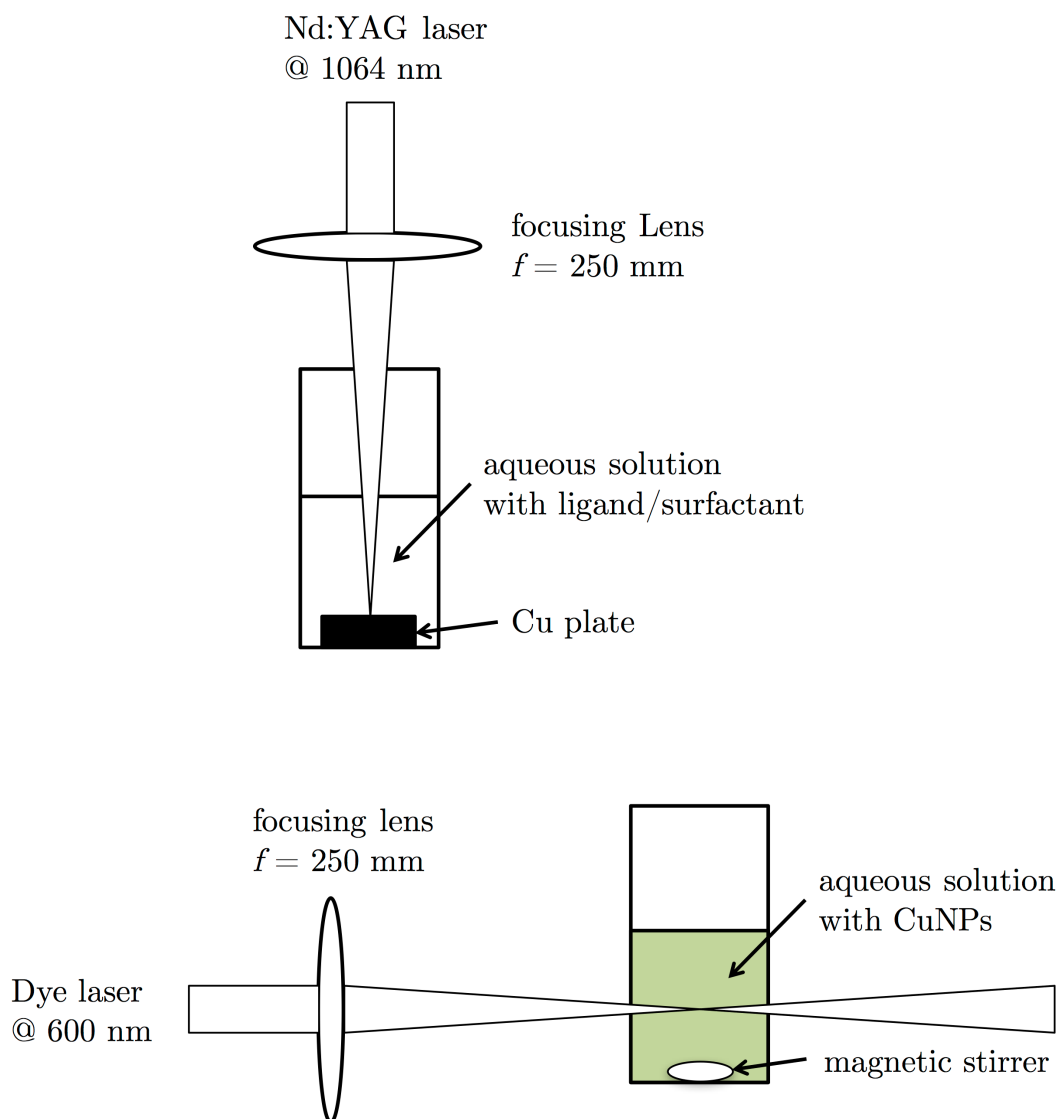


**Figure 2.1** Schematics of the LASiS and annealing setup. TOP PANEL: Schematic of the LASiS setup, with the laser entering from the top of the vial and focused onto the copper plate. The vial is rotated on a stage to prevent the laser ablating a hole in the Cu plate. BOTTOM PANEL: Schematic of the annealing setup, with the laser entering from the side of the vial and focused in the middle of the vial. The focused laser energy then anneals the CuNPs in solution, rather than ablating away the glass vial. A small magnetic stirrer was placed in the bottom to ensure constant movement of the solution to prevent any localisation of the annealing process.

The UV-visible absorption spectra that were used to generate the kinetic data in Chapter 8, as well as the annealing data in Chapter 9.1 were recorded on a PG Instruments T90+ UV-visible spectrometer.

The UV-visible absorption spectra that are presented in Chapters 3, 4, 5 and 6 are representative of spectra recorded in at least 3 different experiments conducted under identical conditions. Presented in Appendix 2A are some representative spectra to illustrate the reproducibility.

### ***2.3 Atomic Force Microscopy (AFM) and Transmission Electron Microscopy (TEM)***

All samples synthesised following 60 minutes of 1064 nm irradiation were prepared for atomic force microscopy (AFM) analysis. The CuNP samples were prepared for examination by depositing a drop of CuNP solution on a freshly cleaved mica surface, and then spun at 2000 rpm for 4 minutes, after which point the procedure was repeated. AFM topography measurements were performed using a Dimension FastScan AFM system (Bruker, California, USA) in Tapping Mode. AFM probes of type TESPA (Bruker, California, USA) with a resonant frequency of 320kHz, a spring constant of 42 N/m and a tip radius of 8nm were used for the acquisition of all AFM data. The data were processed and analysed with the Gwyddion AFM analysis software program.<sup>[141]</sup> Processing steps included data levelling by mean plane subtraction, facet alignment, row alignment, horizontal scar correction and a plane level. If needed, a 2<sup>nd</sup> degree polynomial background subtraction was executed. The size distribution of the data of the imaged nanoparticles was extracted from the height distribution, *i.e.*, the diameter, of the nanoparticles, the data then being processed in SigmaPlot<sup>™</sup> to generate the size distributions. SigmaPlot's descriptive statistics tool was used to

generate the mean and  $1-\sigma$  standard deviation of the size distributions as reported in Table 5.1 and Table 9.1.

As a calibration of the particle size distributions determined via AFM, selected ligated CuNP samples were also characterised by transmission electron microscopy (TEM). TEM experiments were undertaken on a Jeol 2011 electron microscope. A drop of CuNP solution was deposited on a Formvar coated 100-mesh nickel grid (SPI Supplies, Pennsylvania, USA) and dried at room temperature under reduced pressure and left to dry in a desiccator. The TEM images were captured at an emission energy of 200 kV and a magnification of 200,000X. Images were collected using a digital camera with supplier-provided software, and all recorded images were analysed using the ImageJ<sup>™</sup> analysis program to determine particle size, and SigmaPlot<sup>™</sup> to generate the size distributions. SigmaPlot's descriptive statistics tool was used to generate the mean and  $1-\sigma$  standard deviation of the size distributions as reported in Table 5.2.

## ***2.4 pH Measurements***

pH measurements were undertaken using an Elmetron CP-511 pH meter with an attached Ag/AgCl pH probe and temperature probe. The pH of the solutions was measured before LASiS and before N<sub>2</sub> bubbling, before LASiS and after 30 minutes of N<sub>2</sub> bubbling, and finally after N<sub>2</sub> bubbling and 60 minutes of LASiS.

## ***2.5 Bandgap Analysis***

To calculate the bandgap from the optical absorption spectra, the UV-visible absorption spectra need to be converted into a suitable form. While

the UV-visible absorption spectra recorded by the instrument have their x-axis in wavelength scale, the classical Tauc analysis requires it in the electron volt (eV) scale. Therefore, the absorption spectra were converted from a nanometre scale to an eV scale, and the absorbance data was transformed per Equation 5.3 as seen in Chapter 5.5.1. The transformed data was plotted against electron volts, with the linear portion of the plotted data near the absorption edge extrapolated down to the x-axis. To determine the location and first instance of the linear portion of the data, the first derivative of the data was plotted, the linear portion of the original data presenting itself as a flat horizontal feature in the derivative plot.

## ***2.6 X-Ray Photoelectron Spectroscopy (XPS)***

The following XPS analysis was conducted by Rhys Tilbury on CuNP samples prepared by the author.

Samples prepared following 60 minutes of 1064 nm irradiation were also prepared for X-ray photoelectron spectroscopy (XPS) analysis. One drop of solution was placed upon a Pt coated silicon wafer. Solvent was removed from the samples under reduced pressure and left to dry in a desiccator.

The XPS experiments were performed on a Kratos Axis Ultra spectrometer (Kratos Analytical, Manchester, UK) equipped with an Al  $K\alpha$  monochromatic X-ray source running at 15 kV, a hemispherical electron energy analyser, and a multichannel detector. The test chamber pressure was maintained below  $2 \times 10^{-9}$  Torr during spectral acquisition.

The XPS binding energy (BE) was internally referenced to the aliphatic C (1s) peak (BE, 284.6 eV). Survey spectra were acquired at an analyser pass energy of 100 eV, while high-resolution spectra were acquired with a pass energy of 20 eV.

Consistent with previous studies from our laboratory,<sup>[142]</sup> spectra were analysed by fitting each peak with Gaussian-Lorentz functions after subtracting the background using the CasaXPS data processing software package<sup>[143]</sup> under the constraint of setting a reasonable BE shift and characteristic full width at half maximum range. Atomic concentrations were calculated by normalising peak areas to the elemental sensitivity factor data provided by the CasaXPS database.

For each recorded XPS spectrum, the data were deconvoluted to obtain the relative population of each copper oxidation state. This was achieved by fitting the spectra to a sum of peaks using non-linear least squares minimisation. A Shirley background was applied to remove the electron scattering background and maintain the intrinsic line shape from the raw data.<sup>[144]</sup> A pseudo-Voigt function comprised of the sum of Gaussian (30%) and Lorentzian (70%) functions was used, following the approach described by Biesinger et al.<sup>[145]</sup> In this approach, as the binding energies (BE) of Cu(0) and Cu(I) are unresolvable, these two oxidation states are considered to generate a single emission peak. Due to this, a determination is therefore made between the relative proportion of Cu(II) versus the sum of Cu(0) plus Cu(I) (which is now referred to as ‘Cu(0+I)’) contributing to both the main  $2p_{3/2}$  transition and its associated satellite (or ‘shake-up’) transition according to:

$$\%Cu(II) = \frac{B + A1}{A + B} \cdot 100 \quad (2.2)$$

where  $A1$  represents the contribution of Cu(II) to the main  $2p_{3/2}$  transition and  $A$  represents the sum of Cu(II) and Cu(0+I). By contrast only Cu(II) contributes to the shake-up transition, represented as  $B$  in the equation above. The total intensity from Cu(II) species is represented in the

combination of the signals from the direct photoelectron emission ( $A1$ ) and the shake-up photoelectron emission ( $B$ ), as schematically shown in Figure 2.2, while the only contribution to  $A2$  is from the unresolvable  $\text{Cu}(0)$  and  $\text{Cu}(I)$  combination.

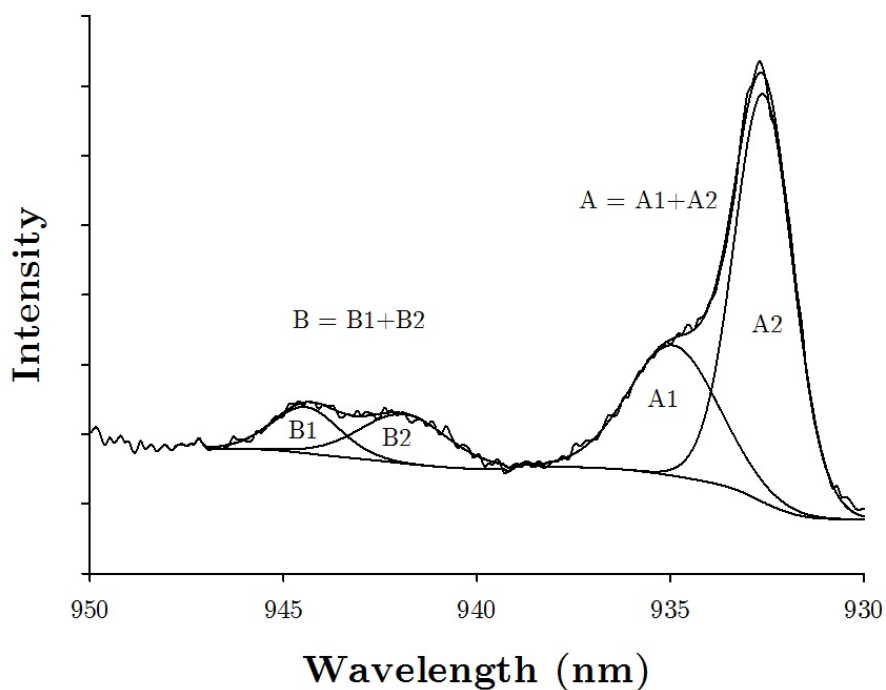


**Figure 2.2** Schematic representation of the contribution of  $\text{Cu}(I)$  and  $\text{Cu}(II)$  species to the  $2p_{3/2}$  transition of copper. The shake-up transition, denoted by  $B$ , is due to the presence of  $\text{Cu}(II)$  species, with  $A1$  being the direct contribution of all  $\text{Cu}(II)$  species, while the contribution of  $A2$  is due to the presence of  $\text{Cu}(0)$  and  $\text{Cu}(I)$

## Chapter 3: Copper Nanoparticles Generated by LASiS

### 3.1 Copper Nanoparticle Surface Plasmon Resonance

In 1908 Mie reported a theoretical model that accounts for the distinct optical properties of small metal nanoparticles, specifically the unique surface plasmon resonance (SPR).<sup>[146]</sup> Mie's ground-breaking work involved solving Maxwell's equations for an electromagnetic light wave interacting with a small sphere having the same dielectric constant as the bulk material. Mie presented a solution that describes the extinction spectra of spherical particles of arbitrary size,<sup>[147]</sup> particularly small metallic particles in which the total extinction coefficient is a product of the total electric and magnetic multipole oscillations that are created in the NPs by interacting with electromagnetic radiation.<sup>[91]</sup>

Mie's theory has found wide spread subsequent use, because if the dielectric of the material is known and the size of the NPs is smaller than the wavelength of light, it is straightforward to calculate the NP extinction spectra.<sup>[8,91,147]</sup> The seemingly complex equations become less complex as the size of the NPs decrease and as the number of oscillation modes decrease. As the NPs decrease in size to slightly larger than 25 nm in diameter, the two oscillation modes that effect the NPs extinction are the dipole and the quadrupole oscillations, and as the size decreases to less than 25 nm the main contributor to the extinction is the dipole oscillation.<sup>[88]</sup>

Mie's theory can then be condensed into the following expression for small particles, where the absorption cross-section of the NPs ( $\sigma$ ) is:<sup>[88,91,92,94,148,149]</sup>

$$\sigma(\lambda) = \frac{18\pi \cdot V \cdot \epsilon_m^{\frac{3}{2}}}{\lambda} \cdot \frac{\epsilon_2}{(\epsilon_1 + 2\epsilon_m)^2 + (\epsilon_2)^2} \quad (3.1)$$

where  $V$  is the volume of the particle,  $\lambda$  is the wavelength of the incident light,  $\varepsilon_m$  is the dielectric function of the medium surrounding the particle, and  $\varepsilon_1$  and  $\varepsilon_2$  are the real and imaginary parts of the bulk dielectric function, respectively. Solving Equation 3.1 for copper nanoparticles (CuNPs), absorption spectra can be derived using the Beer-Lambert law:

$$A(\lambda) = \frac{Np \cdot l \cdot \sigma(\lambda)}{\ln(10)} \quad (3.2)$$

where  $Np$  is the particle concentration in solution and  $l$  is the path length of light through the solution.

Solving Equations 3.1 and 3.2 using the tabulated values of  $\varepsilon_1$  and  $\varepsilon_2$  for copper reported by Roberts<sup>[150]</sup> (whom Temple<sup>[151]</sup> recommends using instead of the well-known values tabulated by Johnson and Christy<sup>[152]</sup>), in a medium of water ( $\varepsilon_m = 1.33$ ) and an arbitrary diameter of 10 nm predicts an absorption spectrum with an absorption feature called the surface plasmon band (SPB) centred at 540 nm. The simulated spectrum is presented in Figure 3.1. The appearance of the spectrum in Figure 3.1 is consistent with that reported by Creighton and Eadon.<sup>[94]</sup>

However, Equation 3.1 is independent of particle size, if it is considered that  $V$  is a pre-factor and has no influence on the SPB position or shape.<sup>[153]</sup> This is due to the fact that the position and shape is dictated by the dielectric function of the material, which is encapsulated in the second half of Equation 3.1. However, experimentally a size effect on the SPB is observed as a dampening of the absorption feature with decreasing size of the NPs.<sup>[91,147,153]</sup> While Mie's model gives a good first approximation, a  $1/r$  dependence on the SPB bandwidth was experimentally determined by the extensive work of Kreibig, explaining the dampening of the SPB that is seen in gold and silver NPs as the size decreases down to 2 nm.<sup>[149,154,155]</sup>

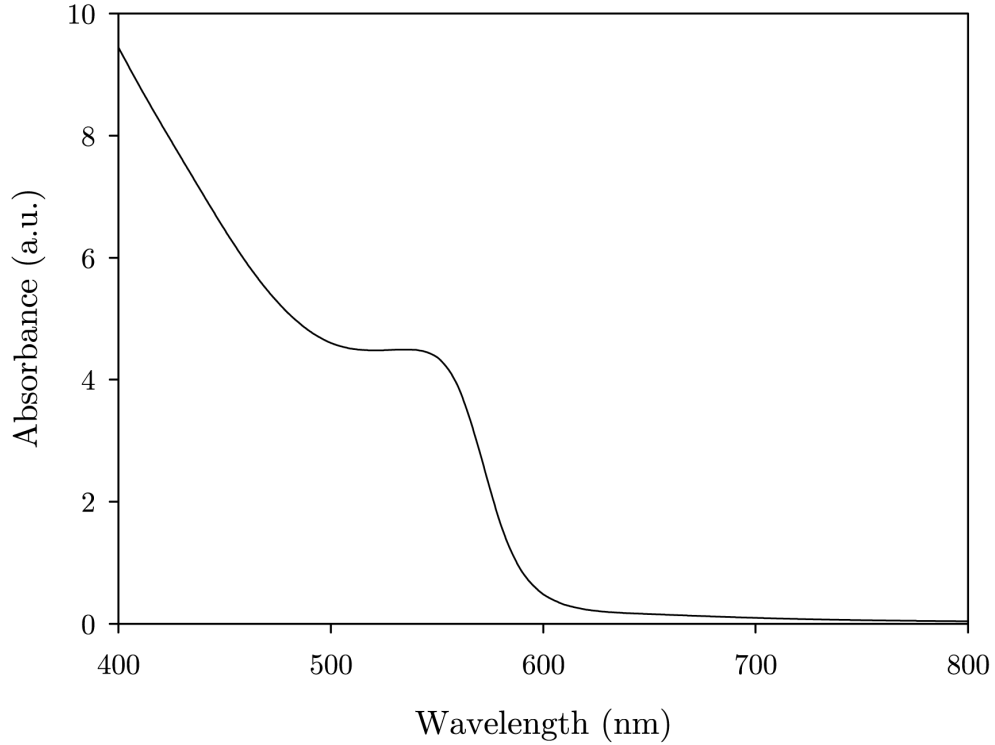


**Figure 3.1** Simulated absorption spectrum of CuNPs of 10 nanometres in diameter demonstrating the SPR absorption feature present at 540 nm. The spectrum was generated from solving Equation 3.1 using tabulated values for  $\epsilon_1$  and  $\epsilon_2$  as described in the text.

Solving Equation 3.1 for various NP diameters of 1 – 5 nm, the SPR absorption feature remains constant in shape and location, as demonstrated in Figure 3.2. The simulations presented in Figure 3.2 show no dampening of the SPR, with the simulated absorption having the same basic shape as the absorption of the NP, irrespective of size. It was then theorised that if the NP diameter is comparable with the mean free path of conduction electrons, then the surface electrons of the NP are dampened by the collisions with the conduction electrons, and this dampening affects the dielectric function of the material, namely the imaginary part  $\epsilon_2$ .<sup>[153]</sup>

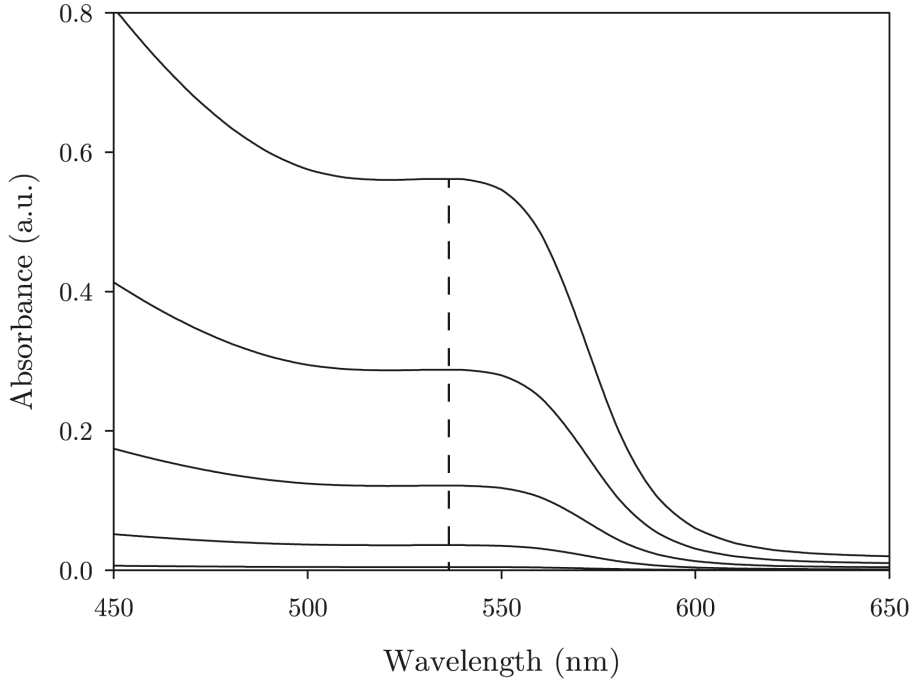


**Figure 3.2** Simulated absorption spectra of CuNPs of varying diameters, from 5 nm down to 1 nm in 1 nm steps generated by solving Equation 3.1. The dashed line is to draw the eye of the reader to illustrate the lack of damping and similarity in the shape of the spectra as the diameter decreases.

Lisiecki *et al.*<sup>[51,52]</sup> explain that a new term must be added to Equation 3.1, based on the extensive work of Kreibig,<sup>[154]</sup> a term which accounts for the damping of electrons,  $\varepsilon_2(r)$ , such that:

$$\varepsilon_2(r) = \varepsilon_2 + \varepsilon_{2r} \quad (3.3)$$

where  $\varepsilon_{2r}$  is the surface contribution due to the small size of the NPs, and can be expressed by:

$$\varepsilon_{2r} = \frac{v_F}{r} \quad (3.4)$$

where  $v_F$  is the Fermi velocity and  $r$  is the radius of the NP. This modified term, now results in Equation 3.1 becoming dependent on particle size, with the size of the NP now influencing the SPB position and shape, as shown below:

$$\sigma(\lambda) = \frac{18\pi \cdot V \cdot \varepsilon_m^{\frac{3}{2}}}{\lambda} \cdot \frac{\varepsilon_2(r)}{(\varepsilon_1 + 2\varepsilon_m)^2 + (\varepsilon_2(r))^2}. \quad (3.5)$$

Solving Equation 3.5 using this new term  $\varepsilon_2(r)$ , with a  $v_F$  value of  $1.57 \times 10^{15}$  nm/s,<sup>[156]</sup> results in the simulated absorption spectrum presented in Figure 3.3. Here, the SPB absorption feature is centred at 550 nm for a NP of 10 nm in diameter, similar to what has previously been reported.<sup>[55,94,95,107,151,157]</sup> Figure 3.4 demonstrates how the SPB is dampened with decreasing NP size, with the SPB peak broadening and red-shifting as the size of the NP decreases. These trends are in accord with experimental observation.<sup>[52,102,103,157,158]</sup>

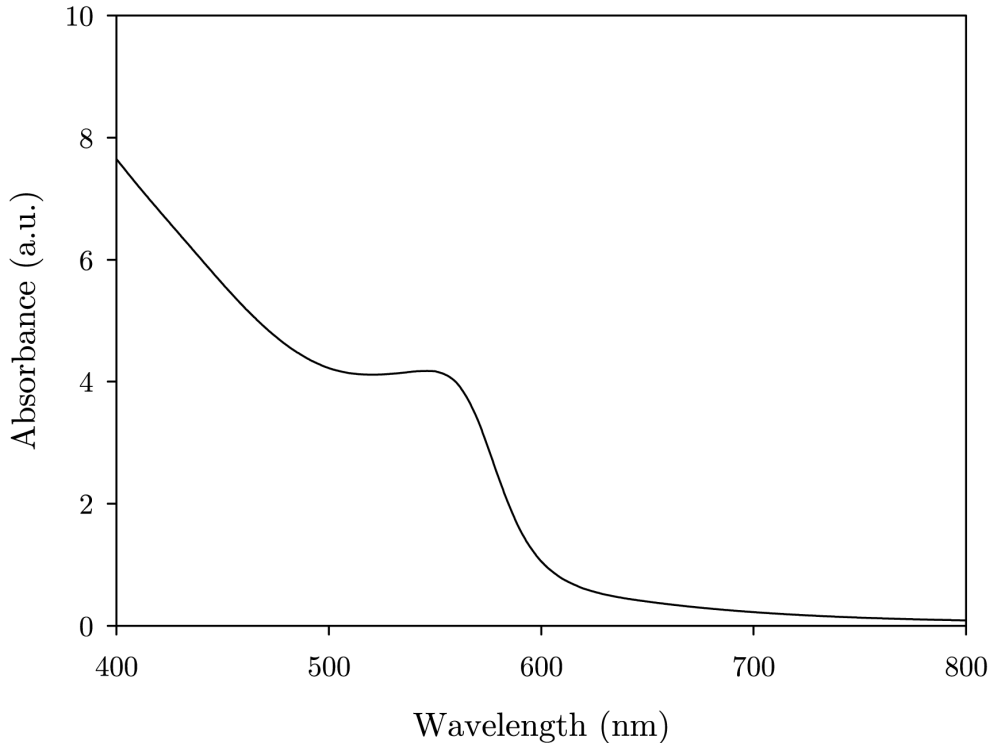


**Figure 3.3** Simulated absorption spectrum of CuNPs of 10 nanometres in diameter demonstrating the SPB absorption feature present at 550 nm. The spectrum was generated from solving Equation 3.5 using tabulated values for  $\varepsilon_1$  and size dependent values for  $\varepsilon_2$  modified via Equation 3.3 as described in the text.

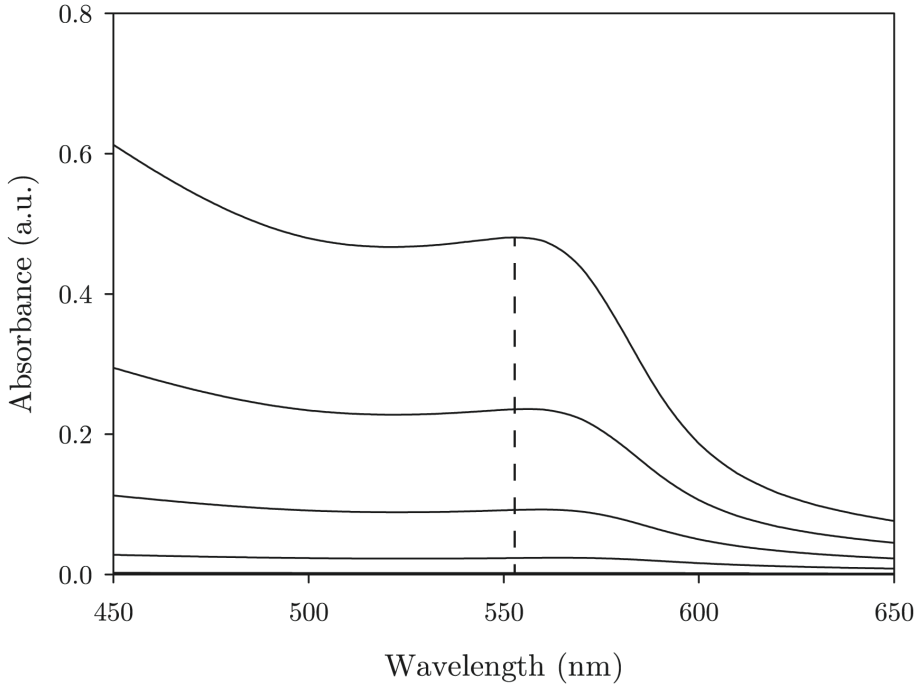


**Figure 3.4** Simulated absorption spectra of CuNPs of varying diameters, from 5 nm down to 1 nm in 1 nm steps generated by solving Equation 3.5 using size dependent values for  $\varepsilon_2$  modified via Equation 3.3. The dashed line is to draw the eye of the reader to illustrate how as the diameter of the CuNPs decrease, the SPB absorption feature peak wavelength position red-shifts and the feature broadens.

The inclusion of the size-dependent term  $\varepsilon_{2r}$  in Equation 3.3 can be understood if we first consider a free-electron metal that obeys the Drude-Lorentz-Sommerfeld model, in which  $\varepsilon(\omega)$  is given by:<sup>[100,153,156,159]</sup>

$$\varepsilon(\omega) = \varepsilon_1(\omega) + i\varepsilon_2(\omega) = 1 - \left( \frac{\omega_p^2}{\omega^2 + i\omega\gamma} \right) \quad (3.6)$$

where  $\omega = 2\pi f$ ,  $\omega_p$  is the bulk plasma frequency and  $\gamma$  is the damping constant arising from the dispersion of electrons. In realistic terms, Equation 3.5 is only valid for metals that show free-electron behaviour and obey Equation 3.6, and therefore Equation 1.1 holds true and that an absorption peak is seen close to the wavelength when  $\varepsilon_1 = -2\varepsilon_m$  and  $\varepsilon_2 = 0$ .<sup>[88,94]</sup> Copper however does not show typical free-electron behaviour,<sup>[88,94]</sup> as  $\varepsilon_2$  does

not become equal to 0, and the SPB absorption peak at 550 nm (which equates to an  $\epsilon_1$  of -6.76<sup>[150]</sup>) is not equal to twice the negative of  $\epsilon_m$  (being 1.33).

The reason as to why the absorption peak for CuNPs exists where it does is due to strong interband character of the metal.<sup>[51,52,88,94]</sup> Interband transitions occur when electrons are promoted to higher, empty levels caused by the absorption of an incident photon. When this occurs in metals, the electron can shift to the Fermi surface, or from near the Fermi surface to the next higher empty energy level. This results in high losses in energy in the visible frequency.<sup>[100]</sup> This interband character then affects the dielectric function  $\epsilon(\omega)$ , which ultimately results in a size dependency on radius  $r$ .<sup>[153]</sup>

Equation 3.6 is, however, independent of radius and therefore needs an addition of terms to account for the interband character of copper. Firstly, the damping constant  $\gamma$  is affected by the mean free path of conduction electrons  $L_\infty$ , such that:<sup>[100,153,156,160,161]</sup>

$$\gamma = \frac{v_F}{L_\infty} \quad (3.7)$$

where  $v_F$  is the Fermi velocity. When the NPs become sufficiently small enough  $\gamma$  becomes dependent on the radius  $r$  of the NP, such that the mean free path can be dominated by collisions with the NP boundary. Therefore the damping constant increases due to the additional collisions with the boundary of the particle.<sup>[88]</sup> The addition of a size-dependent term is added to Equation 3.7 resulting in:<sup>[100,153,156,160-162]</sup>

$$\gamma(r) = \gamma + \frac{v_F}{r}. \quad (3.8)$$

Including this expanded damping constant into the Drude free electron model (3.6) we obtain the size-dependent dielectric function which includes

the contributions of the free electrons, surface damping and interband transitions:<sup>[153,156,159]</sup>

$$\varepsilon(\omega, r) = \varepsilon(\omega) + \frac{\omega_p^2}{\omega^2 + i\omega\gamma} - \frac{\omega_p^2}{\omega^2 + i\omega\gamma(r)} \quad (3.9)$$

where  $\varepsilon(\omega)$  is the bulk dielectric function of the metal. When Equation 3.9 is broken down, the biggest contributor to the size dependency is the subtraction of  $\gamma(r)$  from  $\gamma$ , which is Equation 3.8 subtracted from Equation 3.7, which leaves us with:

$$\gamma - \gamma(r) = \frac{v_F}{r}. \quad (3.10)$$

The  $\frac{v_F}{r}$  feature that we see in Equation 3.10 is the same that is seen in Equation 3.4, and the reason why this term is used to account for the damping of surface electrons is that in Equation 3.9 both the  $\gamma$  and  $\gamma(r)$  terms appear behind the imaginary identifier,  $i$ . When Equation 3.6 is recalled, the part of  $\varepsilon(\omega)$  that is behind the imaginary identifier is  $\varepsilon_2$ . This then suggests that the damping of surface electrons only affects the  $\varepsilon_2$  values, and not the  $\varepsilon_1$  values.

For larger nanoparticles (>approximately 25 nm in diameter), however, Equation 3.1 becomes less valid with increasing NP diameter, even with the size dependency corrections demonstrated in Equation 3.9. For larger NPs, higher multipoles, especially the quadrupole term, come into effect, and they are not described in Equation 3.1.<sup>[92]</sup> For these large NPs, the plasmon bandwidth increases and the location of the SPB red-shifts as a function of the radius of the NP.<sup>[8,91,147]</sup> It can be explained by the fact that as the NPs get larger and the wavelength of light becomes comparable in size to the NP, the light no longer homogeneously polarises the NP and higher order multipoles are excited.<sup>[95]</sup> To generate absorption spectra of NP with diameters larger than 25 nm requires the addition of a quadrupole term, and

this is best achieved by approaching the problem from a purely electrostatic approach, in what is often referred to as a quasistatic approximation.<sup>[147]</sup> It is called thus due to the electric field being considered constant, while still using the wavelength-dependent relative permittivity of the metal particle and of the surrounding medium, in what is an electrostatic theory. Kelly *et al.* have demonstrated that solving Laplace's equation, which is the quasistatic approximation, for a dipole and quadrupole to generate an absorption spectrum for a silver NP of 30 nm in diameter compares very well to that of an absorption spectrum generated by Equation 3.1 for the same NP.<sup>[147]</sup> However, when the diameter is increased to 60 nm, Mie's theory (Equation 3.1) no longer generates the same absorption spectrum as that generated by using a quasistatic approach, although important features are retained despite the spectral differences.<sup>[147]</sup> Clearly then, Mie's theory becomes less accurate and is unable to fully describe absorption spectra as the diameter of the NPs increases larger than approximately 25 nm.

The emergence of the SPB absorption feature in CuNPs then allows for the analysis of CuNPs formed via LASiS by UV-visible spectroscopy. A challenge, however, in experimentally recording CuNP absorption spectra is that they are very susceptible to oxidation. Synthesis of pure CuNPs free from oxidation therefore most commonly occurs under inert nitrogen or argon atmospheres, some methods also employing the use of de-gassed solvents. As mentioned in Section 1.4, when chemical reductive synthesis or physical manufacture of copper nanoparticles is performed in an inert atmosphere, the SPB absorption is centred around 570-580 nm. This indicates that the nanoparticles that are formed are oxide free, and the experiment correlates well with the aforementioned theoretical predictions.<sup>[55,57,158,163-165]</sup> There are several reports that demonstrate potentially oxide-free nanoparticles with methods that do not employ inert atmospheres, but employ the use of novel

capping agents, oxygen scavengers or non-aqueous solvents, and these spectra also agree well with Mie's theory.<sup>[52,54,157,166,167]</sup>

## 3.2 *LASiS in Aqueous Solutions*

### 3.2.1 Pure Water

When LASiS is conducted in pure water (i.e. no surfactants, ligands or additives present) NPs of copper are generated in the solution. This is evident from the colour change in the solution (from colourless to a pale green), with the UV-Vis spectrum presented in Figure 3.5 (upper panel) having a weak absorption feature centred around 650 - 660 nm. The UV-visible spectrum is a typical spectrum seen of CuNPs in aqueous solution, having an absorption feature corresponding to the surface plasmon band (SPB) and a high energy absorption 'tail.' Mie's theory accounts for this high-energy tail as arising from scattering from NPs that are too small to support the SPR.

Due to the relatively weak SPB absorption feature, and the desire to highlight any differences in the SPB absorption feature, for the sake of comparison all further UV-visible spectra will present SPB-normalised data. The SPB normalised UV-visible spectrum of CuNPs generated by LASiS in water is also shown in Figure 3.5 (lower panel), the data being the same data presented in the top panel, with the spectrum focusing on a smaller wavelength range for the sake of clarity.

It is clear to see, however, that the wavelength position of the SPB is not where it would be expected to be based upon the Mie-model predictions. The theoretical location of the SPB, as previously discussed, is at 550 nm as shown in Figure 3.3. Literature experimental results show the SPB to be located at 570 nm under oxide-free conditions.<sup>[55,57,158,163,164,168]</sup>

This suggests that the CuNPs giving rise to the spectrum presented in Figure 3.5 comprise an oxide layer of some description. With a working hypothesis that N-donor ligand encapsulation of CuNPs generated via LASiS could influence oxide formation, equivalent studies were undertaken to explore the influence of these ligands and CuNP spectra. The logic being that spectral shifts can be a proxy for the presence or absence of copper oxides.

### 3.2.2 Neutral N-Donor Ligands

Due to the very well-known behaviour of **phen** and **bipy** in forming covalent bonds in coordination chemistry, previous research has conducted LASiS in  $10^{-4}$  molar solutions of these ligands.<sup>[80]</sup> It was reported by Muniz-Miranda *et al.* that LASiS of a copper target in aqueous solutions of **phen** and **bipy** resulted in CuNPs with an SPB absorbance feature located at 611 nm for **phen** and 614 nm for **bipy**.<sup>[80]</sup> Further, Raman spectroscopy and computer-simulated Raman spectroscopy indicated that both **phen** and **bipy** demonstrated a ligand/metal interaction, and that the ligands were interacting chemically with the surface of the CuNPs. As a matter of course, LASiS was also conducted in similar solutions of **phen** and **bipy** in this research, along with **Py** and **4Ph-Py** (structures in Figure 1.3). Figure 3.6 shows the SPB-normalised UV-visible spectra obtained of the solutions following 60 minutes of LASiS, with the characteristic SPB absorption feature demonstrating the formation of CuNPs. The wavelength position of these CuNP solutions is at 630 nm for **phen** and **bipy**, 635 nm for **Py** and 640 nm for **4Ph-Py**. Figure 3.6 demonstrates that the general appearance of these four CuNP solutions is similar to that of CuNPs generated in pure water. It should be noted, however, that the location of the SPB absorption features in these CuNP solutions is less red-shifted with respect to the Mie-model prediction than CuNPs generated in pure water.

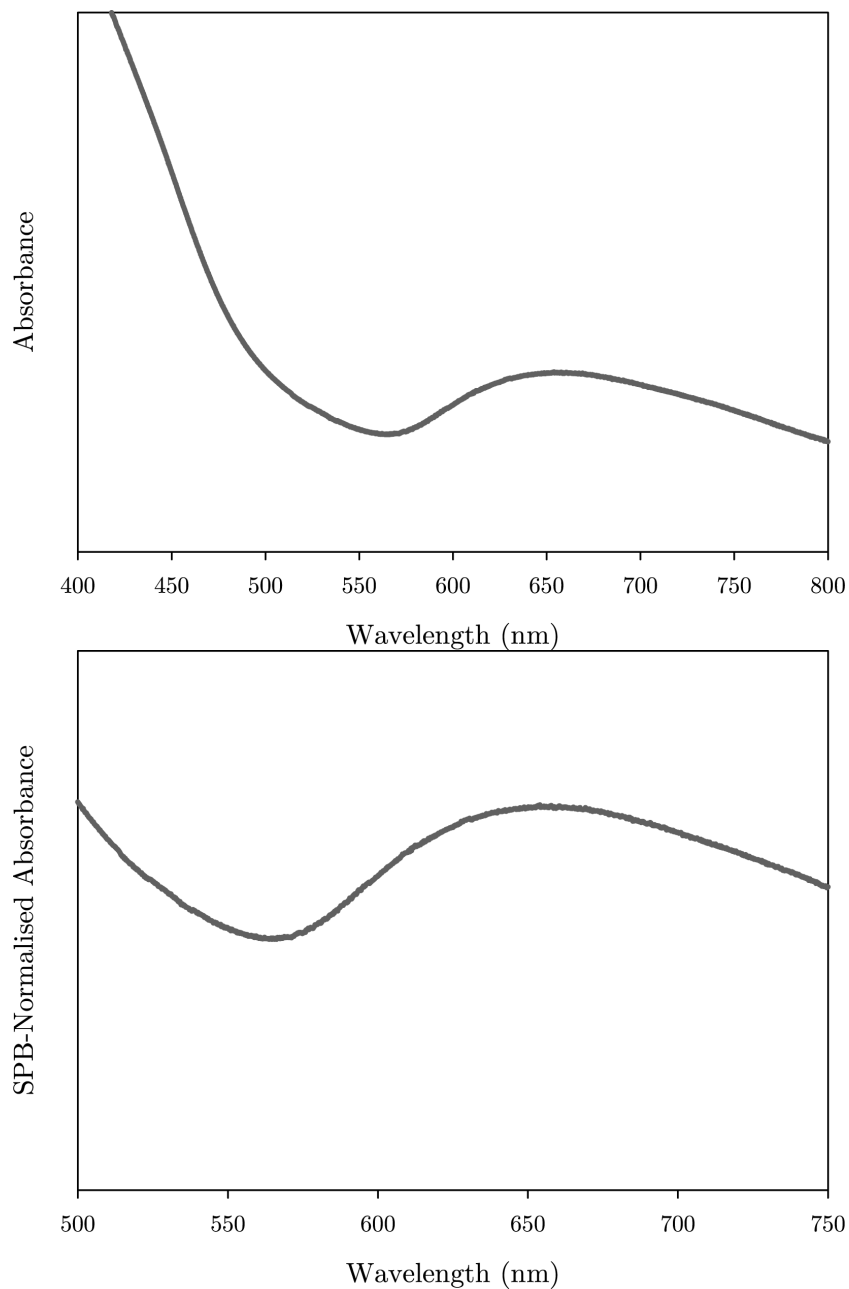


**Figure 3.5** TOP PANEL: UV-visible spectrum of CuNPs prepared in pure water by laser ablation for 60 minutes. BOTTOM PANEL: SPB-normalised absorption spectrum of the data presented in the top panel to highlight the SPB feature and its position. The trace is presented in grey as it will be used for comparison for all the UV-visible spectra that will follow.

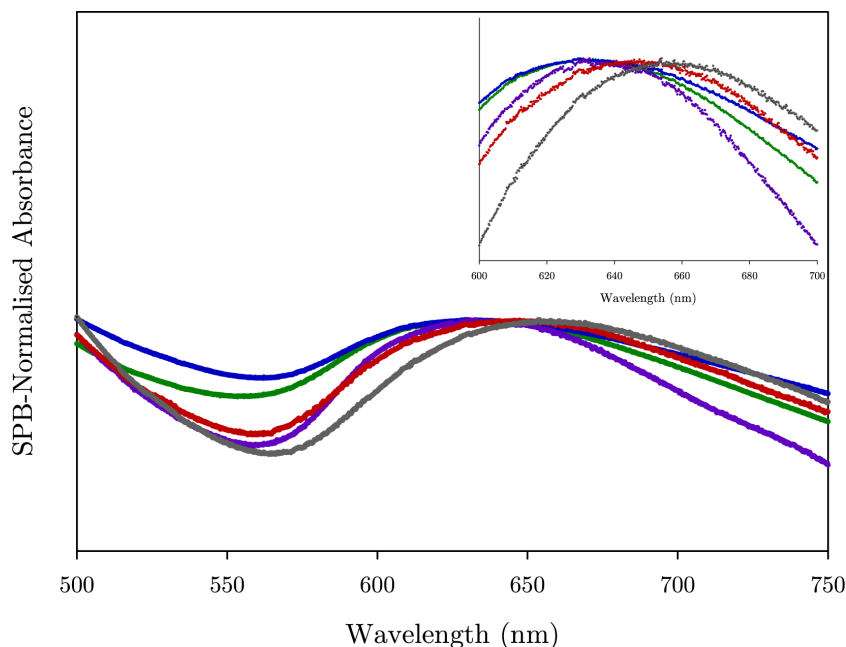


**Figure 3.6** SPB-normalised UV-visible absorption spectra of CuNPs generated by 60 minutes of LASiS in solutions of **bipy** (blue), **phen** (green), **Py** (purple) and **4Ph-Py** (red). The grey trace is that of CuNPs generated by 60 minutes of LASiS in pure water for the sake of comparison. INSET demonstrates the slight blue-shift w.r.t. CuNPs generated in pure water.

The red-shift seen here is approximately 80 nm w.r.t the Mie-model prediction, while in blank water it is some 100 nm shifted. In fact, there are differences seen between the result here with **phen** and **bipy** and the reported literature (630 nm versus 611/614 nm,<sup>[80]</sup> respectively), though these differences can be attributed to different experimental conditions. Muniz-Miranda *et al.* report LASiS times of between 10 and 30 minutes, a laser pulse of 20 mJ/pulse, equating to a laser fluence of 2.5 J/cm<sup>2</sup>,<sup>[80]</sup> while the conditions here are LASiS for 60 minutes, with a laser pulse of 7.5 mJ/pulse, and laser fluence of approx. 2x10<sup>2</sup> J/cm<sup>2</sup>. The 60 minute ablation time used here in these experiments typically results in a SPB absorption feature that is red shifted with respect to the SPB absorption feature of CuNPs generated by 10 – 30 minutes of LASiS. This will be explored later in Chapter 8.1. It is

plausible that the shorter ablation times reported by Muniz-Miranda *et al.* is the reason for the difference in SPB location demonstrated here.

Examining the structure of these four ligands, none of them can deprotonate in aqueous solution. They do have some electron affinity to the CuNP surface due to the nitrogens present in the structures and are thus described as being ‘neutral’ ligands. It is this affinity of the ligands to the CuNP surface that may be the reason for the slight maximum 30 nm blue-shift in the SPB absorption spectra with respect to that of CuNPs formed in pure water (see Figure 3.6 inset).

It is also clear that the structure of the molecule has no significant effect on the SPB absorption feature. The **phen** ligand, with a bidentate type of interaction with the CuNPs has a similar SPB to that of **bipy**, **Py** and **4Ph-Py**, which exhibit a monodentate type of interaction with the CuNPs. The SPB of CuNPs prepared in the smaller **Py** molecule also show that the size of the molecule has no significant effect on the SPB absorption feature either. It is also clear that the visual similarity in the UV-visible spectra of CuNP solutions generated in these four ligands and in pure water suggests that the CuNPs that are formed are similar, though not identically the same.

### 3.2.3 Deprotonated Tetrazolato Ligands

In contrast, the UV-visible spectra of CuNPs prepared by 60 minutes of LASiS in ‘electron-rich’  $10^{-4}$  molar solutions of **T-3Py**, **T-4Py**, **T-Ph** and **T-Me** are presented in Figure 3.7. The SPB absorption feature indicates the formation of CuNPs, and the wavelength position of the absorption feature centred around 580 – 600 nm demonstrates a significant blue-shift of the SPB with respect to that of CuNPs formed in pure water. The location of the SPB here is more in line with the theoretically modelled location for the SPB, and this location of the SPB absorption feature is attributed initially at this point

to the negatively charged deprotonated tetrazoles in the aqueous solutions influencing the CuNP oxidation chemistry.

The tetrazole motif is known to deprotonate in aqueous solutions, thus forming ‘electron-rich’ anionic tetrazolates. In this regard, tetrazoles are often considered as isosteres of carboxylic acids with a  $pK_a$  of approximately 5.<sup>[130]</sup> Another thing to notice in comparison to the ‘neutral’ ligands is the shape of the SPB. With these ‘electron-rich’ ligands, the SPB peak is a lot sharper and defined, not being as broad as the SPB peak seen with the ‘neutral’ ligands. This difference in general SPB absorption feature location would initially indicate that there are some differences in the CuNPs that are formed in these two different groups of aqueous ligand solutions.

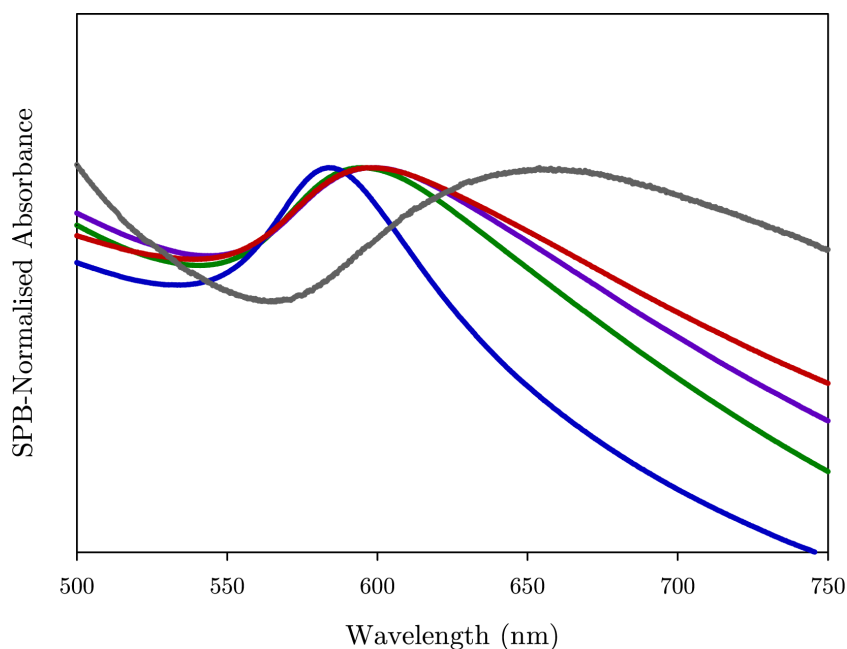


**Figure 3.7** SPB-normalised UV-visible absorption spectra of CuNPs generated by 60 minutes of LASiS in solutions of **T-Ph** (blue), **T-4Py** (green), **T-3Py** (purple) and **T-Me** (red). The grey trace is that of CuNPs generated by 60 minutes of LASiS in pure water for the sake of comparison.

The slight variations seen between **T-Ph** and the other three ligand solutions evident in Figure 3.7 can possibly be explained when the ligand structures are taken into consideration. **T-Ph** and both **T-3Py** and **T-4Py** have a very similar size, and though it is known that both benzene and pyridine  $\pi$  stack, it has been shown that benzene rings have a marginally stronger  $\pi - \pi$  interaction than pyridine when in a sandwich configuration.<sup>[169]</sup> This stronger interaction may result in a tighter packing of **T-Ph** on the surface of the CuNPs in comparison to **T-3Py** and **T-4Py**, which may result in the larger blue-shift for **T-Ph** observed in Figure 3.7.

The difference in size of the ligand has no significant effect on the location of the SPB either, similar to the results seen with the neutral N-donor ligands. While there is a slight blue-shift seen with **T-Ph**, **T-Me** shows no significant difference despite being approximately half the size of the other two ligands. It is also clear that the size of the ligands is not the reason for the large differences in the spectra observed between the CuNPs generated in these ‘electron-rich’ and the ‘neutral’ ligand solutions. This can be explained when it is noted that **phen**, **bipy** and **4Ph-Py** are similar in size to that of **T-Ph**, **T-3Py** and **T-4Py**, yet there are quite marked differences in the UV-visible spectra.

The results observed with these ligand solutions and the significant blue-shift in the SPB location with respect to that of CuNPs formed in pure water and the ‘neutral’ ligands would suggest that the effect these deprotonated tetrazole ligands have on the CuNP surface is different to that of the ‘neutral’ ligands.

### 3.2.4 Alkylated Tetrazolato Ligands

To see if the ability of the tetrazole to deprotonate is a key chemical feature influencing the SPB wavelength position, alkylated analogues of the four ‘electron-rich’ ligands were studied. Figure 3.8 shows the UV-visible spectra of CuNPs prepared in  $10^{-4}$  molar solutions of **BuT-3Py**, **BuT-4Py**, **BuT-Ph** and **BuT-Me**. The four tetrazole ligands have been alkylated with 2-Methylpropan-2-ol to form a *t*-Butyl substituent on the tetrazole, the alkylation having the effect of removing the ability of the ligands to deprotonate in solution (see Figure 1.3).

It is clear to see from these spectra that there is a large red-shift with respect to the non-alkylated ligands discussed above. With the SPB absorption wavelength location being between 640 – 665 nm there is a 40 – 65 nm red-shift in the SPB absorption feature, with the only difference being the alkylation of the tetrazole between the two ligand groups. It is clear that the tetrazole motif is playing a significant role in the position of the SPB of the CuNPs formed in these solutions, as the alkylation is removing the ability of the ligand to deprotonate. It is unclear at this point whether it is the whole deprotonated tetrazole motif or just the ability of the tetrazole to deprotonate that is giving rise to the spectral behaviour reported here.

Figure 3.8 also demonstrates that there is a small amount of variation in the location of the SPB absorption feature (see Figure 3.8 inset). In fact it shows that CuNPs generated in **BuT-Ph** have an SPB location that is more red-shifted than CuNPs generated in pure water, while the other three solutions are slightly blue-shifted with respect to pure water. These results offer further evidence that it is not the size of the structure, nor its method of interaction with the copper surface that is the reason why the ‘electron-rich’ deprotonated tetrazoles exhibit the UV-visible spectra reported herein.

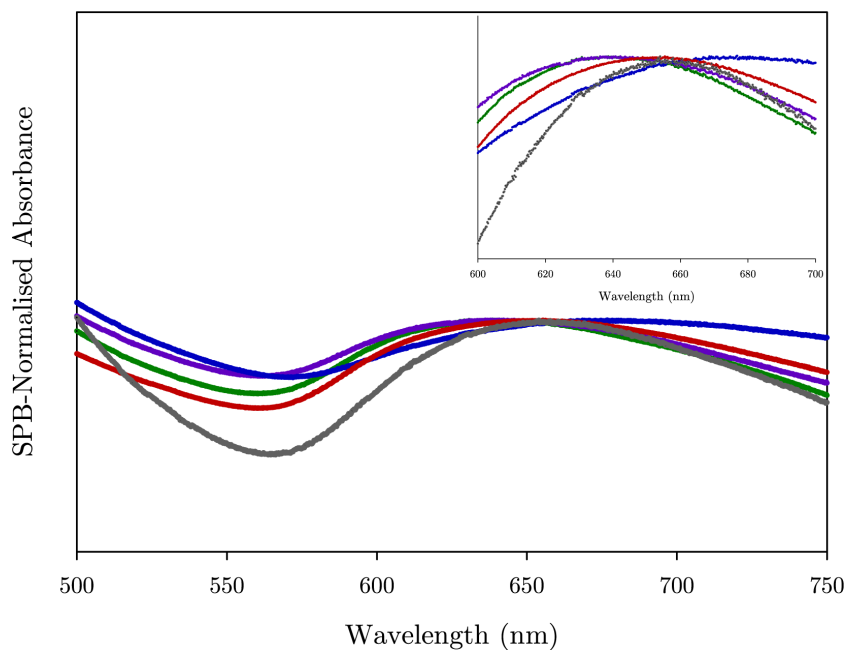


**Figure 3.8** SPB normalised UV-visible absorption spectra of CuNPs generated by 60 minutes of LASiS in solutions of **BuT-Ph** (blue), **BuT-4Py** (green), **BuT-3Py** (purple) and **BuT-Me** (red). The grey trace is that of CuNPs generated by 60 minutes of LASiS in blank water for the sake of comparison. INSET demonstrates the slight blue and red-shift w.r.t. CuNPs generated in pure water.

### 3.2.5 The Curiosity of T-2Py

An interesting result is seen with the last two tetrazole ligands employed in this study, *viz.* **T-2Py** and **BuT-2Py** (structures in Figure 1.3). If the previous results are anything to go by, one would expect **T-2Py** to behave like one of the four ‘electron-rich’ deprotonated tetrazolato ligands, and **BuT-2Py** to behave like one of the four alkylated tetrazolato ligands above. However, this is not the case; while **BuT-2Py** has an SPB centred around 640 nm, similar to the four alkylated tetrazolato ligands, **T-2Py** does not have its SPB centred around 580 – 600 nm, but rather at 630 nm as shown in Figure 3.9. These results suggest that **T-2Py** doesn’t behave like the deprotonated tetrazolato ligands, even though its structure suggests that it

should behave in the same way. A closer inspection of the structure reveals that there may be a reason for the result seen: **T-2Py** can undergo a tautomerisation, the proximity of the hydrogen attached to the tetrazole motif being close enough to the pyridine ring that it is ‘shared’ between both, as illustrated in Figure 3.10.

The effect of this tautomerisation is that **T-2Py** cannot deprotonate as the hydrogen is now ‘bound’ up between the pyridine and tetrazole, leading to the result seen with the SPB location, that it acts like one of the neutral ligands discussed earlier. This result also further suggests that it’s the deprotonating of the tetrazole ligand that is promoting the spectral blue-shifts observed in Figure 3.7.

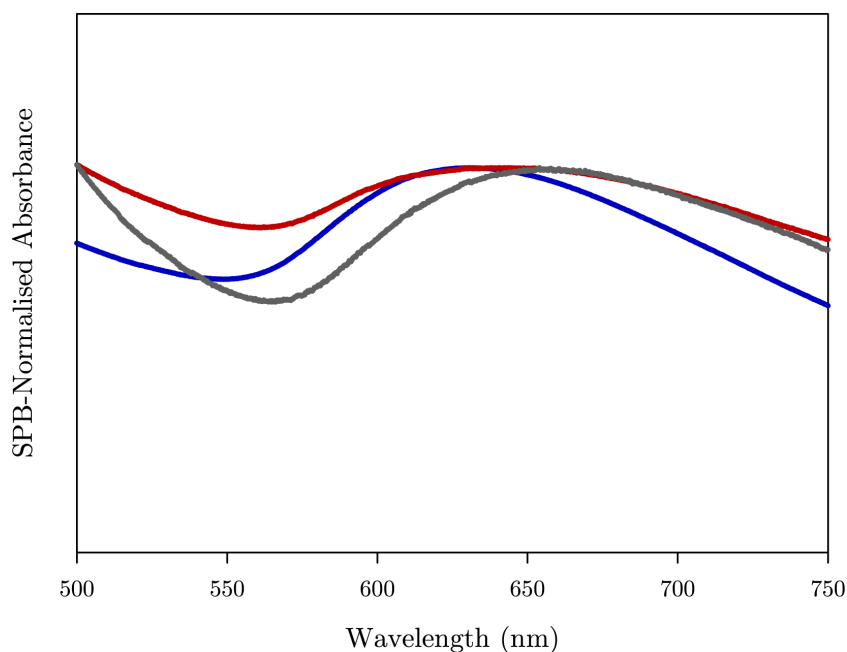


**Figure 3.9** SPB normalised UV-visible absorption spectra of CuNPs generated by 60 minutes of LASiS in solutions of **T-2Py** (blue) and **BuT-2Py** (red). The grey trace is that of CuNPs generated by 60 minutes of LASiS in blank water for the sake of comparison.

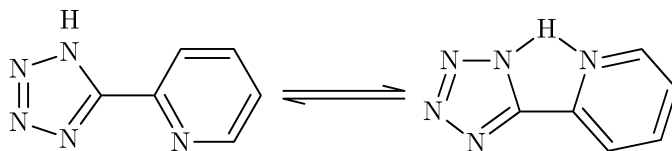


**Figure 3.10** Representation of the tautomerisation of **T-2Py**. The pyridine substituent rotates about the C-C bond between the tetrazole and pyridine, therefore allowing the nitrogen to be in close proximity to the hydrogen from the tetrazole ring. While it is illustrated that the hydrogen is covalently bonded to both nitrogens, in reality the hydrogen would not be bonded.

### 3.3 Conclusion

After examining the UV-visible spectra of CuNPs generated by LASiS in these 14 ligand solutions as well as pure water, it is clear to see that there are two distinct spectral groupings. Firstly, there are the ‘electron-rich’ deprotonated tetrazolato ligands which result in CuNP solutions that have the characteristic SPB absorption feature quite substantially blue-shifted with respect to CuNPs generated in blank water. Secondly, there are the remaining ligands, which include the alkylated tetrazolato ligands. These ligands result in CuNP solutions that are only slightly blue-shifted with respect to CuNPs generated in blank water, or, in some cases, slightly red-shifted. The key to these two groups is the shape of the absorption feature. The first group, also known as the ‘blue’ ligands, have a SPB centred around 600 nm, while the second group, also known as the ‘red’ ligands, have a SPB absorption feature centred around 640 nm.

The hypothesis at this point is that the ability of the tetrazoles to deprotonate in solution is what is driving the wavelength position of the SPB. The alkylation of the tetrazoles has shown that indeed the deprotonation does have an effect, as the SPB absorption feature is like that of CuNPs generated in blank water. Given that there are a few ‘red ligands’

that cannot deprotonate in aqueous solution, it reinforces the suggestion that it's a deprotonated tetrazole effect.

An interesting aspect to consider at this point is that across all the 14 ligands studied, there are multiple ways that the ligands could interact with the CuNP surface, yet there are only two distinct SPB groups that have emerged. This further strengthens the hypothesis that it is the presence, or lack thereof, of the tetrazole group and its ability to deprotonate in solution that is the driving force in the location of the SPB absorption feature, with the mode of interaction with the CuNP being of secondary importance. It has also been shown that the physical size of the ligand molecule has no significant effect on the location of the SPB absorption feature either, with a variety of similar, but different-sized, ligands being used with little to no difference seen in the UV-visible spectra.

The deprotonation ability of the tetrazoles and its importance in controlling the location of the SPB absorption feature will be examined in the next chapter, with the study of some well-known surfactants, carboxylic acids and an organic solvent.



## Chapter 4: CuNPs and Oxidative Control

### 4.1 Oxide Formation on CuNPs

As discussed in Chapter 1, copper oxidises under ambient lab conditions to form copper oxides. This same issue plagues CuNP production, with copper oxides forming if the conditions of CuNP manufacture are not carefully controlled. It has been shown that LASiS of CuNPs in pure water has yielded CuNPs with varying amounts of  $\text{Cu}_2\text{O}$  and  $\text{CuO}$  present, with an SPB absorption feature that is weak, broad and centred at 644 nm.<sup>[106]</sup>

Muniz-Miranda and co-workers also reported a red-shift in the SPB absorption feature when LASiS was conducted in pure water.<sup>[80]</sup> Indeed, the location of the SPB and the conditions that the LASiS are performed under are indicative of oxidation of the CuNPs as previous literature supports the claim that CuNPs will oxidise.<sup>[97-99,107,138,170]</sup> Peña-Rodríguez and Pal have shown in their simulations that as the thickness of the oxide layer increases, the SPB of CuNPs shifts from 560 nm to longer wavelengths, with the intensity of the SPB dampening with the red-shift.<sup>[107]</sup> This shift to longer wavelengths been shown in the results presented in Chapter 3, while Rice *et al.* also demonstrate this experimentally.<sup>[99]</sup>

The shift to longer wavelengths can be rationalised when Equation 1.3 is considered. If it is envisaged that the oxide ‘grows’ on the surface of the CuNP, then as that oxide grows, the dielectric function of the copper oxide has an increasing degree of effect, resulting in the dielectric function of the copper being of decreasing influence. The location of the SPB is then increasingly representative of copper oxide NPs, and less of that of CuNPs.

Peña-Rodríguez and colleagues have theoretically shown that as the oxidation of the CuNPs progresses, the SPB feature broadens and dampens after initially increasing, while simultaneously red-shifting.<sup>[107,156]</sup> These trends are attributed to the CuNP becoming less copper-like with increasing copper oxide content, as per Equation 1.3. As shown in Figure 4.1, the simulated absorption spectrum of copper (I) oxide and copper (II) oxide does not show a typical SPB absorption feature. The simulated absorption spectra were calculated using Equation 3.5 using tabulated values for  $\epsilon_1$  and  $\epsilon_2$  for copper (I) oxide and copper (II) oxide reported by Ribbing and Roos.<sup>[171]</sup> As the amount of oxide present in the CuNPs increases, the absorption spectrum evolves to either CuO or Cu<sub>2</sub>O in appearance, depending on the oxide species present.

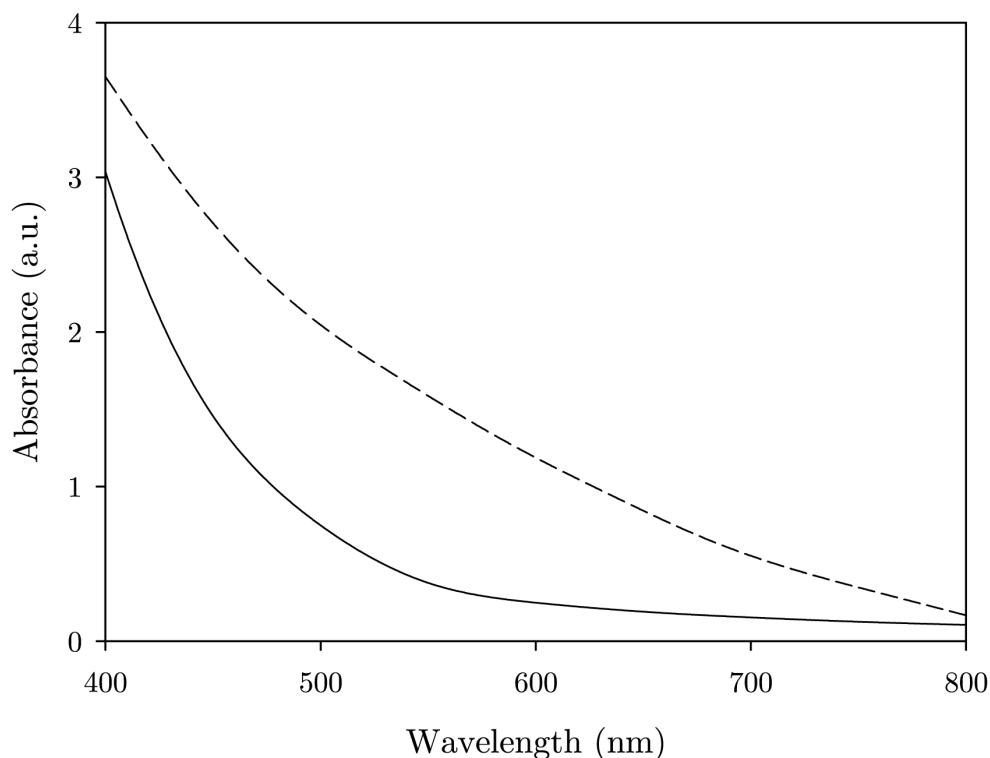


**Figure 4.1** Simulated absorbance spectra of Cu<sub>2</sub>O NPs (solid line) and CuO NPs (dashed line) both of 10 nanometres in diameter. The spectra were generated from solving Equation 3.1 using tabulated values for  $\epsilon_1$  and  $\epsilon_2$  as described in the text.

When theoretically modelling NPs that are no longer pure metal but rather are NPs with a core of one metal and a shell of another metal or metal oxide (core@shell NPs), it is important to consider the effect that the shell has on the values of  $\epsilon_1$  and  $\epsilon_2$  of the core. As per Equation 1.3, the values of the core become more like the shell, and so in effect the values of  $\epsilon_1$  and  $\epsilon_2$  are mixed. The most straightforward way of modelling these type of particles is to consider the electric-magnetic fields that exist inside each layer of the sphere. The linear combination of the inward and outward travelling waves interacting with the layer beneath it and above it generates an overall model of the scattering of light by the core@shell NP.<sup>[107,172]</sup>

Several models exist that solve this mixing effect by using an algorithm that considers each individual layer, its thickness, its specific  $\epsilon_1$  and  $\epsilon_2$  values, and how it interacts with the layer above and below it, to generate solutions that result in relative values of  $\epsilon_1$  and  $\epsilon_2$  that describe the ‘mixed’ NP. These relative values of  $\epsilon_1$  and  $\epsilon_2$  can then be used to generate absorption spectra.<sup>[173]</sup> One of these models, reported by Yang,<sup>[173]</sup> is a refinement to a number of other existing models. The intent being: to develop a more concise and stable algorithm that could be used for a computer program.<sup>[173]</sup> This model was used by Peña-Rodríguez and co-workers to develop a software program called MieLab which will generate theoretical spectra of multilayered spheres.<sup>[172]</sup>

The basics of MieLab allow for the user to compute a theoretical spectrum of a multilayered sphere of the user’s choosing. The software allows for the user to generate spectra of spheres of as many layers as they choose, those layers being as thick as they choose and having the refractive index of their choosing.<sup>[172]</sup> This software then allows for the generation of a theoretical spectrum of a CuNP that has a copper oxide shell on it, and

allows the user to vary the thickness of both the core (copper) and the shell (copper oxide). Peña-Rodríguez have demonstrated this capability when they generated theoretical spectra of a NP with a copper core and a varying thickness copper oxide shell showing how the SPB absorption feature is eventually dampened to non-existence with ever increasing copper oxide shell thickness.<sup>[107]</sup>

The MieLab software package has been used in these studies to explore the role of CuNP oxidation on the experimentally observed absorption spectra. The tabulated values for  $\epsilon_1$  and  $\epsilon_2$  for copper provided by Roberts<sup>[150]</sup> and for copper (I) oxide and copper (II) oxide provided by Ribbing and Roos,<sup>[171]</sup> have been used to generate contour plots of the extinction cross section,  $Q_{\text{ext}}$ , as it varies with changing thickness of the copper oxide layer. The calculations were performed for a CuNP of 10 nm in diameter ( $R_{\text{Cu}} = 5$  nm), with an ever-increasing thickness of copper oxide shell such that the total diameter did not exceed 10 nm (*i.e.*  $R_t = 5$  nm). A schematic representation of the Cu@Cu<sub>x</sub>O NP is shown in Figure 4.2.

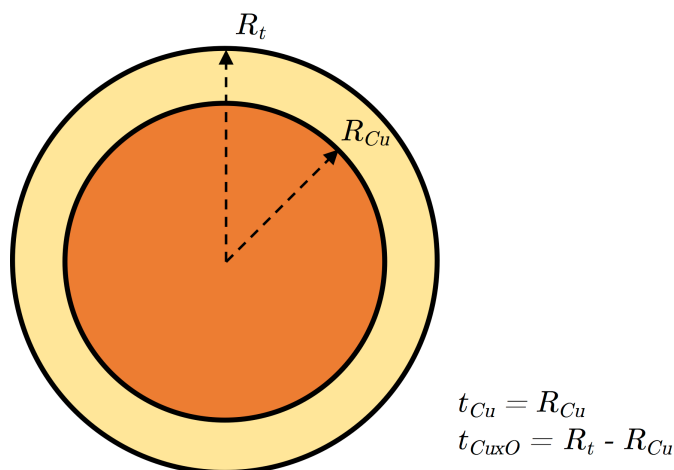


**Figure 4.2** Schematic representation of the studied Cu@Cu<sub>x</sub>O structures, where the x in Cu<sub>x</sub>O is either 1 or 2, for CuO or Cu<sub>2</sub>O, respectively.  $R_{\text{Cu}}$  is the radius of the copper core, while  $R_t$  is the radius of the entire NP. The thickness of the copper core,  $t_{\text{Cu}}$ , is the radius of the copper core,  $R_{\text{Cu}}$ . The thickness of the copper oxide,  $t_{\text{Cu}_x\text{O}}$ , is the radius of the copper core,  $R_{\text{Cu}}$ , subtracted from the total radius,  $R_t$ . When there is no Cu<sub>x</sub>O shell,  $R_t$  is equal to  $R_{\text{Cu}}$ , and  $t_{\text{Cu}_x\text{O}}$  is equal to 0.

The study of the influence of the copper oxide shell was achieved by decreasing the radius of the core,  $R_{Cu}$ , as the thickness of the shell,  $t_{Cu_xO}$ , increased. The ratio between the thickness of the shell and total diameter ( $t_{Cu_xO}/R_t$ ) was varied between 0 and 1, with a ratio of 0 being pure copper and a ratio of 1 being pure  $Cu_2O$  or  $CuO$ . The contour plots were developed for a copper (I) oxide shell ( $x = 2$ ) as well as a copper (II) oxide shell ( $x = 1$ ) on a copper core, the results shown in Figures 4.3 and 4.4, respectively.

Interestingly, both contour plots show that the SPB absorption feature on one hand red-shifts, and on the other increases in intensity (a maximum gain of 35% in  $Cu_2O$  and 13% in  $CuO$ ) before the intensity decreases, with increasing thickness of the oxide shell. Peña-Rodríguez and Pal<sup>[107]</sup> rationalise the red-shift arising from copper oxide being a semi-conductor material.

Copper oxide will polarise in an EM field (*i.e.* incident light) and will screen the Cu core. This reduces the overall surface charge of the NP, lowering the SPR energy, resulting in the SPB red-shifting. It is also important to point out that the maximum red-shift in the SPB is greater in the  $Cu@Cu_2O$  NP than it is in the  $Cu@CuO$  NP. The maximum the SPB red-shifts for the  $Cu@Cu_2O$  NP is 85 nm (out to 640 nm), while for the  $Cu@CuO$  NP it is 50 nm (out to 605 nm).

Peña-Rodríguez and Pal<sup>[107]</sup> conducted the same study reported herein, but only on  $Cu@Cu_2O$  NPs. The difference between this study and theirs is that they used the tabulated values of  $\epsilon_1$  and  $\epsilon_2$  as reported by Johnson and Christy, with an  $\epsilon_m$  of 1.46. This study uses the tabulated values of  $\epsilon_1$  and  $\epsilon_2$  as reported by Roberts, with an  $\epsilon_m$  of 1.33. The trends seen for  $Cu@Cu_2O$  NPs in both studies are very similar, giving us confidence in the  $Cu@CuO$  NP predictions reported herein for the first time.

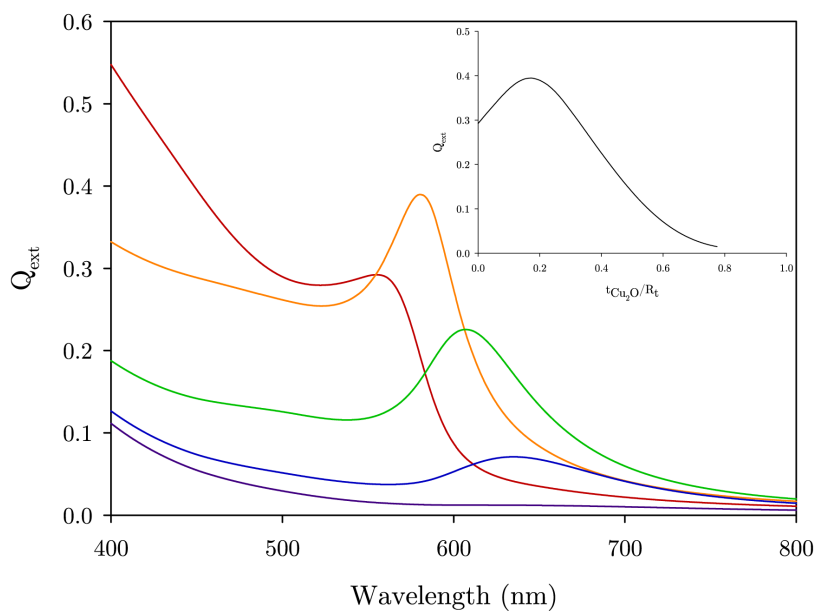
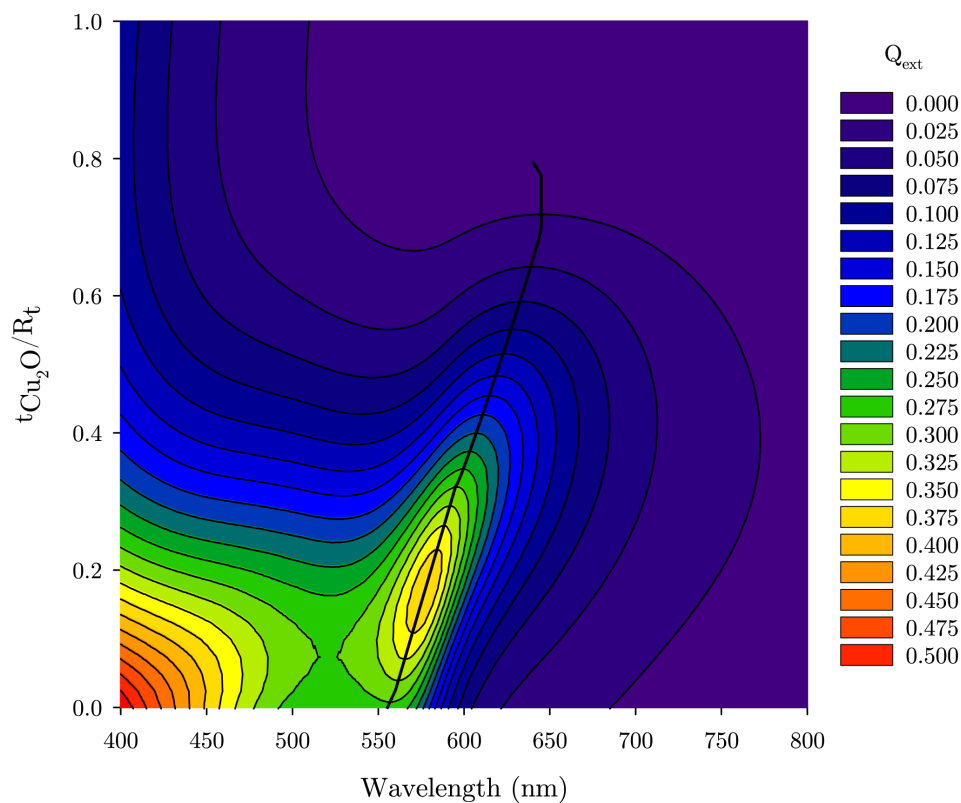


**Figure 4.3** TOP: Contour plot of simulated spectra of CuNPs of 10 nm in diameter and increasing  $t_{\text{Cu}_2\text{O}}/R_t$  ratio. The line is to draw the readers eye to illustrate the peak position of the SPB and how it red-shifts with increasing  $\text{Cu}_2\text{O}$  shell thickness. BOTTOM: Individual simulated spectra of CuNPs of 10 nm in diameter at different  $t_{\text{Cu}_2\text{O}}/R_t$  ratios; 0 (red), 0.2 (orange), 0.4 (green), 0.6 (blue), 0.8 (purple). INSET illustrates how the SPB absorption intensity initially increases before damping.

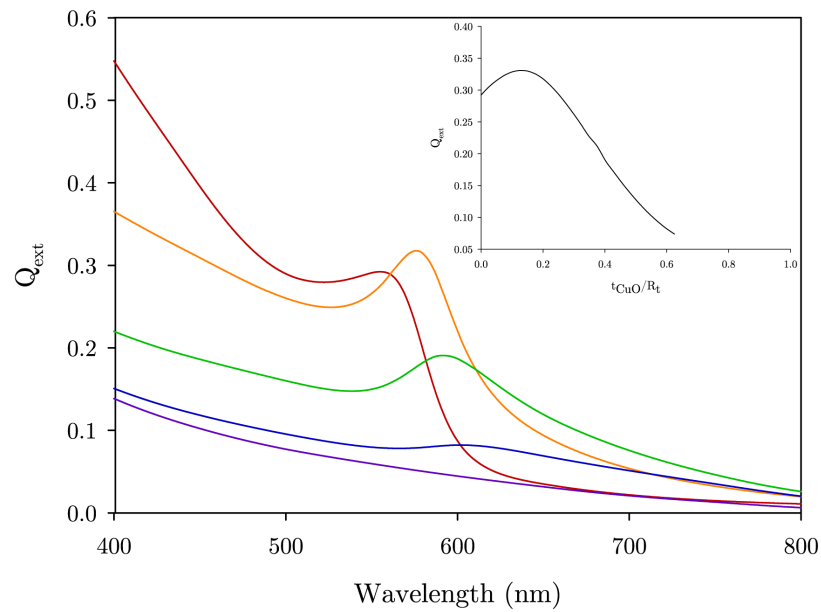
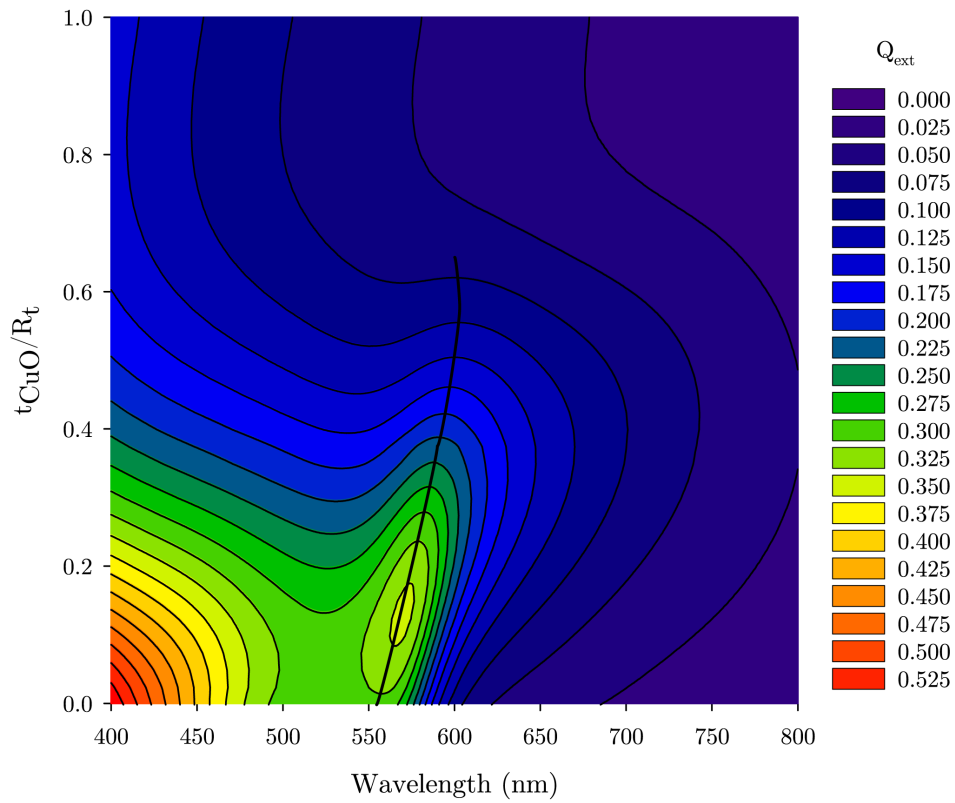


**Figure 4.4** TOP: Contour plot of simulated spectra of CuNPs of 10 nm in diameter and increasing  $t_{\text{CuO}}/R_t$  ratio. The line is to draw the readers eye to illustrate the peak position of the SPB and how it red-shifts with increasing CuO shell thickness. BOTTOM: Individual simulated spectra of CuNPs of 10 nm in diameter at different  $t_{\text{CuO}}/R_t$  ratios; 0 (red), 0.2 (orange), 0.4 (green), 0.6 (blue), 0.8 (purple). INSET illustrates how the SPB absorption intensity initially increases before damping.

Peña-Rodríguez and Pal<sup>[107]</sup> further comment that the initial increase in intensity is due to the red-shift in the SPB absorption feature. They rationalise this by attributing the pure CuNP having its SPB absorption feature inside the region where interband transitions occur. As the SPB absorption feature red-shifts with an increased oxide fraction, it starts to move outside of the interband transition region. As a consequence, this reduces the damping of electrons that occurs in the interband transition region, and the intensity of the SPB absorption feature increases, until at such a point that the screening of the Cu core by the oxide layer is more important. The SPB absorption feature then starts to decrease in intensity.

It appears from first inspection that the location of the SPB of the neutral ligand CuNP solutions in Section 3.2.2, and comparing to the predictions presented in this chapter, indicate that the CuNPs formed have a Cu<sub>2</sub>O coating on them. The absorption spectra shown in Section 3.2.2 demonstrate a SPB location of approximately 630 nm, which Figure 4.3 indicates would be due to a  $t_{Cu_2O}/R_t$  ratio of approximately 0.5 or greater. The contour plot of a CuO coating on a Cu core demonstrates that the red-shift in SPB location is not large enough and does not account for the experimental red-shifts reported in Chapter 3.

The addition of a CuO shell on the CuNP core also dampens the SPB absorption feature more rapidly than the addition of Cu<sub>2</sub>O does. This is also seen with the increase in intensity of the SPB feature being greater for Cu<sub>2</sub>O than CuO (a maximum of a 35% and 13% increase in intensity, respectively). As a comparison, a  $t_{Cu_2O}/R_t$  ratio of 0.6 between the shell and core results in a spectrum that still has a well-defined SPB absorption feature when Cu<sub>2</sub>O is the shell. When CuO is the shell, the SPB absorption feature is markedly

dampened, as demonstrated by the blue spectra in the bottom panels of Figures 4.3 and 4.4, respectively.

The SPB absorption feature of the CuNP solutions formed in the deprotonated tetrazole ligands suggest, in combination with the contour plots, that the CuNPs formed in these solutions may actually have a very small oxide coating on them, contributing to the small red-shift in the SPB from the theoretical position. The contour plots demonstrate that if an oxide does form on the copper core then it could be either  $\text{Cu}_2\text{O}$  or  $\text{CuO}$ . However, given the other ligand solutions indicate a  $\text{Cu}_2\text{O}$  shell and that copper oxidises first to  $\text{Cu}_2\text{O}$  then to  $\text{CuO}$ ,<sup>[157,174]</sup> it would not be amiss to surmise that at this stage LASiS in the deprotonated ligands result in CuNPs with a  $\text{Cu}_2\text{O}$  shell.

## 4.2 Preventing Oxide Formation

The above discussion goes into some detail about how the CuNPs formed by LASiS in aqueous solutions contain what the literature suggests is an oxide coating. Clearly, if the intent is to generate oxide-free CuNPs, then using LASiS in aqueous solutions may be problematic. The negatively-charged ligand solutions, however, have shown that there may be some oxidative protection of the CuNPs. This is hypothesised to be due to the deprotonated tetrazole motif in the ligand being the driving force of this protection.

An explanation for this behaviour of the deprotonated tetrazoles may lie in what is seen when LASiS is conducted in pure acetone. Previous research has shown that CuNPs generated by LASiS in pure acetone are oxide free. Tilaki *et al.* have shown that CuNPs prepared by LASiS in acetone have a SPB at 575 nm,<sup>[138]</sup> with Select Area Electron Diffraction

(SAED) showing that the NPs formed are pure copper. Dorranean *et al.* have showed that by varying the power of the LASiS system CuNPs are generated with an SPB centred from 574 – 581 nm.<sup>[105]</sup> Kumar *et al.* manufactured CuNPs with an SPB centred at 595 nm<sup>[175]</sup> and Kawasaki demonstrated CuNPs generated from cupric oxide have a SPB at 575 nm.<sup>[176]</sup> Muniz-Miranda and co-workers showed that CuNPs generated by LASiS yielded a SPB feature at 588 nm<sup>[80]</sup> and Longano *et al.* had their SPB feature vary from 572 – 576 nm.<sup>[177]</sup>

All these experimental values correlate well with the theoretical SPB location of CuNPs at 570 nm, which all strongly suggest an oxide free NP. The reason for this is due to using acetone as the LASiS solvent. Giorgetti and co-workers<sup>[79]</sup> have shown in the case of gold nanoparticles created by laser ablation in acetone that a negatively charged enolate is formed by the loss of a H<sup>+</sup> ion from the acetone molecule, with the enolate then binding to the surface of the nanoparticle. The key to this work is that the acetone enolate is not found as an ion in acetone, but exists only when it is adsorbed on metal, indicating that the enolate is highly unstable in solution.<sup>[79]</sup> Giorgetti and co-workers demonstrated with the use of infrared spectroscopy that the enolate was adsorbed onto the gold NP surface, the results comparing well with literature values of acetone enolate adsorbing on other metals.<sup>[79]</sup>

It would therefore be natural to assume that this same process of enolate formation and adsorption onto the NP surface also applies to CuNPs generated by LASiS in acetone. Enolate adsorption onto the surface of the CuNPs would prevent the surface of the CuNP from oxidising. This would explain why past research shows that LASiS conducted in acetone gives an

SPB feature that is centred around 572 – 595 nm, SPB locations close to the theoretical position for the SPB feature in oxide-free CuNPs.

The same experiment was performed as part of this project; CuNPs generated by LASiS in acetone had an SPB feature centred at 575 nm as seen in Figure 4.5. The intensity of SPB feature itself is not as pronounced compared to what is seen with the blue ‘electron-rich’ ligands in Figure 3.4. This could be explained by the presence of large number of small NPs that are below the size threshold to support the SPR. Smaller NPs result in high-energy scattering that can partially mask the SPB absorption feature. This is also seen when comparing the non-normalised UV-vis spectra of CuNPs generated by LASiS in acetone against **T-4Py** (see Appendix 4A). While the absorbance values of the SPB feature are very similar, the SPB feature itself is less pronounced in the acetone sample, indicative of small CuNPs masking the SPB feature.

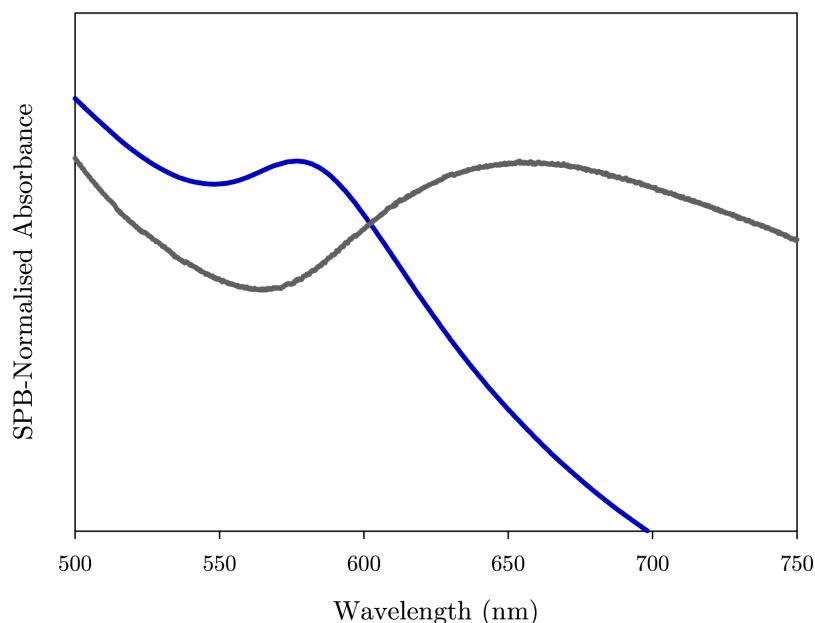


**Figure 4.5** SPB normalised UV-visible absorption spectra of CuNPs generated by 60 minutes of LASiS in acetone (blue). The grey trace is that of CuNPs generated by 60 minutes of LASiS in pure water for the sake of comparison.

The importance of the result here with the acetone providing seemingly oxide free CuNPs is that the method of protection is due to a negatively charged species adsorbing onto the surface of the NP. The four 'blue' negatively-charged tetrazoles show a similar SPB position and shape and this similarity would suggest that the CuNPs formed are similarly oxide free or have a thin oxide coating. It would also suggest that this oxidative protection or limiting of the oxidation of the CuNPs comes from the presence of a negatively charged species existing in solution that has the ability to adsorb onto the surface of the CuNPs.

### ***4.3 The effect of charged species***

#### **4.3.1 Surfactants**

To assess whether in fact it is the presence of a charged species that affords the oxidative protection, two well-known surfactants were studied. LASiS was conducted in  $10^{-4}$  molar solutions of both sodium dodecyl sulfate (SDS) and cetyl trimethylammonium bromide (CTAB), SDS being an anionic surfactant, and CTAB being a cationic surfactant. The UV-visible absorption spectra are shown in Figure 4.6 and it is clear that the CuNPs generated have an SPB location like that of CuNPs generated in pure water.

These results indicate that the surfactants do not provide any sort of protection from oxide formation, despite both these surfactants existing as charged species in aqueous solution. It could be argued that the concentrations of the surfactants here are well below the critical micelle concentration (CMC; 8.2 mM and 1 mM for SDS and CTAB, respectively<sup>[108,137]</sup>) and that therefore the surfactants offer no protection. However, the results seen with the ligands in Chapter 3 indicate that the concentration of  $10^{-4}$  mole/litre is more than sufficient to yield differing

results. While concentrations close to the CMC could provide micellar protection, the intent here is to see if the action of a charged species in solution is sufficient to yield SPB spectral shifts, not to assess the effectiveness of micellar protection.

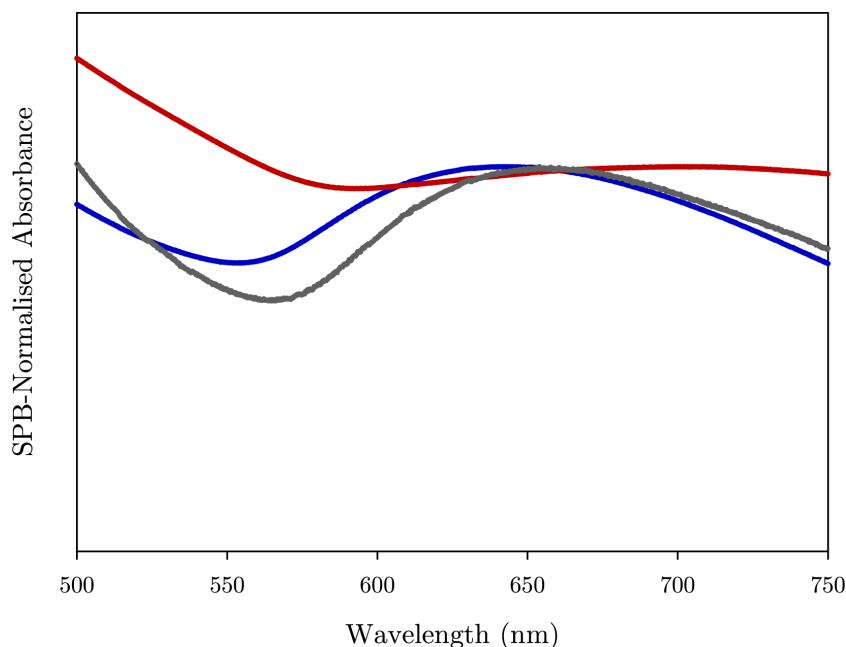


**Figure 4.6** SPB normalised UV-visible absorption spectra of CuNPs generated by 60 minutes of LASiS in  $10^{-4}$  molar solutions of CTAB (blue) and SDS (red). The grey trace is that of CuNPs generated by 60 minutes of LASiS in pure water for the sake of comparison.

It is clear that a physisorption interaction of a positively- or negatively-charged surfactant species and the CuNPs is not electrostatically strong enough to offer oxidative protection. By comparison, a chemisorption interaction between the negatively-charged tetrazoles and the CuNPs offers a stronger electrostatic interaction that offers oxidative protection.

It is interesting to note here at how red-shifted the absorbance of the SDS solution is, while CTAB is slightly more blue-shifted than that of pure water. Perhaps the reasoning for this lies in the structure of the surfactants, as CTAB is cationic and SDS is anionic. It could be surmised that the

negative surface of the CuNPs attracts the positively charged CTAB and repels the negatively charged SDS and this repulsion of the SDS then accelerates the oxidation of the CuNP surface.

#### 4.3.2 Carboxylic Acid Analogues

The hypothesis that the positively charged CTAB molecules are attracted to the CuNP surface and offer a better oxide protection than that of SDS, fails when it is realised that the four tetrazole ligands that give rise to the blue SPB absorption feature are notionally negatively charged when deprotonated in aqueous solutions. To assess whether it is the presence of a negatively charged species existing in solution that is enough to protect from oxidation, two carboxylic acid analogues were studied. The reason for using carboxylic acids is because they behave very similarly to tetrazoles when in aqueous solution, with both the tetrazole motif and the carboxylic acid motif having the ability to deprotonate in solution. In fact, tetrazoles are considered isosteres of carboxylic acids, having a very similar pK<sub>a</sub> to the equivalent carboxylic acid.<sup>[130]</sup> Therefore LASiS was conducted in 10<sup>-4</sup> molar solutions of benzoic acid (**ben-acid**) and nicotinic acid (**nic-acid**), with **ben-acid** being structurally similar to **T-Ph**, and **nic-acid** being structurally similar to **T-3Py**, the structure of these two acids shown in Figure 4.7.

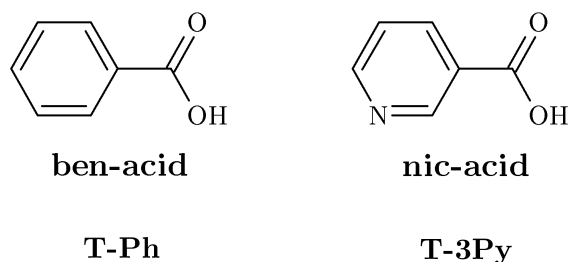


**Figure 4.7** Structure of the two carboxylic acids used in this study. Benzoic acid (**ben-acid**) is an analogue of **T-Ph** and nicotinic acid (**nic-acid**) is an analogue of **T-3Py**.

The absorption spectra (Figure 4.8) clearly show that the CuNPs formed by 60 minutes of LASiS in both **nic-acid** and **ben-acid** are not like those formed in solutions of the four negatively charged tetrazole ligands. This immediately suggests that it is not the deprotonating ability that dictates the position of the SPB. If that were the case it would be expected that both **nic-acid** and **ben-acid** have an SPB feature centred around 590 – 600 nm just like the negatively charged tetrazoles.

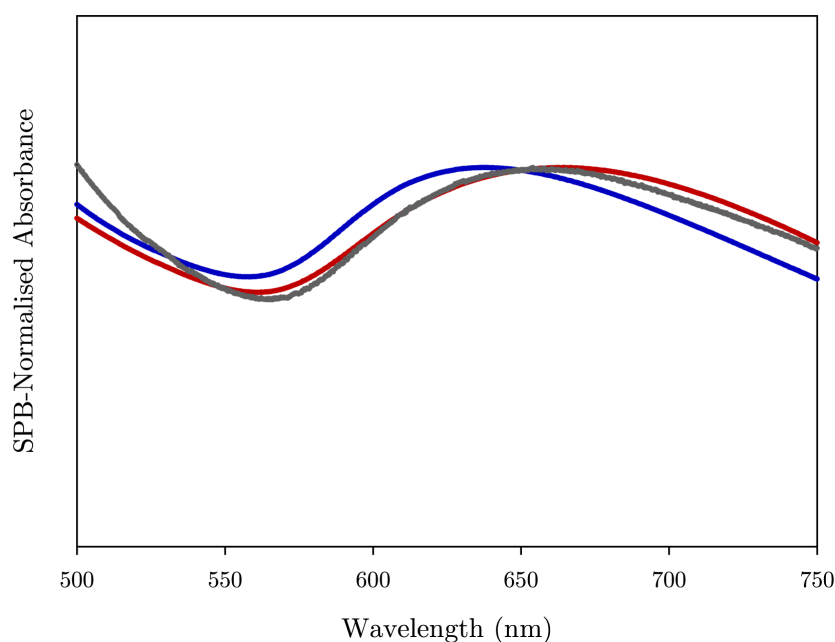


**Figure 4.8** SPB normalised UV-visible absorption spectra of CuNPs generated by 60 minutes of LASiS in  $10^{-4}$  molar solutions of **ben-acid** (blue) and **nic-acid** (red). The grey trace is that of CuNPs generated by 60 minutes of LASiS in blank water for the sake of comparison.

Clearly then there is something more than just the presence of a negatively charged ligand species existing in solution that gives rise to the unique SPB feature that is seen with the negatively charged tetrazole ligands.

### 4.3.3 Hydrazine

As mentioned previously, literature studies on laser-based CuNP production have identified an oxide being present on the CuNPs.<sup>[106,138,139]</sup>

Each of these studies identifies that copper oxides are present, and support the putative suggestion that the four deprotonated tetrazoles in aqueous solution are acting as reducing agents, preventing the formation of copper oxides during LASiS production. The rationale for this being that the SPB absorption feature of CuNPs formed in aqueous solutions of these four ligands is similar to that of CuNPs formed in acetone, which are known to be oxide free. Previously it was discussed that the reason for the protection was hypothesised to have come from a negatively charged enolate adsorbing onto the surface of the CuNP. However, it has now been shown that it is not solely the presence of a negatively charged ligand that causes the oxidative protection, but rather something more.

Therefore, it is suggested that the tetrazoles, in their deprotonated form, act as reducing agents in solution, protecting the CuNP surface. Such behaviour is akin to the reducing behaviour of compounds such as hydrazine during traditional chemical reduction CuNP formation.<sup>[53,59]</sup> Hydrazine is known to differentially coordinate to Cu (111), (100) and (110) surfaces,<sup>[178]</sup> and potentially influence CuNP size and shape during NP formation.<sup>[62]</sup>

Interestingly, the acetone enolate itself is not a reductant, and so the result seen with LASiS in acetone is purely from the preferential adsorption of the enolate ion onto the CuNP surface, protecting it from oxidation.

To test the whether the four deprotonated tetrazoles act as *in situ* reducing agents during the LASiS process, LASiS was undertaken in the presence of a  $10^{-4}$  molar aqueous solution of hydrazine. The absorption spectrum is presented in Figure 4.9 and clearly shows that the SPB absorption feature centred around 585 nm and is very much like that of CuNPs formed in acetone and the four blue deprotonated ligands.

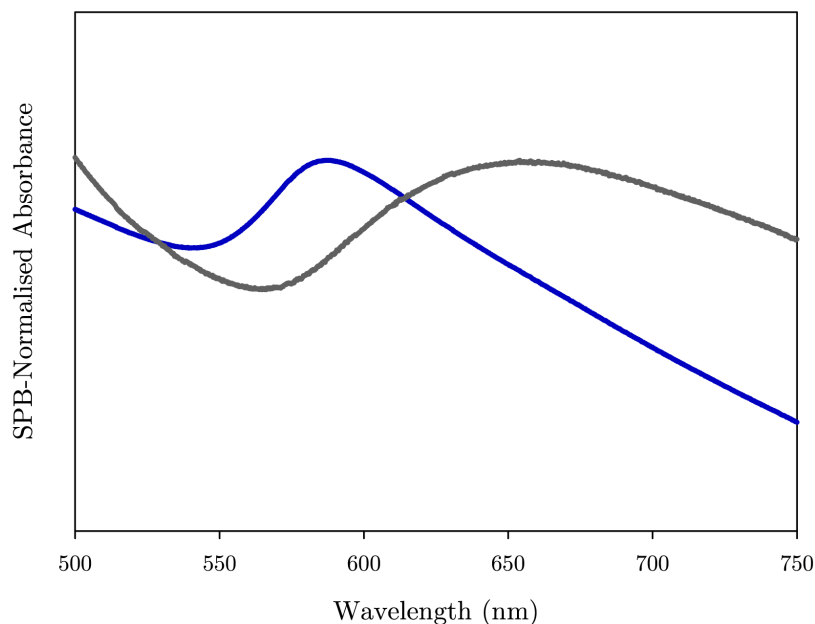


**Figure 4.9** SPB normalised UV-visible absorption spectra of CuNPs generated by 60 minutes of LASiS in  $10^{-4}$  molar solution of hydrazine (blue). The grey trace is that of CuNPs generated by 60 minutes of LASiS in blank water for the sake of comparison.

This is a powerful indicator that the deprotonated tetrazoles are behaving as *in situ* reducing agents, preventing the formation of copper oxides. This is a particularly striking outcome because tetrazolate anions are routinely considered to be relatively stable ligands in terms of their redox behaviour in the presence of redox-active metal cations. For example, it is well-documented that the addition of tetrazolate anions to Cu(II) precursors leads to the formation of stable Cu(II) complexes rather than to a reduction of the metal centre.<sup>[179]</sup>

#### 4.4 Conclusions

The most important aspect to arise from the work presented in this chapter is that it appears that the driving force for the position of the SPB absorbance band, and, the level of oxide protection, is dependent on the presence or absence of the negatively charged, deprotonated tetrazole. The

similarity between the absorption spectrum of CuNPs in acetone and the spectra of the four negatively charged tetrazoles would indicate that the CuNPs formed in both scenarios are very similar in composition, and that if there is copper oxide present it is of a very small amount, resulting in a very small red-shift in the SPB absorption feature.

The results presented with the two surfactants, SDS and CTAB, indicate that the presence of a charged species existing in solution is clearly not the reason for the observed behaviour of the 'blue' negatively charged tetrazole ligands. The presence of a negatively charged species, being the two carboxylic acids, is also indicative that a negatively charged species similar in structure to a tetrazole is still not enough to explain the results observed.

The deprotonation of the tetrazole itself clearly is not the driving force behind the results, as one might expect the carboxylic acids to give rise to a similarly-positioned SPB absorption feature if that were the case. Rather it is the presence of the whole deprotonated tetrazole motif that is the key. The results seen with the hydrazine and the behaviour of hydrazine in traditional reductive synthesis would indicate that the deprotonated tetrazoles are acting as *in situ* reducing agents, preventing the formation of copper oxides. This also confirms that it is the preferential adsorption of the acetone enolate ion onto the CuNP surface that is protecting from oxidation.

Importantly, the absorption spectra presented in this chapter have similarities to the spectra presented in Chapter 3, and this, coupled with the contour plots, would suggest that the ligand solutions studied give rise to some type of copper oxide coating on the CuNPs prepared by LASiS.

## Chapter 5: Particle Size Analysis

### 5.1 *Imaging Techniques*

The results seen in the previous chapters, highlighting the blue-shift of the SPB seen when LASiS is conducted in the presence of the four deprotonated tetrazole ligands, could be explained simply by noting that the spectral shifts may be a result of a difference in size of the NPs. Inspecting Equation 1.2, as the size of the particle changes, so does the Fröhlich frequency, and a change in Fröhlich frequency results in a change in the wavelength of the SPB absorption feature. Therefore, it is natural to assume that because the SPB absorption feature location changes from one group of ligands to another, there could be a change in the size of the nanoparticles between these groups.

However, it has been demonstrated in gold nanoparticles that NPs of diameters less than approximately 20 nm will not show an appreciable shift in SPB location.<sup>[6,8,91]</sup> Rice and co-workers discuss how gold and copper can be expected to behave in a similar manner due to both metals having similar band structures and optical properties.<sup>[55]</sup> Sun *et al.* demonstrate that CuNPs synthesised with diameters of 7.5 nm and 12.2 nm display very similar absorption spectra.<sup>[180]</sup> Ghodselahi *et al.* demonstrate that CuNPs with diameters of 16 nm, 17 nm, 20 nm and 22 nm have similar absorption spectra.<sup>[181]</sup> Finally, El-Sayed and co-workers show that CuNPs with diameters of 12 nm and 30 nm display near identical absorption spectra.<sup>[103]</sup> Therefore, it is not expected that the blue-shift seen in the UV-visible spectra is likely to be attributed to significantly smaller particle size distributions for CuNPs produced via LASiS in the presence of the four blue tetrazole ligands.

Nevertheless, determination of CuNP particle size distributions is required as confirmation.

The most convenient way of determining particle size distributions is to employ the use of microscopy techniques. While there are many different types of microscopy, most techniques fall within three main well-known branches: optical microscopy, electron microscopy (EM) and scanning probe microscopy (SPM). Both optical microscopy and EM involve the diffraction, reflection or refraction of electromagnetic radiation interacting with a sample, and the collection of the scattered radiation in order to create an image. SPM, on the other hand, involves the interaction of a probe and the surface of the sample as the probe is scanned across the sample.

The nature of optical microscopy makes it unsuitable to image nanoparticles. This is due to an inherent maximum practical magnification limit of around 1500 times which is dictated by a decrease in the resolution that results in too poor an image at higher magnifications. This is because there is a finite limit of magnification beyond which it is impossible to resolve separate points in the field of view. This limitation is known as the ‘Abbe diffraction limit’ after Ernst Abbe.<sup>[182]</sup> Abbe found that light with wavelength  $\lambda$  travelling in a medium with refractive index  $n$  and converging on a spot with an angle of  $\theta$  will create a spot with radius:

$$d = \frac{\lambda}{2n \sin\theta}. \quad (5.1)$$

This is known as the Abbe limit or the diffraction size, with the denominator component,  $n \sin\theta$ , also known as the numerical aperture ( $NA$ ). This reduces Equation 5.1 to:

$$d = \frac{\lambda}{2NA}. \quad (5.2)$$

In modern optics  $NA$  is as high as 1.5, and a wavelength of 550 nm is used, due to it having the highest optical sensitivity in the human eye. These conditions result in a  $d$  value of around 180 nanometres, but in practice the lowest values of  $d$  that can be attained are about 250 nanometres or 0.25 micrometres.<sup>[183]</sup> Even at optimum conditions, this resolution is too large when we are concerned with imaging nanoparticles.

This then limits imaging to the EM and SPM techniques, which both have far better resolution limits. EM has a resolution of less than 0.1 nm due to the fact that the wavelength of electrons is around 100,000 shorter than that of visible light, which when applied to Equation 4.2 gives a very small  $d$  value. SPM has an even better resolution, on the order of a few picometres, because resolution is not constrained by diffraction limits but by the point spread function and by the electronics of the detection system.

Because SPM is a physical imaging technique, employing electronics to generate the image, the limiting factor on the resolution of the image is the interaction between the probe tip and the sample, rather than an electron source. This limiting factor is known as the point spread function (PSF), which describes the error associated with the response of the tip to imaging a singular point source. In general terms, the probe tip has a certain volume associated with it, and upon interaction with a singular point source, the resulting image is a combination of the point source and the volume of the tip, resulting in a blurred image of the point source. This blurred image error is very small compared to that of EM sources. In reality, the defining factor for resolution is the bit factor of the tip.

While SPM is not highly resolved in the X and Y axis (this is dependent on user settings, but usually varies between 256 and 1024 data points in each axis), it is much greater resolved in the Z-axis. A 16-bit tip

has 65,536 data points in the Z axis, and while the vertical range of the tip is a user preference, even with a large setting of 5 micrometres of range there is 0.076 nanometres between each data point. The result is that both EM and SPM are techniques that are vastly better than optical microscopy for imaging nanoparticles.

## ***5.2 Principles of Microscopy***

### **5.2.1 Electron Microscopy**

There are two chief methods of EM, those being scanning electron microscopy (SEM) and transmission electron microscopy (TEM). While SEM and TEM both use an electron gun to generate an image, as opposed to a light source in the case of optical microscopy, the way they work is slightly different, and as a consequence they generate a different style of image. The basic principle of SEM involves the focusing of an electron beam at a sample, with the interaction of the electron beam with the atoms in the sample resulting in various changes in the signals that are detected and used to create the image.

In this project, TEM has been used to characterise the particle size distributions of CuNPs formed in aqueous ligand solutions. The basic principle of TEM involves the focusing of an electron beam to be transmitted through a sample, and the interaction of the electron beam with the sample is captured on a CCD camera to yield an image. The classical imaging mode that is used is known as contrast formation, where the change in contrast of the image corresponds to features in the sample. The most common mode of contrast formation is bright field imaging, where areas on the image that appear dark are the specimens (due to the absorption of electrons from the source), and regions that appear bright are regions with no sample.

### 5.2.2 Scanning Probe Microscopy

While SEM and TEM use an electron gun to generate their images, SPM methods physically probe the surface of the sample, generating an image based on the tip deflection. There are many different types of SPM techniques, and all employ the same basic method to image. The method employed in this research is called atomic force microscopy (AFM). AFM is a high-resolution scanning probe microscopy technique, forming an image of a surface with resolution of up to fractions of a nanometre, using a physical probe that scans the surface.

A laser constantly measures the probe tip and uses force curves to generate a virtual image of what it is analysing. The image that is formed by AFM is created, in the basic sense, by ‘feeling’ or ‘touching’ the surface of the sample being scanned. Because the image that is formed is built up from physical interaction with the sample, rather than an electronic interaction as is the case with EM, the AFM only yields information of the surface chemistry, or, at best, a few angstroms into the sample.

There are a few different types of images that can be created by AFM, such as phase and amplitude images; however, the imaging mode used here is the height topographical image. This is an image that is created from the information about the physical amount the probe is deflected by the height of the features of the sample. The advantage of this type of imaging is that the data it yields can be used to determine the size of the nanoparticles quite easily, as the height of the nanoparticles imaged can, with sufficiently low substrate surface coverage, be considered to be a reasonable measure of the diameter of the nanoparticles.

### ***5.3 Imaging of Nanoparticles***

#### **5.3.1 Imaging Considerations**

For AFM imaging to work successfully for this project, that is, to obtain an accurate reflection of the diameter of the nanoparticles, there needs to be a very flat surface on which the nanoparticles are deposited. While it might seem that surfaces such as glass or polished metal are sufficiently flat, in fact they are not. When you consider that the nanoparticles are in the range of possibly 1-100nm in diameter, only a surface that is atomically flat is acceptable. A suitable candidate for this purpose is freshly cleaved mica, as it cleaves clean on the {001} plane, leaving a surface that is flat to within approximately 1 nanometre.<sup>[184,185]</sup>

Due to the fact that freshly cleaved air-exposed mica surfaces can and do get contaminated, all nanoparticle solutions were deposited on the surface of the mica immediately after cleaving, and stored in a sealed container. Keeping in mind the contamination issue, only nanoparticles with diameters larger than approximately 2 nm were counted. This minimum diameter of 2 nm is validated because below this diameter the SPR is no longer supported and doesn't give rise to the SPB absorption feature. This has been affirmed both theoretically<sup>[186]</sup> and experimentally.<sup>[187]</sup>

As a consequence, because the SPB absorption feature exists when there are particles of sufficient size, the argument that a change in the SPB location is due to a change in size therefore means we focus our study on particles that can support the SPR. While AFM is not a commonly used imaging technique for NPs, it has major benefits over TEM or SEM due to its ease of use and there being no need for a high vacuum resulting in quick imaging turn around.

For this work, AFM was used as the primary imaging method, and TEM was used as a comparison technique. It is important to point out from the onset that the two methods of sample preparation for AFM and TEM imaging, as described in Chapter 2.3, are different. The nature of the AFM spin-coating preparation leads to less conglomerates on the mica surface, with larger particles being spun off, while there is no spin-coating with TEM, just a drop-cast process, so there is ample time for conglomerates to form. The TEM imaging process only gives two-dimensional information (as opposed to the AFM technique which gives three-dimensional information), so the diameter of the CuNPs must be measured by software (with appropriate conditions as mentioned in Chapter 2), rather than extracted from the topographical image given by AFM, which means there is a larger degree of ambiguity with the accuracy of the size distribution.

The lack of spin-coating with the TEM samples means that size analysis is inherently more complex due to the presence of conglomerates. While sample dilution could aid in the reduction of these conglomerates forming, the presence of CuNPs was difficult enough to find in practice. While the conglomerates were straight forward to ignore when analysing the TEM images, it is highly likely that a percentage of small (2-5 nm) CuNPs were not counted due to some particle overlap, image quality and human error, while size analysis was also conducted to err on the side of caution such as to not miscount CuNPs. Because of this, a direct comparison between the AFM and TEM images and size distributions cannot be made. Rather, a semi-quantitative comparison of the trends across the two techniques is made. Therefore, TEM imaging was used as a comparison technique to the AFM imaging, the main reason being that TEM is a commonly used technique, which then makes it possible to compare the distributions seen in this research with past research.

### 5.3.2 Analysis Considerations

Once the imaging and particle size analysis was completed as per the discussion in Section 2.3, the data was processed to generate a classical frequency distribution (histogram) of the diameter of the nanoparticles, along with a cumulative frequency distribution (CFD). The main advantage of a CFD is that it provides an easy way to compare between different data sets, and rules out the subjectivity of finding the best-suited bin width for a frequency distribution. It's quite easy to have too many bins and show too much information on a histogram, just as it is with having not enough bins and having not enough information. Another feature of a CFD is that it is easy to see the percentage of data that is between two size points.

While previously postulated that the difference in SPB absorption feature location is not due to a change in size (see Section 5.3.1), a CFD plot makes it easy to calculate what percentage of NPs are less than a certain diameter. In this study, we consider the percentage of NPs that are smaller than 25 nm in size, as these are the NPs that give rise to the majority of the SPB feature (see Section 3.1). If the imaging data shows that, on the whole, the size distributions of the NPs generated by 60 minutes of LASiS in the presence of the multitude of ligands is the same, then clearly the spectral differences seen in the SPB absorption feature are attributable to the ligands and not the CuNP size. Representative AFM images for all CuNP solutions are shown in Appendix 5A, while representative TEM images for all CuNP solutions analysed are shown in Appendix 5B.

### 5.3.3 AFM Analysis Results

The particle size analysis of CuNPs generated following 60 minutes of LASiS in pure water shows that the NPs have what could be considered a very typical particle size distribution (see Figure 5.1). The mean diameter of the distribution is 12.7 nm with a standard deviation of 7.4 nm and

distribution maximum of 8 nm as reported in Table 5.1. The CFD plot shows that 92% of the NPs are smaller than 25 nm in diameter. Appendix 5A demonstrates a representative AFM image.

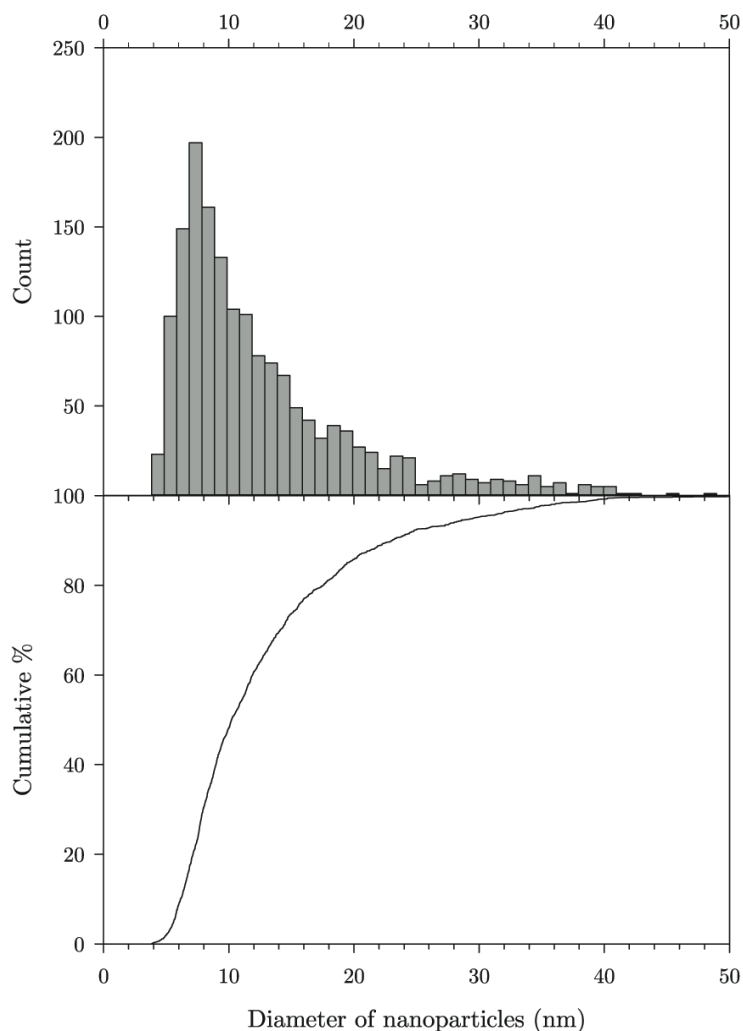


**Figure 5.1** Combined particle size distribution and cumulative function distribution plot of the diameter of CuNPs generated by 60 minutes of LASiS in pure water.

The particle size distributions of CuNPs generated following 60 minutes of LASiS in the presence of each of the four neutral N-donor ligand solutions are shown in Figure 5.2 (with representative AFM images in Appendix 5A). Visually the distributions appear similar to that of CuNPs generated in pure water, and the statistics in Table 5.1 show that there is a

high degree of similarity. The statistics show that there is some minor variability between the particle size distributions, though this is attributed to experimental variability.

**Table 5.1** Descriptive statistics of the particle size distributions determined by AFM of CuNPs generated by 60 minutes of LASiS in the listed solutions.

Ligand ( $10^{-4}$ molar)	Mean (nm)	Std Dev. (nm)	Dist. Max (nm)
None (pure water)	12.71	7.38	8
phen	8.95	6.87	5
bipy	10.17	5.03	6
Py	8.22	4.5	6
4Ph-Py	13.28	6.65	9
T-Me	8.19	7.65	4
T-Ph	7.18	7.6	3
T-3Py	5.69	3.65	3
T-4Py	5.36	5.14	3
BuT-Me	8.64	5.69	5
BuT-Ph	8.75	5.29	5
BuT-3Py	6.98	3.88	5
BuT-4Py	11.61	6.31	7
T-2Py	10.76	7.11	5
BuT-2Py	9.77	5.31	5
acetone (neat)	6.20	4.17	4
CTAB	8.22	7.54	4
SDS	9.99	5.39	6
nic-acid	8.56	6.08	4
ben-acid	15.1	7.63	10
hydrazine	4.27	3.13	3

## Particle Size Analysis

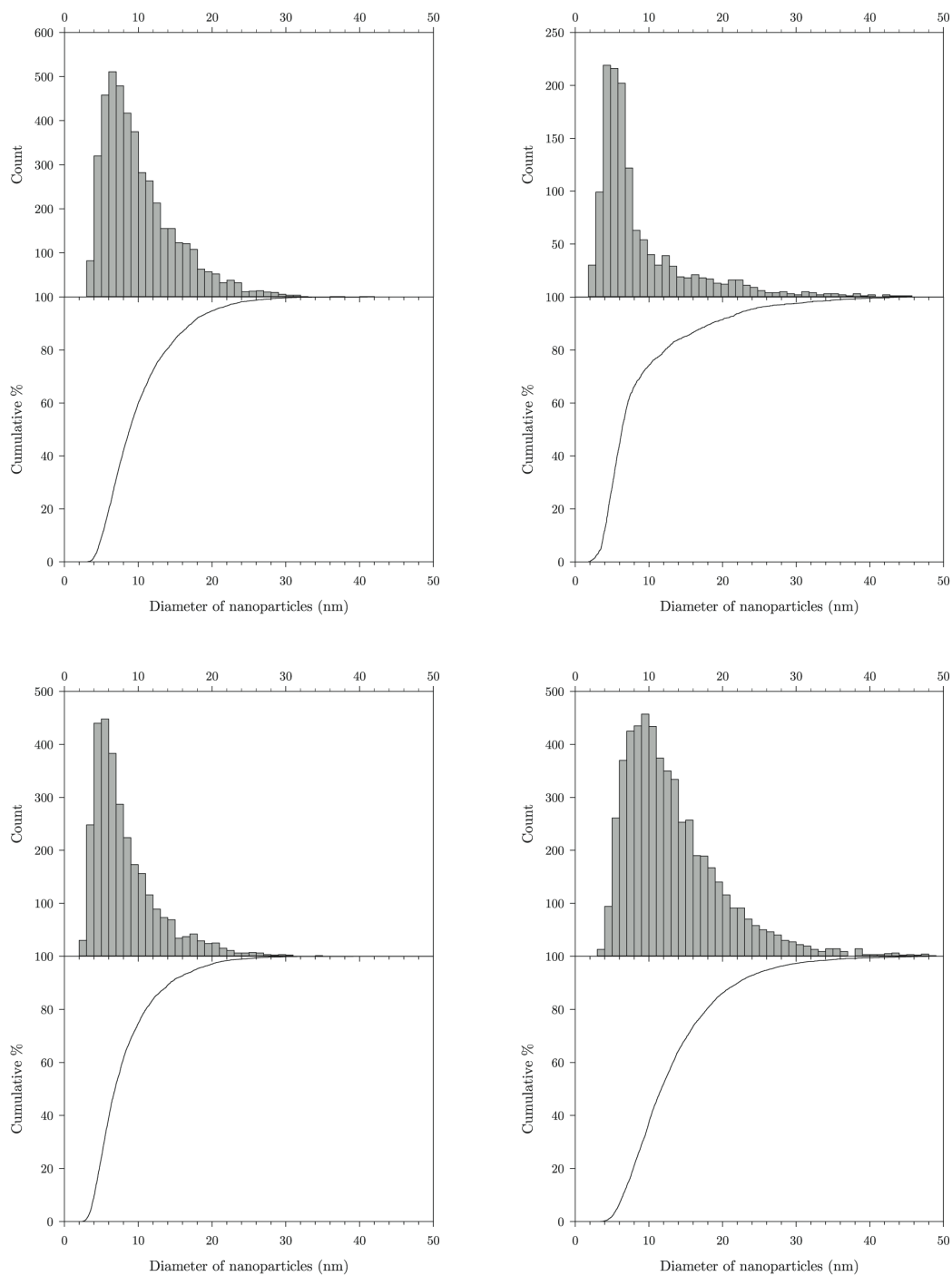


**Figure 5.2** Combined CuNP particle size distribution histogram (top panel) and cumulative function distribution (bottom panel) for NPs generated by 60 minutes of LASiS in  $10^{-4}$  molar solutions of (from left to right, top to bottom): **bipy**, **phen**, **Py** and **4Ph-Py**.

Furthermore, when the CFD plots are examined (Figure 5.2, lower panels) it is seen that they are all very similar in profile, and like the distribution presented in Figure 5.1. Despite the slight variations in size, the UV-visible spectra in Section 3.2.2 show that all four ligands behave very similarly and demonstrate a similar SPB absorption feature and location. The lowest percentage of NPs under 25 nm is 94%, indicating that there is only a very small number of large NPs in solution.

In contrast, CuNPs generated following 60 minutes of LASiS in the presence of the four deprotonated tetrazole ligand solutions (Figure 5.3, representative AFM images in Appendix 5A) demonstrate distributions that visually appear different to that of CuNPs generated in pure water and the neutral N-donor ligands. The statistics show that all four CuNP size distributions have smaller means and distribution maxima compared to that of both pure water and the neutral ligands (Table 5.1), with the lowest percentage of NPs under 25 nm being 95%. However, the distribution maxima values are only smaller by a few nanometres. Like the neutral ligands, the UV-visible spectra in Section 3.2.3 show that the spectra are very similar despite the variation here in the size distributions.

As seen in Figure 5.4, the distribution of NPs generated following 60 minutes of LASiS in the four alkylated tetrazole-based ligand solutions are like that of CuNPs in pure water, and different to that of CuNPs in the four deprotonated ligand solutions (representative images shown in Appendix 5A). The statistics presented in Table 5.1 show that the means and standard deviations are all similar to that of the pure water and neutral ligand CuNP solutions. The distribution maxima are also very similar, and only a few nanometres larger than that of the blue ligand CuNP solutions.

## Particle Size Analysis

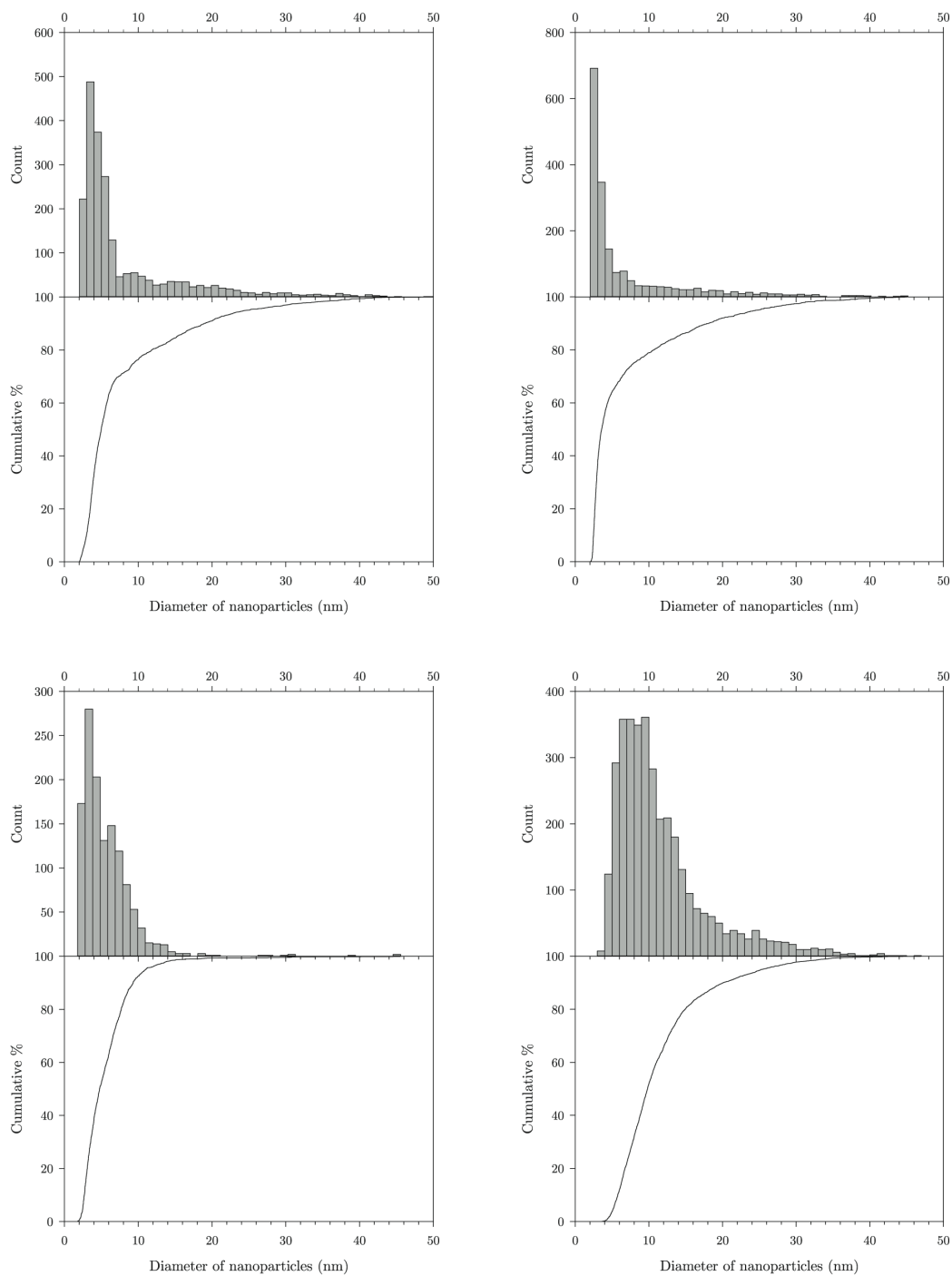


**Figure 5.3** Combined CuNP particle size distribution histogram (top) and cumulative function distribution (bottom) for NPs generated by 60 minutes of LASiS in  $10^{-4}$  molar solutions of (from left to right, top to bottom): **T-Me**, **T-Ph**, **T-3Py** and **T-4Py**.

## Particle Size Analysis

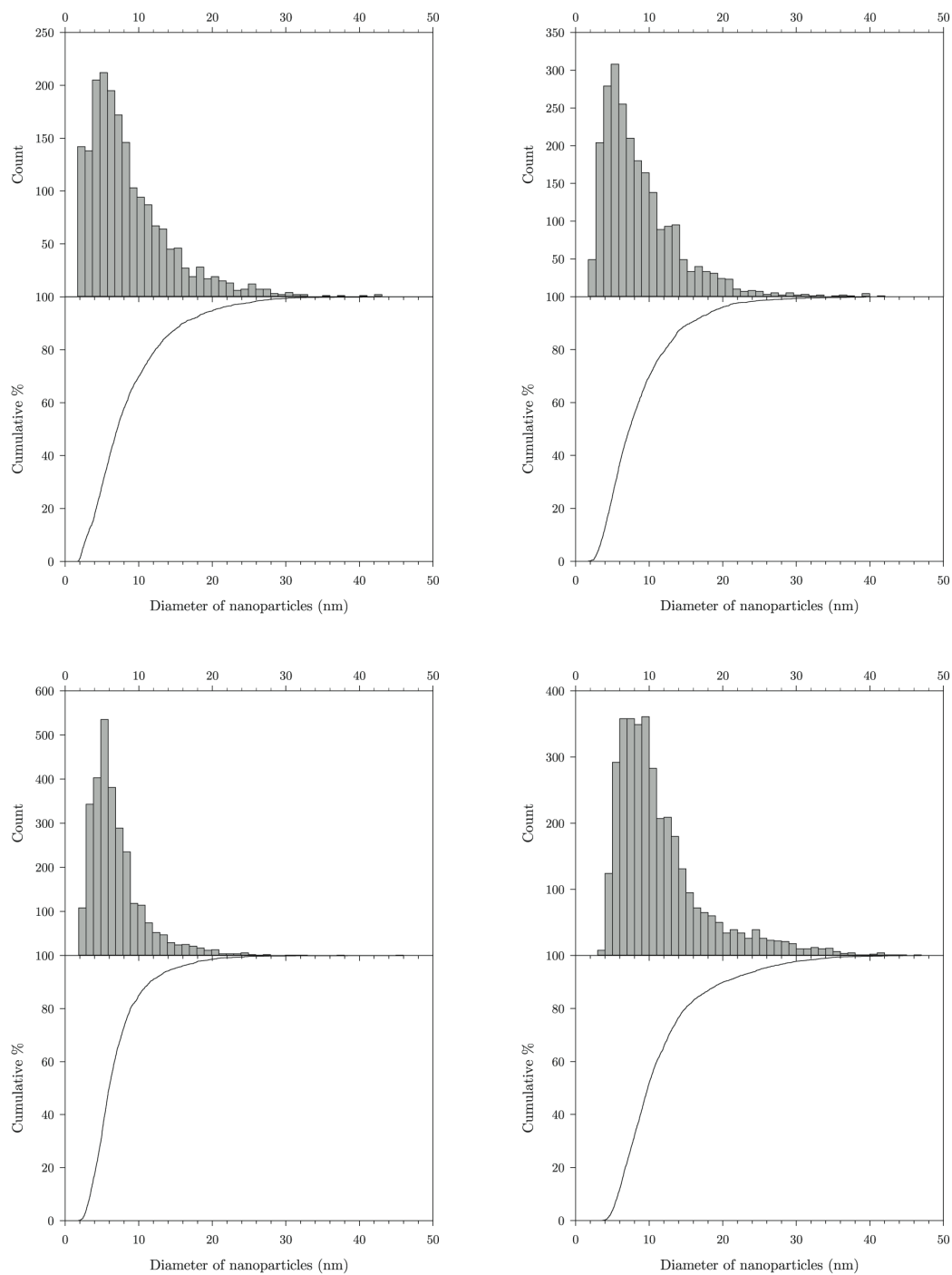


**Figure 5.4** Combined CuNP particle size distribution histogram (top) and cumulative function distribution (bottom) for NPs generated by 60 minutes of LASis in  $10^{-4}$  molar solutions of (from left to right, top to bottom): **BuT-Me**, **BuT-Ph**, **BuT-3Py** and **BuT-4Py**.

The lowest percentage of NPs under 25 nm is 95%. The similarity of the particle size distributions for the ‘neutral’ and alkylated tetrazole-encapsulated CuNP samples, together with the only slightly smaller size distributions observed for the ‘blue’ tetrazole-based ligands indicates that the majority of NPs are smaller than 25 nm in size, and suggests that the blue-shifts observed in the SPB absorption spectra is not attributable to a change in NP size. That is, an approximate 70 nm SPB spectral shift cannot be accounted for by a CuNP particle size distribution peak only 3 nm smaller.

Figure 5.5 shows the histograms and CFD plots of CuNPs generated following 60 minutes of LASiS in **T-2Py** and **BuT-2Py** (representative images in Appendix 5A). The statistics, seen in Table 5.1, reveal that the CuNPs generated in these solutions are again very similar to that of CuNPs generated in pure water, the ‘neutral’ N-donor ligands and the alkylated tetrazole-based ligand solutions.

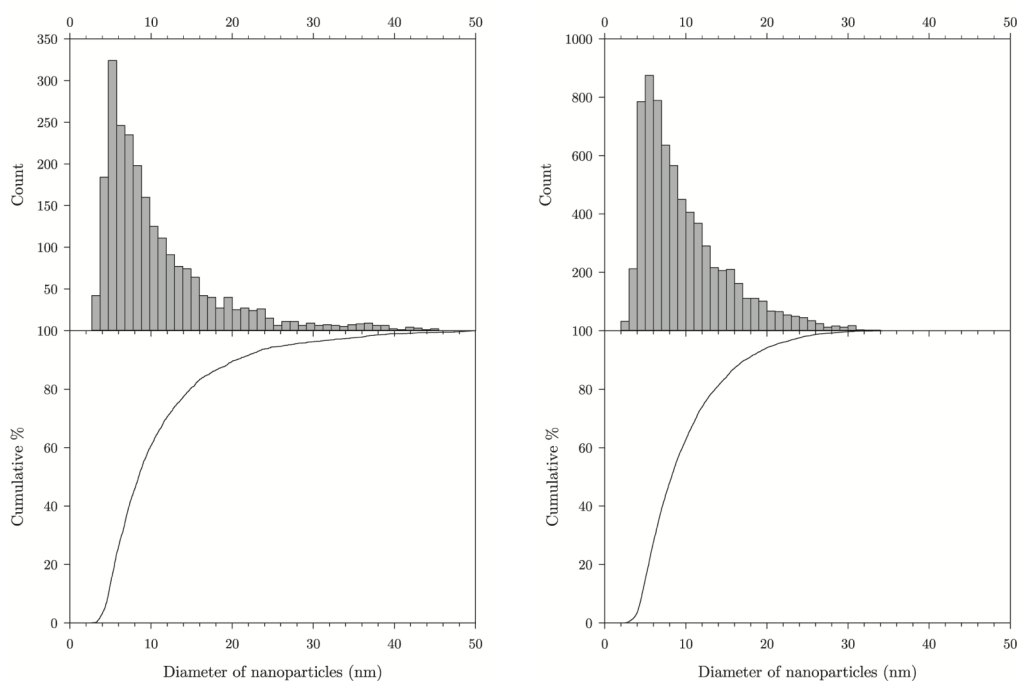


**Figure 5.5** Combined CuNP particle size distribution histogram (top) and cumulative function distribution (bottom) for NPs generated by 60 minutes of LASiS in  $10^{-4}$  molar solutions of (from left to right): **T-2Py** and **BuT-2Py**.

The lowest percentage of NPs under 25 nm is 94%, similar to every CuNP solution discussed to this point. The similarities in the size distributions demonstrated here with these two ligands and previously reported size distributions is further evidence that the spectral shifts are not due to a change in NP size.

CuNPs generated following 60 minutes of LASiS in neat acetone have a size distribution shown in Figure 5.6 (representative image in Appendix 5A). The statistics shown in Table 5.1 show that the NPs formed have a narrow distribution, with a mean of 6.2 nm and a standard deviation of 4.17 nm, with only 1% of NPs being larger than 25 nm in size. It is clear to see that the particle size distribution of CuNPs generated in acetone is very similar to that of CuNPs generated in the four deprotonated tetrazole-based ligands.

The size distributions of CuNPs generated following 60 minutes of LASiS in CTAB and SDS are also shown in Figure 5.6 (representative images in Appendix 5A). The statistics, as seen in Table 5.1, show that the distribution of NPs created in both these solutions is very similar to that of CuNPs generated in pure water and the neutral n-donor ligand solutions, and the lowest percentage of NPs less than 25 nm is 95%.

CuNPs generated following 60 minutes of LASiS in solutions of **nic-acid** and **ben-acid** have size distributions shown in Figure 5.7 (representative images in Appendix 5A). The statistics shown in Table 5.1 reveal that **nic-acid** has a distribution very similar to that of the neutral ligands and pure water, while **ben-acid** has the largest distribution of all the tested solutions in this work, though with 90% of the NPs less than 25 nm in diameter it's not too dissimilar to the neutral ligand and pure-water solutions.

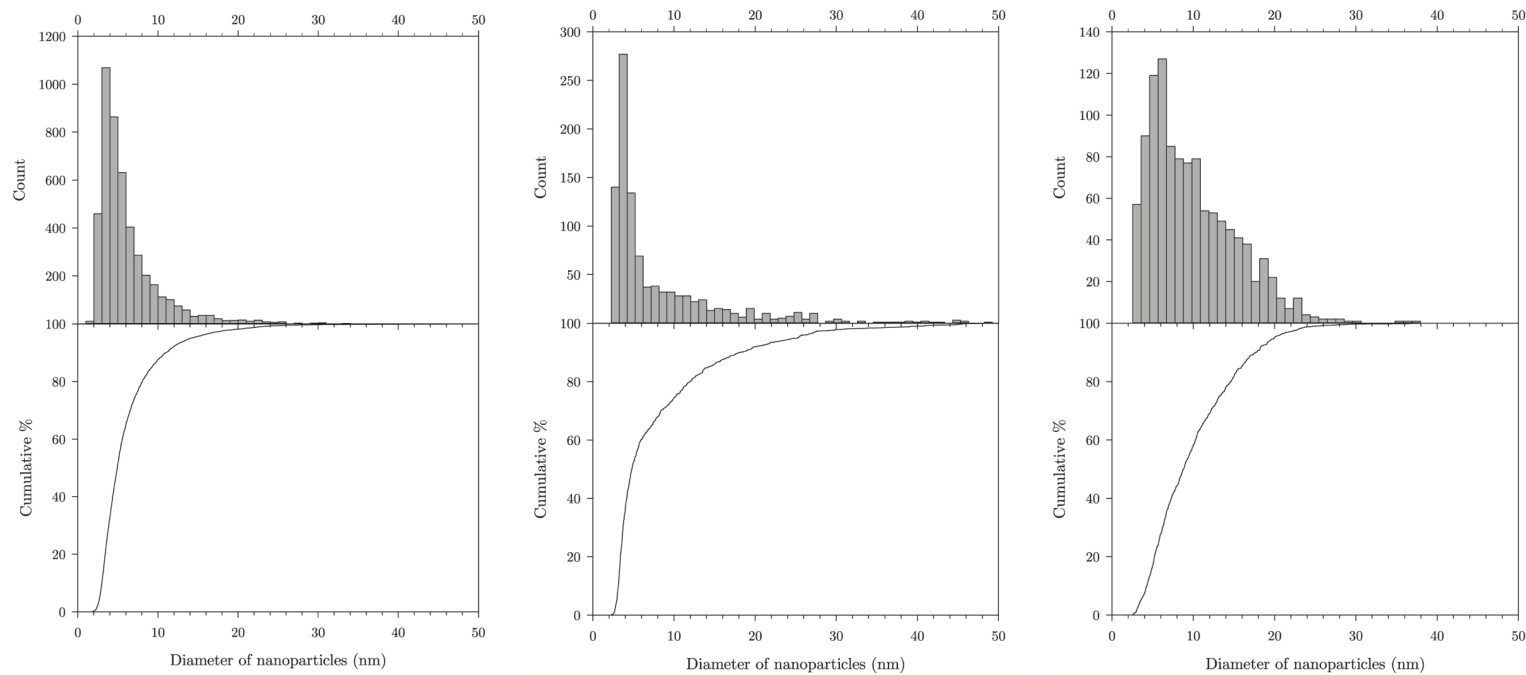


**Figure 5.6** Combined CuNP particle size distribution histogram (top) and cumulative function distribution (bottom) for NPs generated by 60 minutes of LASiS in acetone (left) and  $10^{-4}$  molar solutions of CTAB (middle) and SDS (right).

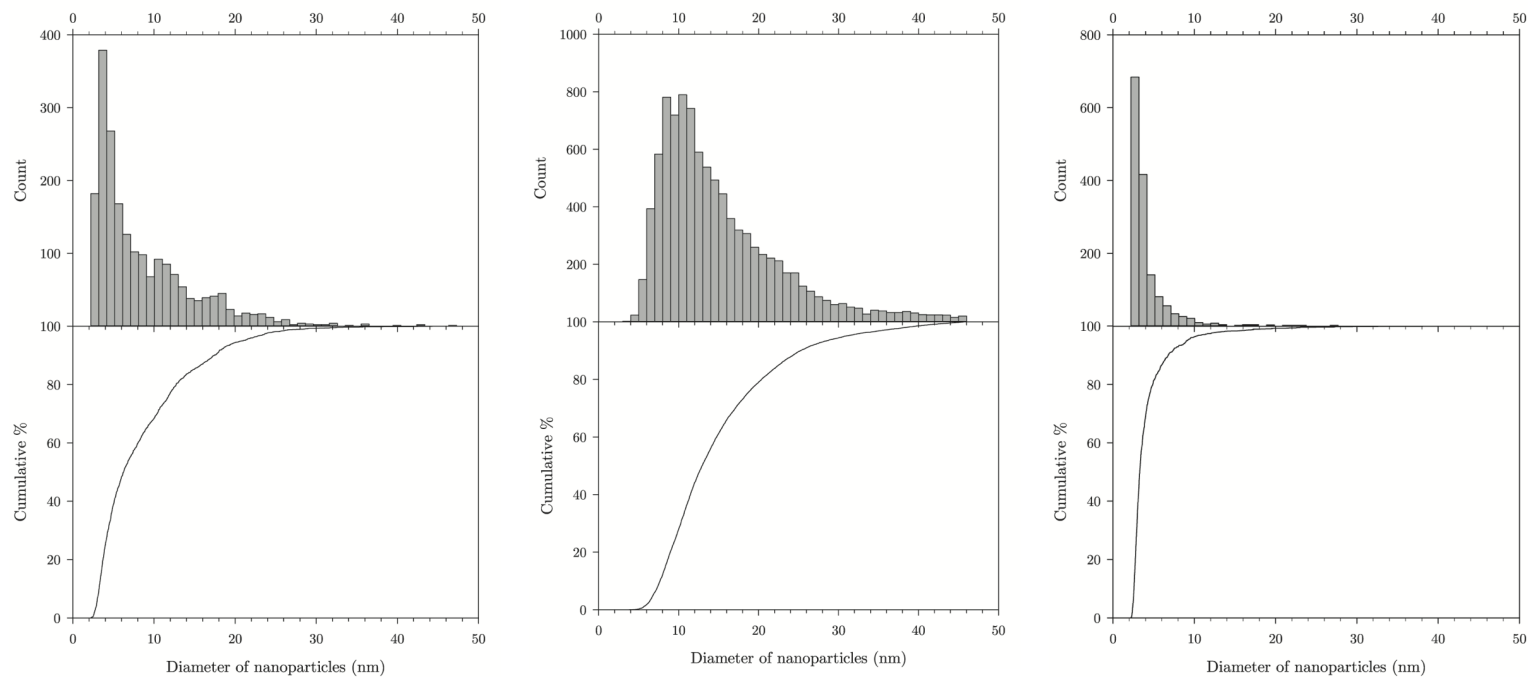


**Figure 5.7** Combined CuNP particle size distribution histogram (top) and cumulative function distribution (bottom) for NPs generated by 60 minutes of LASiS in  $10^{-4}$  molar solutions of **nic-acid** (left), **ben-acid** (middle) and hydrazine (right).

It should be noted that the particle size analysis shows that the CuNPs formed in a solution of **nic-acid** are smaller than CuNPs formed in a solution of **ben-acid**. This is even though the SPB absorption feature of CuNPs formed in a solution of **nic-acid** is slightly red-shifted relative to CuNPs generated in a solution of **ben-acid** (Figure 4.8). This is further evidence to support the putative notion that the SPB spectral shifts are not primarily attributable to CuNP size distributions. If that were the case, it would be expected that the size distribution of CuNPs generated in **nic-acid** be larger than that of CuNPs generated in **ben-acid**.

Finally, CuNPs generated by 60 minutes of LASiS in an aqueous hydrazine solution has a size distribution also presented in Figure 5.7 (representative image in Appendix 5A). The mean and standard deviation, reported in Table 5.1, show that the NPs produced have a distribution like that of NPs generated in the four deprotonated tetrazole-based solutions, as well as pure acetone. It is demonstrated that the CuNPs have a narrow distribution of particles, with a distribution maximum abundance of 3 nm, while the percentage of NPs less than 25 nm in size is 99%. It is possible that the strong chemical reducing environment of hydrazine in solution does limit the size distribution of the CuNPs formed. This also explains the slightly smaller size distributions seen with the deprotonated tetrazole ligand solutions, as it is suggested that they act as *in situ* reducing agents, and both these four ligands and hydrazine exhibit blue-shifted SPB absorption features (this concept is discussed in the next chapter).

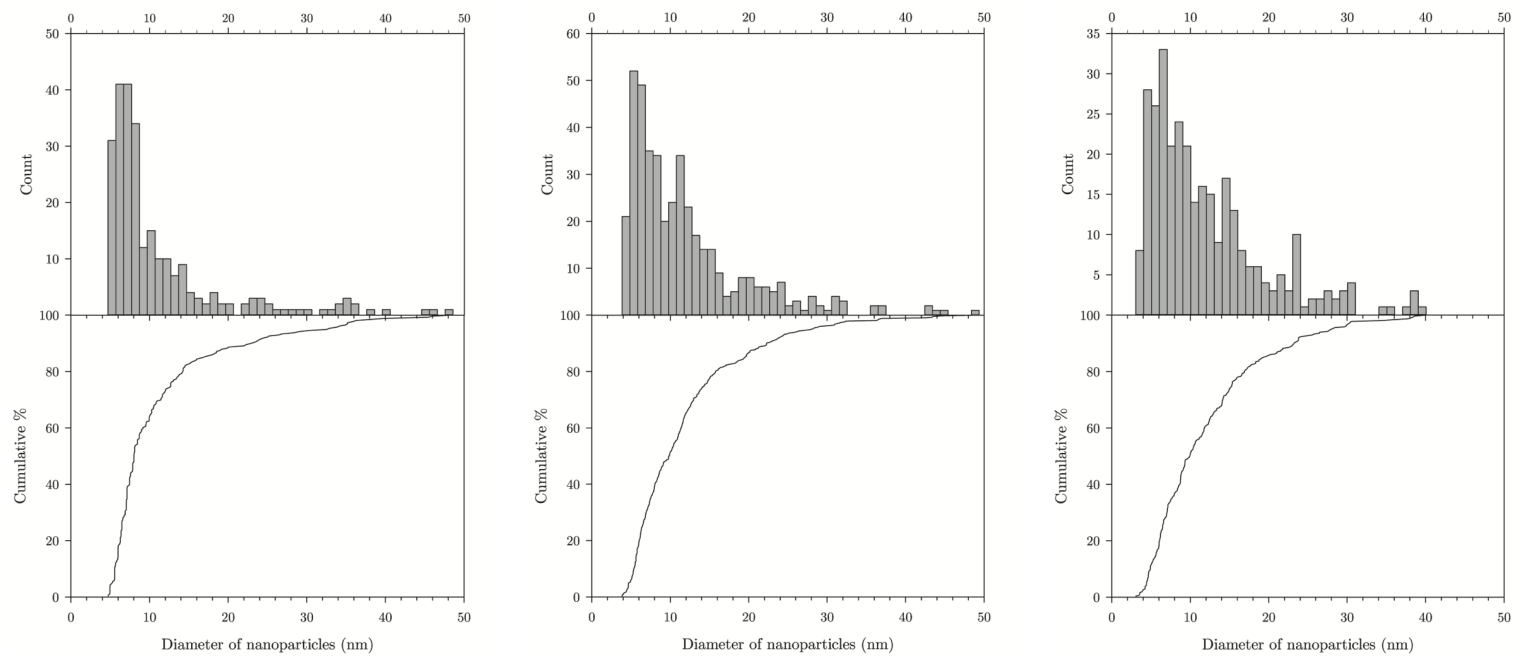


**Figure 5.8** Combined CuNP particle size distribution histogram (top) and cumulative function distribution (bottom) for NPs generated by 60 minutes of LASiS in pure water (left) and  $10^{-4}$  molar solutions of **bipy** (middle) and **phen** (right)

### 5.3.4 TEM Analysis Results

TEM size analysis was not undertaken on all the ligands, but on CuNPs generated in pure water and representative ligand solutions from the neutral, deprotonated tetrazole and alkylated tetrazole groups. The particle size analysis of CuNPs generated following 60 minutes of LASiS in pure water results in a histogram and CFD plot presented in Figure 5.8 (representative image in Appendix 5B).

The statistics in Table 5.2 show that the mean is 11.38 nm and the standard deviation is 8.21 nm, with a distribution maximum of 7 nm, which is similar to the statistics reported in Table 5.1 for the AFM method. The percentage of NPs smaller than 25 nm is 92% which is also similar to that reported by the AFM size analysis.

**Table 5.2** Descriptive statistics of the particle size distributions as determined by TEM of CuNPs generated by 60 minutes of LASiS in the listed solutions.

Ligand ( $10^{-4}$ molar)	Mean (nm)	Std Dev. (nm)	Dist. Max. (nm)
None (pure water)	11.38	8.21	7
<b>phen</b>	12.16	7.51	6
<b>bipy</b>	11.95	7.62	6
<b>T-3Py</b>	9.42	5.05	6
<b>T-4Py</b>	12.97	6.10	8
<b>BuT-3Py</b>	12.33	8.61	6
<b>T-2Py</b>	11.42	7.93	6

TEM size analysis of CuNPs generated following 60 minutes of LASiS in  $10^{-4}$  molar solutions of **phen** and **bipy**, result in histograms and CFD plots that are also seen in Figure 5.8 (representative images in Appendix 5B). The statistics in Table 5.2 show that the means and standard deviations are near

identical and are very similar to that of CuNPs generated in pure water, while the CFD plot reveals that 93% of NPs are smaller than 25 nm in diameter in both cases. The similarity born out here mirrors the similarity seen with the AFM analysis.

The size analysis of CuNPs generated following 60 minutes of LASiS in two tetrazole-based ligands, **T-3Py** and **T-4Py**, have a size distribution as shown in Figure 5.9 (representative images in Appendix 5B). Table 5.2 shows that the means are 9.42 and 12.97 nm, respectively, with the standard deviations being 5.05 and 6.10 nm, respectively. The CFD plot demonstrates that the lowest percentage of NPs smaller than 25 nm is 95%.

Surprisingly, while the AFM size distributions show that the CuNPs formed in these solutions are slightly smaller than the other CuNP solutions, this is not seen here. As seen in Table 5.2, the means and standard deviations of CuNPs generated in these two tetrazole-based ligand solutions are similar to that of CuNPs generated in water and in **phen** and **bipy**. The size distributions for these five CuNP solutions as determined here by TEM suggest that the CuNPs are of similar size. A possible explanation for this similarity may lie in the imaging method. The TEM resolution is not as good as AFM, and the measurement of the size of the NPs was done manually, introducing human error, while AFM was done automatically by software.

CuNPs generated following 60 minutes of LASiS in a  $10^{-4}$  molar solution of **BuT-3Py** were size-analysed by TEM and found to have a mean and standard deviation as shown in Table 5.2. The histogram and CFD as shown in Figure 5.9 demonstrate along with the mean and standard deviation, that the particle size distribution of CuNPs generated in this alkylated tetrazole ligand solution is very similar to that of CuNPs generated in the neutral n-donor ligand solutions and pure water, and slightly larger

than that of **T-3Py** (12.33 nm and 8.61 nm for the mean and standard deviation respectively). A representative image is shown in Appendix 5B.

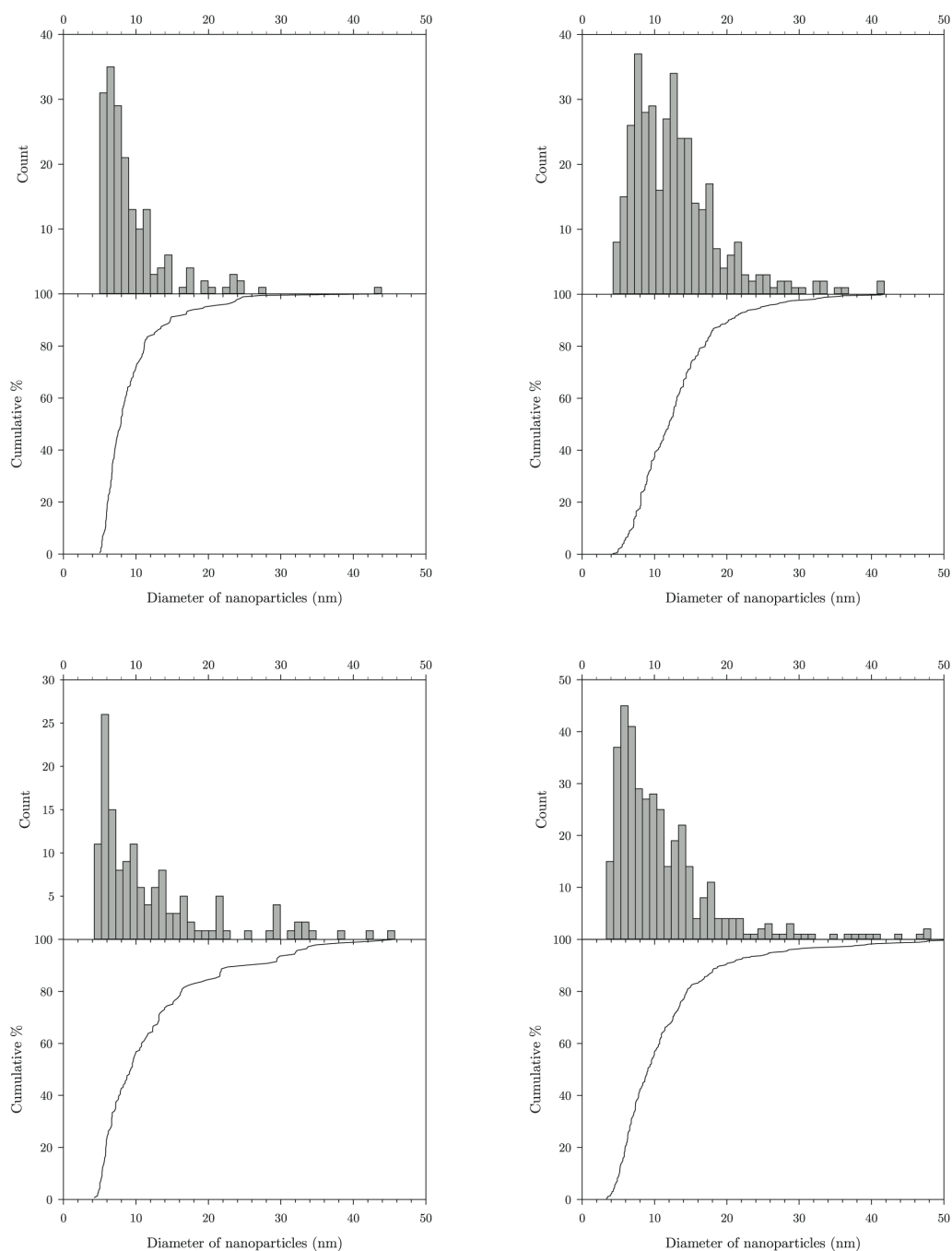


**Figure 5.9** Combined CuNP particle size distribution histogram (top) and cumulative function distribution (bottom) for NPs generated by 60 minutes of LASiS in  $10^{-4}$  molar solutions of (left to right, top to bottom) **T-3Py**, **T-4Py**, **BuT-3Py** and **T-2Py**.

Only 90% of NPs in this solution were smaller than 25 nm in diameter, the smallest percentage reported here by TEM analysis. Compared to the AFM size analysis, the result reported here is somewhat larger, but it compares favourably with the other results obtained by TEM for the other ligand solutions.

Finally, CuNPs generated following 60 minutes of LASiS in a  $10^{-4}$  molar solution of **T-2Py** were analysed by TEM, with the representative histogram and CFD plots also shown in Figure 5.9 (representative image in Appendix 5B). The statistics presented in Table 5.2 and the plots demonstrate that the CuNPs are of a very similar size distribution to the CuNPs generated in pure water and the neutral N-donor ligand solutions, with the CFD plot indicating that 93% of NPs are less than 25 nm in diameter. As before, this TEM size analysis results in a distribution that is slightly larger than what is reported by AFM, though it compares favourably with the other results obtained.

### 5.3.5 Interpreting the Results

The results from the AFM imaging suggests that there is some variation in the size distribution between the CuNPs formed in the different ligand solutions, specifically, that CuNPs formed in the negatively charged tetrazole ligands are slightly smaller than the CuNPs formed in the other ligands. In comparison, the results from the TEM imaging suggests that there is less variation in the size distributions of the CuNPs, though this could be due to the sample preparation for the imaging process as previously explained. Despite the differences in the distributions between the CuNP solutions, and the differences shown in the imaging techniques, the CFD plots for each CuNP solution across both imaging techniques demonstrate that in most cases 95% or greater of CuNPs are below 25 nm in diameter. This is

significant, since Section 3.1 goes into some detail describing how NPs of diameter less than approximately 25 nm contribute equally to the SPR in the CuNPs, giving rise to the SPB absorption feature.

With the wavelength position of the SPB feature being dictated by the dipole oscillations of the CuNPs with diameters less than approximately 25 nm in diameter, as Section 3.1 explains, it is the percentage of CuNPs less than this 25 nm in diameter that is important to consider. It is these NPs that are the main contributor to the SPB and its position, and so a large percentage of CuNPs less than 25 nm in diameter, in theory, should give rise to the same SPB absorption feature at the same wavelength position, regardless of what ligand solution the CuNPs are formed in. In fact, the work by El-Sayed and co-workers show that CuNPs of 12 nm and 30 nm in diameter give rise to a very similar SPB absorption feature, with both being positioned at 570 nm.<sup>[103]</sup>

This then leads to two conclusions: either the difference in location in the SPB absorption feature is due to a marked variation in NP size distribution, or there is something affecting the dipole oscillations of the NPs to change the location of the SPB absorption feature. With the work reported here showing that the NPs size distributions are relatively consistent, with a large percentage of CuNPs being less than 25 nm in diameter, the difference in SPB absorption feature location is therefore most likely due to a change in the dipole oscillations of the NPs.

As explained by Equation 1.3, when a NP is coated the location of the SPB absorption feature will shift due to the coating's different dielectric effecting the frequency of the SPR. A coating on a NP, whether it is another metal or something such as an oxide layer, will affect the dipole oscillations of the NPs and change the frequency at which the SPR is supported. As

previously discussed in Section 4.1, an oxide coating on a CuNP shifts the location of the SPB absorption feature to longer wavelengths and eventually dampens it till it is non-existent.<sup>[107]</sup> It would then be natural to assume that the marked differences in SPB absorption feature location seen in this research, despite the shown relative consistency of CuNP size, is due to an oxide coating of some description on the CuNPs.

## ***5.4 Conclusions***

Both the AFM and TEM imaging techniques demonstrate that the CuNPs generated by LASiS, while showing some variation, are generally sufficiently similar in their size distributions to rule out a change in size being the primary reason for the observed differences in SPB absorption feature location that is seen in the UV-visible spectra. With literature demonstrating that CuNPs of different sizes exhibit similar SPB absorption features, the results seen here, with all but the CuNPs generated in the four blue tetrazole ligands, correlate with what has been previously reported, but fail to explain why there is a difference.

One hypothesis could be that the CuNPs generated in the presence of the deprotonated tetrazole ligands are oxide free, due to their SPB absorption feature location, and that the other CuNPs are not oxide free. However, due to the acidity of the tetrazole ligands, the presence of naturally occurring carbonic acid in aqueous solutions needs to be examined first to see if it has any effect on the SPB absorption feature and the ligand-CuNP interaction. This will be discussed in the next chapter.

## Chapter 6: Further Exploration of CuNP-Ligand Interaction

### *6.1 Changes in the pH of the solution*

It is well known that aqueous solutions are naturally slightly acidic due to dissolved atmospheric carbon dioxide in the solution-forming carbonic acid. There is then a possibility that naturally-occurring carbonic acid can affect the SPB due to the fact that there are some ligands that are acidic in aqueous solutions. It is possible that this natural acidity of the aqueous solutions affects the ligand interaction with the CuNPs. It was demonstrated in Chapter 3 that both **ben-acid** and **nic-acid**, while being able to deprotonate, give rise to a red-shifted SPB absorption feature, while the four deprotonated tetrazole ligands give rise to a blue-shifted SPB absorption feature. Examining the pH of the ligand solutions may give some insight to the reason for these spectral shifts.

To assess whether or not carbonic acid has an effect on the location of the SPB, nitrogen gas was bubbled through a few select solutions before LASiS to remove as much dissolved CO<sub>2</sub> as possible. Though carbon dioxide is readily soluble in water, only a small fraction of it is turned into carbonic acid, and bubbling nitrogen through the liquid causes the carbon dioxide to liberate from the water. Testing the pH of the solutions before and after bubbling with nitrogen gives a quick measure to see to what extent carbonic acid is present, and what effect it might have on the ligands. Testing the pH of the solutions post-LASiS also may give some insight into the behaviour of the ligands during the LASiS process.

Before any LASiS was undertaken, the pH of the solutions was tested before and after bubbling with nitrogen. The results show that there is a

small shift towards a more neutral solution, indicating that there is some carbon dioxide removal (see Figure 6.1). The tetrazoles have a similar pKa to that of acetic acid, and therefore show little change in their pH with the bubbling, due to having an acidic proton, while the alkylated tetrazoles, which do not have an acidic proton, show the greatest shift towards neutral pH.

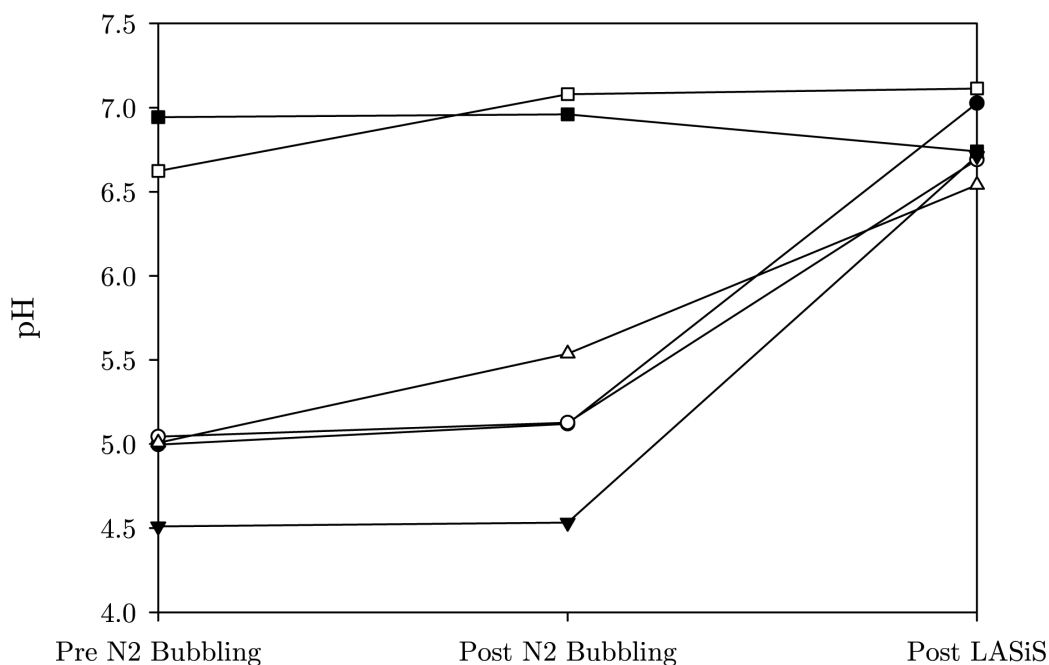


**Figure 6.1** Plot demonstrating the pH change in the solutions before N<sub>2</sub> bubbling, after N<sub>2</sub> bubbling and then after 60 minutes of LASiS. Not all data is presented here (see Table 6.1 for all the data) but a selection to illustrate the general trend. The solutions presented here are: **T-Me** (closed circle), **BuT-Me** (open circle), pure water (closed square), **Py** (open square), **T-2Py** (closed down triangle) and **BuT-2Py** (open up triangle). All solutions are 10<sup>-4</sup> molar.

Post ablation, however, the change in pH is more marked. The majority of the ligands decrease in acidity, with the greatest change occurring with the non-alkylated tetrazole ligands. The fact that the greatest change in pH is seen post-LASiS suggests that the small change in pH seen after nitrogen bubbling has little to no effect on the SPB absorption feature

location. The significant decrease in acidity could indicate that there is some interaction between the ligand and the CuNP surface, resulting in less 'free' ligand contributing to the acidity of the solution. The pyridine solution actually stays fairly constant in pH from after nitrogen bubbling to after ablation, which suggests that there are a series of competing interactions occurring.

The pH of a ligand-free solution (that is, pure water) actually increases in acidity, indicating that the LASiS process generates some ionic species. It could be assumed then that if  $H^+$  is being generated, that also  $OH^-$  is being generated from the laser process, which would result in a solution as neutral as pre-ablation. However, as has been demonstrated in literature,<sup>[139,188-190]</sup> copper hydroxide is formed as an intermediate in the copper oxide formation, and if this happens, the  $OH^-$  would be consumed, resulting in excess  $H^+$  in solution resulting in the increase in acidity, as observed here.

Importantly in all cases, the difference in location of the SPB absorption feature between solutions that were bubbled with nitrogen prior to LASiS and those that were not bubbled with nitrogen prior to LASiS was not significantly different. This is demonstrated by an example in Figure 6.2, where the variation is around 8 nanometres, which is in the order of what was normally seen in the variation from experiment to experiment. What these results also indicate is that the location of the SPB cannot be due to firstly, dissolved carbon dioxide in the solutions, and secondly, the acidity of the ligand itself. The nitrogen bubbling changed the pH in the most extreme case by less than 1 pH unit, and the SPB location didn't change, which indicates that the pH is not a critical factor here.

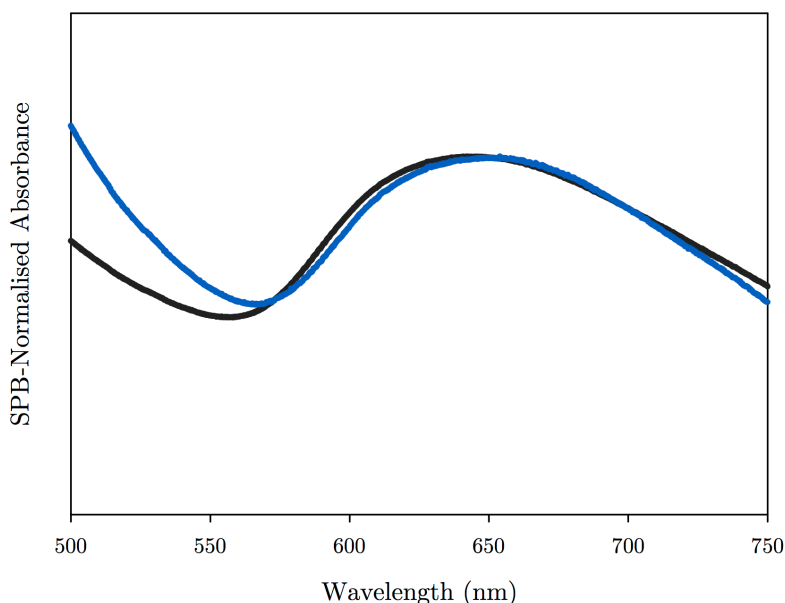


**Figure 6.2** SPB normalised UV-visible absorption spectra of CuNPs generated by 60 minutes of LASiS in pure water. One sample (blue trace) was degassed with N<sub>2</sub> gas for 60 minutes prior to LASiS, with continual degassing during LASiS, while the other sample (black trace) received no degassing treatment.

The acidity of the ligand itself doesn't seem to be the driving factor in the SPB location, as **T-2Py** has a similar pH to that of **T-3Py** and **T-4Py**. These ligands, however, result in CuNP solutions that have different SPB absorption locations, with **T-2Py** being a 'red' ligand, and **T-3Py** and **T-4Py** being 'blue' ligands. **T-Me**, also a blue ligand, has a similar pH to that of the alkylated ligands, which are red (see Table 6.1).

The results reported here suggest that the SPB location is dictated by the ligand structure, not by the acidity of the ligand, despite the fact that all four tetrazole ligands can deprotonate in solution. The decrease in ligand acidity indicates that there is some interaction happening between the ligand and the CuNP. Moreover, with the greatest pH change occurring with the deprotonated tetrazoles it suggests that the tetrazole structure is the major driving force of the interaction and subsequent SPB location.

**Table 6.1** pH data for various ligand solutions before nitrogen gas bubbling, after nitrogen gas bubbling and after 60 minutes of LASiS

Ligand ( $10^{-4}$ molar)	pH before N2	pH after N2	pH after LASiS
None (pure water)	6.94	6.96	6.74
Py	6.62	7.08	7.11
T-Me	5.00	5.12	7.03
T-3Py	4.45	4.56	6.91
T-4Py	4.62	4.64	6.59
BuT-Me	5.04	5.13	6.69
BuT-3Py	3.54	5.58	6.73
BuT-4Py	4.92	5.30	6.42
T-2Py	4.51	4.53	6.71
BuT-2Py	5.01	5.54	6.54

To further explore this structure-based hypothesis for the observed SPB spectral signatures, we return to exploring how the different ligand families influence the CuNP surface chemistry.

## 6.2 Bandgap Analysis

### 6.2.1 Calculating the bandgap of CuNPs

The working hypothesis to this point is that the four deprotonated tetrazole ligands, and hydrazine, are protecting the CuNPs from oxidation and that the other ligands offer little to no oxidative protection during LASiS. The AFM and TEM imaging has ruled out size being the primary reason for the change in the SPB location, and the pH studies indicate that the ligands are interacting with the surface of the copper but not effecting the SPB, strengthening the ‘oxidative control’ hypothesis.

If oxidation is occurring, it will be in the form of copper oxide on the CuNP surface, either as copper (I) or copper (II) oxide. A property of copper oxides is that they are semi-conductors, and a unique feature of a semi-conductor is that it contains a bandgap, an energy range between the insulating and conducting behaviour of the material. The bandgap generally refers to the energy difference (typically reported in electron volts) between the top of the valence band and the bottom of the conduction band and is closely related to the molecular HOMO/LUMO gap. The reason why the bandgap is of interest is that copper (I) oxide has a larger bandgap to that of copper (II) oxide,<sup>[191,192]</sup> so if the bandgap of the CuNPs could be measured, then perhaps some insight into the nature of the oxide could be gained.

Jan Tauc showed in 1966 that an optical absorption spectrum can be used to determine the optical bandgap of semiconductors.<sup>[193,194]</sup> He noticed that the optical absorption spectrum of amorphous germanium resembled the spectrum of the indirect transitions in crystalline germanium. He proposed that an extrapolation of the absorption spectrum would find the optical bandgap of the micro-crystalline states of the amorphous germanium. This technique has since been applied to many semi-conductor materials to determine the four different transitions present: the direct allowed, direct forbidden, indirect allowed and indirect forbidden transitions.<sup>[195]</sup>

The raw absorption data that is gathered to form the UV-visible spectrum has to be first transformed before it can be of use. Absorption data is converted into absorption coefficient data, and this is undertaken using the following equation:

$$\alpha = \frac{Abs}{L \cdot \log(e)} \quad (6.1)$$

where  $\alpha$  is the absorption coefficient,  $Abs$  is the absorption data,  $L$  is the path-length of the UV-visible instrument and  $e$  is the base of the natural logarithm. The absorption coefficient data can then be analysed, creating a Tauc plot from which we can determine the bandgap energy.<sup>[193,196]</sup> The raw absorption data from which the Tauc plots are generated in this research are presented in Appendix 6A.

A Tauc plot, or a bandgap energy plot, is a plot of energy (in electron volts) against  $(\alpha \cdot hv)^{\frac{1}{r}}$  where  $\alpha$  is the previously calculated absorption coefficient of the material,  $hv$  is the photon energy (in electron volts) and the  $r$  value denotes the nature of the transition;  $r = 1/2$  for direct allowed transitions,  $r = 3/2$  for direct forbidden transitions,  $r=2$  for indirect allowed transitions and  $r=3$  for indirect forbidden transitions.<sup>[196]</sup>

In short, direct transitions are ones that occur between the top of the valence band and the bottom of the conduction band in a vertical manner such that the wave-vector is maintained. An indirect transition is like a direct transition, but the wave-vector is no longer maintained and is phonon assisted. An allowed transition is one where the transition from the valence band to the conduction band is allowed by selection rules, while a forbidden transition is one where the transition is forbidden by selection rules.

The transition of interest in this study is the direct allowed transition, where the energy transition occurs from the energy maximum of the valence band to the energy minimum of the conduction band. Therefore, an  $r$  value of  $1/2$  is used, which results in the Tauc plot being a plot of energy (in eV) against  $(\alpha \cdot hv)^2$ . Once the data has been plotted, the first linear region of the plot at the absorption edge can be extrapolated to the abscissa, and where it crosses is the energy of the bandgap.

### 6.2.2 Experimental considerations

There is some inherent subjectivity in determining the linear portion of the resulting plot. There is also an inherent problem with the UV-Vis data at wavelengths shorter than approx. 300 nm due to the UV-vis reference subtraction. As has been mentioned previously (see Section 6.1), post-LASiS pH changes suggest that there may be a decrease in the ‘available’ ligand after ablation due to ligand-CuNP interactions. This leads to problematic reference subtraction in the UV-visible spectrum as the theoretical concentration of the ligands is no longer  $10^{-4}$  molar, but rather, some slightly lower concentration. As seen in the raw absorbance data (see Appendix 6A) it is easy to see that the UV-visible absorption becomes un-useable at wavelengths shorter than 300 nm.

Being unable to quantitatively specify what the final concentration of ligand is in the post-LASiS CuNP solution, pure water was used for the reference signal. This did lead to some unusual absorbance features of the ligand itself at wavelengths longer than approx. 300 nm. However, as described in Chapter 2.5 the first derivative of the transformed data was used to find the linear portion of the data. This firstly removed much of the subjectivity associated with assigning the linear area, and secondly meant that the absorbance data of wavelengths shorter than 300 nm were of little consequence as the bandgap linear component occurred well before where the majority of ligands have their absorbance.

### 6.2.3 Results

A surprising initial result from the analysis of CuNPs generated in pure water shows that the bandgap energy of the NPs is 3 eV, as seen in Figure 6.3. The reason why this is a surprising result is that the bandgap reported here is larger than the well-established values for both bulk copper (I) and copper (II) oxide. Bulk  $\text{Cu}_2\text{O}$  (copper (I) oxide) has a bandgap of 2.17

eV,<sup>[191,192]</sup> while bulk CuO (copper (II) oxide) has a bandgap of 1.2 eV.<sup>[191,192]</sup> The result here of 3 eV is well above that of both Cu<sub>2</sub>O and CuO. We will return to this apparent discrepancy shortly.

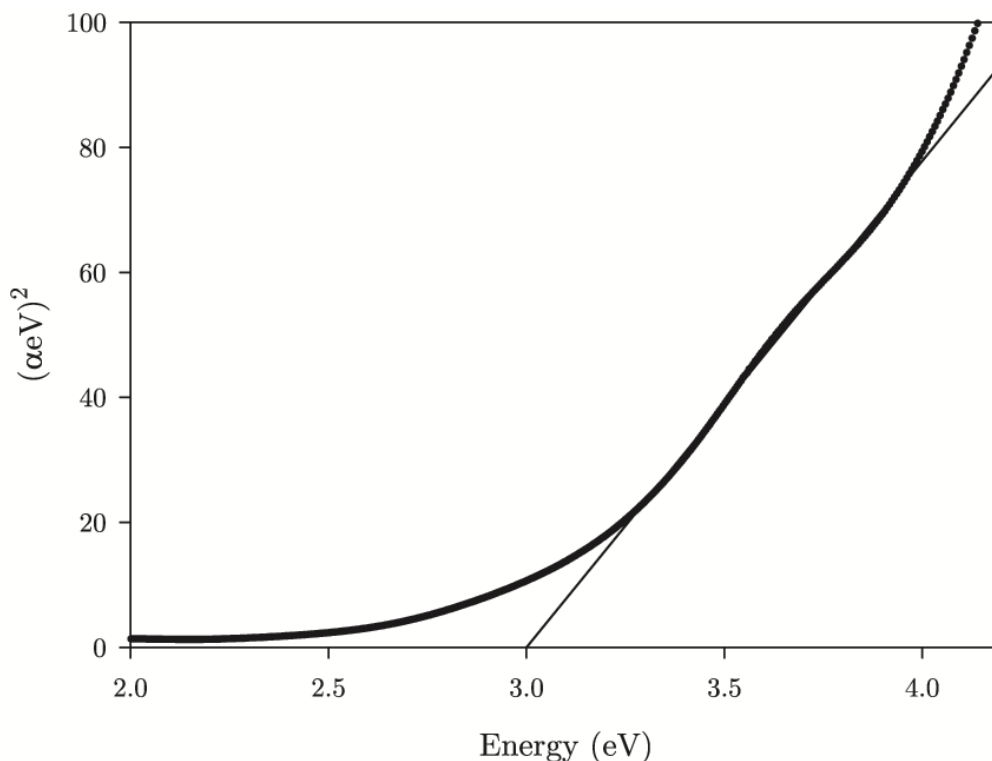


**Figure 6.3** Tauc plot of CuNPs generated following 60 minutes of LASiS in pure water. The thin black line represents the extrapolation of the first linear portion of the spectra down to the abscissa.

When Tauc plots are generated for CuNPs generated following 60 minutes of LASiS in the four neutral solutions (**phen**, **bipy**, **Py** and **4Ph-Py**) it is clear to see that the bandgap obtained with the CuNPs generated in pure water is not an isolated case. As demonstrated in Figure 6.4, the extrapolated linear portion of the spectra indicates that the bandgap of the CuNPs is 3.1 – 3.2 eV. This further confirms that the NPs generated in these four solutions generate CuNPs of similar composition to CuNPs generated in pure water.

These apparently discrepant results whereby the Tauc-determined bandgaps are higher than those of the bulk are actually not that peculiar upon consultation with the literature. Literature has reported higher values for both copper oxides when the size regime decreases in size; 1.35 – 1.4 eV for large CuO plates,<sup>[197,198]</sup> 1.7 eV for two micron diameter particles,<sup>[168]</sup> and up to 1.9 eV for thin films,<sup>[199,200]</sup> while Cu<sub>2</sub>O thin films have a similar bandgap to that of the bulk,<sup>[199,200]</sup> and nanoparticulate Cu<sub>2</sub>O has reported values of between 2.4 eV to 2.8 eV.<sup>[110,201,202]</sup>

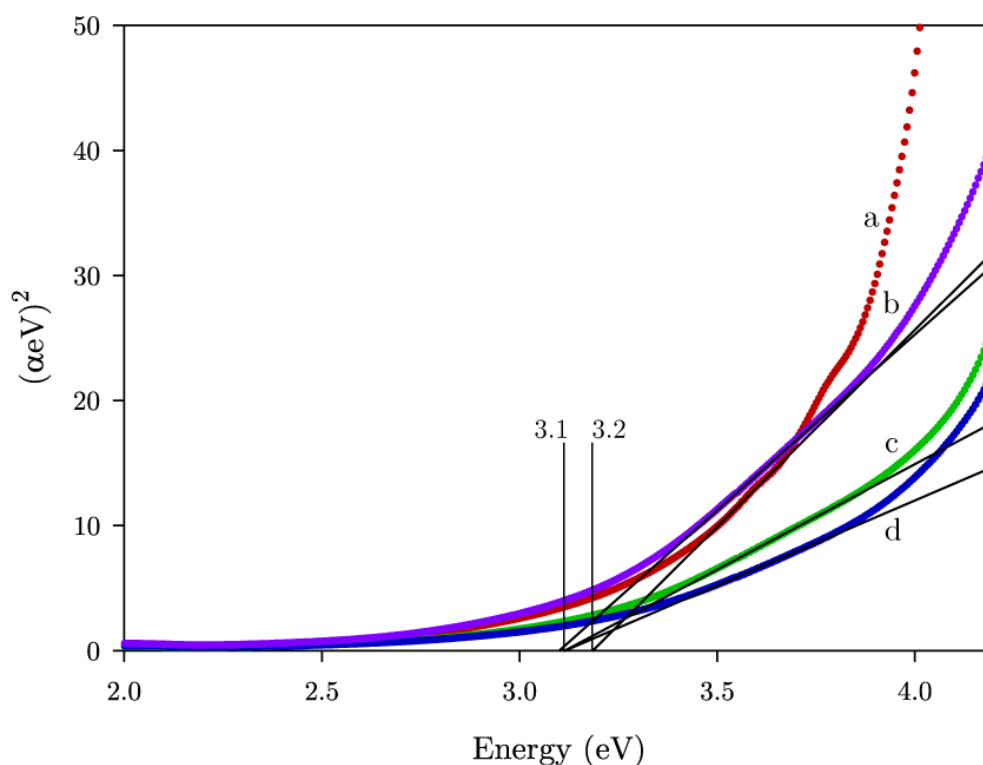


**Figure 6.4** Tauc plots of CuNPs generated following 60 minutes of LASiS in four  $10^{-4}$  molar ligand solutions: a (red) **phen**; b (purple) **Py**; c, (green) **bipy**; d, (blue) **4Ph-Py**. The thin black line represents the extrapolation of the first linear portion of the spectra down to the abscissa.

The main reason why the bandgap values reported here are much greater than the values of the bulk material is due to quantum confinement effects.<sup>[203]</sup> It also explains why the literature-reported values for thin films

and other nanoparticulates are higher than the corresponding bulk value. Quantum confinement is a phenomenon that is observed when the diameter of a material is reduced such that it starts to approach the wavelength of the electron. As the size of the material decreases, the energy levels of the material become more succinct and discrete as the confining dimensions decrease. This results in the material's electronic and optical properties deviating substantially from those of the bulk, therefore also increasing the bandgap of the material. The bandgap then becomes dependent on the size of the particle; with decreased size there is a blue-shift in the bandgap to higher energies,<sup>[203]</sup> a similar phenomenon that is also seen with the location of the SPB.<sup>[88]</sup> There is then the potential that nanoparticles of different size regimes give a different bandgap; however, this can be ruled out due to the similarity in NP size distributions as reported in the Chapter 5.

There is also a possibility that the determined bandgap values are higher than the bulk values due to the CuNPs not being homogenous in their composition. If there is a copper oxide shell on a pure copper core, it is feasible that, due to the interaction of the copper core and copper oxide shell, along with changes in the thickness of the copper oxide shell, the bandgap values presented here are indicative of the thickness of the copper shell. The similarity in the UV-visible spectra of CuNPs generated in pure water and the neutral N-donor ligand solutions, coupled with the similarity in the bandgap values, would indicate that the copper oxide shell is of similar thickness and composition between these samples.

The UV-visible spectra of CuNPs generated following 60 minutes of LASiS in the four deprotonated tetrazole ligands yield Tauc plots as presented in Figure 6.5. The extrapolation of the linear portion of the plot down to the abscissa reveals that the bandgap of these CuNPs is between 3.6

eV and 3.9 eV. This is higher than reported for CuNPs generated in blank water and the four neutral ligands by at least 0.4 eV. This immediately suggests that the composition of the CuNPs generated in these solutions is different to the blank and neutral solutions. Importantly, this also indicates that the putative notion that LASiS undertaken in the four deprotonated ligands yields CuNPs that are oxide free is incorrect. The reason for this being that if the CuNPs are oxide free, then there is no semiconducting material. Typical organic semiconductors exist in thin-film or crystal form,<sup>[204]</sup> which means that the solution concentrations found here ( $10^{-4}$  molar) are too low for the solutions themselves to contribute to the Tauc analysis as organic semiconductors.

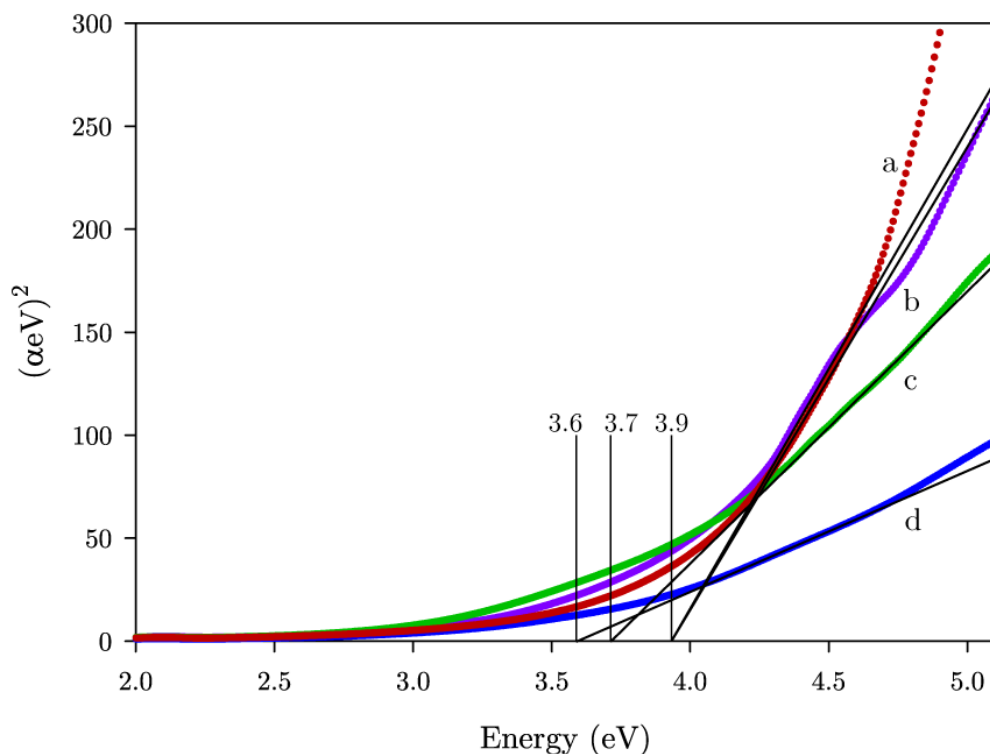


**Figure 6.5** Tauc plot of CuNPs generated following 60 minutes of LASiS in four  $10^{-4}$  molar ligand solutions: a (red) **T-Ph**; b (purple) **T-3Py**; c, (green) **T-4Py**; d, (blue) **T-Me**. The thin black lines represent the extrapolation of the first linear portion of the spectra down to the abscissa.

Undertaking bandgap analysis of a theoretically-generated ‘pure’ CuNP absorption spectrum results in a Tauc plot, a plot that indicates there may be a bandgap present. This is demonstrated in Figure 6.6 with the bandgap value being 2.4 eV. The theoretical absorption spectrum was derived from Equation 3.5, using optical constants for copper as reported by Johnson and Christy,<sup>[152]</sup> as the previously used optical constants reported by Roberts<sup>[150]</sup> did not extend into the UV as far as required.

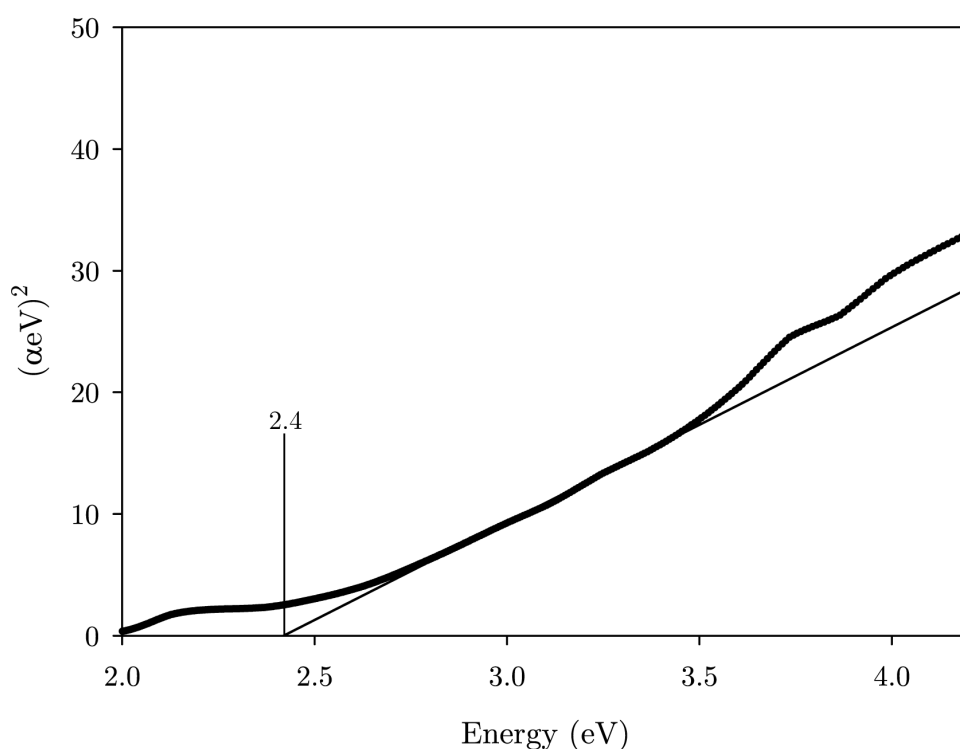


**Figure 6.6** Tauc plot generated from a theoretical absorption spectrum of CuNPs which are 10 nm in diameter, as derived by Equation 3.5. The thin black line represents the extrapolation of the first linear portion of the spectra down to the abscissa.

This theoretically-determined bandgap, however, may arise from the previously mentioned quantum confinement effects. The physical size of the CuNPs leads to a separation of the various energy-states in the NP, energy-states that in the bulk would be mixed. The few, now discrete, energy-states

gives rise to the bandgap demonstrated in the Tauc plot. What is important to see is that this bandgap is small in comparison to what is reported in Figures 6.3 - 6.5. This would indicate that the chemical composition of the CuNPs generated by LASiS in the ligand solutions and pure water are not pure copper.

CuNPs generated by 60 minutes of LASiS in acetone yields a Tauc plot which is presented in Figure 6.7 (top panel). The onset of acetone's absorption begins at approximately 340 nm, therefore the Tauc plot does not extend beyond 3.6 eV, the equivalent photon energy. The Tauc plot reveals that there is no linear portion to the plot, though this could be due to the fact that the bandgap analysis cannot extend into the UV past wavelengths of 340 nm. As previously described, CuNPs generated in acetone are purported to be oxide-free. The bandgap analysis here suggests that there is no oxide present, though this could be hindered by acetone's absorption in the UV (see Appendix 6A). A similar situation arises with the Tauc analysis of CuNPs generated in a  $10^{-4}$  molar hydrazine solution: no linear extrapolation is possible.

CuNPs generated by 60 minutes of LASiS in the four alkylated tetrazole solutions yield Tauc plots as also presented in Figure 6.7 (bottom panel). The extrapolation of the linear portion of the plot down to the abscissa reveals that the bandgap of these CuNPs is comparable to that of CuNPs generated in pure water and the neutral solutions, and different to that of CuNPs generated in the four 'blue' tetrazole solutions. It also suggests that the composition of the CuNPs formed in these solutions is similar to that of CuNPs formed in pure water, and perhaps with a similar oxide shell coating a copper core.

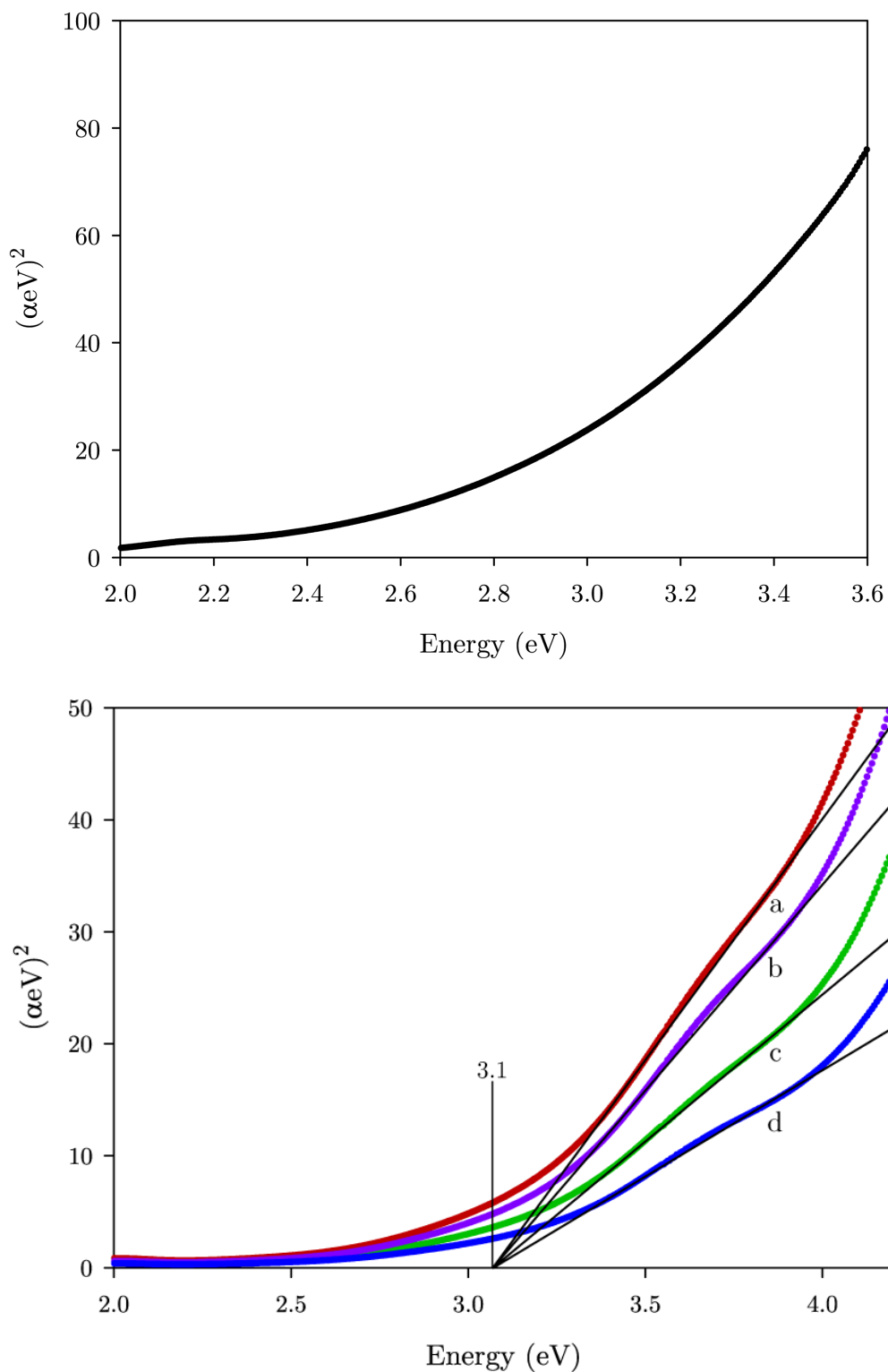


**Figure 6.7** Tauc plot of CuNPs generated following 60 minutes of LASiS in acetone (neat, TOP PANEL) and four  $10^{-4}$  molar ligand solutions (BOTTOM PANEL): a (red) **BuT-4Py**; b (purple) **BuT-Me**; c, (green) **BuT-3Py**; d, (blue) **BuT-Ph**. The thin black line represents the extrapolation of the first linear portion of the spectra down to the abscissa. There is no linear extrapolation down to the abscissa in the case of acetone (see text).

LASiS performed in solutions of **T-2Py** and **BuT-2Py** demonstrate Tauc plots that are shown in Figure 6.8. The calculated bandgap energy of 3.1 eV is identical to CuNPs generated in the alkylated tetrazole ligands and practically the same as CuNPs generated in pure water and the neutral N-donor ligands. This result is further confirmation that the chemical composition of the CuNPs formed in these solutions is similar to that of CuNPs formed in pure water, the neutral N-donor ligand solutions and the alkylated tetrazole ligand solutions. The similarity of this result echoes the similarity seen with the UV-visible spectra presented in Chapter Three, suggesting that the type of copper oxide is similar.

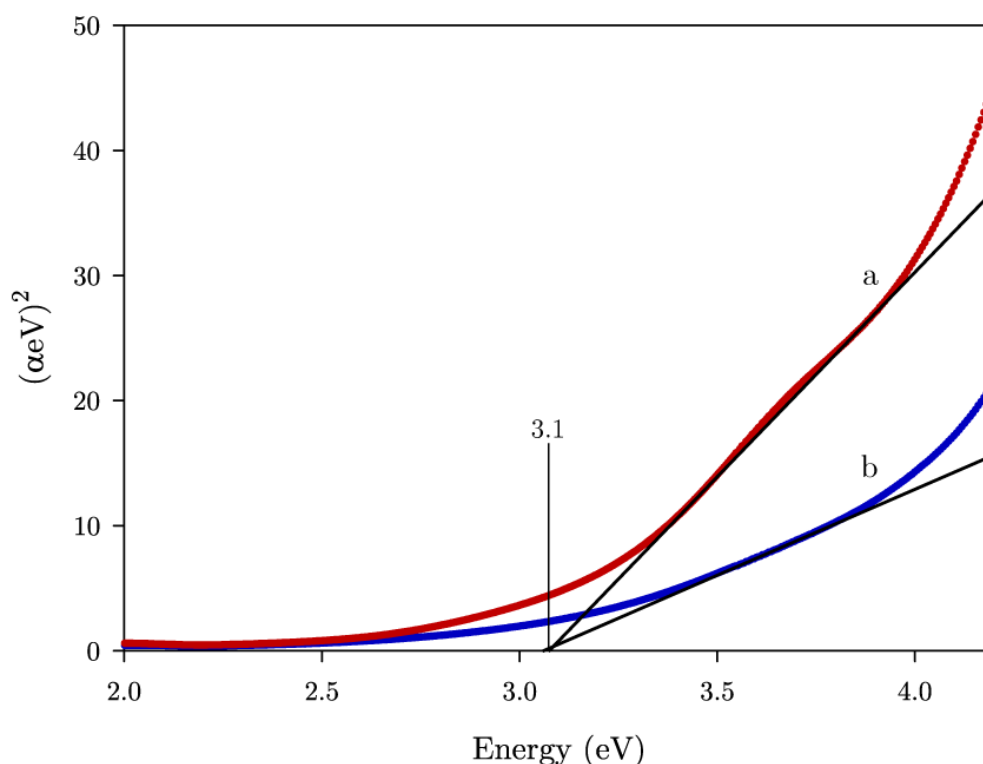


**Figure 6.8** Tauc plot of CuNPs generated following 60 minutes of LASiS in two  $10^{-4}$  molar ligand solutions: a (red) **BuT-2Py**; b (blue) **T-2Py**. The thin black line represents the extrapolation of the first linear portion of the spectra down to the abscissa.

The UV-visible spectra of CuNPs generated by 60 minutes of LASiS in solutions of CTAB and SDS generate Tauc plots that are shown in Figure 6.9 (top panel). The calculated bandgap of CuNPs generated in these solution is the smallest seen, indicating that the composition of the copper oxide here is different to any other CuNPs formed. The bandgaps reported here are actually closer to what is expected to be seen with bulk  $\text{Cu}_2\text{O}$  and  $\text{CuO}$ , which suggests that the composition of these CuNPs is tipped towards a large amount of copper oxide being present. In fact, correlating the location of the SPB absorption feature of CuNPs generated in SDS (which is centred at nearly 700 nm), with the low bandgap value, indicates that there is a large amount of copper oxide present. This further strengthens the suggestion that an electrostatic force, such as is present in a surfactant, is not sufficient enough to protect from oxidation of the CuNPs.

Finally, the Tauc plots generated from the UV-visible spectra of CuNPs generated by 60 minutes of LASiS in both **ben-acid** and **nic-acid** are also shown in Figure 6.9 (bottom panel). The calculated bandgaps of these CuNPs are like all other CuNPs, apart from those generated in the four ‘blue’ deprotonated tetrazole ligands.

The similarities with the calculated bandgaps seen between CuNPs generated in all solutions, bar the four ‘blue’ deprotonated tetrazole ligands, suggests that there is a high level of similarity in the chemical composition of these NPs. These results would indicate that the amount and composition of the oxidation is similar amongst these samples, and that the differences seen between the bandgaps of CuNPs generated in the four deprotonated tetrazole solutions and all the other solutions is indicative of a difference in the composition of the oxide that is present.

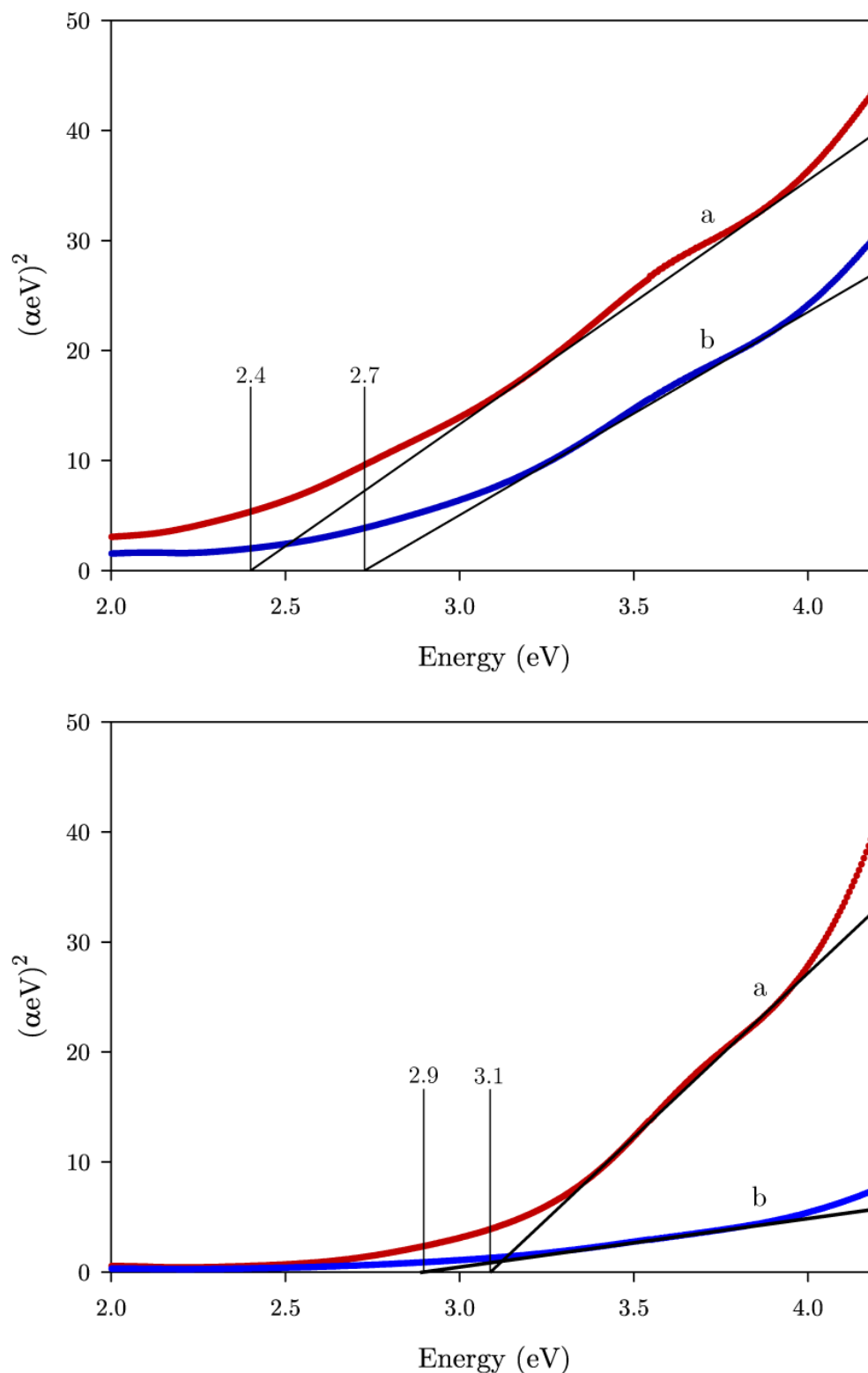


**Figure 6.9** Tauc plots of CuNPs generated by 60 minutes of LASiS in four  $10^{-4}$  molar ligand solutions. TOP PANEL: a (red) SDS; b (blue) CTAB. BOTTOM PANEL: a (red) **ben-acid**; b (blue) **nic-acid**. The thin black lines represent the extrapolation of the first linear portion of the spectra down to the abscissa.

It has previously been reported that CuNPs generated in pure water form copper (II) oxide,<sup>[138]</sup> which then suggests that the results shown here demonstrate CuNPs generated in all solutions bar the four deprotonated tetrazole ligands have a similar composition of oxide. With the difference seen between the bandgap of bulk copper (II) oxide and copper (I) oxide (1.2 eV and 2.17 eV, respectively), it could be deduced that the larger bandgap determined for the CuNPs generated in the four 'blue' tetrazole ligands indicates that the composition of those CuNPs is more like that of copper (I) oxide.

The over-arching suggestion then is that the lower the calculated bandgap of the CuNPs, the greater the chemical composition is likely to be copper (II) oxide, while the larger the calculated bandgap of the CuNPs, the more likely they are to be copper (I) oxide. One could argue that the difference of 0.4 – 0.8 eV between these two groups of ligands is not due to a different oxidation state but rather down to experimental error. However, Ray<sup>[199]</sup> showed that CuO and Cu<sub>2</sub>O thin films prepared in an identical way had only a difference of 0.2 eV between their bandgaps, which then indicates that the difference seen in this research would be sufficient enough to discern between copper (II) oxide and copper (I) oxide.

These results presented thus far indicate that there may be a strong link between the location of the SPB absorption feature and the oxide composition of the CuNPs. However, the theoretical modelling presented in Section 4.1, and discussed therein, suggests that the UV-visible spectra demonstrate Cu<sub>2</sub>O and not CuO, which is contrary to the results presented in this chapter. However, though the use of optical spectra to generate Tauc plots is a useful technique to quickly analyse oxide content in the NPs, a more robust technique exists to probe the chemistry of the CuNPs, that

being XPS. XPS analysis was therefore employed to get a better understanding of the chemical composition of the CuNPs and ascertain what form of copper oxide is present.

### ***6.3 XPS Studies***

The XPS analysis of the CuNP solutions was conducted by colleague Rhys Tilbury, as per Section 2.6, with the results shown in Table 6.2. The analysis of the percentage content of Cu(II) in each sample is shown, and this was calculated using Equation 2.1. Presented in Table 6.2 alongside the %Cu(II) is the wavelength position at which the SPB absorption feature is centred, which reveals that there is a strong link between the location of the SPB absorption feature and the presence of certain Cu oxidation states.

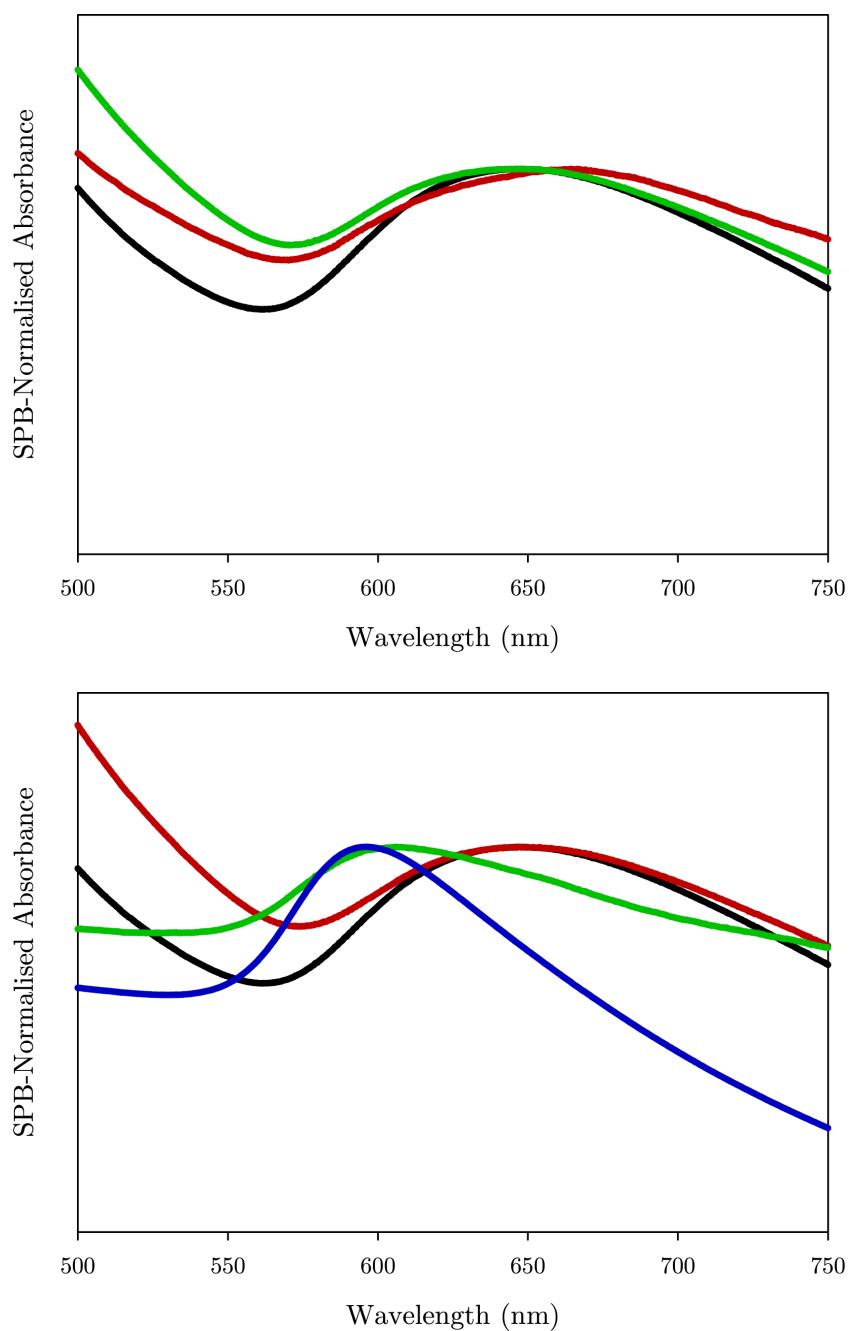
As can be seen from Table 6.2 there is quite a variation in the amount of Cu(II) present in the various samples, from 0% all the way up to 86%. An interesting result to come from this analysis is that there was oxygen present in all the samples due to the presence of an O (1s) signal in all the XPS spectra. This confirms what was proposed earlier in Section 4.1, where the contour plots seemed to indicate that all the CuNPs formed by the LASiS procedure in all the studied solutions have an oxide coating.

Following on from this, the significant blue-shift in the location of the SPB absorption feature seen with these four deprotonated ligands is clearly correlated with the absence of Cu(II) in the CuNPs formed. This suggests that the deprotonated tetrazole ligands suppress the formation of Cu(II) during the NP formation process, because, as demonstrated in Figure 6.10, the addition of these ligands post LASiS to CuNP generated in blank water does not yield any significant shift in the location of the SPB absorption

feature, much less the approximately 80 nm blue-shift seen when LASiS is conducted in the presence of these four ligands.

**Table 6.2** CuNPs formed by LASiS in various solutions, their corresponding SPB absorption feature wavelength location, and the %Cu(II) present as calculated by Equation 2.1

Ligand solution	SPB absorption wavelength (nm)	%Cu(II)
Bare CuNP	655	28
phen	630	23
bipy	630	39
Py	635	32
4Ph-Py	640	55
T-3Py	595	0
T-4Py	595	0
T-Me	595	0
T-Ph	582	0
BuT-3Py	640	48
BuT-4Py	640	28
BuT-Me	650	18
BuT-Ph	675	32
T-2Py	630	58
BuT-2Py	640	32
nic-acid	665	86
ben-acid	635	53
hydrazine	590	0



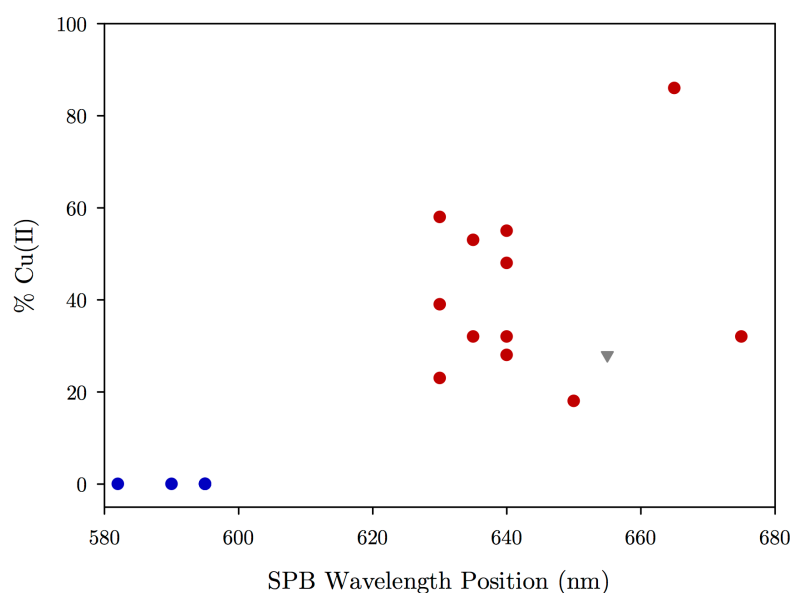
**Figure 6.10** UV-visible spectra of CuNPs generated following 60 minutes of LASiS in pure water, with the addition of two ligands post-LASiS. TOP PLOT: UV-visible spectra of pure water (black trace), immediately after the addition of an equivalent amount of **T-Me** to bring the concentration to  $10^{-4}$  molar (red trace), and 72 hours after the addition of **T-Me** (green trace). BOTTOM PLOT: UV-visible spectra of pure water (black trace), immediately after the addition of an equivalent amount of hydrazine to bring the concentration to  $10^{-4}$  molar (red trace), 48 hours after the addition of hydrazine (green trace), and 120 hours after the addition of hydrazine (blue trace).

Figure 6.10 demonstrates that even 48 hours after the addition of **T-Me** to a CuNP solution generated in pure water results in no significant change in the SPB absorption feature. The equivalent experiment, the addition of hydrazine to a CuNP solution generated in pure water, results in a significant blue-shift in the SPB spectral feature. This would indicate the hydrazine is reducing the oxide that is present on the CuNPs, while **T-Me** does not.

It is also important to remember that the XPS analysis conducted cannot easily distinguish between the overlapping Cu(0) and Cu(I) signals, so it is assumed, due to the presence of the oxygen in all samples, that Cu(I) is present as copper (I) oxide ( $\text{Cu}_2\text{O}$ ) in the CuNPs prepared with the ‘blue’ deprotonated tetrazole solutions. This then suggests that the hydrazine is, post-ablation, a strong enough reducing agent to reduce the copper (II) oxide to copper (I) oxide, based on the blue SPB spectral shift. The **T-Me** can only prevent the formation of copper (II) oxides during LASiS, and does not reduce the copper (II) oxide to copper (I) oxide post-LASiS, due to the SPB absorption feature not markedly changing.

An interesting result to be revealed is the very poor correlation between the amount of Cu(II) present and the wavelength position of the SPB absorption feature as shown in Figure 6.11. Literature says that as the amount of copper oxide present in CuNPs increases, the location of the SPB absorption feature becomes more and more red-shifted with respect to oxide free CuNPs, and this was also demonstrated theoretically in Section 4.1. While the amount of Cu(II) present in the CuNPs does not directly correlate to the same amount of copper(II) oxide, it would be expected to be a good indicator. However, what is seen here is that, for example, CuNPs generated in **BuT-Me** have only 18% Cu(II) while having a SPB absorption location of

650 nm, with CuNPs generated in **4Ph-Py** having 55% Cu(II) while having a SPB absorption feature location of 640 nm. One would expect that **4Ph-Py** having the larger percentage of Cu(II) would have an SPB centred at a longer wavelength to that of **BuT-Me**, but this is clearly not the case. Conversely, CuNPs generated in pure water and **BuT-Me** have similar SPB positions (650 and 655 nm respectively) but have different percentages of Cu(II) present (28 and 18% respectively). This suggests that the XPS-determined amount of Cu(II) present in the CuNPs is not directly correlated with the amount of copper(II) oxide.



**Figure 6.11** Correlation plot between SPB wavelength position and % Cu(II) content of CuNPs generated in the various solutions. The blue dots represent CuNPs generated in the deprotonated tetrazole solutions, the red dots represent CuNPs generated in the remaining ligand solutions, while the grey triangle represents CuNPs generated in pure water.

## 6.4 Conclusions

The examination of the pH of a few select solutions demonstrates that, importantly, the acidity of the ligand is not the primary reason for the difference in SPB absorption feature location, as it's been shown that **T-2Py**,

a 'red' ligand, has the same pH as that of both **T-3Py** and **T-4Py** which are both 'blue' ligands. The small change in pH seen with bubbling with nitrogen to remove dissolved carbon dioxide also indicates that the natural acidity of the solution is of little significance. However, the large pH change seen in the solutions after LASiS does suggest that the ligands are being bound to the CuNP surface, and due to the continued similarity in pH seen between **T-2Py**, **T-3Py** and **T-4Py** it demonstrates that the interaction occurs during the LASiS process, and that the results seen are due to the specific interactions of the ligand with the CuNP.

With the AFM and TEM imaging demonstrating that the size distributions of the CuNPs are similar (see Chapter 5), and the pH testing showing that the ligands seemingly are being bound to the CuNP surface, it then would suggest that the chemical composition of the CuNPs is different, leading to the grouping that is seen in the absorption spectra data.

With literature reporting firstly that CuNPs generated by LASiS contain copper (II) oxide, and that secondly, as the proportion of oxide in the NP increases the SPB absorption feature shifts to longer wavelengths, it could be assumed that the CuNPs generated in the presence of everything but the 'blue' tetrazole ligands results in copper (II) oxide coated NPs while the 'blue' ligands give oxide free or copper (I) oxide coated NPs. The fact that oxide is present means that bandgap analysis can be utilised with a classic Tauc analysis.

The results of the bandgap analysis suggest that, in fact, while the majority of ligands yield what is believed to be copper (II) oxide NPs, LASiS in the presence of the blue ligands results in CuNPs that are not oxide-free but actually copper (I) oxide. Meanwhile, XPS analysis of the CuNP solutions in fact confirms this hypothesis, with the deprotonated tetrazole-based ligand

solutions resulting in CuNPs that contain no Cu(II) while all the other ligand solutions demonstrate CuNPs with varying percentages of Cu(II). It was proposed in Section 4.3.3 that the four deprotonated tetrazoles are acting as *in-situ* reducing agents, and the results seen here with the XPS provide a more compelling argument to support that case, given that CuNPs generated in hydrazine and the four blue tetrazole ligands demonstrate 0% Cu(II).

So, in summary, the results of the TEM and AFM imaging show that the relative consistency of the size distributions of the CuNPs is not the reason for the differences in the SPB absorption feature, while the bandgap analysis suggests that it is actually the copper oxide composition that is the primary reason. The XPS analysis shows that, in fact, there seem to be two oxide species present on the surface of the CuNPs, namely copper (I) oxide and copper (II) oxide.

## Chapter 7: Further Theoretical Modelling of the Copper Oxide coated CuNPs

Chapter 5 concluded that the particle size distributions of the CuNPs were not sufficiently varied enough to account for the variation in the position of the SPB absorption feature. The results from the bandgap analysis in Chapter 6 indicate that there are two forms of copper oxide (namely, copper (I) oxide and copper (II) oxide) that are formed on the surface of the CuNPs. This was reinforced through the use of XPS, with no Cu(II) being present in the CuNP samples prepared in the four deprotonated tetrazole or hydrazine solutions. However, if we go back to Section 4.1, it was concluded that the contour plots (Figure 4.2 and 4.3) show that the results observed with the UV-visible spectra indicate the presence of only copper (I) oxide in all CuNP solutions, as the red-shift and the damping of the SPB absorption feature with a copper (II) oxide coating cannot describe the UV-visible spectra.

So, what then do we say about seemingly contradictory results? It would be amiss to discredit the UV-visible spectra obtained from the various CuNP solutions, as the weight of literature-reported spectra suggests strong similarities between the reported results and what has been presented herein. The XPS results are convincing, and what is seen in the results presented here are consistent with literature reports of copper and its various oxidation states,<sup>[145]</sup> so there is little doubt to discount their accuracy. It is possible that the theoretical calculations may not accurately describe the experimental results. However, previously reported literature demonstrates experimental results that align with the theoretical results presented here.<sup>[106]</sup>

There may be a perfectly acceptable explanation for the results in this thesis. The UV-visible spectra of the CuNP solutions are obtained

immediately after the LASiS process is completed, so it is entirely plausible that the CuNPs at the point of analysis have a copper (I) oxide coating on them, which would explain the correlation between the theoretical spectra and the experimentally-obtained spectra. The XPS analysis is, however, not taken immediately after the LASiS process has concluded. The CuNP samples need to be prepared, which involves vacuum evaporation of the samples to remove the water that is present, while there is wait time (in the order of a few hours) before the samples are placed under vacuum in the XPS analyser after the samples are dried.

All this time allows for the possibility of natural oxidation of copper (I) oxide into copper (II) oxide, which would explain the results seen from the XPS data. It is known that oxidation of copper (I) oxide to copper (II) oxide progresses under ambient laboratory conditions,<sup>[96]</sup> so it is not unfeasible that the time taken for the water to be vacuum evaporated, combined with the wait time for the XPS analysis to commence, gives sufficient time for the oxidation to occur.

If this oxidation step is taking place, it then raises an interesting issue. The bandgap analysis suggested that the CuNPs formed in the presence of the four 'blue' deprotonated tetrazoles demonstrated the presence of copper (I) oxide, while the other ligand solutions demonstrated the presence of copper (II) oxide. However, if the bandgap analysis is conducted on UV-visible spectra that are obtained immediately after the LASiS process has finished, then by extension of the above discussion, only copper (I) oxide is present, which goes against what the results initially imply. An explanation then for the differences that are seen may arise simply from the variation in the thickness of the oxide coating. As shown in Section 4.1, as the oxide layer increases in thickness, the SPB absorption feature red-shifts. It is then

probable that the ‘red’ ligands result in CuNPs with a thicker oxide coating than CuNPs generated in the presence of the ‘blue’ ligands. This variation in thickness of the oxide coating is then a probable explanation for the differences seen in the bandgap analysis. Curtin University has recently commissioned a state-of-the-art FEI Talos transmission electron microscope (TEM). This instrument will allow for high-resolution TEM, diffraction capability and dispersive x-ray spectroscopy to further probe the CuNP oxide surface chemistry. However, this future work is beyond the scope of this project.

Another possible explanation for the bandgap results is that copper (II) oxide may be forming in small amounts during the LASiS process. While the XPS results indicate that the four deprotonated tetrazole ligand solutions stop the formation of Cu(II) oxidation, the ‘red’ ligands do not. There is a very real possibility that the CuNPs formed in the ‘red’ ligand solutions are, during the LASiS process, slowly oxidising from copper (I) oxide to copper (II) oxide. The tens of percent of Cu(II) seen in the XPS analysis is due to then the delay in the XPS analysis after LASiS is completed, giving time for the Cu(I) oxide present to further oxidise to Cu(II) oxide.

The small amount of copper (II) oxide then present wouldn’t be significant enough to have a dramatic effect on the UV-visible spectra, but would have enough of an effect on the bandgap analysis. A mixture of both copper (I) and copper (II) oxide would plausibly lead to the results seen. Given that the bulk bandgap for copper (II) oxide is lower than copper (I) oxide, a small amount of copper (II) oxide would start to lower the bandgap energy, making it less like copper (I) oxide. This would explain why the bandgap of CuNPs generated in the four ‘blue’ tetrazole ligand solutions are very similar, as there is no copper (II) oxide present.

The conclusion to be drawn from these results then is that the deprotonated tetrazole ligands must be stopping the further oxidation from occurring. This is confirmed with the XPS data, with there being no Cu(II) species present in those samples. The remaining ligands then, by extension, don't limit the further oxidation, because despite the UV-visible spectra demonstrating copper (I) oxide, the XPS results definitively show the presence of Cu(II) species.

One of the features of the MieLab software<sup>[172]</sup> is that it can take experimental UV-visible data and, using a recursive algorithm, fit theoretical data to the experimental data. It does this based on end-user inputs, including: the number of layers in the NP, the  $\epsilon_1$  and  $\epsilon_2$  values for the material of that layer and what sort of background correction (if any) there is. The software then takes the theoretical data and fits it to the experimental data. It achieves this by employing a bounded, limited memory Broyden-Fletcher-Goldfarb-Shanno algorithm to iteratively find better fits for the theoretical data, achieving a fit by minimising the  $\chi^2$  value.<sup>[172]</sup> This ability of MieLab to fit theoretical data to experimental data was utilised here; however, it was noticed that the software's fitting algorithm was not optimised for multi-core processors nor large amounts of RAM, and so fitting the experimental data was a slow process.

A few select UV-visible absorption spectra were used in the MieLab software to illustrate that the 'red' ligand solutions demonstrate the presence of copper (I) oxide. These plots are presented in Figure 7.1, along with the important fitting data shown in Table 7.1.

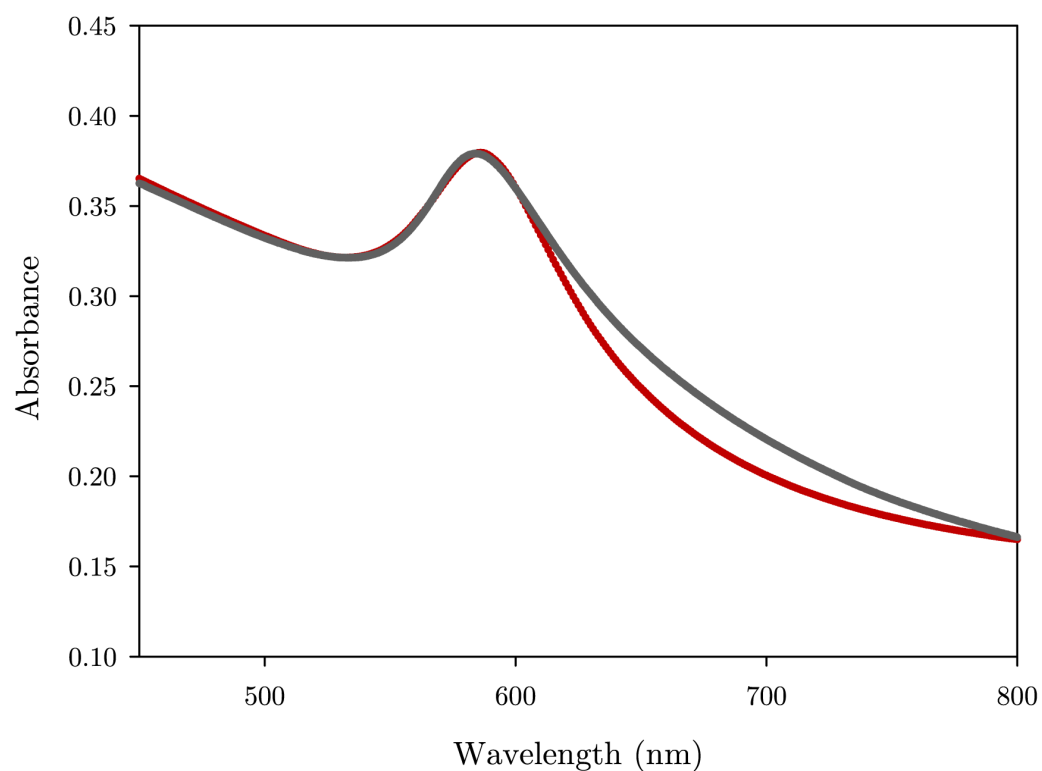
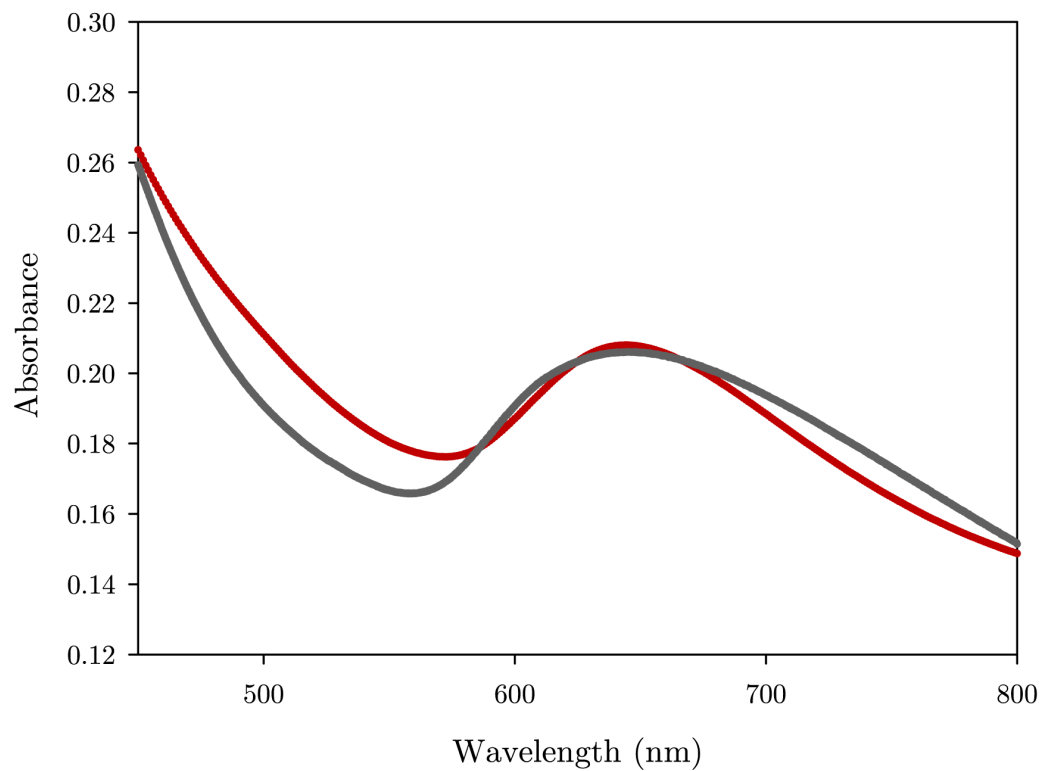


**Figure 7.1** Plots of the UV-visible absorbance data (grey trace) with the fitted theoretical data of a Cu@Cu<sub>2</sub>O NP as determined by MieLab (red trace). CuNPs are formed following 60 minutes of LASIS in pure water (TOP PLOT) and 10<sup>-4</sup> molar **T-Ph** (BOTTOM PLOT).

**Table 7.1** Table of statistics from the MieLab fitting. The values reported represent the thickness of each layer (in nm). Included is the  $t_{\text{Cu}_2\text{O}}/R_t$  ratio which is calculated from the determined diameters/thicknesses.

		Mean (nm)	Std. Dev (nm)
Pure Water	Cu (layer one)	1.4	0.57
	Cu <sub>2</sub> O (layer two)	2.77	0.87
	Total radius	4.17	1.44
	$t_{\text{Cu}_2\text{O}}/R_t$	0.66	
T-Ph	Cu (layer one)	2	0.3
	Cu <sub>2</sub> O (layer two)	0.5	0.3
	Total radius	2.5	0.6
	$t_{\text{Cu}_2\text{O}}/R_t$	0.2	

It can be seen that while the fits are very close, more computing time would see these fits improve. It is important to note also that the values for calculated fits represent the thickness of that representative layer. It is assumed that layer one, the inner layer, is a sphere and that layer two has a certain thickness. The combined total of these two layers results in the overall radius of the NP.

The one downside to the software is that it is unable to deal with NPs that are not spherical. While not abundantly clear in the TEM imaging (of which representative images are seen in Appendix 5B), there are some non-spherical CuNPs being formed, although the vast majority are spherical in nature. It is also important to note that copper (I) oxide has an excitonic peak at approx.. 720 nm that cannot be replicated by the MieLab software, which would contribute in a small way to the non-optimum fitting.<sup>[55,107]</sup>

These two factors are what contribute to the non-optimum fitting seen in Figure 7.1.

It is clear to see, however, that the ‘blue’ **T-Ph** ligand has much less copper (I) oxide present in comparison to CuNPs generated in pure water, with the  $t_{\text{Cu}_2\text{O}}/R_t$  ratios making this clear. To demonstrate that it is copper (I) oxide that is contributing to the position of the SPB absorption feature, the MieLab software was tasked to fit the UV-vis spectrum of CuNPs generated in pure water to a Cu@CuO model. The result of this fitment is seen in Figure 7.2, and it is immediately clear that the fit is not good. In comparison, the top plot of Figure 7.1 is the same UV-vis spectrum fitted to a Cu@Cu<sub>2</sub>O model, and this fitment is much better.

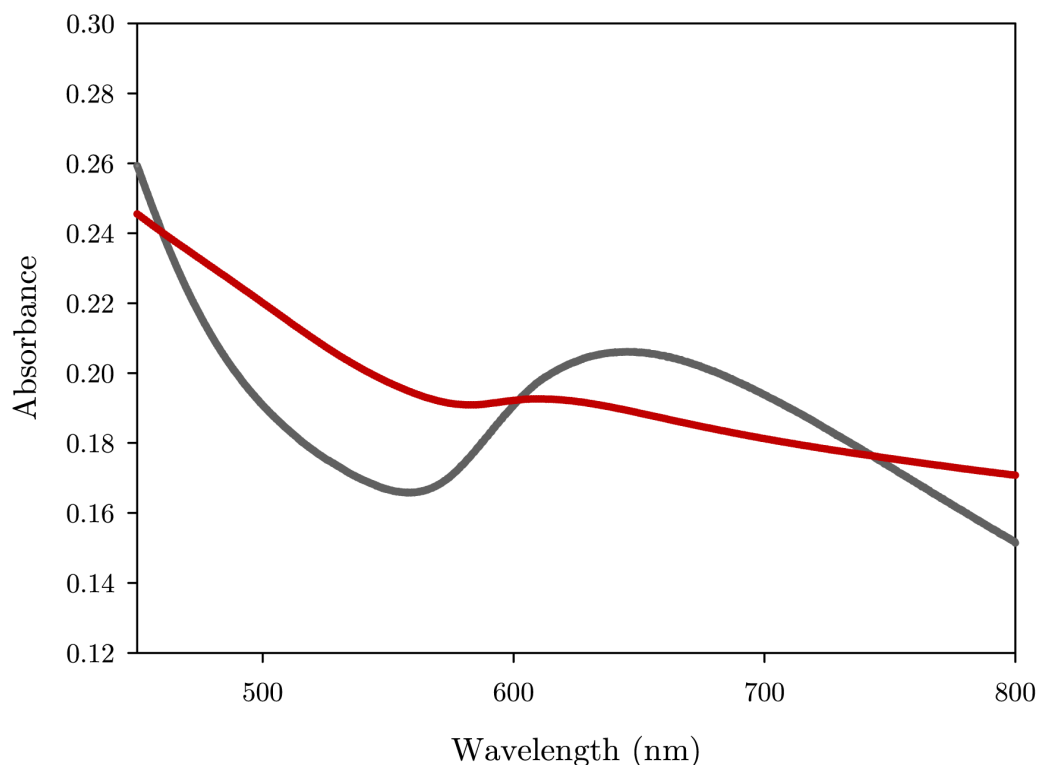


**Figure 7.2** Plot of the UV-visible absorbance data (grey trace) with the fitted theoretical data of a Cu@CuO NP as determined by MieLab (red trace). CuNPs are formed following 60 minutes of LASIS in pure water

It is clear from this fitment process that the LASiS process in the ‘red’ ligands generate CuNPs that contain copper (I) oxide. The presence of copper (II) oxide, as determined by XPS, then is assumed to be due to further post-LASiS oxidation.

It is important to point out that the MieLab software treats the CuNP and its oxide as separate individual layers. The fitting results indicate that for CuNP generated by LASiS in blank water there should be an oxide layer of more than 2.5 nm in thickness.  $\text{Cu}_2\text{O}$  of this thickness should be visible on the TEM imaging, but inspection of the representative TEM images (seen in Appendix 5B) does not clearly indicate this. Because LASiS is recognised as a complex series of events,<sup>[39,67,69]</sup> it’s entirely likely that oxide formation occurs as the CuNPs grow immediately after the individual laser pulses cease, and that the composition of the CuNPs is mixed with areas of  $\text{Cu}_x\text{O}$  and Cu, with no clear oxide coating on the CuNPs. With this in mind, the MieLab software gives what could be considered as a first approximation to the composition of the CuNPs.

The hypothesis that the deprotonated tetrazole ligands are acting as *in-situ* reducing agents, first suggested in Section 4.3.3, is supported by the combination of results seen here. This is a feature that is unique to the deprotonated tetrazoles, as the other ligands, including ligands that deprotonate in solution, don’t offer the oxidative protection that these deprotonated tetrazoles do. The combination of the UV-visible spectra and the XPS results then indicate that the oxidation from copper (I) to copper (II) oxide is a process that occurs mostly post-LASiS. To see if this is the case, it is important to probe the formation mechanisms of the CuNPs.

## Chapter 8: Exploration of the Formation Process of CuNPs

### 8.1 Time Dependent Formation Studies

#### 8.1.1 Kinetic Analysis

As discussed in Section 1.3.3, the formation of nanoparticles generated by LASiS is recognised as being a complex series of events occurring over a very short period of time.<sup>[39,64,69,205]</sup> The understanding of these NP formation dynamics has intrigued research groups for many years. However, due to the various LASiS experimental setups there is no one set way to go about undertaking mechanistic studies. The issue arises due to the various types of lasers that are employed in the LASiS systems. From high-repetition kHz-pulsed lasers, to lasers operating at 10 Hz or less and pulse widths in the femto-second range up to nano- and micro-second range there are many variations between research groups, which conversely leads to variations in the formation dynamics.<sup>[64,66,104,206]</sup>

One difficulty in analysis arises when trying to probe shot-to-shot dynamics, especially when using high repetition rate lasers. This difficulty is that the time between shots is in the range of 100 milliseconds (for a typical 10 Hz 1064 nm Nd:YAG laser) down to less than 1 millisecond (for kHz repetition rate lasers). With such a short time between laser pulses to work with, traditional *in-situ* investigation techniques do not work so well. Most structural investigation techniques do not have the time-resolution required while the light emission from the plasma interferes with sensitive optical techniques.

Another issue is that the amount of material ablated is very low, in the order of 0.1 – 0.001  $\mu\text{g}$  per pulse, which is below the sensitivity limit for

most structural investigation techniques, even if they can operate in the time-resolution required.<sup>[39]</sup> Amendola and Meneghetti have comprehensively reviewed the various techniques that research groups have employed to probe these ultra-fast dynamics,<sup>[39]</sup> with techniques such as ultra-fast shadow photography, photoacoustic spectroscopy and time resolved X-ray techniques all being employed to try to further understand the processes taking place.<sup>[63,69]</sup> Computer simulations have the potential to give some understanding on the effect of the laser on the bulk material; however, simulations cannot account for the nonlinear optical phenomena that take place, and while they can approximate the ablation process, simulations are less reliable at modelling the nucleation of NPs away from the surface of the bulk. There are, of course, *ex-situ* techniques that can be used, such as those described elsewhere in this thesis (e.g. TEM and UV-visible spectrometry); however, these techniques are less useful for shot to shot analysis, though *in-situ* UV-visible spectrometry can be used through the use of fibre optics.<sup>[80]</sup>

To probe the short-time effects of NP formation can then be very difficult, often requiring specialised equipment. Another way to get an understanding of the formation processes, albeit on a slightly longer time scale, is to undertake kinetic studies. While a kinetic study cannot probe the shot-to-shot interaction, it can still give a very good understanding to what happens on a longer time-scale such as a per minute scale.

It has been previously demonstrated in our laboratory that gold nanoparticles do not follow a linear formation process when generated by LASiS.<sup>[136]</sup> What is seen is that at early times there are formation AND depletion processes taking place, and then after a certain amount of time the formation process becomes linear. The suggestion is that in the first few minutes NPs are forming larger and larger nanoparticles, but also, conversely,

breaking apart again to a small extent, until such a time as there are sufficient ‘seed’ nanoparticles to allow for continuous growth in the number of NPs.

A large amount of work went into developing a model to describe the observed behaviour, to try and give some understanding to the mechanism of formation. What was found was that the best fit to the data came about by creating a system where there existed three size regimes, namely, NPs that are too small to support the SPR, NPs that are medium-sized and can support the SPR, but give rise to only a weak SPB absorption, and NPs that are large in size and can comfortably support the SPR and give rise to a strong SPB absorption.<sup>[136]</sup>

The fitment suggested that the main process was the creation of medium-sized nanoparticles, followed by the creation of large-sized nanoparticles. The fitment of a reverse process whereby medium-particles were broken down, helped explain the non-linear formation process. This so called ‘sink’ channel is well supported by other researchers, who acknowledge that there are many complex processes that occur during the formation, including the breakdown of particles and re-deposition of material.<sup>[39,207]</sup>

Due to copper and gold having similar band structures and optical properties, and with the size of gold NPs formed by LASiS in our laboratory being reported to be similar to that of CuNPs formed here,<sup>[136]</sup> it would not be a far stretch to suggest that the formation of CuNPs follows a similar behaviour to that of gold NPs.

The most straightforward technique to study the kinetics of formation is to record the UV-visible spectra at set time intervals. This then allows for the intensity of the SPB absorption feature to be monitored over time as the concentration of the NPs in solution increases.

### 8.1.2 Kinetic Analysis Results

The kinetic analysis of gold as reported by Fong *et al.*<sup>[136]</sup> showed that after approximately 15 minutes of LASiS the formation process stabilised and progressed at a linear rate thereafter. Therefore, assuming the formation of CuNPs formed via LASiS follows a similar formation process to that of AuNPs, a similar method of analysis was employed. The UV-visible absorbance of CuNPs generated by LASiS was monitored every minute for the first 10 minutes, then at 15, 20, 25 and 30 minutes, followed by 40, 50 and 60 minutes, and finally at 80 and 100 minutes of ablation.

It was shown in previous research that the kinetics of formation of CuNPs formed in pure water showed that the growth of the plasmon band demonstrated short- and long-range oscillations, and it was imagined that this was due to a competing behaviour between the formation and removal of the oxide layer on the NPs themselves and also on the copper target.<sup>[80]</sup> However, these oscillations were not seen in this research, with Figure 8.1 illustrating the results of LASiS conducted in pure water in our laboratory.

Unlike as was reported with gold NPs,<sup>[136]</sup> the growth in absorbance of CuNPs does not show a clear linearity after 15 minutes, but has a gentle longer time-curve to it. This suggests that there is an extra influence in the formation process, perhaps indicative of the copper (I) oxide formation process, or a conversion of copper (I) oxide to copper (II) oxide. A possibility as to why oscillations in the absorbance were not seen in this research is that the UV-visible analysis was conducted *ex-situ* whereas the research presented by Muniz-Miranda and co-workers was *in-situ* analysis of the absorbance while the LASiS was taking place by using fibre-optic technology.<sup>[80]</sup>

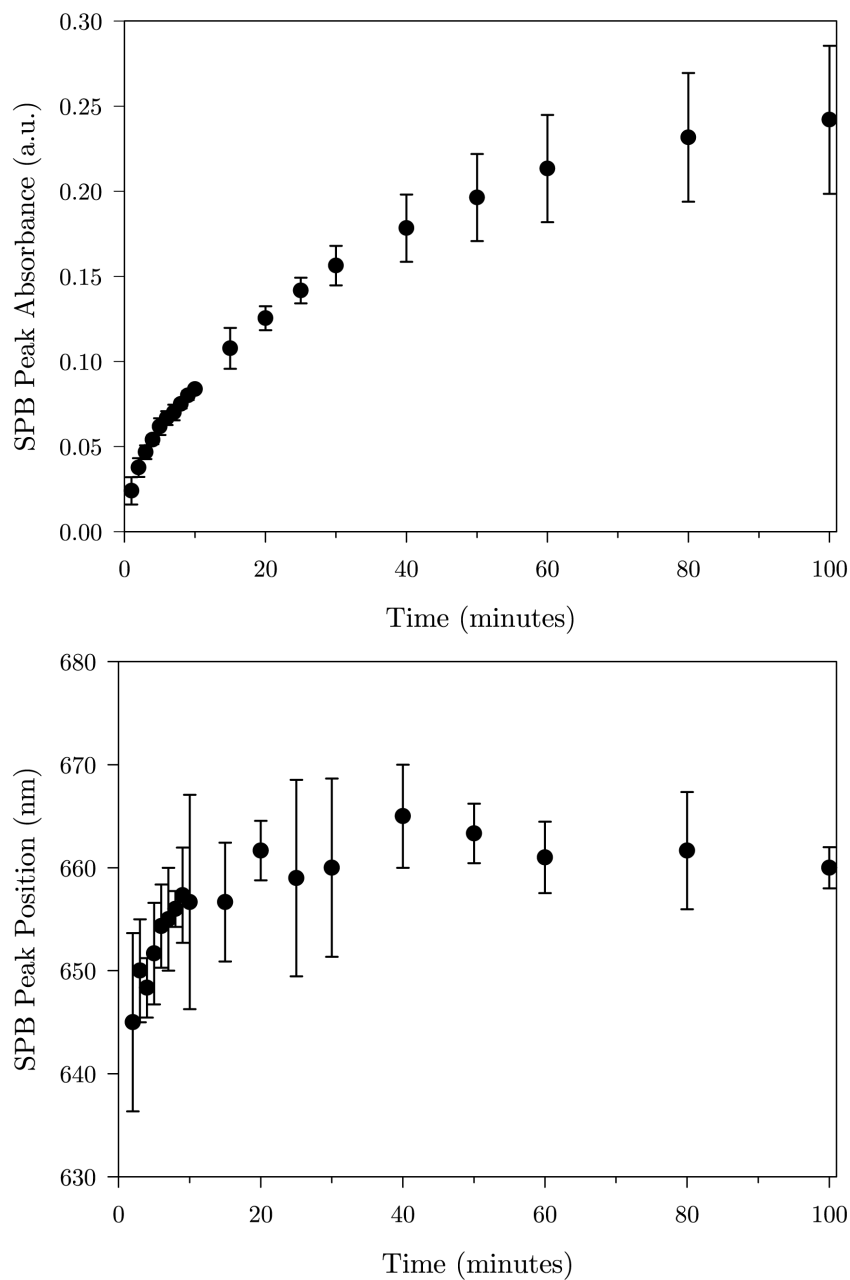


**Figure 8.1** Kinetic plots of the formation of CuNPs generated by LASiS in pure water. TOP PANEL: demonstration of the increase in the SPB absorption feature maxima over time. BOTTOM PANEL: demonstration of the variation in the location of the SPB absorption feature over time. In both panels the Y error bars represent one standard deviation from the mean.

With the nature of the LASiS method, it was important that the solution was made as homogenous as possible before analysis, and this was accomplished by gently swirling the solution to disperse the CuNPs. Too vigorous shaking can introduce air into the solution and can artificially increase the oxide on the NPs. In theory a solution to this problem would be to conduct the experiments in a sealed evacuated environment, however the sealing device on the vessel would have to withstand repeated exposure to the laser ablation. It should be noted that the SPB absorption feature wavelength position presented here is slightly red-shifted with respect to the UV-visible spectra presented in Chapter 3 and 4. This may be due to the fact that the CuNPs are oxidising more rapidly, unfortunately due to a combination of the swirling and the on/off nature of the LASiS process that was required to study the formation processes.

Ensuring homogeneity of the solution during UV-visible spectrometry was not mentioned by Muniz-Miranda and co-workers and so it is possible that the data they present in some instances represents the absorbance of freshly made NPs that are not homogeneously dispersed but rather exist in high concentrations directly above the copper target, and at other times represents areas of low NP concentration. It is also important to point out that they analysed for up to 10,000 laser shots, which corresponds to just over 16 minutes of ablation time and probes the shorter time-formation mechanisms, while this work focuses on a time scale that is over five times longer.

Figure 8.1 further demonstrates how the location of the peak of the SPB absorption feature changes over time. It should be noted that initially, in the first 10 minutes or so, the SPB shifts to longer wavelengths and then plateaus out after about 20 minutes. The error-bars represent one standard

deviation from the mean, with the kinetic analysis having been conducted three times, with the results being compiled and averaged. These error-bars illustrate how much variation there is in the location of the SPB, demonstrating in part the complexity of the CuNP formation process, and possibly the oxide formation process. It is also noteworthy that the variation seen with the SPB location is much greater than the variation seen with the SPB absorbance, which only becomes notable from 40 minutes and onwards, and progressively becomes larger. These results also give some justification for the decision to perform 60 minutes of LASiS, as both the mean absorbance is then at an acceptable value (an absorbance of 0.2 means 37% of the incident light is absorbed) and the location of the SPB is at a reasonably steady state.

Figure 8.1 also provides a possible explanation for the differences in SPB absorption location reported in this research and by Muniz-Miranda *et al.*<sup>[80]</sup> as reported in Chapter 3.2. While the comparison was between CuNPs formed in both **bipy** and **phen**, the results demonstrated here with CuNPs formed in blank water can also apply. The size of the error bars illustrates that the variation between experiments identical in nature result in a large variation in the SPB absorption feature location. This large variation, and the red shifting of the SPB absorption feature location in the first 20 minutes' gives a reasonable explanation of the differences seen.

In a similar manner to the kinetic analysis of CuNPs generated in pure water, the same analysis was conducted of CuNPs generated in a neutral ligand, namely **bipy**. Like what was seen with the analysis of CuNPs formed in pure water, the increase in absorbance does not show any real linearity, but a constant gentle curve, as shown in Figure 8.2. The absorbance, however, is greater than that seen with the analysis in water, and demonstrates a much

smaller degree of variation in the absorbance, as shown by the smaller error bars. Figure 8.2 also shows how again, much like the analysis of CuNPs generated in pure water, the SPB absorption feature location red-shifts and then plateaus out after approximately 20 minutes.

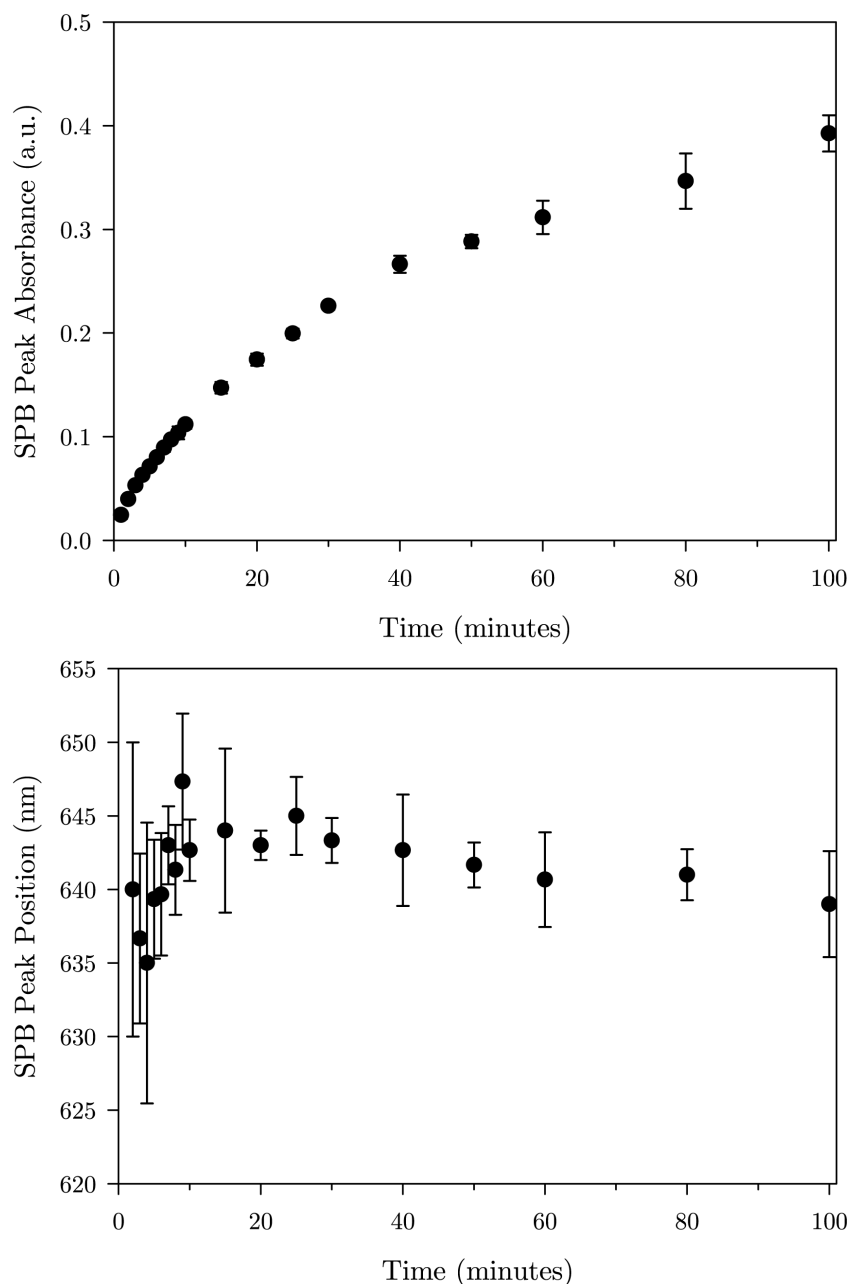


**Figure 8.2** Kinetic plots of the formation of CuNPs generated by LASiS in a  $10^{-4}$  molar aqueous solution of **bipy**. TOP PANEL: demonstration of the increase in the SPB absorption feature maxima over time. BOTTOM PANEL: demonstration of the variation in the location of the SPB absorption feature over time. In both panels the Y error bars represent one standard deviation from the mean.

In contrast, CuNPs generated in a ‘blue’ deprotonated tetrazole ligand, that being **T-4Py**, demonstrate a slightly different story (see Figure 8.3). Immediately noticeable is that the absorption maxima is higher than that seen with CuNPs generated by **bipy** and pure water, in fact, the absorption after 60 minutes of ablation is more than double that seen with CuNPs generated in pure water, though the plot exhibits a similar initial curve that is also seen with CuNPs generated in **bipy** and pure water (see Figures 8.1 and 8.2).

What is different also is that after 80 minutes of ablation the maximum SPB absorbance decreases (Figure 8.3, top panel) and this is due to the fact that the CuNPs are visibly falling out of solution due to agglomeration. In fact, in one repeat of this experiment, the absorption maxima at 80 minutes had already started to decrease in comparison to 60 minutes, and the fact that this agglomeration occurs at around 80-100 minutes is further justification for the LASiS process to be conducted for 60 minutes, thus avoiding this occurrence.

Figure 8.3 further demonstrates the CuNPs falling out of solution, with the location of the SPB starting to red-shift at 80 minutes, which indicates the CuNPs are appearing to grow in size, characteristic of them falling out of solution. This plot also shows that unlike seen previously, the SPB location actually blue-shifts by a few nanometres over 30 minutes (Figure 8.3, bottom panel), before plateauing out somewhat, then red-shifts markedly as the CuNPs start to agglomerate.

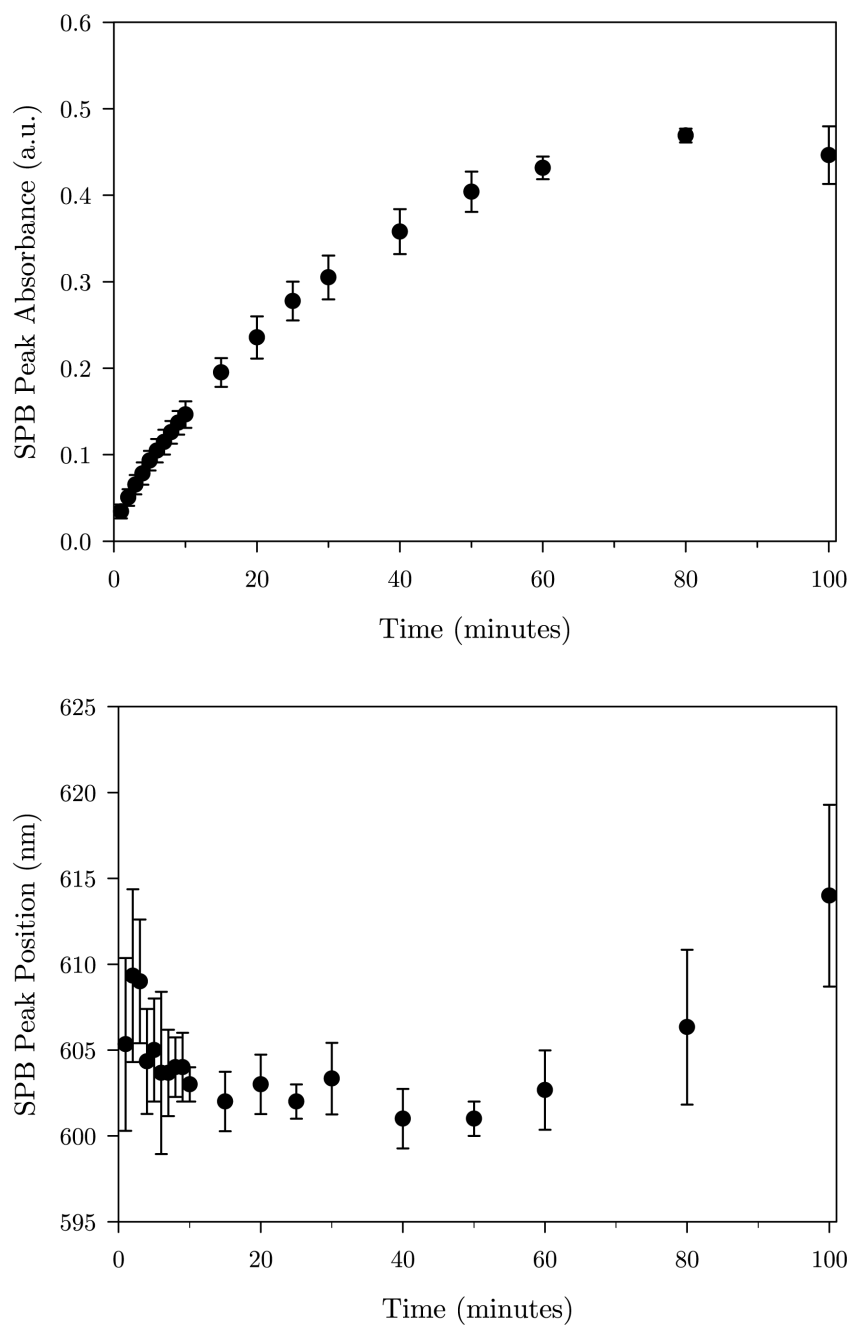


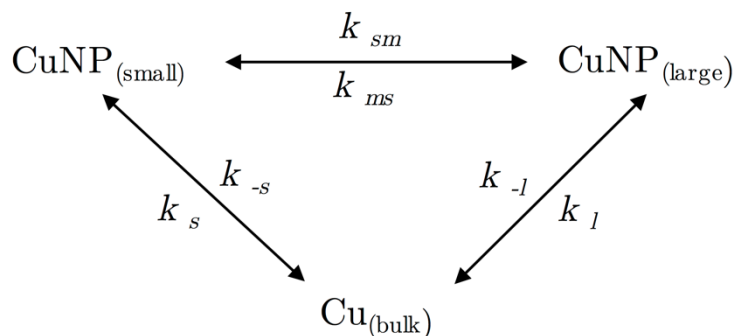
**Figure 8.3** Kinetic plots of the formation of CuNPs generated by LASiS in a  $10^{-4}$  molar aqueous solution of **T-4Py**. TOP PANEL: demonstration of the increase in the SPB absorption feature maxima over time. BOTTOM PANEL: demonstration of the variation in the location of the SPB absorption feature over time. In both panels the Y error bars represent one standard deviation from the mean.

Another aspect worth mentioning here is that the location of the SPB absorption feature is different between CuNPs generated in **T-4Py** and **bipy** and pure water. While both the pure water and **bipy** analysis show the SPB absorption to range from 635 – 665 nm, the absorption range with **T-4Py** is from 600 – 615 nm. This difference is compelling evidence that the deprotonated tetrazoles are acting as *in-situ* reducing agents, because if they were *ex-situ* reducing agents it would be expected that the SPB absorption feature wavelength position in all three experiments would start at a similar location, with the blank and **bipy** red-shifting rapidly.

The previously published research conducted on gold NPs from our laboratory demonstrated the need for a kinetic model that contained three-size regimes to accurately describe the experimental results.<sup>[136]</sup> The fitment of the kinetic data gathered in this research was conducted in a similar way as described by Fong *et al.* in the attempt to try and understand the kinetics of formation. It should be made clear that a key assumption is made in this preliminary study, namely that the extinction coefficient ratios that were determined for gold also were used here for copper. There is some validity to this assumption, as firstly, the extinction coefficient determined for small NPs that cannot support the SPR was found to be very similar (0.73 for AuNPs,<sup>[136]</sup> and between 0.73 and 0.76 for CuNPs in this work), and secondly, neither Au or Cu behave like a classical free-electron (or Drude) metal,<sup>[88]</sup> with the onset of the interband transitions occurring right where the SPB absorption feature is located. This suggests that the CuNPs would exhibit very similar behaviour to that of AuNPs in terms of the kinetics of formation, and that the model developed for AuNPs would fit with this data.

Firstly, it is important to see if it possible to fit the data presented here to a kinetic model that only encompasses two-size regimes, namely,

small NPs (that are too small to support the SPR) and large NPs (that are large enough to support the SPR). The kinetic model that describes these two-size regimes is presented in Scheme 8.1.



**Scheme 8.1** Illustration of the two-size regime for the formation of CuNPs. The model demonstrates the six different transformations that can take place in the formation of CuNPs. See text for an explanation of all terms highlighted in this model.

The model, as presented in Scheme 8.1, describes the formation of CuNPs generated by LASiS to form these small NPs (denoted as  $\text{CuNP}_{\text{small}}$ ) and large NPs (denoted as  $\text{CuNP}_{\text{large}}$ ). It is considered that LASiS of bulk copper initiates two simultaneous formation channels to form  $\text{CuNP}_{\text{small}}$  and  $\text{CuNP}_{\text{large}}$ , these being denoted as  $k_s$  and  $k_l$ , with both of these processes considered to be reversible (identified by  $k_{-s}$  and  $k_{-l}$ , respectively). It is also plausible that each size,  $\text{CuNP}_{\text{small}}$  or  $\text{CuNP}_{\text{large}}$ , can interconvert because at least one interconversion step is required to account for the observed curvature in the UV-visible data presented in Figures 8.1 – 8.3. These interconversions occur from large NPs to small NPs and from small NPs to large NPs ( $k_{ls}$  and  $k_{sl}$ , respectively).

Numerical integration of the rate expressions combined with a least-squares fit to the absorbance data yields the lines of best fit presented in Figure 8.4. The goodness of fit was determined by minimising the Chi-squared value of the fit, and it is clear to see that from the lines of best fit and the Chi

squared values presented in Table 8.1 that the two-size regime model is insufficient to fit the experimental data. This is mainly in part due to the fact that every transformation that involves small CuNPs is invalidated, as they have no bearing on the SPB absorbance and therefore cannot be investigated. This leaves only the formation and ‘sink’ of large CuNPs ( $k_l$  and  $k_{-l}$ ), and the interconversion from large to small CuNPs ( $k_{ls}$ ), as the three permissible transformations. The rate constants for these three transformations are presented in Table 8.1.

**Table 8.1** The rate constants for the various transformations that result in the presented Chi-squared values from the numerical integration and least-squares fit of the absorbance data presented in Figures 8.1, 8.2 and 8.3.

	Pure water	bipy	T-4Py
$k_l$ (pulse <sup>-1</sup> )	$1.37 \times 10^{-5}$	$1.60 \times 10^{-5}$	$1.98 \times 10^{-5}$
$k_{-l}$ (pulse <sup>-1</sup> )	$1.22 \times 10^{-4}$	$8.35 \times 10^{-5}$	$6.90 \times 10^{-5}$
$k_{ls}$ (pulse <sup>-1</sup> )	$3.13 \times 10^{-5}$	$3.55 \times 10^{-5}$	$2.57 \times 10^{-5}$
$\chi^2$ value	$1.125 \times 10^{-3}$	$7.403 \times 10^{-4}$	$1.287 \times 10^{-3}$

It is clear from Figure 8.4 that the lines of best fit do not accurately describe the kinetic process, and that more terms need to be introduced into the scheme. It follows then that the kinetic scheme as presented in Scheme 8.2, which involves three sizes of CuNPs, must be utilised to describe the formation more accurately.

The presented scheme is a modification of Scheme 8.1, with the addition of a term which describes medium sized NPs (CuNP<sub>medium</sub>). These NPs are big enough to support the SPR, but only weakly contribute to the SPB absorption feature. The formation and ‘sink’ processes are denoted by  $k_m$  and  $k_{-m}$ , respectively. The transformations to smaller and larger particles are denoted by  $k_{ms}$ ,  $k_{sm}$ ,  $k_{ml}$  and  $k_{lm}$ .

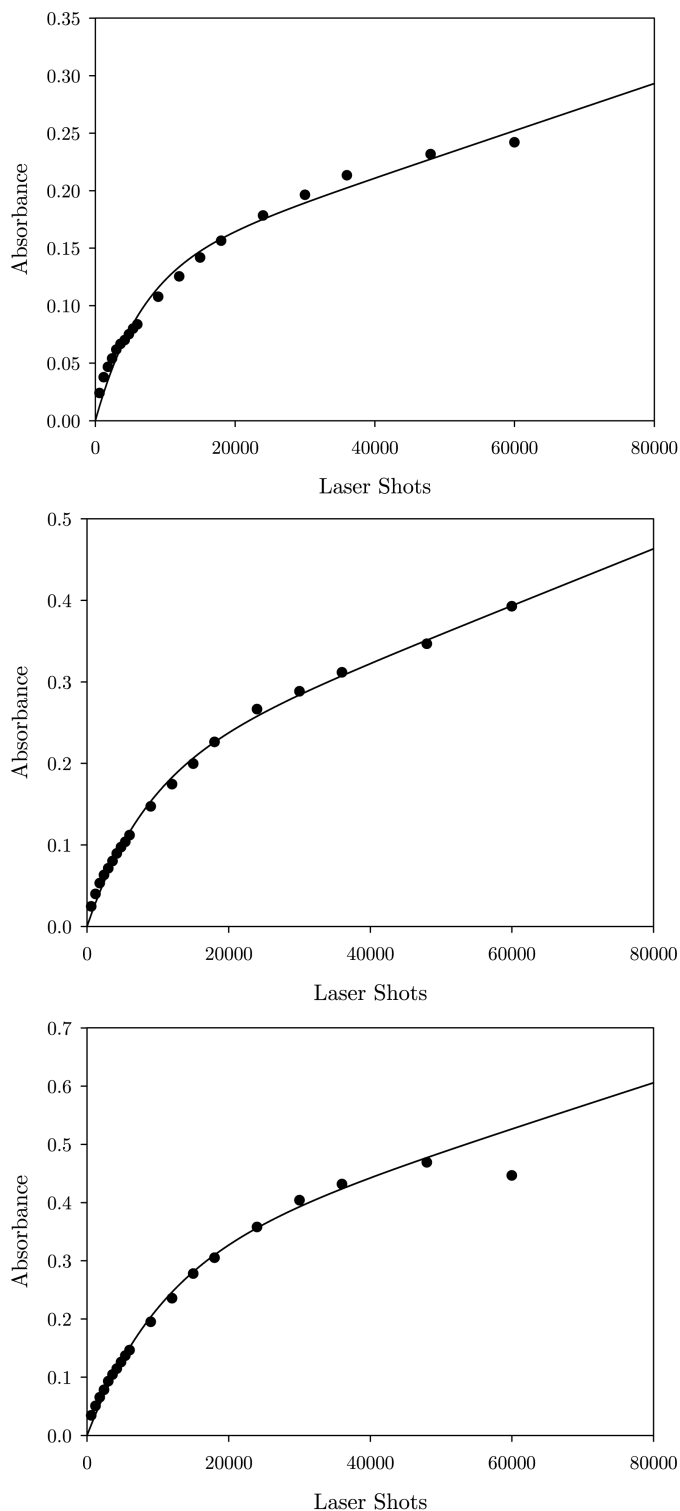
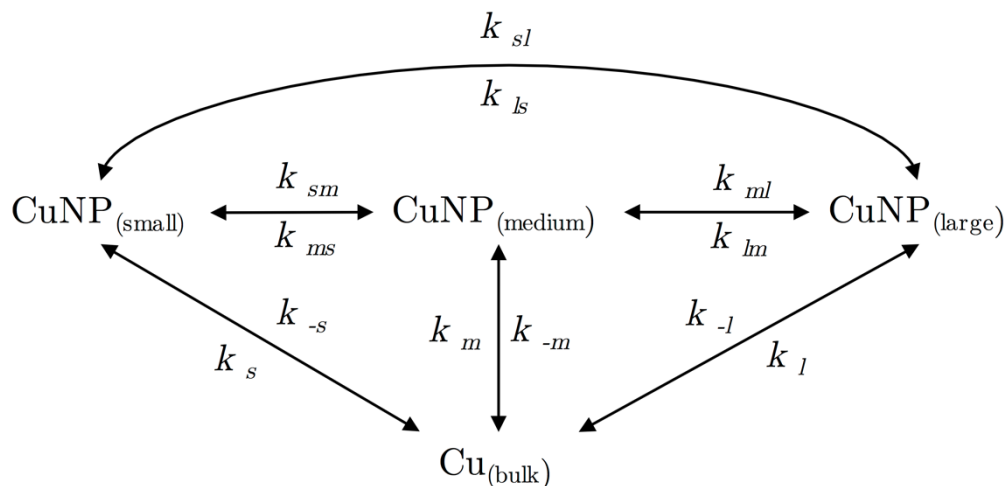


**Figure 8.4** Plots of the numerical integration and least squares fit of the UV-visible spectra of CuNPs generated by LASiS. The dots represent the experimental absorbance data shown in Figures 8.1 – 8.3, while the solid line represents the line of best fit to the data after applying the two-size regime illustrated in Scheme 8.1. TOP PANEL: CuNPs generated in pure water. MIDDLE PLOT: CuNPs generated in  $10^{-4}$  molar solution of **bipy**. BOTTOM PLOT: CuNPs generated in a  $10^{-4}$  molar solution of **T-4Py**.



**Scheme 8.2** Illustration of the three-size regime for the formation of CuNPs. The model demonstrates the twelve different transformations that can take place in the formation of CuNPs. See text for an explanation of all terms highlighted in this model.

Numerical integration of the rate expressions combined with a least-squares fit to the absorbance data yields the lines of best fit presented in Figure 8.5. The goodness of fit, like with the two-size model, was determined by minimising the Chi squared error value. The most important aspect of the data fitting is that while all 12 transformation channels could be used, only four of them are implemented, and only four have to be implemented to describe the kinetics, with the addition of a fifth or sixth term being found to be unnecessary and not improving the fit.

Figure 8.5 illustrates that the lines of best fit are a more accurate representation of the data with this model as opposed to what was seen in Figure 8.4 with the two-size model. An extensive study of the kinetic model determined that only four of the twelve transformation must be implemented to fit the experimental data. However, unlike in the precious studies into AuNP formation,<sup>[136]</sup> a single unique solution with a minimum set of parameters was not found. Rather two indistinguishable pathways are able to

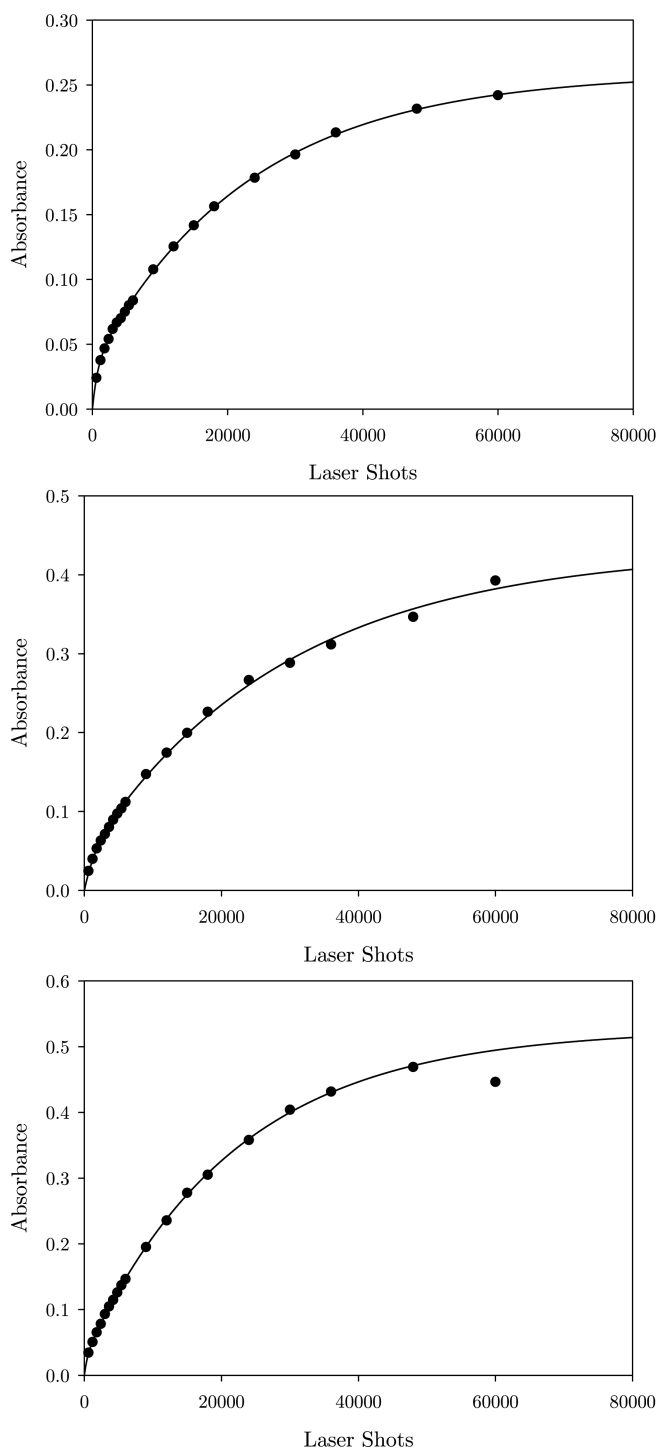


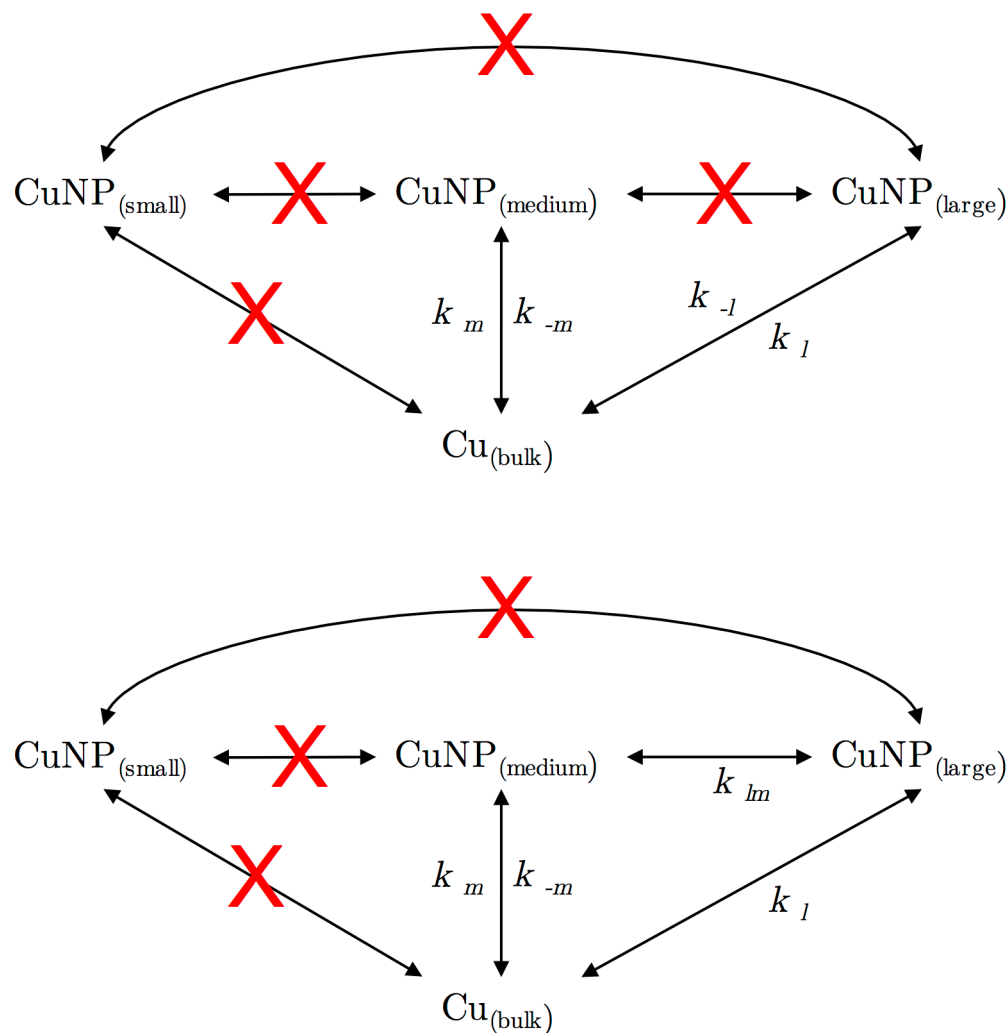
**Figure 8.5** Plots of the numerical integration and least squares fit of the UV-visible spectra of CuNPs generated by LASiS. The dots represent the experimental data obtained from Figures 8.1 – 8.3, while the solid line represents the line of best fit to the data after applying the three-size regime illustrated in Scheme 8.2. TOP PANEL: CuNPs generated in pure water. MIDDLE PLOT: CuNPs generated in  $10^{-4}$  molar solution of **bipy**. BOTTOM PLOT: CuNPs generated in a  $10^{-4}$  molar solution of **T-4Py**.

account for the experimental observations. Table 8.2 presents the transformations that are implemented, along with the associated rate constants and Chi-squared value from the fit of the UV-visible spectra presented in Figures 8.1 – 8.3.

**Table 8.2** The rate constants for the various transformations that result in the presented Chi-squared values from the numerical integration and least-squares fit of the absorbance data presented in Figures 8.1, 8.2 and 8.3.

<b>Scenario 1</b>	Pure water	<b>bipy</b>	<b>T-4Py</b>
$k_m$ (pulse <sup>-1</sup> )	$2.85 \times 10^{-5}$	$1.91 \times 10^{-5}$	$3.61 \times 10^{-5}$
$k_l$ (pulse <sup>-1</sup> )	$6.14 \times 10^{-6}$	$8.46 \times 10^{-6}$	$1.43 \times 10^{-5}$
$k_{-m}$ (pulse <sup>-1</sup> )	$1.15 \times 10^{-3}$	$6.40 \times 10^{-4}$	$1.78 \times 10^{-3}$
$k_{-l}$ (pulse <sup>-1</sup> )	$4.32 \times 10^{-5}$	$3.43 \times 10^{-5}$	$4.55 \times 10^{-5}$
$\chi^2$ value	<b><math>1.513 \times 10^{-5}</math></b>	<b><math>3.811 \times 10^{-4}</math></b>	<b><math>5.571 \times 10^{-5}</math></b>
<b>Scenario 2</b>	Pure water	<b>bipy</b>	<b>T-4Py</b>
$k_m$ (pulse <sup>-1</sup> )	$2.88 \times 10^{-5}$	$1.96 \times 10^{-5}$	$3.64 \times 10^{-5}$
$k_l$ (pulse <sup>-1</sup> )	$5.95 \times 10^{-6}$	$8.07 \times 10^{-6}$	$1.40 \times 10^{-5}$
$k_{-m}$ (pulse <sup>-1</sup> )	$1.15 \times 10^{-3}$	$6.41 \times 10^{-4}$	$1.77 \times 10^{-3}$
$k_{lm}$ (pulse <sup>-1</sup> )	$4.32 \times 10^{-5}$	$3.43 \times 10^{-5}$	$4.55 \times 10^{-5}$
$\chi^2$ value	<b><math>1.513 \times 10^{-5}</math></b>	<b><math>3.811 \times 10^{-4}</math></b>	<b><math>5.571 \times 10^{-5}</math></b>

The data presented in Table 8.2 represent two four-parameter fits to the experimental results that are indistinguishable. These are identified as Scenarios 1 and 2, respectively. These two Scenarios were the only identified four-parameter fits to the experimental data, and the new kinetic schemes that represent these Scenarios are demonstrated in Scheme 8.3. It was found that no two- or three-parameter fits converged to agreement with the experimental results.



**Scheme 8.3** Illustration of the three-size regime for the formation of CuNPs. The model demonstrates the four different transformations that can take place in the formation of CuNPs as determined by the fitting of the experimental data. The TOP PANEL is representative of Scenario 1, while the BOTTOM PANEL is representative of Scenario 2, both described in Table 8.2. In both Scenarios, the red crosses demonstrate that the transformations between those species are not taking place.

Interestingly, in previous reports on the formation kinetics of AuNPs, it was found that only three channels were required to fit the experimental data. These three channels were  $k_l$ ,  $k_m$  and  $k_{-m}$ . However, despite these three channels being implemented here in the four-parameter fit, the fitment of these three channels alone yielded  $\chi^2$  values up to two orders of magnitude

larger than those reported in Table 8.2. Careful analysis of the resultant fits showed poor agreement with experiment during the first 10 minutes of LASiS irradiation. This confirms the need to invoke a four-parameter fit to the experimental data of the entire 100-minute timeframe.

As seen in Table 8.2, there are only small variations in the kinetics constants between each scenario, and the Chi squared values are the same to the third decimal between each scenario. The key reason as to why the implementation of  $k_l$  (Scenario 1) and  $k_{lm}$  (Scenario 2) are undistinguishable from each other is that these rate constants are each almost two orders of magnitude smaller than the dominant sink rate constant,  $k_m$  (see Table 8.2).

### 8.1.3 Inferences

The fact that the study of the kinetics of formation in these three solutions demonstrate such high levels of similarity, indicates that a similar series of processes are occurring across all three ligand solutions. The fact that all three ligands demonstrate a similar curved increase in the SPB absorption intensity suggests that, unlike AuNPs that demonstrate a linear increase in the intensity after approx. 15 – 20 minutes, these kinetic plots are demonstrating an oxide-formation process. Also striking is that although the intensity values across all three solutions is different, there isn't a marked variation in the rate constants across all three solutions. All rate constants for similar transformation processes are well within one order of magnitude of each other, which indicates that all solutions are showing a very similar formation process without any marked outlier in one or more of the solutions.

What these results also indicate is that the formation process of CuNPs in a representative 'blue' deprotonated tetrazole ligand solution is very much like that of the formation process of CuNPs in a representative

'red' ligand solution. These results suggest that the formation kinetics are essentially indistinguishable from each other, despite the different SPB wavelength locations demonstrated by these solutions. This suggests that the oxide influence and the formation of the oxide is similar regardless of the ligand solution. This further strengthens the suggestion that the initial oxidation of the CuNPs is to copper (I) oxide, and that the further oxidation to copper (II) oxide in the 'red' ligand solutions occurs subsequently, while in the 'blue' ligand solutions, and hydrazine, this further oxidation is prevented.

## Chapter 9: Conclusions and Future Work

### *9.1 Future Work*

#### **9.1.1 Modification of CuNPs after LASiS**

Once LASiS has been concluded and the CuNPs have been generated, there is the possibility to further modify the NPs, not by the addition of ligands or surfactants but by further laser ablation. It is possible to take advantage of the unique SPB absorption feature and utilise it to modify the NPs. This can be achieved through a process known as photo-fragmentation or annealing, where exposing the NPs to laser irradiation post LASiS reduces the size of the NPs. The process involves exposing the NP solution to laser irradiation with a wavelength frequency that is similar to the peak of the SPB absorbance feature, which results in the NPs absorbing the energy of the laser pulse. The energy the NPs absorb is such a large amount that it forces the NPs to fragment, thus reducing their size. It has been previously demonstrated in our laboratory that by exposing gold NPs to laser irradiation with a wavelength of 532 nm the size of the NPs was reduced.<sup>[136]</sup> This reduction in the size of the gold NPs was shown with TEM imaging, and the UV-visible absorption demonstrated a decrease in the intensity of the SPB absorption feature as the size of the gold NPs decreases to a size such that they could no longer support the SPR.

This annealing process was examined to see if it would also work with the CuNPs generated in this research. The work presented here is a proof of concept, and doesn't examine all the CuNP solutions that were formed by LASiS. Further research would need to be conducted on the annealing process on all CuNP solutions, as well as a comprehensive study of the size determination.

### 9.1.2 Annealing

As proof of concept, the annealing process was undertaken as described in Chapter 2, on CuNPs generated in pure water and  $10^{-4}$  molar solutions of **T-Me** and **T-2Py** following 60 minutes of LASiS. These three solutions were exposed to laser irradiation with a wavelength of 600 nm, as the absorption profile of all these CuNP solutions shows that there is an appreciable absorption cross section at 600 nm, such that the CuNPs should absorb enough energy to photofragment.

Figures 9.1 and 9.2 illustrate that after just 10 minutes of annealing the SPB absorption feature is practically gone in all three CuNP solutions. The disappearance of the SPB absorption feature in all three solutions is indicative of a decrease in size of the CuNPs. Interestingly, the absorbance doesn't really change between 10 and 20 minutes of annealing in the **T-Me** solution, though there is an increase in the absorbance at high energies above 450 nm. This would be indicative of CuNPs that are just big enough in diameter to give rise to a very weak SPB absorption being broken down into CuNPs that can no longer support the SPR.

AFM imaging was performed on CuNPs generated in the **T-2Py** solution, after 60 minutes of LASiS but before annealing, after 10 minutes and after 20 minutes of annealing. Table 9.1 reports the means and standard deviations of the size distributions, while Figure 9.3 demonstrates the histograms of the CuNP particle size distribution.

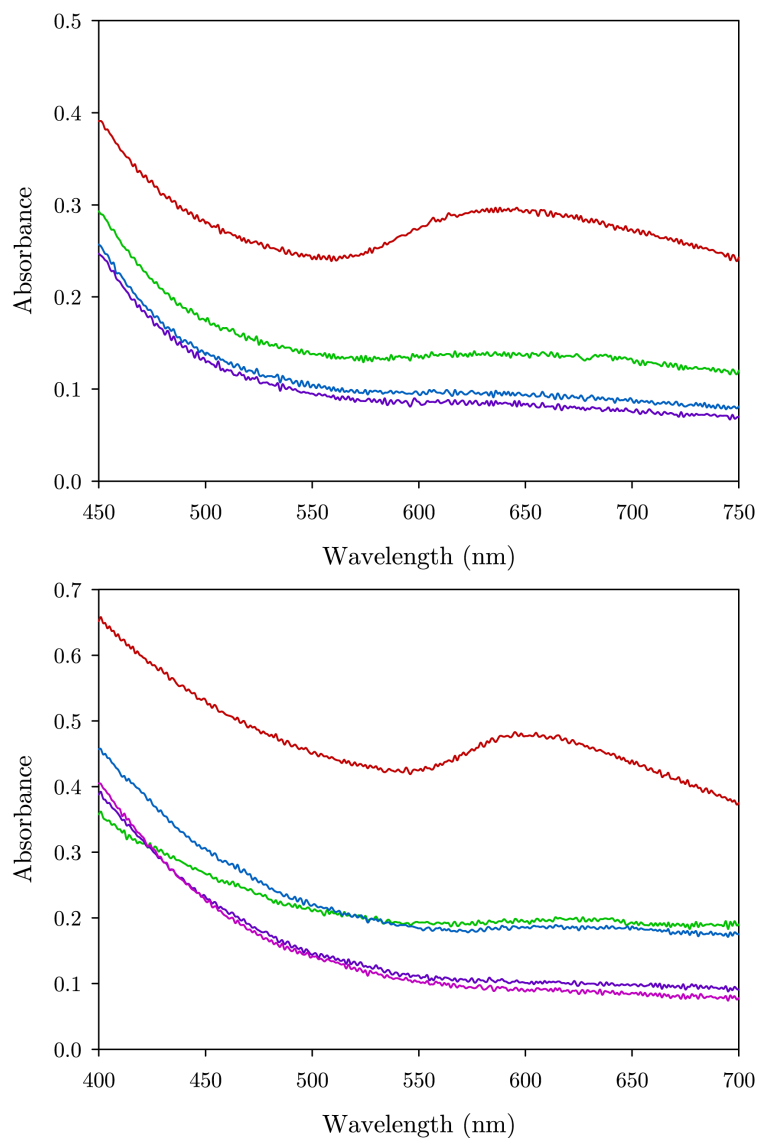


**Figure 9.1** UV-visible plots of CuNP solutions taken during the annealing process. All CuNP solutions were generated by 60 minutes of LASiS. TOP PLOT: CuNPs generated in pure water after (red) 0 minutes of annealing, (green) 10 minutes of annealing, (blue) 20 minutes of annealing, (purple) 30 minutes of annealing. BOTTOM PLOT: CuNPs generated in a  $10^{-4}$  molar solution of **T-Me** after (red) 0 minutes of annealing, (green) 10 minutes of annealing, (blue) 20 minutes of annealing, (purple) 30 minutes of annealing, (pink) 40 minutes of annealing.

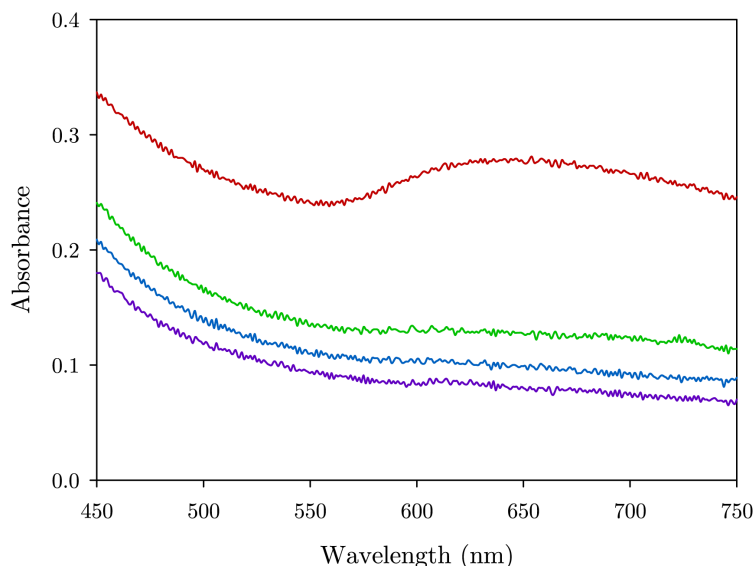


**Figure 9.2** UV-visible plot of a CuNP solution taken during the annealing process. The CuNP solution was generated by 60 minutes of LASiS. The UV-visible plots of CuNPs generated in a  $10^{-4}$  molar solution of **T-2Py** after (red) 0 minutes of annealing, (green) 10 minutes of annealing, (blue) 20 minutes of annealing, (purple) 30 minutes of annealing.

The imaging shows that with longer annealing time, the smaller and tighter the distribution becomes, confirming the behaviour of what is seen in the UV-visible spectra. However, it would be expected that there would be a much larger shift to smaller particle diameters, since the SPB absorption feature is almost non-existent after 10 minutes of annealing. Given that the SPR is only supported by, and gives rise to a SPB absorption feature, NPs greater than approximately 2 nm in diameter, the disappearance of the SPB absorption here in the UV-vis spectra would suggest a large abundance of very small CuNPs. It would be expected that the size distribution is such that the mean of the distribution is close to or less than 2 nm. Clearly this is not the case, with the results indicating that while the mean does decrease by some 3 nm, it does not decrease as significantly as the UV-visible spectra suggest.

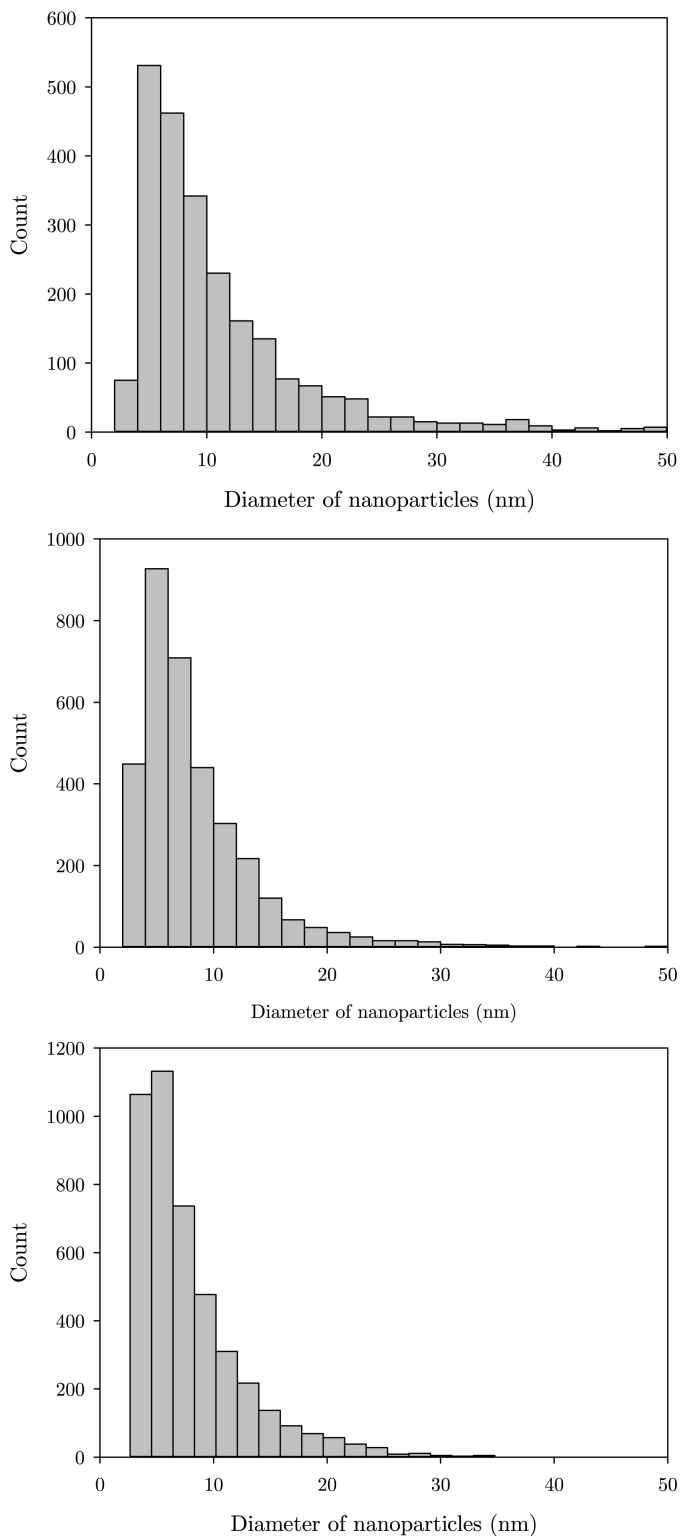


**Figure 9.3** Size distribution histograms of CuNPs generated following 60 minutes of LASiS in a  $10^{-4}$  molar solution of **T-2Py** followed by an annealing process. TOP PANEL: Size distribution of CuNPs after 0 minutes of annealing. MIDDLE PANEL: Size distribution of CuNPs after 10 minutes of annealing. BOTTOM PANEL: Size distribution of CuNPs after 20 minutes of annealing.

**Table 9.1** Statistical data of the size distributions of CuNPs as presented in the histograms in Figure 9.3

Annealing Time	Mean (nm)	Std Dev. (nm)	Dist. Max (nm)
<b>Start (0 Minutes)</b>	10.97	7.62	5
<b>10 Minutes</b>	8.40	5.40	5
<b>20 Minutes</b>	7.91	4.72	4

A possible explanation for the results that are seen is that the smaller the CuNPs get, the more problematic the AFM imaging becomes. As mentioned in Section 5.3.1, freshly cleaved mica will exhibit naturally-occurring structures on the surface, of no more than 2 nm in height, which makes identifying tiny CuNPs amongst the background problematic. The new TEM recently purchased by Curtin University will be used to further study this phenomenon.

It was also seen that the smaller CuNPs started to agglomerate on the mica surface and made it problematic to successfully image these small NPs. Nonetheless, the proof of principle research was successful, and mimics the results seen with the annealing of gold NPs, confirming that an extensive study into the annealing of CuNPs is possible.

If the information in Section 5.1 is recalled, it is seen that previous research groups have demonstrated that CuNPs of various sizes (from 7.5 nm to 30 nm in diameter) exhibit similar SPR features. The annealing results presented here don't call these reported results into question however, despite the statistical data of the size distributions demonstrating a decrease in mean and standard deviation which correlates with a change in the UV-visible absorption spectra presented in Figure 9.1 and 9.2. These annealing results illustrate that the CuNPs can be reduced in size such that the vast majority

are too small to support the SPR (as shown in Figure 9.1 and 9.2). The theoretical application of Mie's theory in Section 3.1 demonstrated that even down to 2-3 nm a SPR is supported by the NPs, while the discussion in Section 5.3.1 points out that CuNPs in size greater than 2 nm in diameter both experimentally and theoretically support a SPR. It is possible however that the size distributions presented here fail to account for the large amount of small CuNPs that are smaller than 2 nm in diameter, due to the problematic AFM imaging. It is envisaged that the use of the new TEM (which was not commissioned in time for this project) would make the analysis of the size distribution of the annealing process easier and give better results. What is more important here with these results is that the trend in the size distribution is decreasing, which is consistent with a decrease in the SPB absorption feature.

## ***9.2 Conclusions***

As stated in the introduction, a remaining challenge of CuNP LASiS generation is to easily generate oxide-free CuNPs. There is also an advantage to developing methods to be able to tune and dictate the location of the SPB absorption feature, that is, to have a quasi-tuneable SPR.

The results from Chapter 3 illustrate that the CuNPs formed in the ligand solutions demonstrate two groupings. The key to the groupings is the 'blue' ligands, where the deprotonated tetrazole ligands result in CuNPs with an SPB absorption feature located more in line with the theoretically modelled SPB location. CuNPs formed in pure water and the other ligands, the 'red' ligands, are not like those in the theoretically modelled SPB location. The stark blue-shift of the SPB location (with respect to CuNPs generated by LASiS in pure water) of CuNPs generated in the 'blue' ligands

is initially attributed to the deprotonation ability of the tetrazole ligands in solution. The results presented in Chapter 3 also demonstrate that it's not so much about the way these ligands interact with the CuNPs, nor their physical size, but rather the deprotonation, or lack thereof, that is dictating the position of the SPB absorption feature. These results also give an avenue to tune the SPB absorption feature location by the choice of ligand solution.

Chapter 4 commences by demonstrating that the 'red' ligand solutions potentially form oxidised CuNPs, which is like what has been reported previously in the literature. Theoretical modelling of the growth of both copper (I) and copper (II) oxide on a CuNP demonstrates that the CuNPs generated in the 'red' ligand solutions have a copper (I) oxide coating, an oxide coating that is the reason for the location of the SPB absorption feature. The focus then turned to preventing this oxide formation on the CuNPs, as the 'blue' ligands seem to offer some oxidative protection. This is due to the very slight red-shift in the SPB absorption feature, with respect to the theoretical position, indicating that there may be the presence of a small amount of copper (I) oxide.

Acetone has shown to give oxide free CuNPs due to the enolate ion binding to the surface of the CuNPs. A similar mechanism was assumed to be present in the 'blue' ligand solutions, due to the ligands deprotonating and forming a charged species in solution. However, charged surfactants and carboxylic acid analogues to two of the 'blue' tetrazole ligands, (ligands that also deprotonate in solution), do not show the same spectral features. The SPB absorption feature for these ligands is very much like the 'red' ligand solutions, suggesting very little oxidative protection. It is suggested then that the negatively charged 'blue' ligands are acting as *in-situ* reducing agents, which limit the oxidation of the CuNPs. When hydrazine, a common

reducing agent, is used as a LASiS solution, the CuNPs formed demonstrate a SPB absorption spectrum similar to that of the ‘blue’ ligand solutions.

However, it is possible that the spectral shifts that are seen are due to a change in the size of the CuNPs. Therefore, AFM and TEM imaging was employed to analyse the CuNP size distributions to see if there was any significant difference in the distributions. The imaging revealed that there is no significant difference in the size distributions, not significant enough to account for the spectral changes, in any case. The conclusion then is that due to similar size distributions the ‘blue’ ligand solutions give rise to oxide-free CuNPs while the ‘red’ ligand solutions do not.

pH analysis confirmed that both the ‘blue’ and ‘red’ ligands are interacting with the CuNPs due to the decrease in acidity. The decrease in acidity seen across all the tetrazole ligands (of which some are ‘blue’ and some are ‘red’ ligands) was fairly consistent, therefore suggesting that both the ‘blue’ and ‘red’ ligands interact with the CuNPs in a similar manner.

Bandgap analysis by a classic Tauc-analysis showed that there seem to be two oxides that are formed on the CuNPs, copper (I) and copper (II) oxide. The ‘blue’ ligands show the presence of copper (I) oxide, while the ‘red’ ligands show the presence of copper (II) oxide. This contrasts with the suggestion that the ‘blue’ ligands form oxide free CuNPs. It is therefore assumed that the ‘blue’ ligands offer more oxidative protection than that of the ‘red’ ligands by acting as reducing agents. The bandgap analysis of CuNPs formed in pure acetone seem to show no copper oxides, which is in line with literature.

XPS analysis revealed that the ‘blue’ ligand solutions didn’t show the presence of any copper (II) species, while the ‘red’ ligand solutions did. The XPS analysis also showed the presence of a strong oxygen signal in all the

samples, suggesting that oxides are present. The absence of a copper (II) signal in the ‘blue’ ligand solutions and the presence of an oxygen signal is further evidence that the CuNPs formed in these solutions have a copper (I) oxide surface.

However, Chapter 7 highlights the point that the contour plots shown in Chapter 4 indicate that ALL ligand solutions give rise to copper (I) oxide coated CuNPs. This contrasts with the results shown in Chapter 6 which seemingly indicate the presence of copper (I) and copper (II) oxide. The explanation for the conflicting results is proposed to be quite simple: continued oxidation of the CuNPs formed in the ‘red’ ligand solutions gives rise to the copper (II) signal seen in the XPS. Another issue then arises with the results of the bandgap analysis. This analysis suggested that there were copper (I) and copper (II) oxides present, however this now doesn’t seem to be the case. The explanation for these results seen in the bandgap analysis is that the bandgaps that are seen are all just due to copper (I) oxide. Due to larger amounts (that is, thicker coatings) of copper (I) oxide being present on the CuNPs formed in the ‘red’ ligand solutions results in lower bandgaps than CuNPs formed in the ‘blue’ ligand solutions. Because the XPS analysis is showing the presence of copper (II) species, further oxidation must be taking place on the CuNPs formed in the ‘red’ ligand solutions. These results support the hypothesis that the ‘blue’ ligands are acting as *in-situ* reducing agents, preventing further oxidation to copper (II) oxide.

The hypothesis that all CuNPs form copper (I) oxide is supported by the kinetic results. The kinetic analysis indicates that the formation processes are very similar between CuNPs formed in pure water, a representative ‘blue’ ligand solution and a representative ‘red’ ligand solution. Interestingly, however, is that the location of the SPB immediately after LASiS commences

is different. This would indicate that the ‘blue’ ligands can protect from large amounts of copper (I) oxidation. The ‘red’ ligands don’t have this ability, and so the SPB location is already red-shifted from the very start. Because the formation processes are very similar (the rate constants are similar to within an order of magnitude) it can be proposed that the oxidation of CuNPs from copper (I) oxide to copper (II) oxide occurs mostly after LASiS has finished. This also correlates with what is seen with the UV-visible spectra results shown in Chapters 3 and 4.

What these results all show is that the tetrazole motif provides an interesting solution to oxidative control of CuNPs. The key seems to be the ability of the tetrazole to deprotonate in solution, and when it can do so, it acts as an *in-situ* reducing agent, limiting the oxidation of the CuNPs. While these tetrazoles seemingly don’t prevent oxidation (only limit it), what they do do is allow for the tuning of the oxidation of the CuNPs. This then gives an avenue to tune the SPB absorption feature location.

Interestingly, the kinetics results also demonstrate that the formation processes of CuNPs by LASiS are similar to that of AuNPs generated by LASiS. In both cases a three-size model needs to be employed to accurately describe the formation kinetics in the minimum amount of terms.

So, while these results don’t demonstrate a pathway to manufacture oxide free CuNPs via LASiS, they do illustrate a way to control the oxide formation of the CuNPs. This can be advantageous, as it has been proposed that copper (I) oxide coated CuNPs have characteristics that are desirable for light-harvesting applications.<sup>[107]</sup> The proof of concept experiments into the annealing of the CuNPs indicated that a more in-depth study is warranted. This annealing allows for an avenue to generate CuNPs of a more uniform size, possibly also allowing for the manufacture of CuNPs of a specific size.

Further work could also be undertaken into looking at the role of oxygen and/or OH<sup>-</sup> scavengers in the LASiS solutions and what effect that they would have in controlling, or even preventing, oxide formation.

With research undertaken into the addition of CuNPs to motor oils to decrease friction and to heat-exchange fluids to improve heat transfer,<sup>[208-215]</sup> there is an avenue to undertake LASiS of CuNPs directly in these fluids. There is an avenue to also study the effects of tetrazole addition and of the deprotonated tetrazole-protected CuNPs to these fluids.

The deprotonated tetrazoles have opened a new avenue of research to investigate why and how these ligands are behaving as *in-situ* reducing agents, a new project in itself.

## Chapter 10: References

- (1) Oxford English Dictionary "*particle, n.*"; Oxford University Press.
- (2) Module 3: Characteristics of Particles In: *Basic Concepts in Environmental Science*. Environmental Protection Agency; 2012 [cited March 30, 2016]. Available from: [http://www.apti-learn.net/lms/content/epa/courses/re\\_100/index.htm?cid=2&userID=43049&bookmarks=](http://www.apti-learn.net/lms/content/epa/courses/re_100/index.htm?cid=2&userID=43049&bookmarks=).
- (3) ISO/IEC 80004-2:2015, *Nanotechnologies - Vocabulary - Part 2: Nano-objects*. Geneva, Switzerland, (2015).
- (4) Springer Handbooks *Springer Handbook of Nanomaterials*, 1 ed.; Springer-Verlag Berlin Heidelberg, 2013.
- (5) Jarvie, H.; Dobson, P.; King, S. Nanoparticle. Encyclopedia Britannica, inc.; 2016 [Available from: <https://www.britannica.com/science/nanoparticle>].
- (6) Link, S.; El-Sayed, M. A. *Int. Rev. Phys. Chem.* **2000**, *19*, 409-453.
- (7) Kamat, P. V. *J. Phys. Chem. B* **2002**, *106*, 7729-7744.
- (8) Link, S.; El-Sayed, M. A. *Annu. Rev. Phys. Chem.* **2003**, *54*, 331-366.
- (9) Daniel, M.-C.; Astruc, D. *Chem. Rev.* **2004**, *104*, 293-346.
- (10) Burda, C.; Chen, X.; Narayanan, R.; El-Sayed, M. A. *Chem. Rev.* **2005**, *105*, 1025-1102.
- (11) Michalet, X.; Pinaud, F. F.; Bentolila, L. A.; Tsay, J. M.; et al. *Science* **2005**, *307*, 538-44.
- (12) Medintz, I. L.; Uyeda, H. T.; Goldman, E. R.; Mattoussi, H. *Nat. Mater.* **2005**, *4*, 435-46.
- (13) Willets, K. A.; Van Duyne, R. P. *Annu. Rev. Phys. Chem.* **2007**, *58*, 267-297.
- (14) Anker, J. N.; Hall, W. P.; Lyandres, O.; Shah, N. C.; Zhao, J.; Van Duyne, R. P. *Nat. Mater.* **2008**, *7*, 442-453.

## References

- (15) Jain, P. K.; Manthiram, K.; Engel, J. H.; White, S. L.; Faucheaux, J. A.; Alivisatos, A. P. *Angew. Chem., Int. Ed.* **2013**, *52*, 13671-13675.
- (16) Schlücker, S. *Angew. Chem., Int. Ed.* **2014**, *53*, 4756-4795.
- (17) Peer, D.; Karp, J. M.; Hong, S.; Farokhzad, O. C.; Margalit, R.; Langer, R. *Nat. Nanotechnol.* **2007**, *2*, 751-60.
- (18) Mura, S.; Nicolas, J.; Couvreur, P. *Nat. Mater.* **2013**, *12*, 991-1003.
- (19) Zhu, Y.; Liao, L. *J. Nanosci. Nanotechnol.* **2015**, *15*, 4753-4773.
- (20) Hou, W.; Cronin, S. B. *Adv. Funct. Mater.* **2013**, *23*, 1612-1619.
- (21) Guo, S.; Zhang, S.; Sun, S. *Angew. Chem., Int. Ed.* **2013**, *52*, 8526-8544.
- (22) Sellappan, R.; Nielsen, M. G.; González-Posada, F.; Vesborg, P. C. K.; Chorkendorff, I.; Chakarov, D. *J. Catal.* **2013**, *307*, 214-221.
- (23) El-Sayed, M. A. *Acc. Chem. Res.* **2004**, *37*, 326-333.
- (24) Huang, X.; Han, S.; Huang, W.; Liu, X. *Chem. Soc. Rev.* **2013**, *42*, 173-201.
- (25) Noh, H. S.; Cho, E. H.; Kim, H. M.; Han, Y. D.; Joo, J. *Organic Electronics* **2013**, *14*, 278-285.
- (26) Sebo, B.; Huang, N.; Liu, Y.; Tai, Q.; Liang, L.; Hu, H.; Xu, S.; Zhao, X.-Z. *Electrochim. Acta* **2013**, *112*, 458-464.
- (27) Tong, C.; Yun, J.; Song, H.; Gan, Q.; Anderson, W. A. *Sol. Energy Mater. Sol. Cells* **2014**, *120, Part B*, 591-595.
- (28) Lu, A.-H.; Salabas, E. L.; Schüth, F. *Angew. Chem., Int. Ed.* **2007**, *46*, 1222-1244.
- (29) Langille, M. R.; Personick, M. L.; Mirkin, C. A. *Angew. Chem., Int. Ed.* **2013**, *52*, 13910-13940.
- (30) Mangelson, B. F.; Park, D. J.; Ku, J. C.; Osberg, K. D.; Schatz, G. C.; Mirkin, C. A. *Small* **2013**, *9*, 2250-2254.
- (31) Mangelson, B. F.; Jones, M. R.; Park, D. J.; Shade, C. M.; Schatz, G. C.; Mirkin, C. A. *Chem. Mater.* **2014**, *26*, 3818-3824.

- (32) Young, K. L.; Ross, M. B.; Blaber, M. G.; Rycenga, M.; Jones, M. R.; Zhang, C.; Senesi, A. J.; Lee, B.; Schatz, G. C.; Mirkin, C. A. *Adv. Mater. (Weinheim, Ger.)* **2014**, *26*, 653-659.
- (33) Sugimoto, T. *Adv. Colloid Interface Sci.* **1987**, *28*, 65-108.
- (34) Niederberger, M.; Colfen, H. *Phys. Chem. Chem. Phys.* **2006**, *8*, 3271-3287.
- (35) Sau, T. K.; Rogach, A. L.; Jäckel, F.; Klar, T. A.; Feldmann, J. *Adv. Mater. (Weinheim, Ger.)* **2010**, *22*, 1805-1825.
- (36) Chen, J.; Clay, N. E.; No-hyung, P.; Kong, H. *Chem. Eng. Sci.* **2015**, *125*, 20-24.
- (37) Mathaes, R.; Winter, G.; Besheer, A.; Engert, J. *Expert Opinion on Drug Delivery* **2015**, *12*, 481-492.
- (38) Noble Metal. Encyclopedia Britannica, inc; 2008 [cited February 22, 2017]. Available from: <https://www.britannica.com/science/noble-metal>.
- (39) Amendola, V.; Meneghetti, M. *Phys. Chem. Chem. Phys.* **2013**, *15*, 3027-3046.
- (40) British Museum - The Lycurgus Cup. Google; 2016 [cited April 4, 2016]. Available from: <https://www.google.com/culturalinstitute/u/0/asset-viewer/the-lycurgus-cup/aQG7BXUoa7xwug>.
- (41) Faraday, M. *Phil. Trans. Royal Soc. London* **1857**, *147*, 145-181.
- (42) Turkevich, J.; Stevenson, P. C.; Hillier, J. *Discuss. Faraday Soc.* **1951**, *11*, 55-75.
- (43) Frens, G. *Kolloid-Z. u. Z. Polymere* **1972**, *250*, 736-741.
- (44) Frens, G. *Nat. Phys. Sci.* **1973**, *241*, 20-22.
- (45) Brust, M.; Walker, M.; Bethell, D.; Schiffrin, D. J.; Whyman, R. *J. Chem. Soc., Chem. Commun.* **1994**, 801-802.
- (46) Fievet, F.; Lagier, J. P.; Figlarz, M. *MRS Bulletin* **1989**, *14*, 29-34.
- (47) Henglein, A.; Mulvaney, P.; Linnert, T.; Holzwarth, A. *J. Phys. Chem* **1992**, *96*, 2411-2414.

## References

- (48) Henglein, A. *J. Phys. Chem* **1993**, *97*, 5457-5471.
- (49) Linnert, T.; Mulvaney, P.; Henglein, A. *J. Phys. Chem* **1993**, *97*, 679-682.
- (50) Barcikowski, S.; Devesa, F.; Moldenhauer, K. *J. Nanopart. Res.* **2009**, *11*, 1883-1893.
- (51) Lisiecki, I.; Pileni, M. P. *J. Am. Chem. Soc.* **1993**, *115*, 3887-3896.
- (52) Lisiecki, I.; Billoudet, F.; Pileni, M. P. *J. Phys. Chem.* **1996**, *100*, 4160-4166.
- (53) Khodashenas, B.; Ghorbani, H. *Korean J. Chem. Eng.* **2014**, *31*, 1105-1109.
- (54) Huang, H. H.; Yan, F. Q.; Kek, Y. M.; Chew, C. H.; Xu, G. Q.; Ji, W.; Oh, P. S.; Tang, S. H. *Langmuir* **1997**, *13*, 172-175.
- (55) Rice, K. P.; Walker, E. J.; Stoykovich, M. P.; Saunders, A. E. *J. Phys. Chem. C* **2011**, *115*, 1793-1799.
- (56) Henglein, A. *Chem. Mater.* **1998**, *10*, 444-450.
- (57) Barta, J.; Pospisil, M.; Cuba, V. *J. Radioanal. Nucl. Chem.* **2010**, *286*, 611-618.
- (58) Bin Ahmad, M.; Lim, J. J.; Shameli, K.; Ibrahim, N. A.; Tay, M. Y. *Molecules* **2011**, *16*, 7237-7248.
- (59) Umer, A.; Naveed, S.; Ramzan, N.; Rafique, M. S. *Nano* **2012**, *07*, 1230005.
- (60) Gawande, M. B.; Goswami, A.; Felpin, F.-X.; Asefa, T.; Huang, X.; Silva, R.; Zou, X.; Zboril, R.; Varma, R. S. *Chem. Rev.* **2016**, *116*, 3722-3811.
- (61) Dagher, S.; Haik, Y.; Ayeshe, A. I.; Tit, N. *J. Lumin.* **2014**, *151*, 149-154.
- (62) Engels, V.; Benaskar, F.; Jefferson, D. A.; Johnson, B. F. G.; Wheatley, A. E. H. *Dalton Trans.* **2010**, *39*, 6496-6502.
- (63) Lorazo, P.; Lewis, L. J.; Meunier, M. *Phys. Rev. B* **2006**, *73*, 134108.

- (64) Amendola, V.; Meneghetti, M. *Phys. Chem. Chem. Phys.* **2009**, *11*, 3805-3821.
- (65) Barcikowski, S.; Mafune, F. *J. Phys. Chem. C* **2011**, *115*, 4985-4985.
- (66) Yan, Z.; Chrisey, D. B. *Journal of Photochemistry and Photobiology C: Photochemistry Reviews* **2012**, *13*, 204-223.
- (67) Zeng, H. B.; Du, X. W.; Singh, S. C.; Kulinich, S. A.; Yang, S. K.; He, J. P.; Cai, W. P. *Adv. Funct. Mater.* **2012**, *22*, 1333-1353.
- (68) Barcikowski, S.; Compagnini, G. *Phys. Chem. Chem. Phys.* **2013**, *15*, 3022-3026.
- (69) Dell'Aglio, M.; Gaudiuso, R.; De Pascale, O.; De Giacomo, A. *Appl. Surf. Sci.* **2015**, *348*, 4-9.
- (70) Lam, C.; Zhang, Y. F.; Tang, Y. H.; Lee, C. S.; Bello, I.; Lee, S. T. *J. Cryst. Growth* **2000**, *220*, 466-470.
- (71) Chen, D.; Ni, S.; Chen, Z. H.; Chen, G. L.; Chen, G. *J. Inorg. Mater.* **2007**, *22*, 1251-1254.
- (72) Knieke, C.; Steinborn, C.; Romeis, S.; Peukert, W.; Breitung-Faes, S.; Kwade, A. *Chem. Eng. Technol.* **2010**, *33*, 1401-1411.
- (73) Neddersen, J.; Chumanov, G.; Cotton, T. M. *Appl. Spectrosc.* **1993**, *47*, 1959-1964.
- (74) Mafune, F.; Kohno, J.; Takeda, Y.; Kondow, T.; Sawabe, H. *J. Phys. Chem. B* **2000**, *104*, 9111-9117.
- (75) Mafune, F.; Kohno, J.; Takeda, Y.; Kondow, T.; Sawabe, H. *J. Phys. Chem. B* **2001**, *105*, 5114-5120.
- (76) Mafune, F.; Kohno, J. Y.; Takeda, Y.; Kondow, T. *J. Phys. Chem. B* **2003**, *107*, 4218-4223.
- (77) Amendola, V.; Polizzi, S.; Meneghetti, M. *Langmuir* **2007**, *23*, 6766-6770.
- (78) Saito, M.; Yasukawa, K.; Umeda, T.; Aoi, Y. *Opt. Mater.* **2008**, *30*, 1201-1204.
- (79) Giorgetti, E.; Muniz-Miranda, M.; Marsili, P.; Scarpellini, D.; Giammanco, F. *J. Nanopart. Res.* **2012**, *14*, 648.

## References

- (80) Muniz-Miranda, M.; Gellini, C.; Giorgetti, E. *J. Phys. Chem. C* **2011**, *115*, 5021-5027.
- (81) Muniz-Miranda, M.; Gellini, C.; Simonelli, A.; Tiberi, M.; Giammanco, F.; Giorgetti, E. *Applied Physics A* **2013**, *110*, 829-833.
- (82) Dhawan, A.; Sharma, V. *Anal. Bioanal. Chem.* **2010**, *398*, 589-605.
- (83) Jenkins, S. I.; Pickard, M. R.; Furness, D. N.; Yiu, H. H. P.; Chari, D. M. *Nanomedicine* **2012**, *8*, 951-968.
- (84) Bootz, A.; Vogel, V.; Schubert, D.; Kreuter, J. *European Journal of Pharmaceutics and Biopharmaceutics* **2004**, *57*, 369-375.
- (85) Datye, A. K.; Hansen, P. L.; Helveg, S.; Electron Microscopy and Diffraction. In *Handbook of Heterogeneous Catalysis*; Wiley-VCH Verlag GmbH & Co. KGaA, 2008.
- (86) Baer, D. R.; Engelhard, M. H.; Johnson, G. E.; Laskin, J.; Lai, J.; Mueller, K.; Munusamy, P.; Thevuthasan, S.; Wang, H.; Washton, N.; Elder, A.; Baisch, B. L.; Karakoti, A.; Kuchibhatla, S. V. N. T.; Moon, D. *J. Vac. Sci. Technol., A* **2013**, *31*, 050820.
- (87) Baer, D. R.; Gaspar, D. J.; Nachimuthu, P.; Techane, S. D.; Castner, D. G. *Anal. Bioanal. Chem.* **2010**, *396*, 983-1002.
- (88) Bohren, C. F.; Huffman, D. R. *Absorption and Scattering of Light by Small Particles*; Wiley-Interscience: New York, 1983.
- (89) Tonks, L.; Langmuir, I. *Physical Review* **1929**, *33*, 195-210.
- (90) Ritchie, R. H. *Physical Review* **1957**, *106*, 874-881.
- (91) Link, S.; El-Sayed, M. A. *J. Phys. Chem. B* **1999**, *103*, 8410-8426.
- (92) Garcia, M. A. *J. Phys. D: Appl. Phys.* **2011**, *44*, 283001.
- (93) Frölich, H. *Theory of Dielectrics: Dielectric Constant and Dielectric Loss*; Clarendon Press, 1949.
- (94) Creighton, J. A.; Eadon, D. G. *J. Chem. Soc., Faraday Trans.* **1991**, *87*, 3881-3891.
- (95) Kreibig, U.; Vollmer, M. Springer Series in Materials Science *Optical Properties of Metal Clusters*; Springer Berlin Heidelberg, 1995.

## References

- (96) Chan, G. H.; Zhao, J.; Hicks, E. M.; Schatz, G. C.; Van Duyne, R. P. *Nano Lett.* **2007**, *7*, 1947-1952.
- (97) Qin, L.-X.; Jing, C.; Li, Y.; Li, D.-W.; Long, Y.-T. *Chem. Commun. (Cambridge, U. K.)* **2012**, *48*, 1511-1513.
- (98) Gonzalez-Posada, F.; Sellappan, R.; Vanpoucke, B.; Chakarov, D. *RSC Advances* **2014**, *4*, 20659-20664.
- (99) Rice, K. P.; Paterson, A. S.; Stoykovich, M. P. *Particle & Particle Systems Characterization* **2015**, *32*, 373-380.
- (100) West, P. R.; Ishii, S.; Naik, G. V.; Emani, N. K.; Shalaev, V. M.; Boltasseva, A. *Laser & Photonics Reviews* **2010**, *4*, 795-808.
- (101) Kanninen, P.; Johans, C.; Merta, J.; Kontturi, K. *J. Colloid Interface Sci.* **2008**, *318*, 88-95.
- (102) Salzemann, C.; Lisiecki, I.; Brioude, A.; Urban, J.; Pileni, M. P. *J. Phys. Chem. B* **2004**, *108*, 13242-13248.
- (103) Darugar, Q.; Qian, W.; El-Sayed, M. A.; Pileni, M.-P. *J. Phys. Chem. B* **2006**, *110*, 143-149.
- (104) Kazakevich, P. V.; Simakin, A. V.; Voronov, V. V.; Shafeev, G. A. *Appl. Surf. Sci.* **2006**, *252*, 4373-4380.
- (105) Dorranean, D.; Ahmadi Afshar, S.; Tahmasebi, N.; Fotovat Eskandari, A. *J. Cluster Sci.* **2014**, *25*, 1147-1156.
- (106) Gondal, M. A.; Qahtan, T. F.; Dastageer, M. A.; Saleh, T. A.; Maganda, Y. W.; Anjum, D. H. *Appl. Surf. Sci.* **2013**, *286*, 149-155.
- (107) Peña-Rodríguez, O.; Pal, U. *J. Opt. Soc. Am. B* **2011**, *28*, 2735-2739.
- (108) Fong, Y.-Y.; Gascooke, J. R.; Visser, B. R.; Harris, H. H.; Cowie, B. C. C.; Thomsen, L.; Metha, G. F.; Buntine, M. A. *Langmuir* **2013**, *29*, 12452-12462.
- (109) Kaur, R.; Giordano, C.; Gradzielski, M.; Mehta, S. K. *Chemistry – An Asian Journal* **2014**, *9*, 189-198.
- (110) Kuo, C.-H.; Huang, M. H. *J. Phys. Chem. C* **2008**, *112*, 18355-18360.
- (111) Siddiqui, H.; Qureshi, M. S.; Haque, F. Z. *Optik - International Journal for Light and Electron Optics* **2016**, *127*, 2740-2747.

## References

- (112) Cai, X.; Anyaogu, K. C.; Neckers, D. C. *Photochem. Photobiol. Sci.* **2009**, *8*, 1568-1573.
- (113) Wang, Z.; von dem Bussche, A.; Kabadi, P. K.; Kane, A. B.; Hurt, R. H. *ACS Nano* **2013**, *7*, 8715-8727.
- (114) Basheer, N. S.; Kumar, B. R.; Kurian, A.; George, S. D. *Applied Physics B* **2013**, *113*, 581-587.
- (115) Chung, H. Y.; Leung, P. T.; Tsai, D. P. *Opt. Express* **2013**, *21*, 26483-26492.
- (116) Li, C.; Zhu, J. *Mater. Lett.* **2013**, *112*, 169-172.
- (117) Li, J.; Zhu, J.-J.; Xu, K. *Trends Anal. Chem.* **2014**, *58*, 90-98.
- (118) Chowdhury, S.; Bhethanabotla, V. R.; Sen, R. *Plasmonics* **2011**, *6*, 735-740.
- (119) Garcia-Amorós, J.; Swaminathan, S.; Sortino, S.; Raymo, F. M. *Chemistry – A European Journal* **2014**, *20*, 10276-10284.
- (120) Giorgetti, E.; Marsili, P.; Canton, P.; Muniz-miranda, M.; Caporali, S.; Giammanco, F. *J. Nanopart. Res.* **2013**, *15*, 1-12.
- (121) Pockrand, I. *Chem. Phys. Lett.* **1982**, *85*, 37-42.
- (122) Peters, T.; Blumenstock, F. A. *J. Biol. Chem.* **1967**, *242*, 1574-1578.
- (123) Kroneck, P. M. H.; Vortisch, V.; Hemmerich, P. *Eur. J. Biochem.* **1980**, *109*, 603-612.
- (124) Pensa, E.; Cortés, E.; Corthey, G.; Carro, P.; Vericat, C.; Fonticelli, M. H.; Benítez, G.; Rubert, A. A.; Salvarezza, R. C. *Acc. Chem. Res.* **2012**, *45*, 1183-1192.
- (125) Castner, D. G.; Hinds, K.; Grainger, D. W. *Langmuir* **1996**, *12*, 5083-5086.
- (126) de Carvalho, D. F.; da Fonseca, B. G.; Barbosa, I. L.; Landi, S. M.; de Sena, L. Á.; Archanjo, B. S.; Sant'Ana, A. C. *Spectrochim. Acta, Part A* **2013**, *103*, 108-113.
- (127) Gordon, K. C.; McGarvey, J. J. *Inorg. Chem.* **1991**, *30*, 2986-2989.

- (128) McGarvey, J. J.; Bell, S. E. J.; Gordon, K. C. *Inorg. Chem.* **1988**, *27*, 4003-4006.
- (129) Fiorini, V.; Ranieri, A. M.; Muzzioli, S.; Magee, K. D. M.; Zacchini, S.; Akabar, N.; Stefan, A.; Ogden, M. I.; Massi, M.; Stagni, S. *Dalton Trans.* **2015**, *44*, 20597-20608.
- (130) Werrett, M. V.; Chartrand, D.; Gale, J. D.; Hanan, G. S.; MacLellan, J. G.; Massi, M.; Muzzioli, S.; Raiteri, P.; Skelton, B. W.; Silberstein, M.; Stagni, S. *Inorg. Chem.* **2011**, *50*, 1229-1241.
- (131) Downard, A. J.; Steel, P. J.; Steenwijk, J. *Aust. J. Chem.* **1995**, *48*, 1625-1642.
- (132) Koguro, K.; Oga, T.; Mitsui, S.; Orita, R. *Synthesis-Stuttgart* **1998**, 910-914.
- (133) Mulder, A. J.; Tilbury, R. D.; Werrett, M. V.; Wright, P. J.; Becker, T.; Jones, F.; Stagni, S.; Massi, M.; Buntine, M. A. *Manuscript in Preparation* **2017**
- (134) Wright, P. J.; Muzzioli, S.; Werrett, M. V.; Raiteri, P.; Skelton, B. W.; Silvester, D. S.; Stagni, S.; Massi, M. *Organometallics* **2012**, *31*, 7566-7578.
- (135) Lisakova, A. D.; Ryabukhin, D. S.; Trifonov, R. E.; Ostrovskii, V. A.; Vasilyev, A. V. *Tetrahedron Lett.* **2015**, *56*, 7020-7023.
- (136) Fong, Y.-Y.; Gascooke, J. R.; Visser, B. R.; Metha, G. F.; Buntine, M. A. *J. Phys. Chem. C* **2010**, *114*, 15931-15940.
- (137) Fong, Y.-Y.; Gascooke, J. R.; Metha, G. F.; Buntine, M. A. *Aust. J. Chem.* **2012**, *65*, 97-104.
- (138) Tilaki, R. M.; Zad, A. I.; Mahdavi, S. M. *Appl. Phys. A: Mater. Sci. Process.* **2007**, *88*, 415-419.
- (139) Haram, N.; Ahmad, N. *Applied Physics A* **2013**, *111*, 1131-1137.
- (140) Siegman, A. E. *Lasers*; University Science Books: Mill Valley, California, 1986.
- (141) Nečas, D.; Klapetek, P. *Open Physics* **2012**, *10*, 181.

## References

- (142) Fong, Y.-Y.; Visser, B. R.; Gascooke, J. R.; Cowie, B. C. C.; Thomsen, L.; Metha, G. F.; Buntine, M. A.; Harris, H. H. *Langmuir* **2011**, *27*, 8099-8104.
- (143) Fairley, N.; Carrick, A. *The CASA Cookbook, Part 1: Recipes for XPS Data Processing*; Acolyte Science: Knutsford, Cheshire, 2005.
- (144) Végh, J. *J. Electron Spectrosc. Relat. Phenom.* **2006**, *151*, 159-164.
- (145) Biesinger, M. C.; Lau, L. W. M.; Gerson, A. R.; Smart, R. S. C. *Appl. Surf. Sci.* **2010**, *257*, 887-898.
- (146) Mie, G. *Ann. Phys. (Berlin)* **1908**, *330*, 377-445.
- (147) Kelly, K. L.; Coronado, E.; Zhao, L. L.; Schatz, G. C. *J. Phys. Chem. B* **2003**, *107*, 668-677.
- (148) Prasad, P. N.; Plasmonics. In *Nanophotonics*; John Wiley & Sons, Inc., 2004; pp 129-151.
- (149) Kreibig, U. *Journal of Physics F: Metal Physics* **1974**, *4*, 999-1014.
- (150) Roberts, S. *Physical Review* **1960**, *118*, 1509-1518.
- (151) Temple, T. L. *Plasmonics* **2015**, *10*, 455-467.
- (152) Johnson, P. B.; Christy, R. W. *Phys. Rev. B* **1972**, *6*, 4370-4379.
- (153) Hövel, H.; Fritz, S.; Hilger, A.; Kreibig, U.; Vollmer, M. *Phys. Rev. B* **1993**, *48*, 18178-18188.
- (154) Kreibig, U. *J. Phys. Colloques* **1977**, *38*, C2-97-C2-103.
- (155) Kreibig, U.; Genzel, L. *Surf. Sci.* **1985**, *156*, 678-700.
- (156) Peña, O.; Pal, U.; Rodríguez-Fernández, L.; Crespo-Sosa, A. *Journal of the Optical Society of America B* **2008**, *25*, 1371-1379.
- (157) Alsawafta, M.; Badilescu, S.; Packirisamy, M.; Truong, V. V. *Reaction Kinetics, Mechanisms and Catalysis* **2011**, *104*, 437-450.
- (158) Celep, G.; Cottancin, E.; Lermé, J.; Pellarin, M.; Arnaud, L.; Huntzinger, J. R.; Vialle, J. L.; Broyer, M.; Palpant, B.; Boisron, O.; Mélinon, P. *Phys. Rev. B* **2004**, *70*, 165409.
- (159) Coronado, E. A.; Schatz, G. C. *J. Chem. Phys.* **2003**, *119*, 3926-3934.

- (160) Mulvaney, P. *Langmuir* **1996**, *12*, 788-800.
- (161) Senoy, T.; Saritha, K. N.; Jamal, E. M. A.; Al-Harthi, S. H.; Manoj Raama, V.; Anantharaman, M. R. *Nanotechnology* **2008**, *19*, 075710.
- (162) Scholl, J. A.; Koh, A. L.; Dionne, J. A. *Nature* **2012**, *483*, 421-427.
- (163) Kapoor, S.; Mukherjee, T. *Chem. Phys. Lett.* **2003**, *370*, 83-87.
- (164) Pedersen, D. B.; Wang, S. *J. Phys. Chem. C* **2007**, *111*, 17493-17499.
- (165) Xia, Y.; Xiong, Y.; Lim, B.; Skrabalak, S. E. *Angew. Chem., Int. Ed.* **2009**, *48*, 60-103.
- (166) Yeh, M.-S.; Yang, Y.-S.; Lee, Y.-P.; Lee, H.-F.; Yeh, Y.-H.; Yeh, C.-S. *J. Phys. Chem. B* **1999**, *103*, 6851-6857.
- (167) Wu, C.; Mosher, B. P.; Zeng, T. *J. Nanopart. Res.* **2006**, *8*, 965-969.
- (168) Xia, J.; Li, H.; Luo, Z.; Shi, H.; Wang, K.; Shu, H.; Yan, Y. *J. Phys. Chem. Solids* **2009**, *70*, 1461-1464.
- (169) Hohenstein, E. G.; Sherrill, C. D. *J. Phys. Chem. A* **2009**, *113*, 878-886.
- (170) Yin, M.; Wu, C. K.; Lou, Y. B.; Burda, C.; Koberstein, J. T.; Zhu, Y. M.; O'Brien, S. *J. Am. Chem. Soc.* **2005**, *127*, 9506-9511.
- (171) Ribbing, C. G.; Roos, A.; Copper Oxides (Cu<sub>2</sub>O, CuO) A2 - Palik, Edward D. In *Handbook of Optical Constants of Solids*; Academic Press: Burlington, 1997; pp 875-882.
- (172) Peña-Rodríguez, O.; Pablo, P.; Pal, U. *International Journal of Spectroscopy* **2011**, *2011*, 1-10.
- (173) Yang, W. *Appl. Opt.* **2003**, *42*, 1710-1720.
- (174) Wu, J.; Li, X.; Yadian, B.; Liu, H.; Chun, S.; Zhang, B.; Zhou, K.; Gan, C. L.; Huang, Y. *Electrochem. Commun.* **2013**, *26*, 21-24.
- (175) Kumar, B.; Kaur, G.; Rai, S. B. *Indian J. Phys.* **2015**, *89*, 629-634.
- (176) Kawasaki, M. *J. Phys. Chem. C* **2011**, *115*, 5165-5173.

## References

- (177) Longano, D.; Ditaranto, N.; Cioffi, N.; Di Niso, F.; Sibillano, T.; Ancona, A.; Conte, A.; Del Nobile, M. A.; Sabbatini, L.; Torsi, L. *Anal. Bioanal. Chem.* **2012**, *403*, 1179-1186.
- (178) Daff, T. D.; Costa, D.; Lisiecki, I.; de Leeuw, N. H. *J. Phys. Chem. C* **2009**, *113*, 15714-15722.
- (179) Saha, M.; Das, M.; Nasani, R.; Choudhuri, I.; Yousufuddin, M.; Nayek, H. P.; Shaikh, M. M.; Pathak, B.; Mukhopadhyay, S. *Dalton Trans.* **2015**, *44*, 20154-20167.
- (180) Sun, Q.-C.; Ding, Y.; Goodman, S. M.; H. Funke, H.; Nagpal, P. *Nanoscale* **2014**, *6*, 12450-12457.
- (181) Ghodselahi, T.; Vesaghi, M. A.; Shafiekhani, A.; Baghizadeh, A.; Lameii, M. *Appl. Surf. Sci.* **2008**, *255*, 2730-2734.
- (182) Abbe, E. *Arch. Mikrosk. Anat.* **1873**, *9*, 413-418.
- (183) Rottenfusser, R.; Wilson, E.; Davidson, M. Numerical Aperture and Resolution In: *Education in Microscopy and Digital Editing*. Zeiss; [cited April 18, 2017]. Available from: <http://zeiss-campus.magnet.fsu.edu/articles/basics/resolution.html>.
- (184) Poppa, H.; Elliot, A. G. *Surf. Sci.* **1971**, *24*, 149-163.
- (185) Ostendorf, F.; Schmitz, C.; Hirth, S.; Kühnle, A.; Kolodziej, J. J.; Reichling, M. *Nanotechnology* **2008**, *19*, 305705.
- (186) Ziashahabi, A.; Ghodselahi, T.; Heidari saani, M. *J. Phys. Chem. Solids* **2013**, *74*, 929-933.
- (187) Ghodselahi, T.; Vesaghi, M. A.; Shafiekhani, A. *J. Phys. D: Appl. Phys.* **2009**, *42*, 015308.
- (188) Lim, Y.-F.; Choi, J. J.; Hanrath, T. *J Nanomater* **2012**, *2012*, 1-6.
- (189) Saadaldin, N.; Alsloum, M. N.; Hussain, N. *Energy Procedia* **2015**, *74*, 1459-1465.
- (190) Zoolfakar, A. S.; Rani, R. A.; Morfa, A. J.; O'Mullane, A. P.; Kalantar-zadeh, K. *Journal of Materials Chemistry C* **2014**, *2*, 5247-5270.
- (191) Park, E.; Park, H. W.; Lee, J. *Colloids and Surfaces A: Physicochemical and Engineering Aspects* **2015**, *482*, 710-717.

- (192) Dahlang, T.; Sven, T. *J. Phys.: Condens. Matter* **2012**, *24*, 175002.
- (193) Tauc, J.; Grigorovici, R.; Vancu, A. *physica status solidi (b)* **1966**, *15*, 627-637.
- (194) Tauc, J. *Mater. Res. Bull.* **1968**, *3*, 37-46.
- (195) Pankove, J. I. *Optical Processes in Semiconductors*; Prentice-Hall: Englewood Cliffs, N.J., 1971.
- (196) Davis, E. A.; Mott, N. F. *Philos. Mag.* **1970**, *22*, 0903-0922.
- (197) Zarate, R. A.; Hevia, F.; Fuentes, S.; Fuenzalida, V. M.; Zúñiga, A. *J. Solid State Chem.* **2007**, *180*, 1464-1469.
- (198) Bayansal, F.; Kahraman, S.; Çankaya, G.; Çetinkara, H. A.; Güder, H. S.; Çakmak, H. M. *J. Alloys Compd.* **2011**, *509*, 2094-2098.
- (199) Ray, S. C. *Sol. Energy Mater. Sol. Cells* **2001**, *68*, 307-312.
- (200) Santra, K.; Sarkar, C. K.; Mukherjee, M. K.; Ghosh, B. *Thin Solid Films* **1992**, *213*, 226-229.
- (201) Chang, Y.; Teo, J. J.; Zeng, H. C. *Langmuir* **2005**, *21*, 1074-1079.
- (202) Ng, C. H. B.; Fan, W. Y. *J. Phys. Chem. B* **2006**, *110*, 20801-20807.
- (203) Koole, R.; Groeneveld, E.; Vanmaekelbergh, D.; Meijerink, A.; de Mello Donegá, C.; Size Effects on Semiconductor Nanoparticles. In *Nanoparticles: Workhorses of Nanoscience*; de Mello Donegá, C., Ed.; Springer Berlin Heidelberg: Berlin, Heidelberg, 2014; pp 13-51.
- (204) Ahmad, S. *J. Polym. Eng* **2014**, *34*, 279.
- (205) Pfeiffer, C.; Rehbock, C.; Hühn, D.; Carrillo-Carrion, C.; de Aberasturi, D. J.; Merk, V.; Barcikowski, S.; Parak, W. J. *J. R. Soc. Interface* **2014**, *11*
- (206) Zhang, D.; Gökce, B.; Barcikowski, S. *Chem. Rev.* **2017**, *117*, 3990-4103.
- (207) Hastrup, N.; Sedao, X. X. X.; Conneely, A. J.; O'Connor, G. M. *J. Phys. Chem. C* **2011**, *115*, 5028-5037.
- (208) Zhou, J.; Wu, Z.; Zhang, Z.; Liu, W.; Xue, Q. *Tribol. Lett.* **2000**, *8*, 213-218.

## References

- (209) Ghaednia, H.; Jackson, R. L.; Khodadadi, J. M. *J. Exp. Nanosci.* **2015**, *10*, 1-18.
- (210) Thottackkad, M. V.; Rajendrakumar, P. K.; Nair, K. P. *Ind. Lubr. Tribol.* **2014**, *66*, 289-297.
- (211) Khaleduzzaman, S. S.; Saidur, R.; Mahbubul, I. M.; Ward, T. A.; Sohel, M. R.; Shahrul, I. M.; Selvaraj, J.; Rahman, M. M. *Ind. Eng. Chem. Res.* **2014**, *53*, 10512-10518.
- (212) Rimbault, B.; Nguyen, C. T.; Galanis, N. *Int. J. Therm. Sci.* **2014**, *84*, 275-292.
- (213) Jatti, V. S.; Singh, T. P. *J. Mech. Sci. Technol.* **2015**, *29*, 793-798.
- (214) Hernández Battez, A.; González, R.; Viesca, J. L.; Fernández, J. E.; Díaz Fernández, J. M.; Machado, A.; Chou, R.; Riba, J. *Wear* **2008**, *265*, 422-428.
- (215) Hernández Battez, A.; Viesca, J. L.; González, R.; Blanco, D.; Asedegbega, E.; Osorio, A. *Wear* **2010**, *268*, 325-328.

Every reasonable effort has been made to acknowledge the owners of copyright material. I would be pleased to hear from any copyright owner who has been omitted or incorrectly acknowledged.

## Chapter 11: Appendices

## Appendix 2A

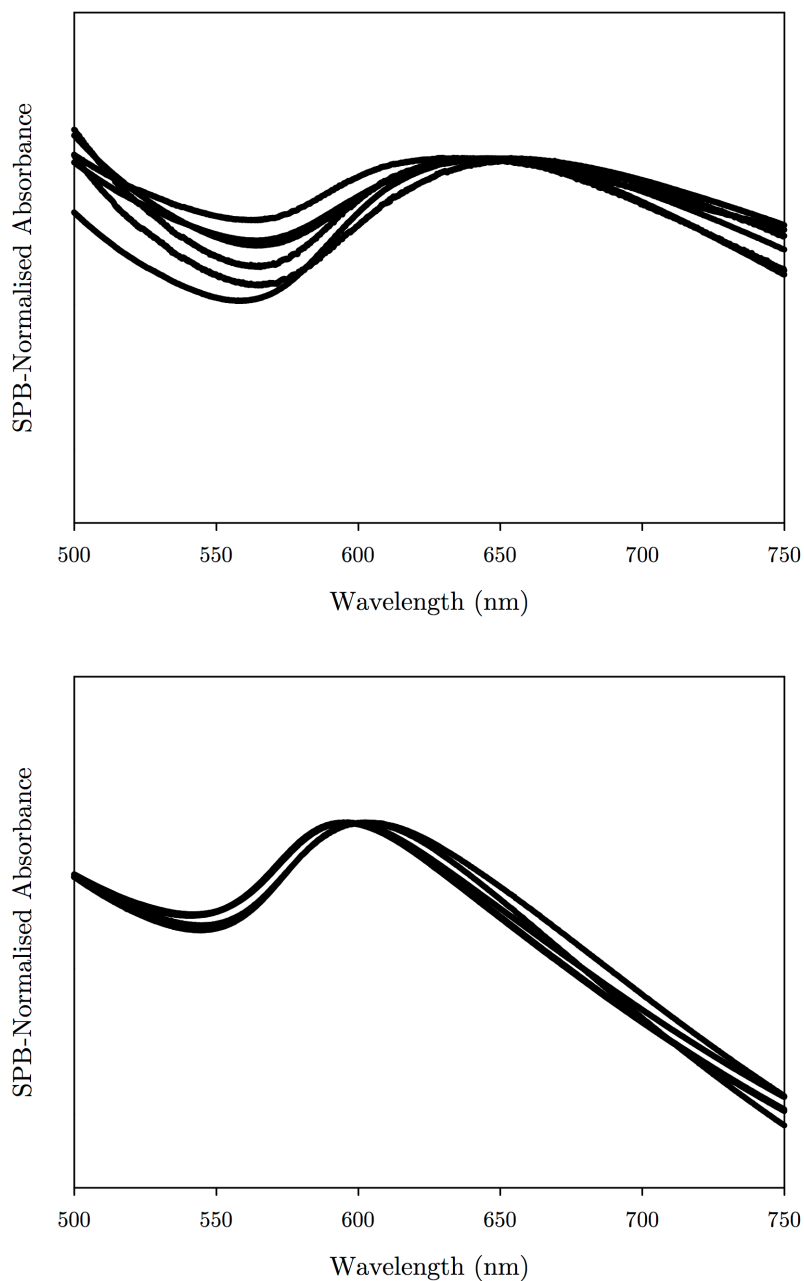


**Figure 11.1** SPB-Normalised UV-vis absorption spectra of CuNPs generated by 60 minutes of LASiS in pure water (TOP PANEL) and  $10^{-4}$  molar **T-4Py** solution (BOTTOM PANEL). In the top panel are six spectra from six different experiments conducted under identical conditions, and in the bottom panel are five spectra from five different experiments. The SPB location in the top panel varies from 638 – 655 nm, while in the bottom panel it varies from 594 – 602 nm.

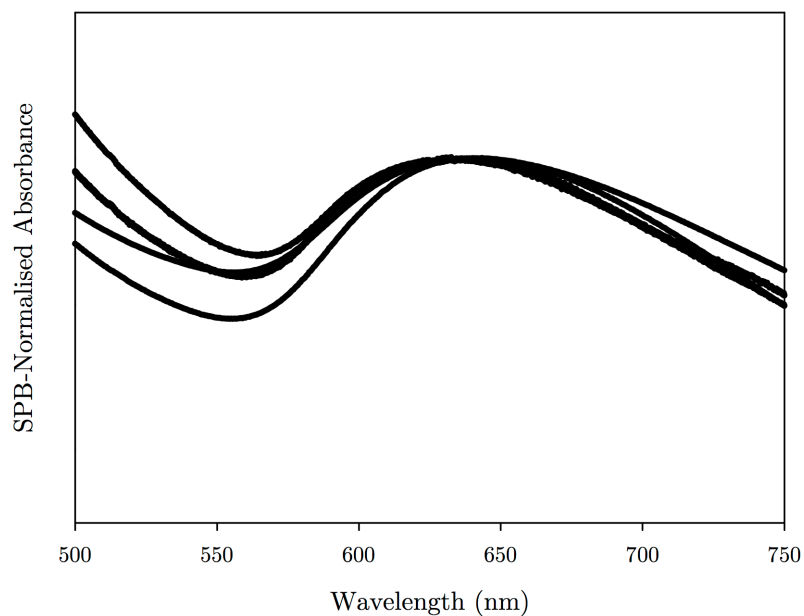


**Figure 11.2** SPB-Normalised UV-vis absorption spectra of CuNPs generated by 60 minutes of LASiS in  $10^{-4}$  molar **Py** solution. In this plot are five spectra from five different experiments conducted under identical conditions. The SPB location varies from 632 – 642 nm.

#### Appendix 4A

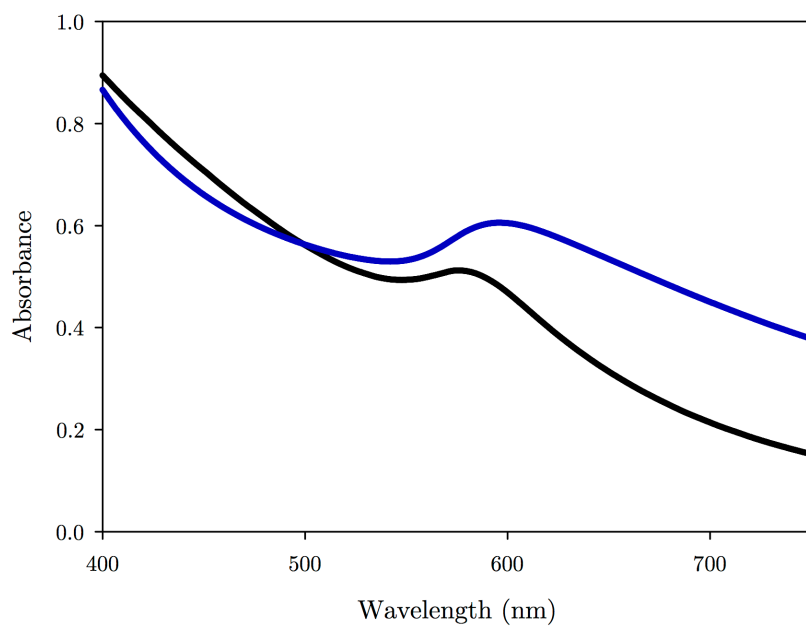


**Figure 11.3** UV-vis absorption spectra of CuNPs generated by 60 minutes of LASiS in  $10^{-4}$  molar **T-4Py** solution (blue trace) and in neat acetone (black trace).

## Appendix 5A

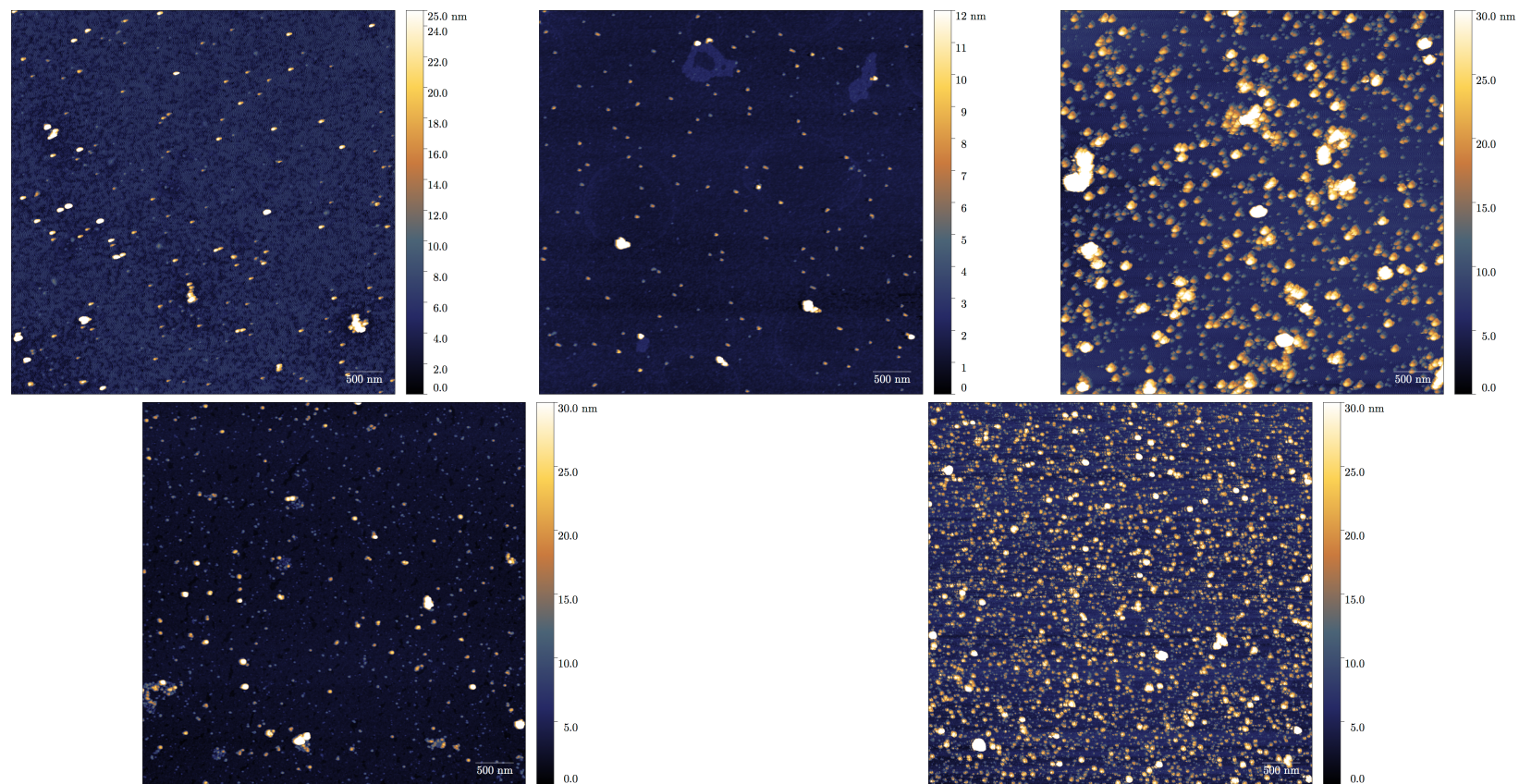


**Figure 11.4** Representative AFM images of CuNPs generated in: (Left to right, top to bottom) Pure Water, **phen**, **bipy**, **Py**, and **4Ph-Py**.

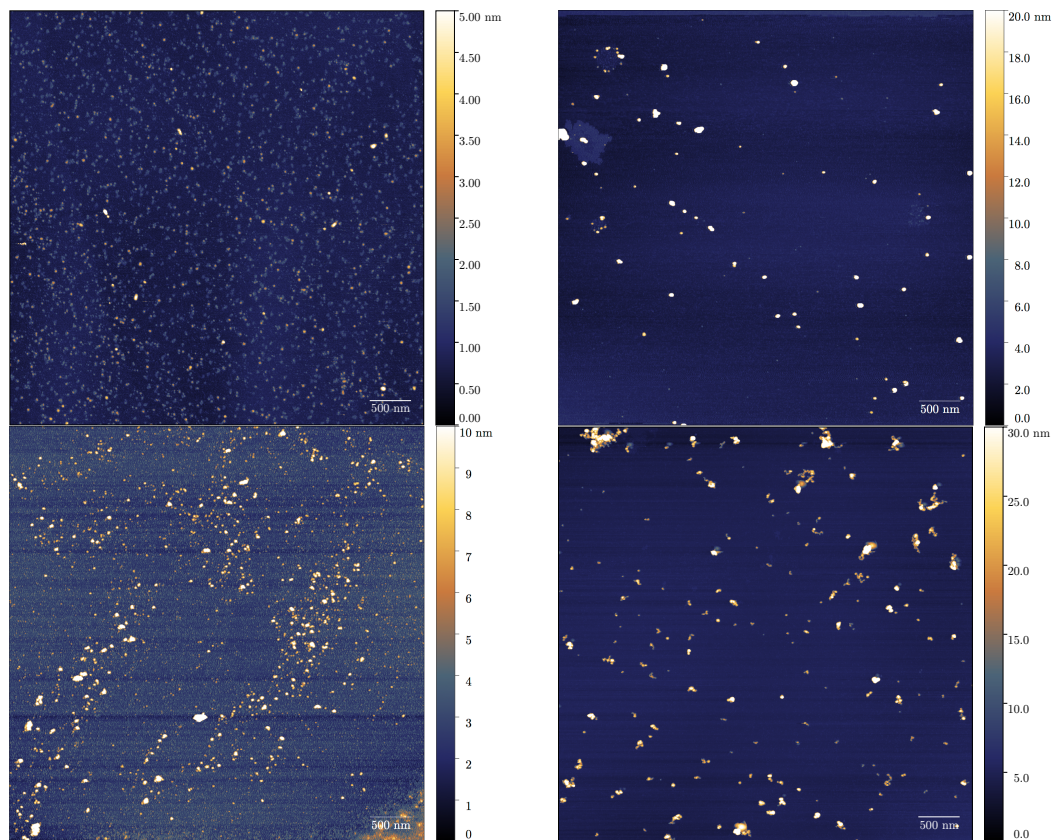


**Figure 11.5** Representative AFM images of CuNPs generated in: (Left to right, top to bottom) **T-Me**, **T-Ph**, **T-3Py**, and **T-4Py**.

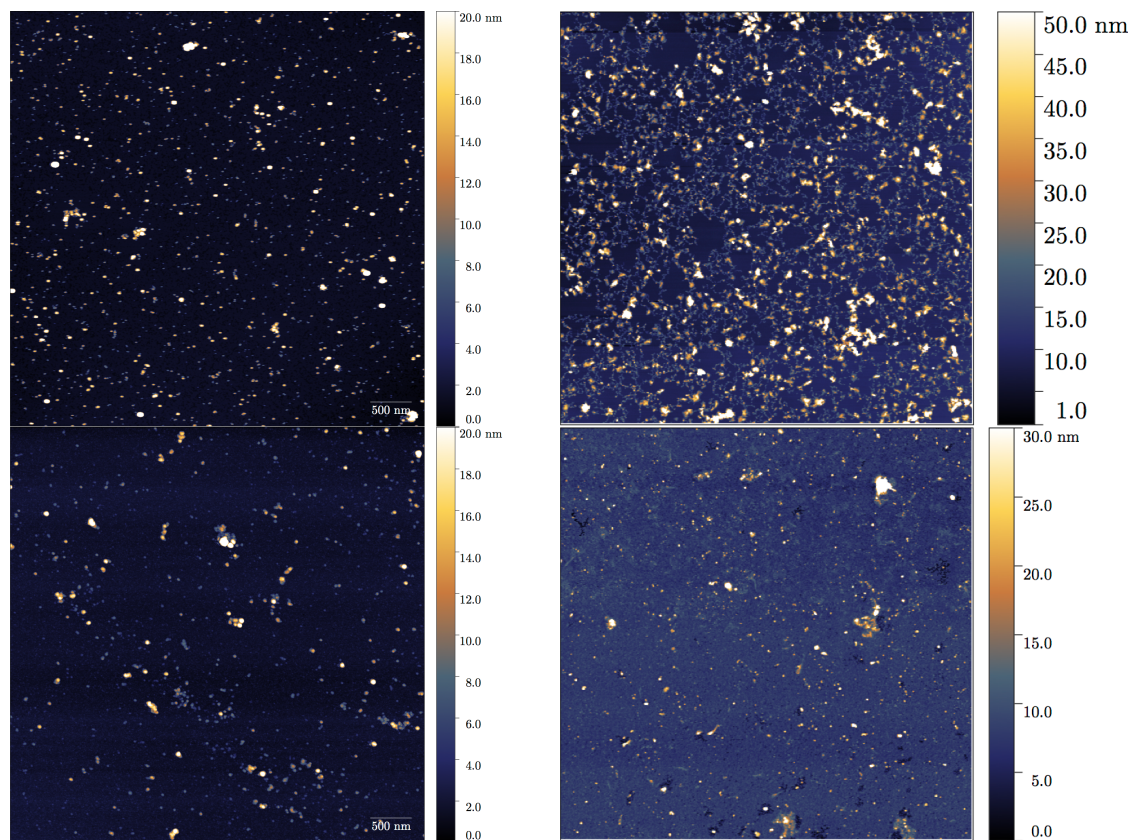


**Figure 11.6** Representative AFM images of CuNPs generated in: (Left to right, top to bottom) **BuT-Me**, **BuT-Ph**, **BuT-3Py**, and **BuT-4Py**.

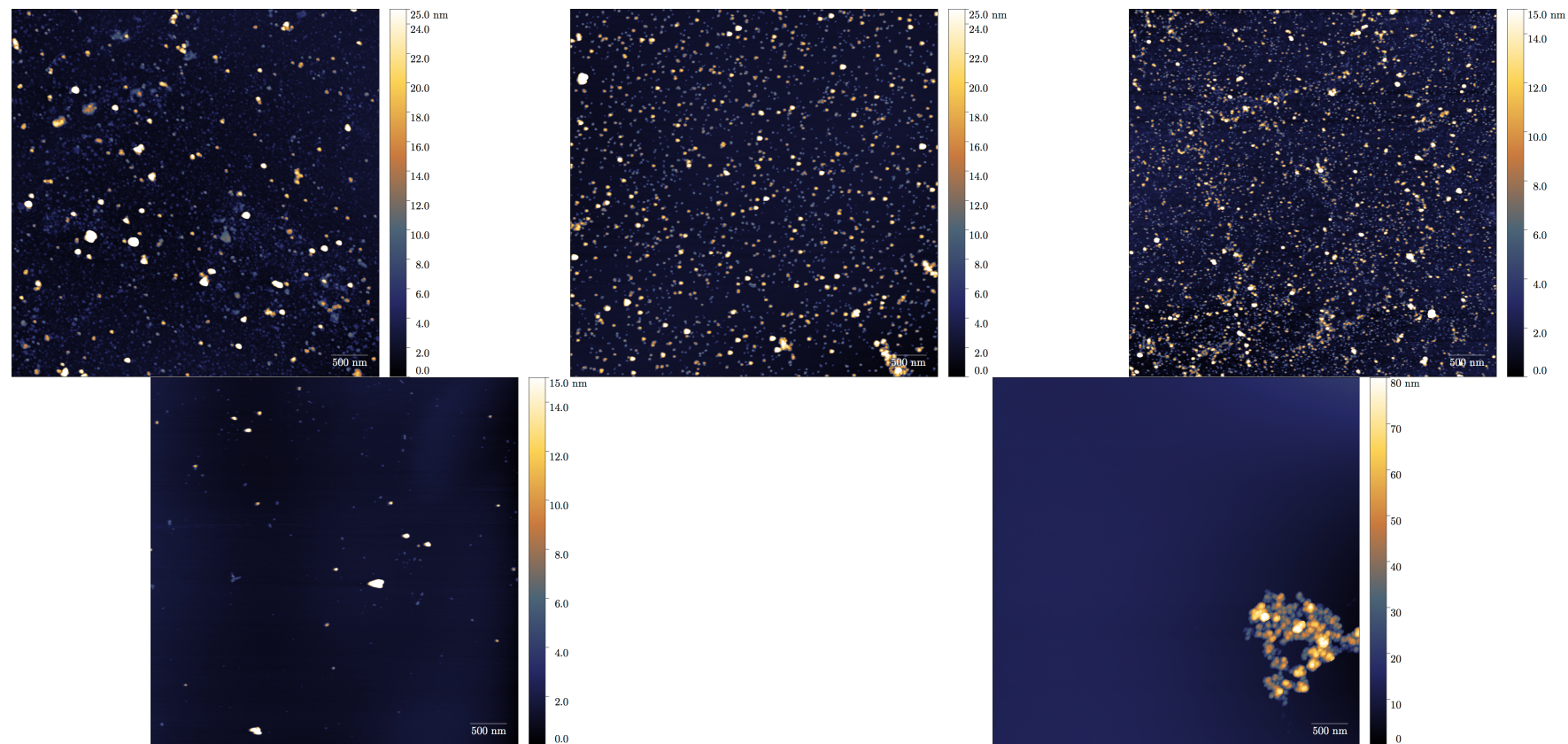


**Figure 11.7** Representative AFM images of CuNPs generated in: (Left to right, top to bottom) **T-2Py**, **BuT-2Py**, acetone, CTAB, and SDS.

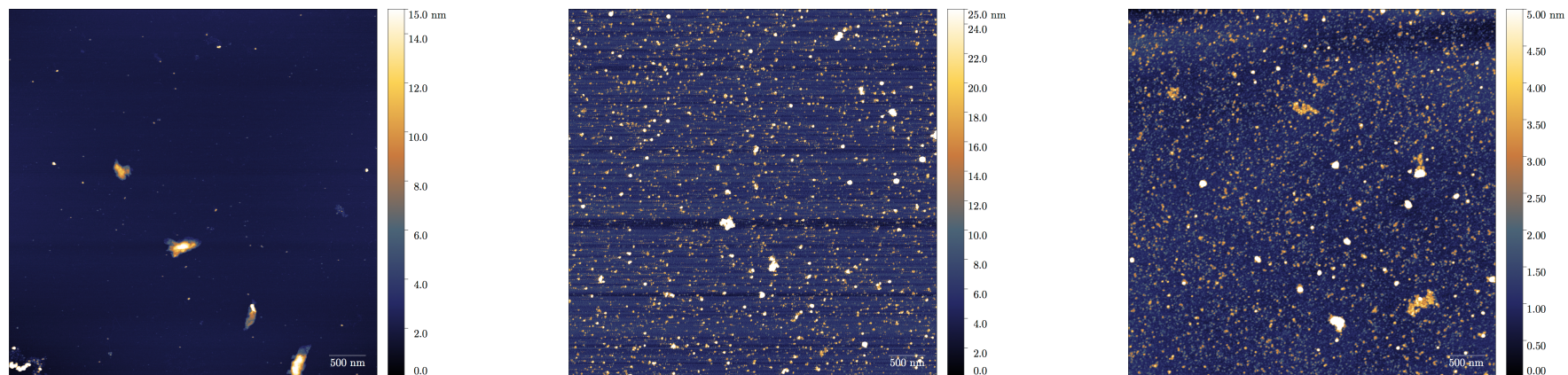


**Figure 11.8** Representative AFM images of CuNPs generated in: (Left to right) **nic-acid**, **ben-acid**, and hydrazine.

## Appendix 5B

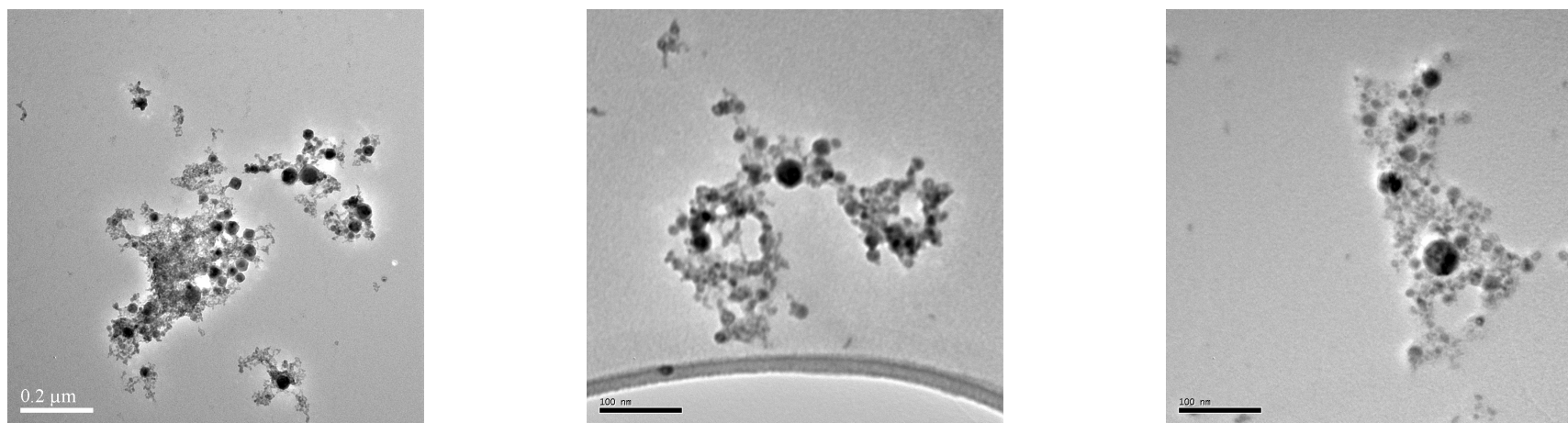


**Figure 11.9** Representative TEM images of CuNPs generated in: (Left to right) blank water, **Phen**, and **Bipy**.

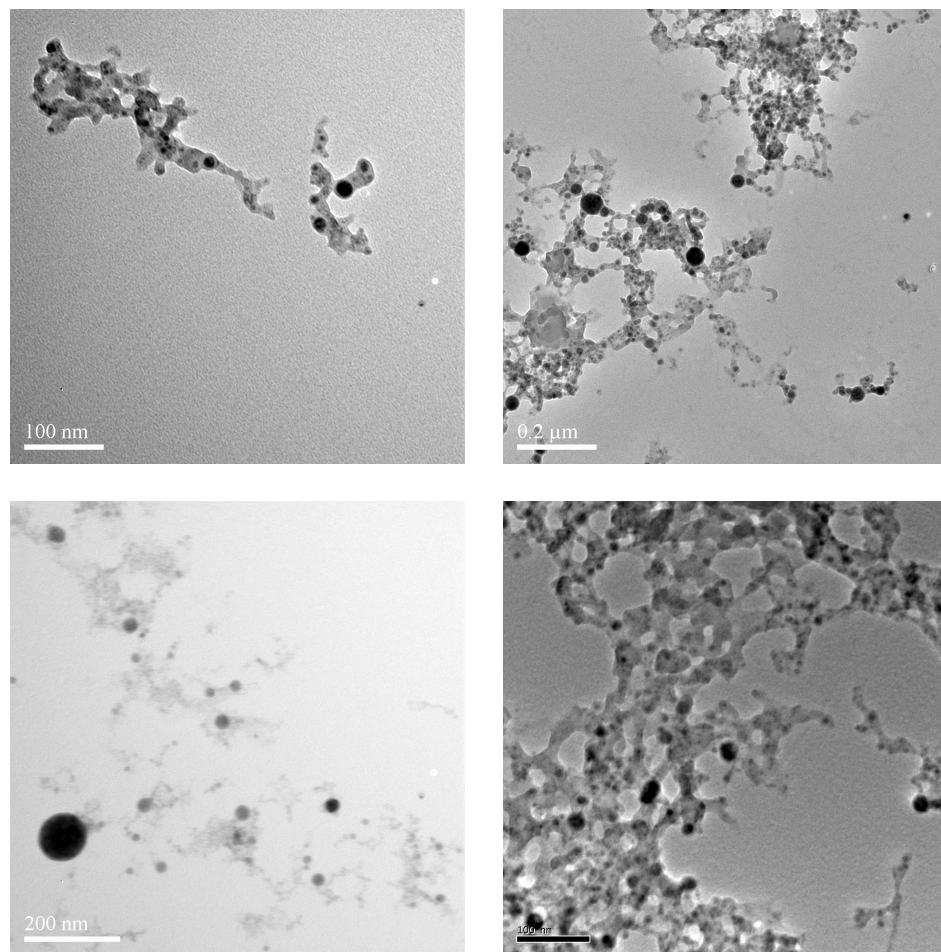


**Figure 11.10** Representative TEM images of CuNPs generated in: (Left to right, top to bottom) **T-3Py**, **T-4Py**, **BuT-3Py** and **T-2Py**

## Appendix 6A

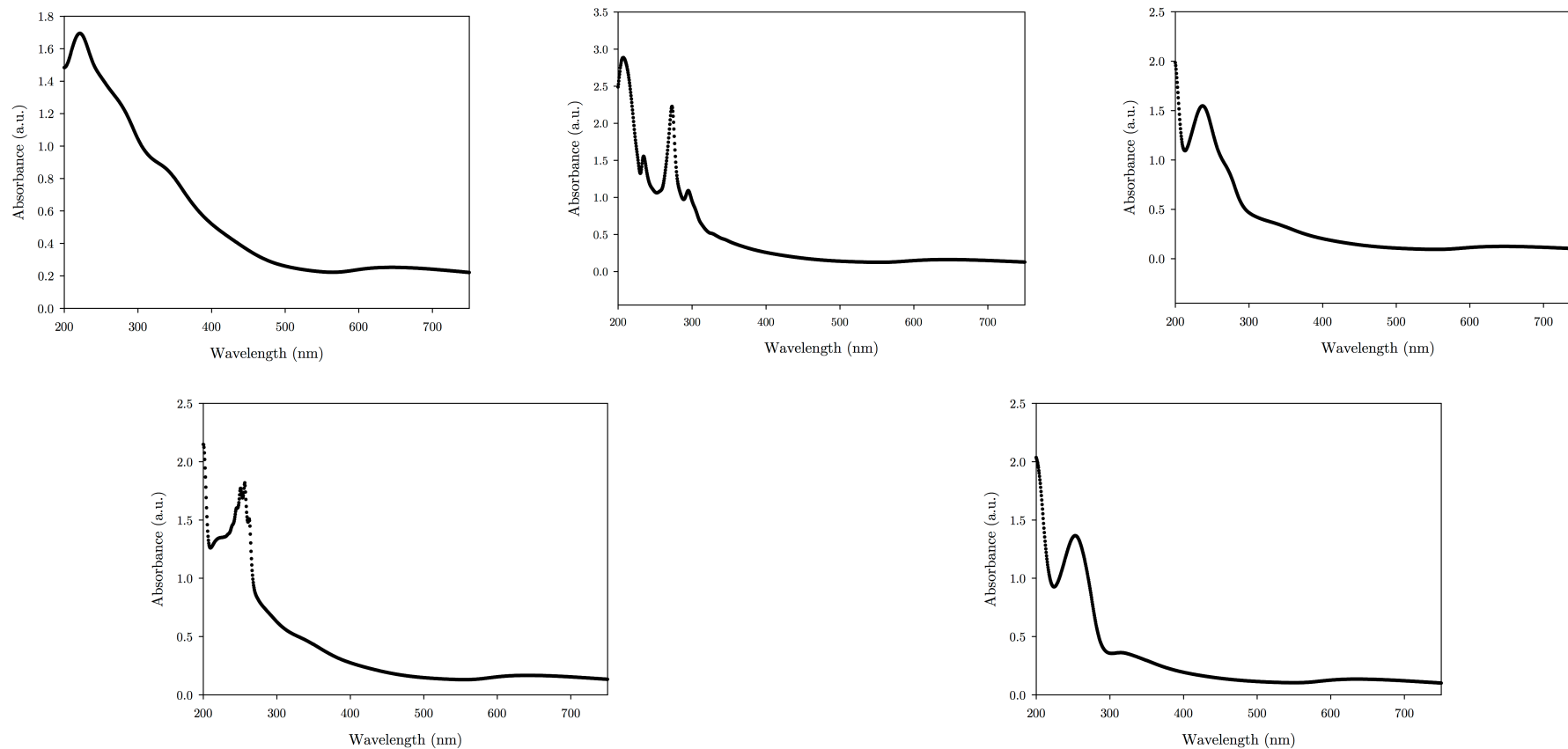


**Figure 11.11** UV-visible absorption data prior to Tauc analysis of CuNPs generated by 60 minutes of LASiS in: (left to right, top to bottom) pure water, **bipy**, **phen**, **Pyr** and **4Ph-Py**.

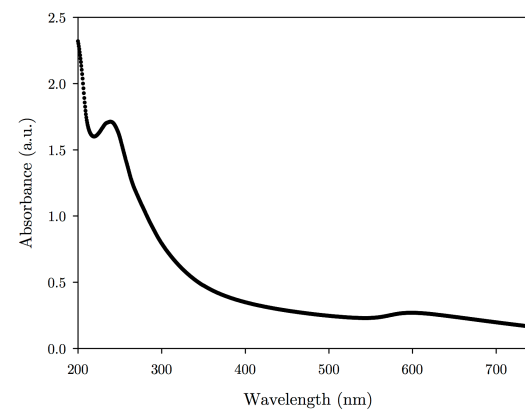
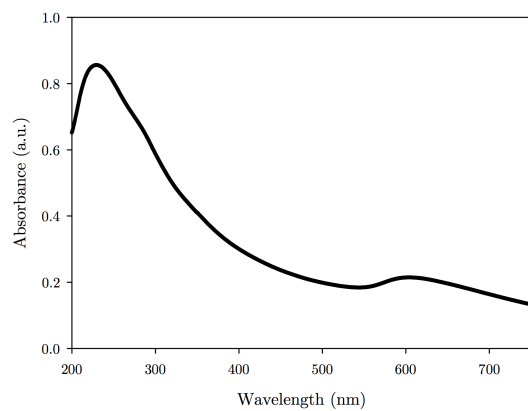
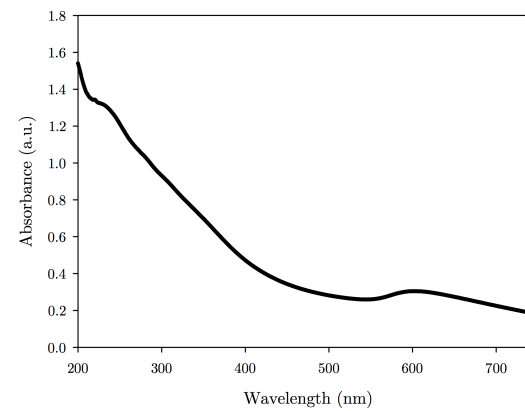
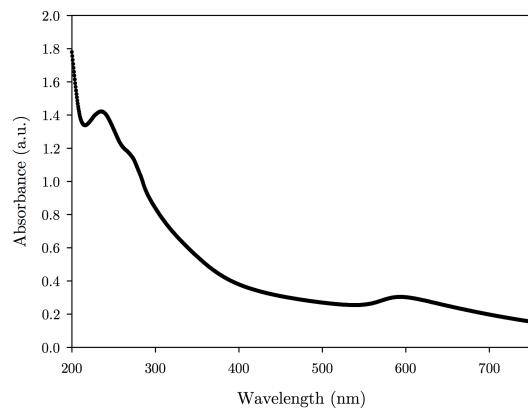


**Figure 11.12** UV-visible absorption data prior to Tauc analysis of CuNPs generated by 60 minutes of LASiS in: (left to right, top to bottom) **T-3Py**, **T-4Py**, **T-Me** and **T-Ph**.

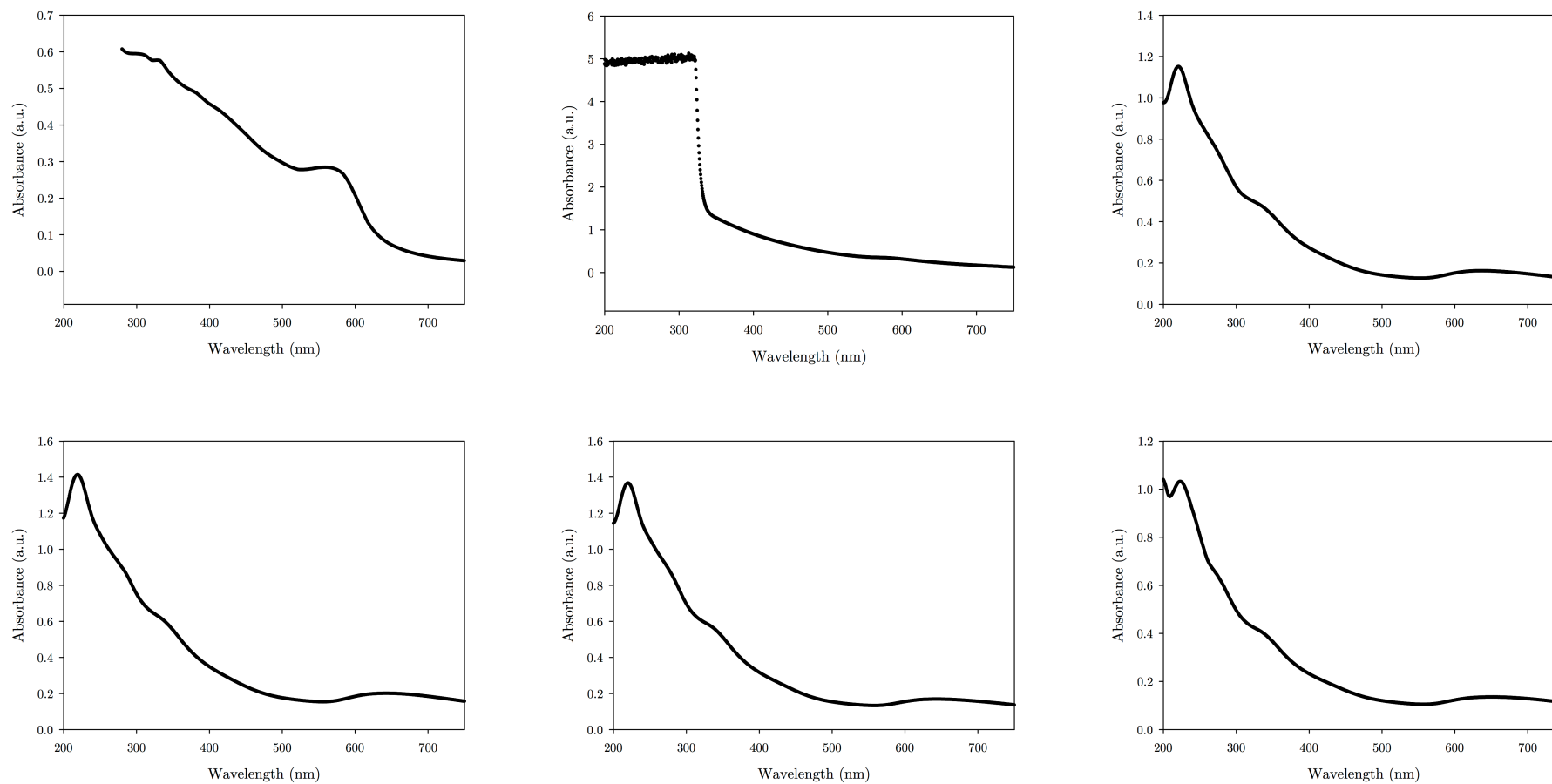


**Figure 11.13** UV-visible absorption data prior to Tauc analysis of theoretical 10 nm diameter CuNPs (top left) and CuNPs generated by 60 minutes of LASiS in: (left to right, top to bottom) neat acetone, **BuT-3Py**, **BuT-4Py**, **BuT-Me** and **BuT-Ph**.

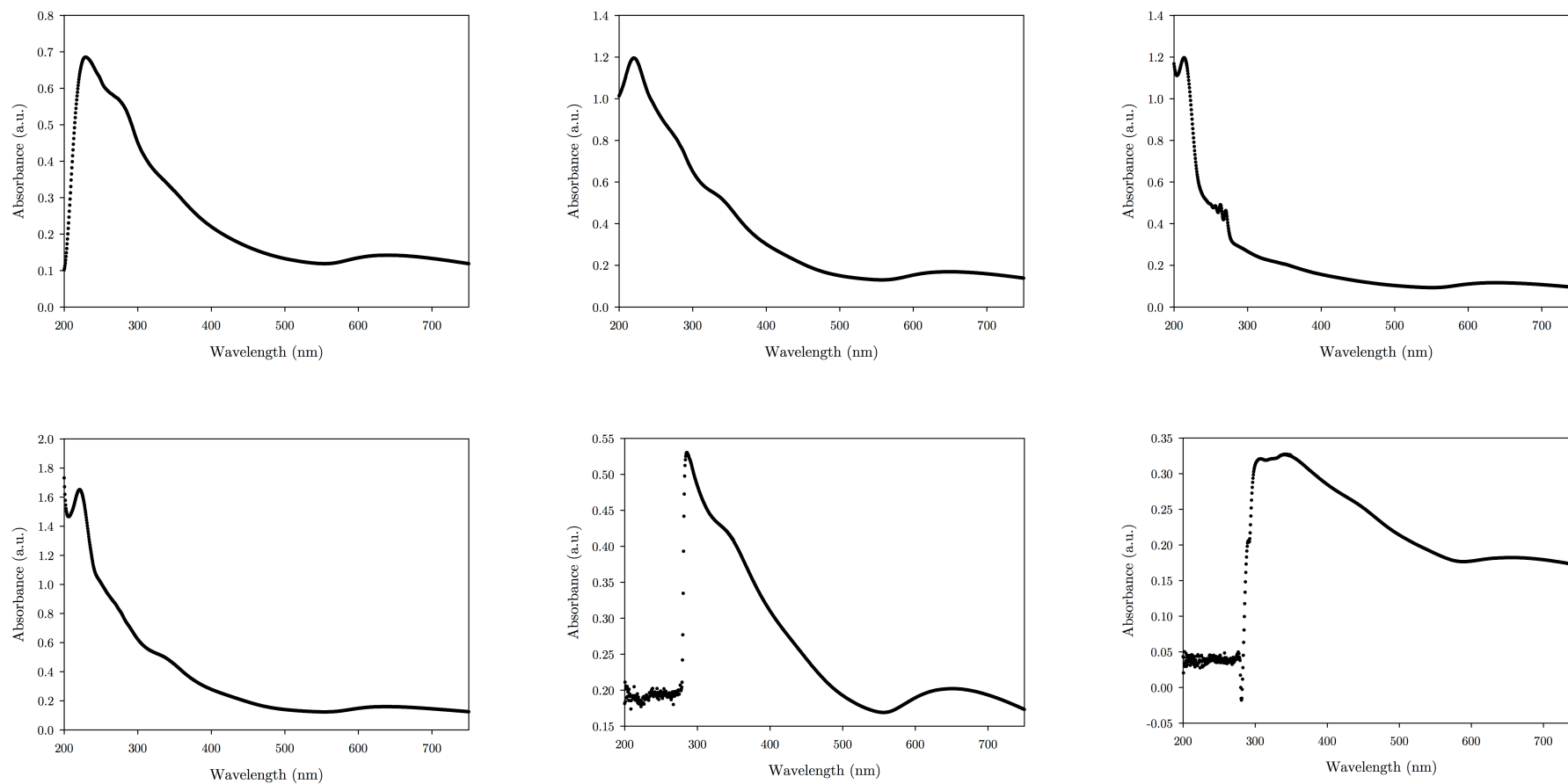


**Figure 11.14** UV-visible absorption data prior to Tauc analysis of CuNPs generated by 60 minutes of LASiS in: (left to right, top to bottom) **T-2Py**, **BuT-2Py**, **nic-acid**, **ben-acid**, **CTAB** and **SDS**.